Title
The role of groundwater in volcanic and fault zone processes

Author
Randolph-Flagg, Noah Gabriel

Publication Date
2019

Peer reviewed|Thesis/dissertation

The role of groundwater in volcanic and fault zone processes

by

Noah Randolph-Flagg

A dissertation submitted in partial satisfaction of the

requirements for the degree of

Doctor of Philosophy

in

Earth and Planetary Science

in the

Graduate Division

of the

University of California, Berkeley

Committee in charge:

Professor Michael Manga, Chair
Professor Roland Bürgmann
Professor Stephen Self
Professor Laura Lammers

Spring 2019

The role of groundwater in volcanic and fault zone processes

Abstract

The role of groundwater in volcanic and fault zone processes

by

Noah Randolph-Flagg

Doctor of Philosophy in Earth and Planetary Science

University of California, Berkeley

Professor Michael Manga, Chair

Groundwater affects volcanic and fault processes at a wide range of spatiotemporal scales. This dissertation focuses on two questions. First, what role does groundwater play in volcanoes and fault zones? Evenly spaced columns of alteration within the Bishop Tuff and numerical models show that boiling controls the cooling rate and pressure within shallow volcanic systems (Chapter 2). Geodetic data and seismic catalogs show that regional hydrologic loads trigger seismic and aseismic slip on faults in and around the Tibetan Plateau (Chapter 6) and on the Longitudinal Valley Fault in Taiwan (Chapter 5) by changing pore pressure within the fault zone. Observations of water level changes in groundwater wells are coincident with dynamically triggered seismicity. I propose that changing permeability during the passage of surface waves drives flow into fractures and faults potentially triggering earthquakes. The second question addressed is how do distant earthquakes change groundwater systems? I document changes in groundwater wells (Chapter 3 and 4), fault zones (Chapter 5), and seismic velocity (Chapter 4 and 5) after the passage of surface waves. These interactions can extend thousands of kilometers from earthquake epicenters and require mechanisms for small stresses to resonate and amplify. This thesis shows that resonances form between tectonic forces and hydrologic systems by changing pore pressure in dilating fractures (Chapter 3), boiling fronts (Chapter 2), and fault zones (Chapter 5 and 6). Together, this dissertation contributes to our understanding of how hydrology and the solid earth interact.

Contents

List of Figures

List of Tables

Acknowledgments

I would like to thank –

My advisor, Michael Manga, for his conscientiousness, kindness, and boundless curiosity.

My mentors and colleagues in the hydrothermal research group at USGS in particular Steve Ingebritsen, Shaul Hurwitz, Bill Evans, Bob Mariner, Deb Bergfeld, and Laura Clor for their support both professional and personal for the past decade, starting even before I decided to study geology.

My mentors at Berkeley—Roland Bürgmann, Steve Self, Laura Lammers, David Shuster, Chi-Yuen Wang, Nick Swanson-Hysell—for so much of their time, support, and guidance.

My time at Berkeley has been shaped by classmates and colleagues. In particular, I would like to thank Ben Black, Steve Breen, Rafael Castro, Brent Delbridge, Jake Edman, Kristen Fauria, Isabel Fendley, Doug Hemingway, Andres Hernandez, Mong-Han Huang, Chris Johnson, Morgan King, Nate Lindsey, Tushar Mittal, Carolina Muñoz-Saez, Avinash Nayak, Ian Rose, Seth Saltiel, Jake Seeley, Courtney Sprain, Taka'aki Taira, Marissa Tremblay, Chelsea Willet, Stephanie Wuerth, and Lian Xue for their insights and conversations.

My postdoc supervisor Tori Hoehler for his patience and for supporting me as I jump into a new field.

My fiancée Alex for her fearlessness in starting a life together, her support through school, her brilliance, and her editing.

Chapter 1

Introduction

Scholars have speculated about the feedbacks among groundwater, volcanoes, and fault zones since antiquity. For example, classical explanations for volcanism and earthquakes focused on the destructive flow of water (*e.g.,* Thales, 580 BC) or vapor (*e.g.*, Aristotle, 395 BC) underground (Howell, 2005). Similarly, hydrologic responses to earthquakes and volcanoes have been documented for millennia (*e.g.,* Pliny, 44 BC). In the modern era, quantitative models for these interactions have largely emerged from laboratory experiments (*e.g.,* Terzaghi, 1951; Biot, 1954) and, more recently, numerical simulations (*e.g.,* Pruess et al., 1983 ; Perfettini and Avouac, 2007). Historically, field observations of fault zones or volcanic centers have been sparse in space and time yet have led to major advances in our understanding. For example, Hubbert and Rubey (1959) proposed a mechanism for water pressure to reduce fault friction inferred from outcrops in northern Europe while Zoback et al. (1987) showed that this reduction in friction in and around the San Andreas Fault suggests that many faults are near failure and sensitive to very small stress perturbations. Despite this long-standing interest and transformative conceptual advances, fundamental questions about tectonic hydrology persist: How do tectonic processes affect distant groundwater? How are volcanic eruptions and earthquakes triggered? The heterogeneity of the earth's crust, the vast spatiotemporal scales at which tectonic processes occur, and the complex coupling between systems that are difficult to observe mean that these larger questions benefit from well-constrained case studies.

This dissertation comprises five studies at three sites that build toward an understanding of the coupling among faults, volcanoes, and groundwater (Figure 1.1). The first two chapters describe work done at Long Valley caldera in eastern California – one of the most seismically and volcanically active areas in the world. In chapter two, I focus on how water boils underground and how long it takes for volcanic deposits to cool. In chapter three, I focus on how the miniscule stresses (equivalent to the weight of an espresso) due to distant earthquakes can cause changes in water wells and cause other earthquakes. The next two chapters describe studies in Taiwan — which has dense monitoring, numerous earthquakes, and a vigorous hydrologic cycle. In chapter four, I focus on how an earthquake in 2016 caused mixing between shallow and deep fluid sources in wells, mud volcanoes, and possibly deeper in the

crust. In chapter five, I examine how seasonal hydrologic loads modulate aseismic creep on a fault in eastern Taiwan and how this behavior changed after a large earthquake in 2003. In chapter six, I look at seasonal modulation of fault slip at the regional scale examining how hydrology, in particular the monsoon, affects seismicity rate.

Figure 1.1: Map of field sites and their assosciated chapters.

While the study of groundwater-tectonic interactions is as old as the study of tectonics itself, new observational tools provide some of the first opportunities to explore these linkages in spatially and temporally resolved, quantitative ways. Satellite observations of ground deformation (GPS and InSAR) and gravity (GRACE) allow an unprecedented regional view of groundwater and stresses (Chapters 4, 5, and 6). New signal processing techniques allow for the identification of background seismicity rates (Chapters 3 and 6), very small earthquakes (Chapter 3), and subtle changes in seismic velocity (Chapters 4 and 5). New hydrologic monitoring (*e.g.,* Chapters 3, 4, and 5), field observations (Chapter 2 and 3), and chemical observations (Chapters 2, 4, and 5) also inform new conceptual models while advances in computing power can now be leveraged to quantitatively interpret observations and test conceptual models (Chapters 2, 3, 4, 5, and 6).

In chapter two, I studied how water boils underground and how volcanic deposits cool at Long Valley Caldera in eastern California (Figure 1.2). Many volcanic eruptions are initiated by hydrothermal explosions, including in the Long Valley region (*e.g.*, Miller, 1985). Disentangling the effects of cooling volcanic deposits from underlying magmatic systems is the source many heated debates (e.g. Chiodini et al., 2016; Hildreth, 2017.) Unlike many other hydrothermal systems, cooling volcanic deposits are short lived and provide a snapshot of hydrothermal processes that may be widespread. Evenly spaced columns of mordenite precipitation record the pattern of groundwater flow due to boiling in an otherwise homogenous porous material. We suggest that this pattern reflects the infiltration of water into a still-cooling volcanic deposit and the geometry of flow induced by this boiling controls the cooling rate of the deposit. We test this conceptual model using two-dimensional fully

coupled computer simulations. This work suggests that patterns of flow that develop due to boiling may control the cooling rate of volcanic deposits and the location and extent of hydrothermal explosions.

In chapter three, I examined how small stresses due to distant earthquakes can cause changes in water wells and trigger other earthquakes also within Long Valley Caldera in eastern California (Figure 1.3). About 10 km west of the columns studied in chapter two, we examined water level and temperature records at a well in fractured crystalline rock that had been shown to respond to large California earthquakes (Roeloffs et al., 2003). Using this new data, we find that water levels drop in response to Rayleigh waves from earthquakes all over the world and that the magnitude of the response is proportional the amplitude of these Rayleigh waves. We also observe that earthquakes that produce large changes in water levels also cause increases in seismicity in and around the caldera. We propose an idealized one-dimensional model to amplify the stresses from these dilatational seismic waves. By allowing hydrologic permeability to increase during dilatation we find that teleseismic waves can cause water to pump into fractures and out of reservoirs. This work establishes a connection between large global earthquakes, small local earthquakes, and groundwater levels and provides a testable quantitative model to link these phenomena.

In chapter four, I examine how nearby earthquakes can cause mixing between shallow and deep fluid reservoirs in Taiwan (Figure 1.3). The 1999 ChiChi Earthquake in Taiwan induced one of the best documented hydrologic responses and greatest number of past studies (*e.g.,* Wang et al., 2001; 2004; 2012; 2016; Geballe, 2011; Jia et al., 2001). Wang et al. (2012) proposed that broad increases in permeability would facilitate mixing between shallow and deep fluid reservoirs. I compiled data from 575 wells within 100 km of a M6 earthquake. Of these records, 270 show water level changes and in settings where there are multiple piezometers at different depths. Changes suggest that breached aquitards allowing different fluid reservoirs to mix. Local mud volcanoes may reflect even deeper fluid sources and isotopic ratios from water samples I collected from four nearby mud volcanoes differ from past measurements, suggesting mixing with isotopically different reservoirs. Finally, I compare these findings with changes in seismic velocity due to the cross-correlation of different components of ground motion at nearby broadband stations. We find decreases in seismic velocity at stations near to wells that also experienced changes in water level. This suggests that changes in seismic velocity reflect changes in permeability which, in turn, facilitate mixing of reservoirs.

In chapter five, I examine how a shallowly creeping fault, about 50 kilometer west of the study site in chapter four, is influenced by the hydrologic cycle and large earthquakes. Slip on the fault during the rainy season is roughly 10 times faster than during the dry season (Chang et al., 2009). I compare these observations to GPS measurements of seasonal deformation suggesting that the seasonal creep is limited to the upper kilometer of the crust. By comparing the timing of the hydrologic load and the increase in slip, we estimate the hydrologic properties of the fault. We observed that seasonality increased after a larger M6.8 earthquake nearby. I model the afterslip on the fault to show that the increase in seasonality persisted for 1-3 years, similar to the recovery of fault permeability observed in

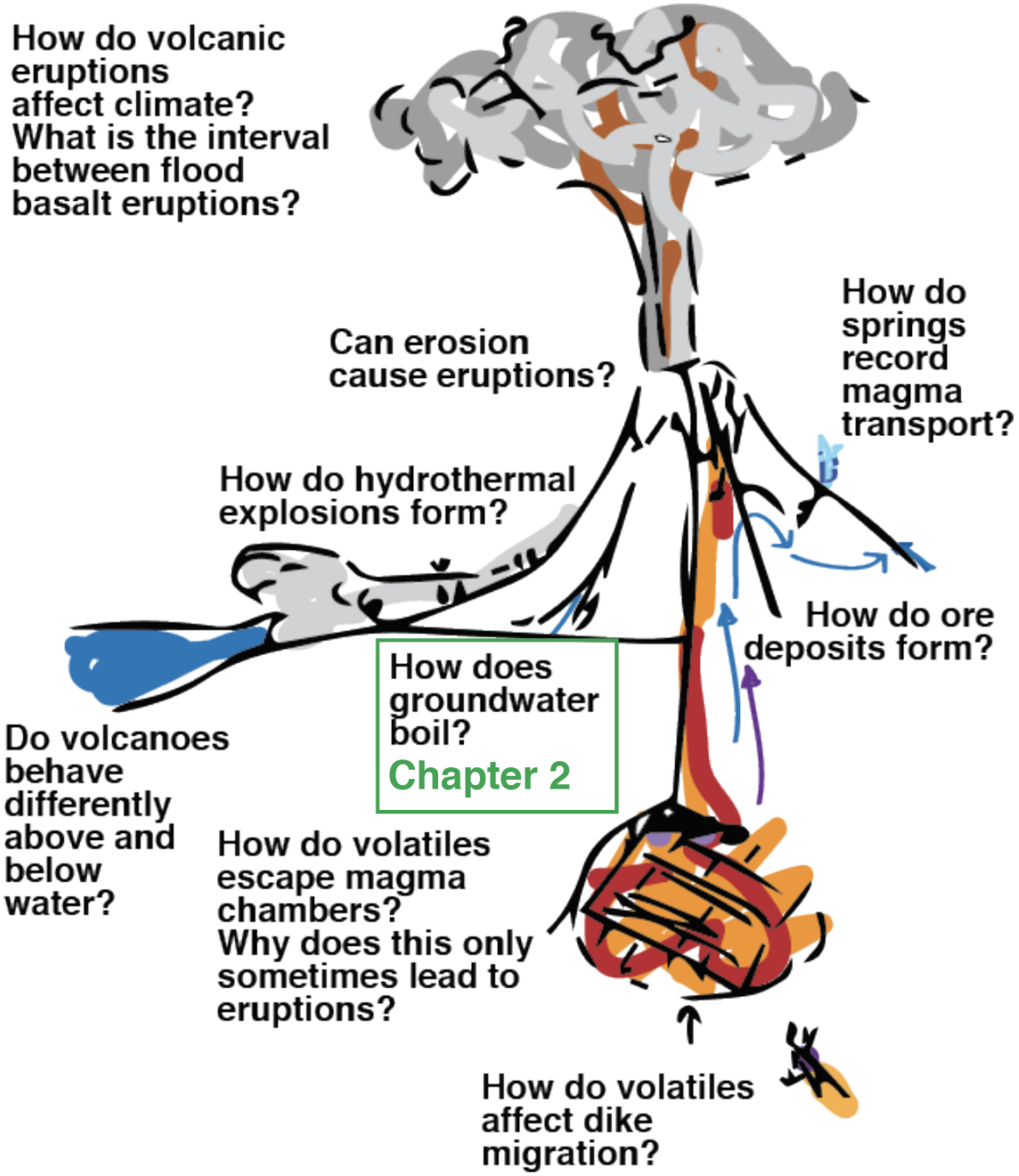

Figure 1.2: Schematic diagram of groundwater and volcano interactions. The green box shows one of the questions addressed in Chapter 2.

other fault zones (*e.g.,* Xue et al., 2011; Fulton et al., 2012). This increase in seasonality is coincident with a change in seismic velocity calculated from a nearby broadband station. We propose that the shallow crust stores elastic energy and that seasonal loads release that elastic energy at depths where the pore pressure is sufficient to permit slip. After the earthquake, the increase in permeability, also recorded by the change in ambient noise seismic velocity, allow for pore pressures to propagate more deeply into the fault and therefore release elastic energy stored more deeply. We model this change using a depth-resolved one-dimensional fluid diffusion model.

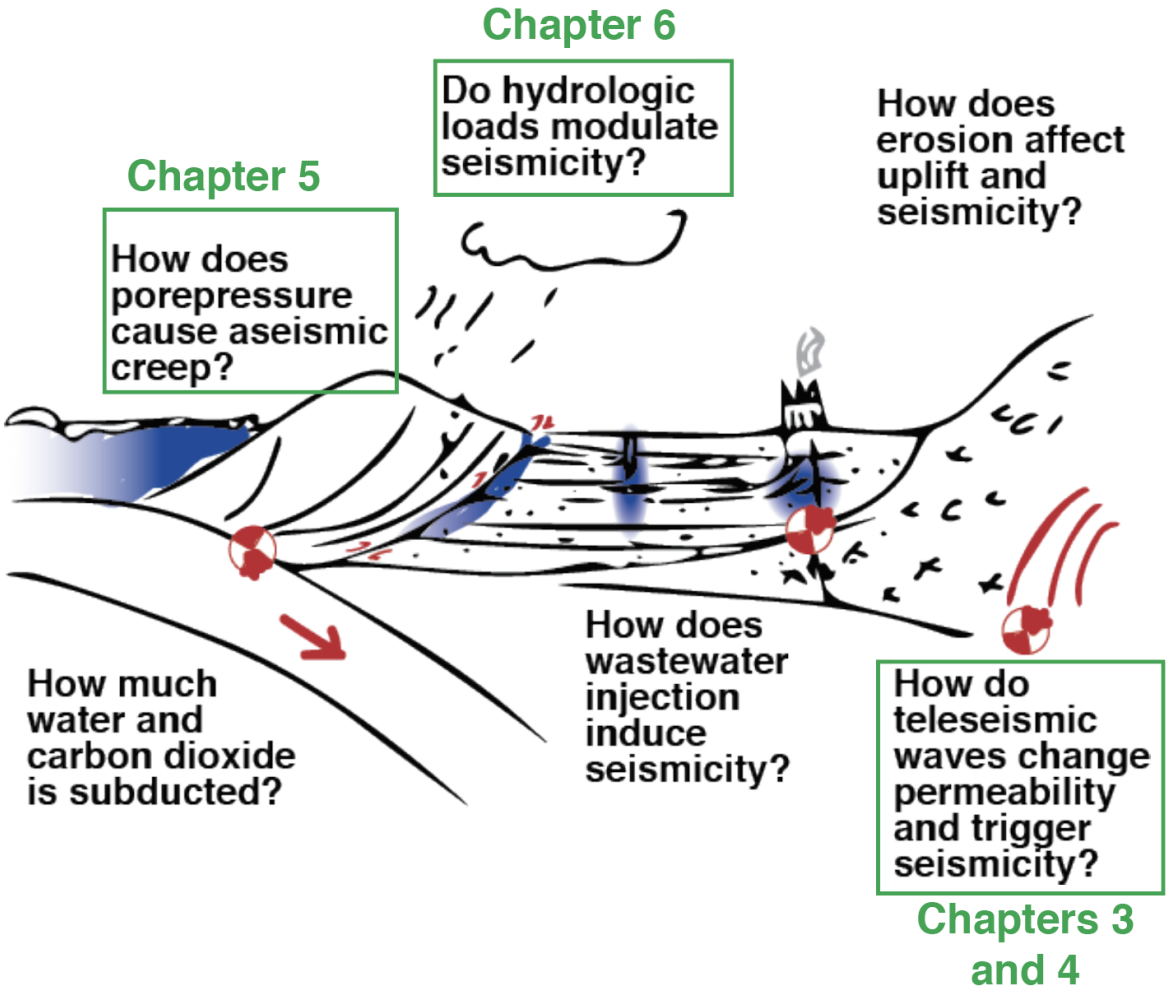

Figure 1.3: Schematic diagram of fault zone and groundwater interactions. The chapters addressing some of these questions are highlighted in green.

In chapter six, I examine seasonal load and seasonal slip at the regional scale to ask if earthquakes are also seasonally modulated and how this modulation occurs. The largest

seasonal hydrologic loads in the world occur due to the monsoon. Indeed, past studies have found that seismicity on the Main Himalayan Thrust Fault may be seasonally modulated, consistent with a two-dimensional model of monsoon loading (Bollinger et al., 2007; Adler et al., 2013). The small number of events on a single fault and the complex three-dimensional loads have made the mechanism of triggering difficult to interpret. To address this, we compare the regional water load inferred from gravity measurements to seismicity rates in and around the Tibetan Plateau. By looking at a very large area, there are many more events to examine the statistical significance of seasonal modulation. We find that a small percentage of regional earthquakes may be seasonally modulated. We use statistical tests to remove aftershock clusters and to test the periodicity in different regions. We find that this modulation is consistent with a complex spatial pattern of loading. We also suggest that the delay in seismicity after loading may be more consistent with pore pressure diffusion rather than the immediate elastic effects of hydrologic loads. This work shows that a small percentage of earthquakes over a broad region may be triggered by increases in pore pressure due to the monsoon.

Together, these studies build towards an understanding of how the groundwater and tectonic processes interact. These studies are motivated by field observations, provide new quantitative measurements, and inspire conceptual models that are then tested with numerical methods. These studies are also unified by the use of periodic forcing (*e.g.*, seismic waves or seasonal loads) to understand the response of tectonic systems or the emergent periodicity that occurs due to groundwater processes (*e.g.*, boiling). Below I briefly return to the overarching questions of this dissertation.

How do tectonic processes affect distant groundwater? At Long Valley Caldera (Chapter 3) we found that dilatational Rayleigh waves cause pumping from fractured reservoirs into faults or fractures. In Taiwan, we found that earthquakes increase permeability (Chapter 4 and 5) allowing for mixing between deep and shallow reservoirs (Chapter 4) and that this permeability change may be reflected in changes in ambient noise seismic velocity (Chapter 4 and 5).

How are volcanic eruptions and earthquakes triggered? At Long Valley Caldera we find that hydrothermal explosions are likely controlled by the emergent patterns of flow due to boiling (Chapter 2). Nearby earthquakes may be triggered due to the dilatational Rayleigh waves which cause pumping from fracture zones into faults increasing their pore pressure (Chapter 3). In eastern Taiwan, we found that seasonal loads release elastic strain and the depth of the release is controlled by the fault zone permeability which, in turn, changed after a distant earthquake (Chapter 5). In and around the Tibetan Plateau, we found that some seismicity is likely caused by the spatially complex monsoonal loading (Chapter 6).

Chapter 2

Evenly spaced columns in the Bishop Tuff (California, USA) as relicts of hydrothermal cooling

This chapter was previously published in Randolph-Flagg, N.G., Hernandez, A., Breen, S. Manga, M., Self, S. (2017) Erosional columns in the Bishop Tuff as relicts of hydrothermal cooling, *Geology*, doi: 10.1130/G39256.1

2.1 Abstract

A few square kilometers of the Bishop Tuff in eastern California (USA) have evenly spaced columns that are more resistant to erosion than the surrounding tuff owing to the precipitation of mordenite, a low-temperature (100–130 °C) zeolite. We hypothesize that the columns are a result of instabilities at the liquid water and steam interface as cold water seeped into the still-cooling Bishop Tuff. We use two methods to quantitatively assess this hypothesis. First, scaling shows which hydrodynamic instabilities exist in the system. Second, to account for the effects of multiphase flow, latent heat, and the finite amplitude and temporal evolution of these instabilities we use two-dimensional numerical models of liquid water infiltrating hot tuff. These tests highlight several features of boiling hydrothermal systems. (1) The geometry of at least some convection appears to be broadly captured by linear stability theory that neglects reactive transport, heterogeneity of the host rock, and the finite amplitude of instabilities. (2) Slopes >10% set the wavelength of convection, meaning that these columns formed somewhere with relatively gentle topography. (3) For permeabilities of $>10^{-13}$ m^2, the wavelength of the instability changes through time, slowing infiltration, while for permeabilities $<10^{-15}$ m^2, cooling is dominated by conduction. The spacing and stability of columns increase with higher vertical permeability and decrease with higher horizontal permeability. These columns are a rare window into hydrothermal processes that may be widespread.

2.2 Introduction

Observations of active hydrothermal systems are sparse and, even in geothermal wells, constrained to relatively shallow depths. By contrast, exhumed fossil hydrothermal systems can be fully exposed but preserve the complicated, time-integrated history of each system. In either case, it is difficult to observe the fine-scale dynamic processes transporting heat and mass. Laboratory, analytical, and numerical studies have tried to understand how liquid water and steam interact within permeable rocks and whether they produce periodic instabilities in space (*e.g.*, Woods, 1999; Coumou et al., 2008) and/or time (*e.g.*, Vandemeulebrouck et al., 2005) or produce stable multiphase zones (*e.g.*, Udell, 1985). Hydrothermal alteration in pyroclastic flow deposits (ignimbrites or ash-flow tuffs), preserves the short-lived cooling history of relatively homogeneous rock and thus offers an unusual opportunity to understand widespread but difficult to observe processes such as groundwater boiling.

The cooling rates of volcanic deposits are accelerated by groundwater flow (*e.g.*, Keating, 2005). Quartz-hosted glass inclusions in the Bishop Tuff (eastern California, USA) suggest that some of the interior of the tuff cooled ∼1 °C/yr, consistent with conductive (not advective) cooling models (Wallace et al., 2002). However, evidence of hydrothermal cooling is pervasive in the tuff, including high-temperature fumaroles that persisted for only ∼10 yr after the caldera-forming eruption (Holt and Taylor, 1998). The analogous Valley of Ten Thousand Smokes ignimbrite (Alaska) continues to hydrothermally cool a century after the AD 1912 Novarupta eruption (Hogeweg et al., 2005).

Previously reported columnar erosional features in the Bandelier Tuff (New Mexico) are attributed to the interaction between the nonwelded tuff and circulating hot water (Bailey and Self, 2010). We integrate field observations of unstudied columns in the Bishop Tuff, theory, and numerical simulations to evaluate the hypothesis that these columns are relicts of hydrothermal instabilities.

2.3 Geologic Setting

The Bishop Tuff formed at the eastern foot of the Sierra Nevada range during the 760 ka Long Valley explosive rhyolite (74%–78% SiO_2) eruption (Hildreth and Wilson, 2007). The tuff produced by this 600–650 km^3 supereruption extends >70 km downslope of the Long Valley caldera, and, within the caldera, up to 1.5 km thick. The tuff erupted over a few days to years (Hildreth and Wilson, 2007) with welding, high-temperature vapor phase zones, devitrified fumarolic mounds (*e.g.,*Holt and Taylor, 1998), and elutriated gas-escape pipes all forming soon after due to reactions between volatiles and rhyolitic glass.

2.4 Observations

Evenly spaced erosional columns pervade at least a few square kilometers of the nonwelded Bishop Tuff (Figure 2.1). The highest elevation outcrops are below the oldest paleolake

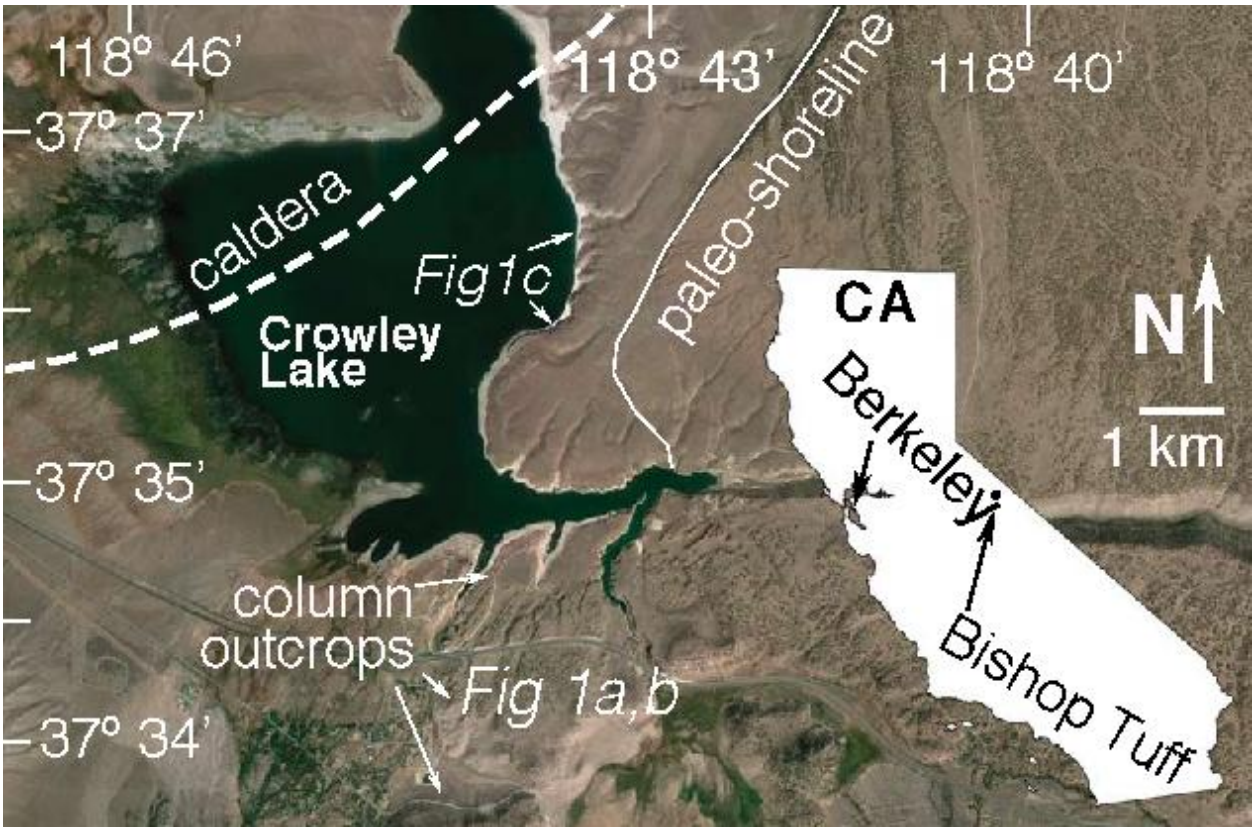

Figure 2.1: Map of Bishop Tuff near Lake Crowley reservoir (California, USA). White dashed line shows approximate location of the caldera topographic margin from Bailey et al. (1976).

terrace at ∼2250 m elevation (Bailey et al., 1976). Columns occur in some (but not all) nonwelded regions of the tuff, for example, they are widespread in the marked positions on Fig. 2.1; they are not visible in any welded or vapor-phase altered regions. Nearly identical columns exist in white tuff with >10 cm pumice and lithic clasts, some of the first tuff erupted (ignimbrite unit Ig1Ea; Hildreth and Wilson, 2007), and in more homogeneous pinkish tuff with <1 cm clasts (Supplemental Figure 2.6), some of the last tuff erupted (Ig2b; Hildreth and Wilson, 2007).

The erosional columns are usually vertical with some tilted (Supplemental Figure 2.7) and rare branching columns (Figure 2.2A, bottom right). A survey of hundreds of columns (Supplemental Figure 2.8) suggests regular spacing locally (∼0.8–4 m column center to column center) with column diameters ranging from 0.3 to 1 m. Figure 2.2C is representative of outcrops along the northeast shore of the human-made Lake Crowley, where unaltered tuff has been eroded since A.D. 1941 to expose columned caves. Beach and road outcrops have column nubs that have similar spacing and morphology. A few of these exposures appear to have north-northeast–south-southwest–trending lineaments of columns and rarer parallel and pseudo-cellular walls with roughly similar spacing (Supplemental Figure 2.8A). Columns

persist with constant aspect ratio through minor compositional changes in the tuff and are continuous across thin horizontal Plinian deposits. Vertical elutriation pipes are crosscut by tilted columns (Supplemental Figure 2.7). All columns that we observed have joints perpendicular to the column with a width/joint spacing ratio of ∼0.8. This ratio is similar to the ratio of vertical joints to horizontal sedimentary bed thickness. This suggests that similar differences in the elastic properties of horizontal layers that cause strain localization (*e.g.*, Bai et al., 2000) may be occurring on the vertical cylindrical columns during cooling or unloading.

The quarry outcrops (Supplemental Figure 2.6) show the base of the Bishop Tuff with a thick (>5 m) white Plinian deposit overlain by ∼8 m of pinkish tuff with no erosional columns. Where developed, the columns grow from nothing to ∼50 cm diameter over 3 m of massive tuff. Outcrops are mostly within several meters of the Bishop Tuff base and, in some places, hundreds of meters of overlying tuff have been eroded since the columns formed. Similar columns in the Bandelier Tuff also exist a few meters above the base of the tuff (Bailey and Self, 2010).

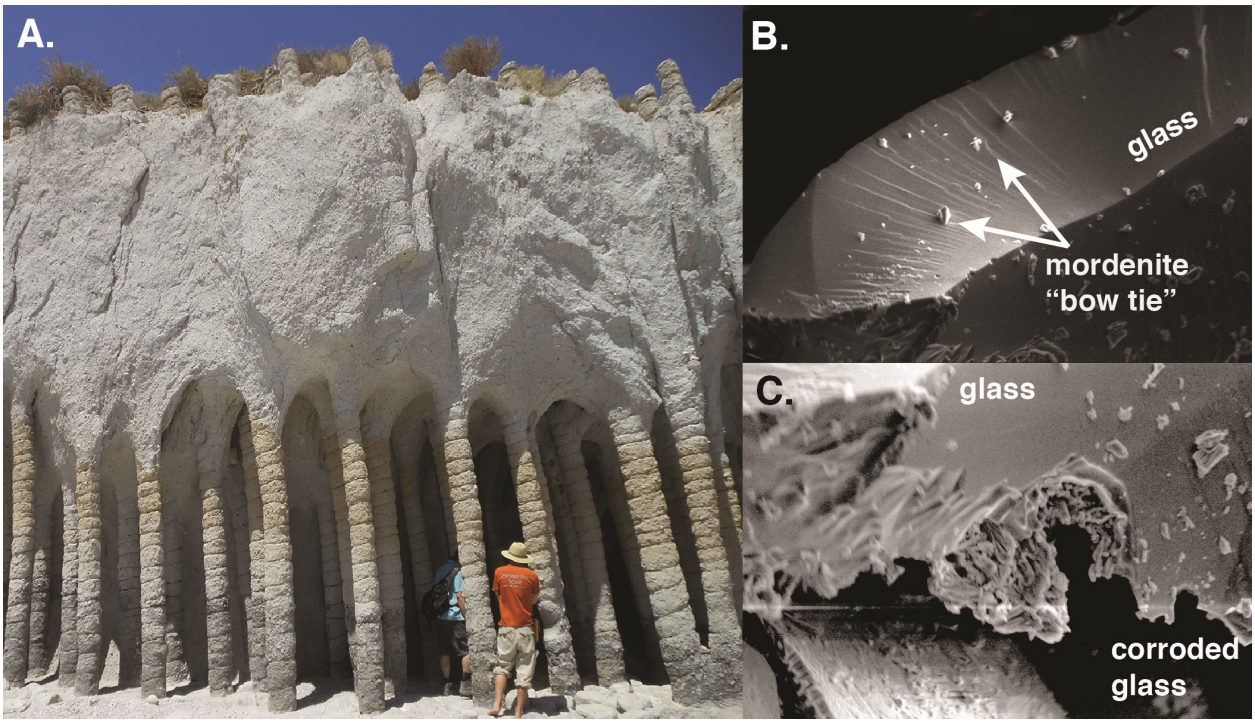

Figure 2.2: A. Photo from beach of Lake Crowley (California, USA; people for scale). Columns extend from wave eroded caves through non-welded tuff and up above the outcrop. B,C. Scanning electron microscope images for the columns (37°34′20.8″N, 118°42′57.9″W) showing distinctive mordenite crystal structures on pitted volcanic glass fragments.

X-ray diffraction (XRD) spectra show that the only mineralogical difference between

the columns and surrounding material is the mineral mordenite [(Ca, Na_2, K_2)$Al_2Si_{10}O_{24}$• $7H_2O$], a low-temperature zeolite also found in similar columns in the Bandelier Tuff (Bailey and Self, 2010). XRD of the noncemented tuff surrounding the columns shows no measurable zeolite precipitation (Supplemental Figure 2.9); samples taken from the columns show mordenite precipitation. Scanning electron microscope images from the columns show distinctive 1–3 µm mordenite "bow-tie" crystals every few micrometers on pitted volcanic glass shards (Figure 2.2 B and C). Dry experiments in Yucca Mountain Tuff (Nevada) found mordenite growth when heated to 120–200 °C, although those samples also had clinoptilite [(Na, K, $Ca)_2$-$3Al_3$(Al, $Si)_2Si_{13}O$• $12H_2O$], another zeolite. Field observations in the Yucca Mountain Tuff using illite and smectite ratios as a paleothermometer imply that clinoptilolite forms from 90 to 100 °C, mordenite forms from 100 to 130 °C, and analcime forms from 175 to 200 °C (Bish and Aronson, 1993).

2.5 Hypothesis

We test the "heat-pipe" steam-liquid counterflow hypothesis. In our conceptual model, the tuff is emplaced and instantly begins to slump along paleodrainages. At the surface, where heat can be transported by wind (forced convection), the tuff cools quickly. By contrast, the interior of the tuff cools much more slowly due to conduction alone. Water pools in low-lying regions, forming ponds or lakes, and then percolates into the tuff. Infiltrating water heats and boils, generating evenly spaced fingers of upwelling steam that condenses before reaching the surface, and downwelling water that boils at its base (Bailey and Self, 2010). We suggest that downwellings may precipitate mordenite because ions are only transported in the liquid phase and, in plan view, the columns are small relative to the surrounding material, implying that they record the denser phase. Later, when the tuff begins to erode (Figure 2.3), these mordenite-cemented downwellings are preserved while the uncemented tuff is eroded away.

Although columnar jointing is common in the welded Bishop Tuff, jointing cannot explain the distances between columns, the lack of visible fractures in the surrounding material, or the hydrothermal alteration. These columns crosscut subvertical elutriation pipes and are cemented by a low-temperature zeolite, indicating that they formed after the elutriation pipes and at lower temperatures. Similarly, fossil fumaroles caused by the escape of water and gas trapped beneath or within pyroclastic density current deposits produce high-temperature (>500 °C) alteration and devitrification (*e.g.*, Holt and Taylor, 1998) rather than the low-temperature alteration we observe.

2.6 Scaling

If surface water sank into the cooling tuff from above, there would be three possible drivers of groundwater flow: thermal convection within the steam or liquid, instabilities at the steam-liquid interface, and topographically forced flow.

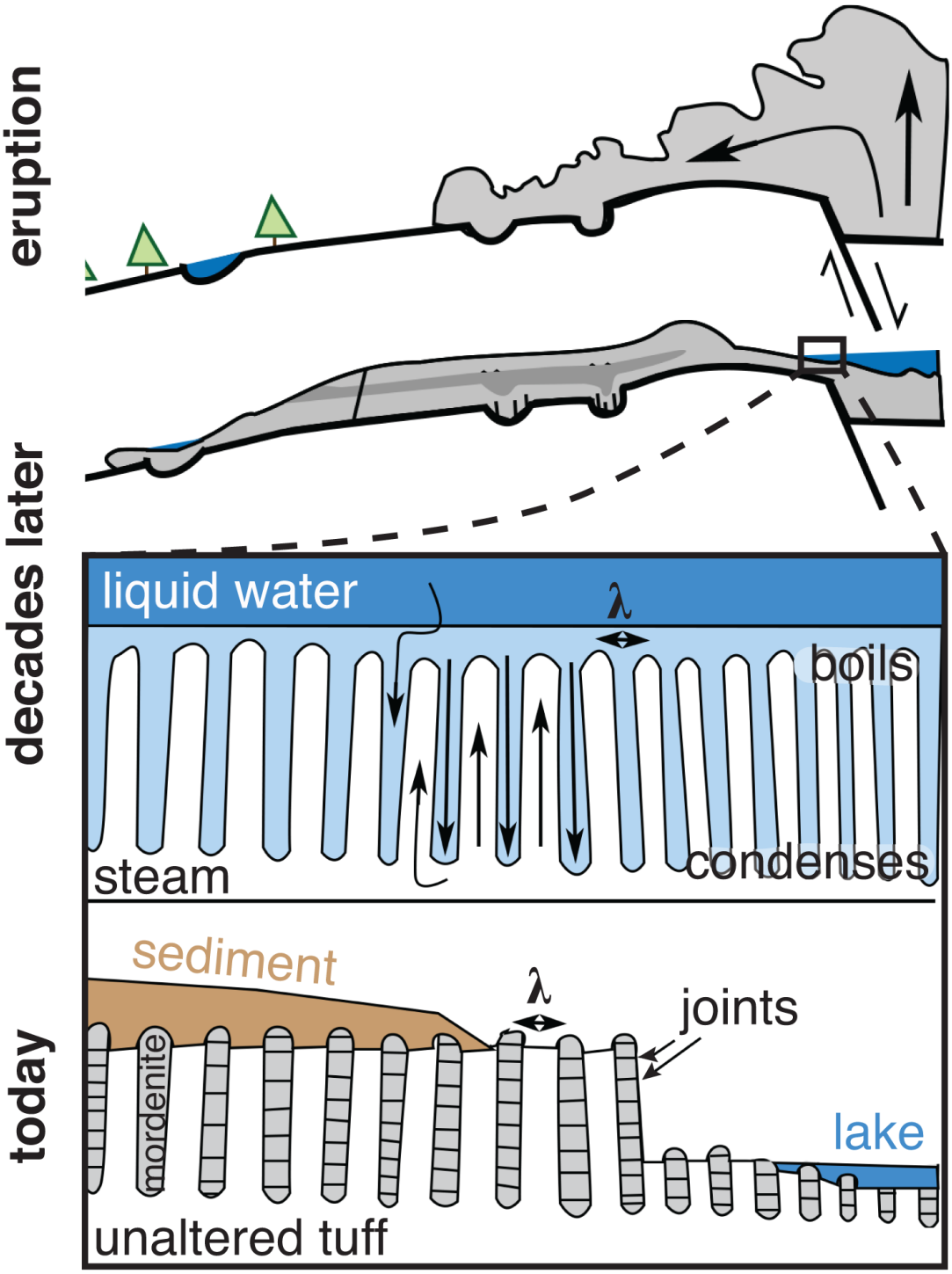

Figure 2.3: Schematic illustration of the Long Valley caldera (California, USA) forming eruption (top), our hypothesis of the still-cooling deposit (middle), and the modern outcrop similar to that in Figure 2C (bottom). λ denotes the spacing of columns and downwellings.

Thermal convection is the process by which cold dense material sinks and warm buoyant material rises. Porous media thermal convection occurs if the Rayleigh-Darcy number is greater than the critical Rayleigh number, i.e., $\mathrm{Ra} > \mathrm{Ra}_{CR} = 4\pi^2$(see Phillips, 1991). Using reasonable values (Table 2.1) we find that the relatively dense liquid water convects while the steam does not (Supplemental Figure 2.10). The velocity of this convection in the liquid phase is given by Darcy's law:

$$\mathbf{u_{conv}} = \frac{k}{\mu_l}\nabla P = \frac{k}{\mu_l}\rho_l g \alpha_l \Delta T, \tag{2.1}$$

where k is the permeability, μis the viscosity, ρ is the density, and the pressure gradient ∇P is given by buoyancy, where g is the acceleration of gravity, α is the thermal expansivity for a change in temperature, ΔT, and the subscript l denotes the liquid phase.

If we assume that liquid water seeps into the tuff due to its own weight, the Darcy velocity of the interface (u_i) is

$$\mathbf{u_i} = (1-F)\mathbf{u_l} = (1-F)\frac{k}{\mu_l}\nabla P = (1-F)\rho_l \mathbf{g}, \tag{2.2}$$

where F is the fraction that vaporizes due to boiling and u_l is the Darcy velocity of the liquid phase. Comparing Equations 2 and 3, this Darcy interfacial velocity dominates if (1 – F) > $\alpha\Delta T$, where F is the mass fraction vaporizing given by

$$F = (1 + S\phi)^{-1} = [1 + \phi L/(c_p \Delta T)]^{-1}, \tag{2.3}$$

where ϕ is the porosity and S is the saturation, which is equal to the latent heat of vaporization L divided by the heat capacity c_p, and the temperature change between the superheated steam and the boiling water, ΔT (Woods, 1999). For representative values, the mass fraction vaporizing should be ∼0.7 and the interfacial velocity will be ∼0.3 u_l or ∼100 u_{conv}. Therefore, the processes occurring at the liquid water-steam interface dominate thermal convection.

Short-wavelength perturbations to a planar liquid front seeping into steam are damped by thermal diffusion, while long-wavelength downwellings are suppressed by an increase in vapor pressure (Woods, 1999). Linear stability analysis (Sondergeld and Turcotte, 1978; Woods, 1999) predicts that the spacing between gravitational fingers at the onset of the instability is meters, similar to observations (Figure 2.3).

Although we do not know the topography of the tuff immediately after the eruption, for the columns to form the interfacial Darcy velocity must have been greater than the Darcy velocity due to topographic flow (u_{topo}). That is,

$$\mathbf{u_i} > \mathbf{u_{topo}} = (1-F)\frac{k}{\mu_l}\mathbf{g} > \frac{k}{\mu_l}\rho_l g G = (1-F) > G \tag{2.4}$$

where G is the topographic grade. This implies that a grade of 10%–100% would be required to dominate the flow (see Phillips, 1991). An average stream gradient for the modern Owens

River is <0.01%, so the columns could have formed beneath either a lake or stream. Assuming a high permeability ($k = 10^{-13}$ m^2) and no boiling ($F = 0$), the fastest infiltration rate is ∼1 m/yr. The modern average rainfall near Long Valley is ∼0.5 m/yr. Integrating the precipitation over a catchment, this implies that a reservoir could maintain a constant water level even with rapid infiltration.

Scaling arguments and stability analysis suggest that the liquid water–steam interface is the source of the columnar geometry of flow, that this interface is unstable at the meter length scale, and that there is enough water in the region to sustain a roughly continuous hydrothermal system and provide upper and lower bounds on the rate that the tuff cooled. However, these scalings assume a sharp liquid water–steam interface without multiphase flow. The linear stability analysis also identifies the wavelength of the initial instability but does not capture the finite amplitude and temporal evolution of instabilities such as boiling along the sides of downwellings. These limitations motivated our two-dimensional numerical simulations.

2.7 Numerical Model

To test our hypothesis, we use the U.S. Geological Survey program HYDROTHERM (Kipp et al., 2008) to solve the coupled multiphase groundwater and energy conservation equations in two dimensions. These models fully account for the effects of latent heat and two-phase flow but do not capture chemical reactions. Our two objectives are (1) to see if numerical models using known rock properties produce the spacing, formation temperatures, and shape of the observed columns, and (2) to systematically change permeability and topography to identify the patterns of flow that develop when a tuff is cooled by water from above.

We impose closed (no fluid or heat flow) boundaries at the base and sides and a fixed-temperature, fixed-pressure boundary (30 °C, 20 atm) at the surface. Many of the column outcrops (*e.g.*, Figure 2.2C) are exposed due to ∼200 m of erosion of overlying tuff. The upper boundary condition reflects these estimates of erosion below a shallow lake of relatively constant head while hydrostatic pressure is assumed in the rest of the model. Because steam is highly compressible, the pressure within the tuff relates to its cooling history and may change some details of flow geometry. We assume an initial tuff temperature of 500 °C with temperatures grading in the upper 2 m to 30 °C and a slight perturbation of the isotherms at the center of the domain. This upper boundary temperature does not appear to set the wavelength of convection but is necessary for numerically stability in the first several time steps. Unless otherwise stated, all models use Corey relative permeability functions.

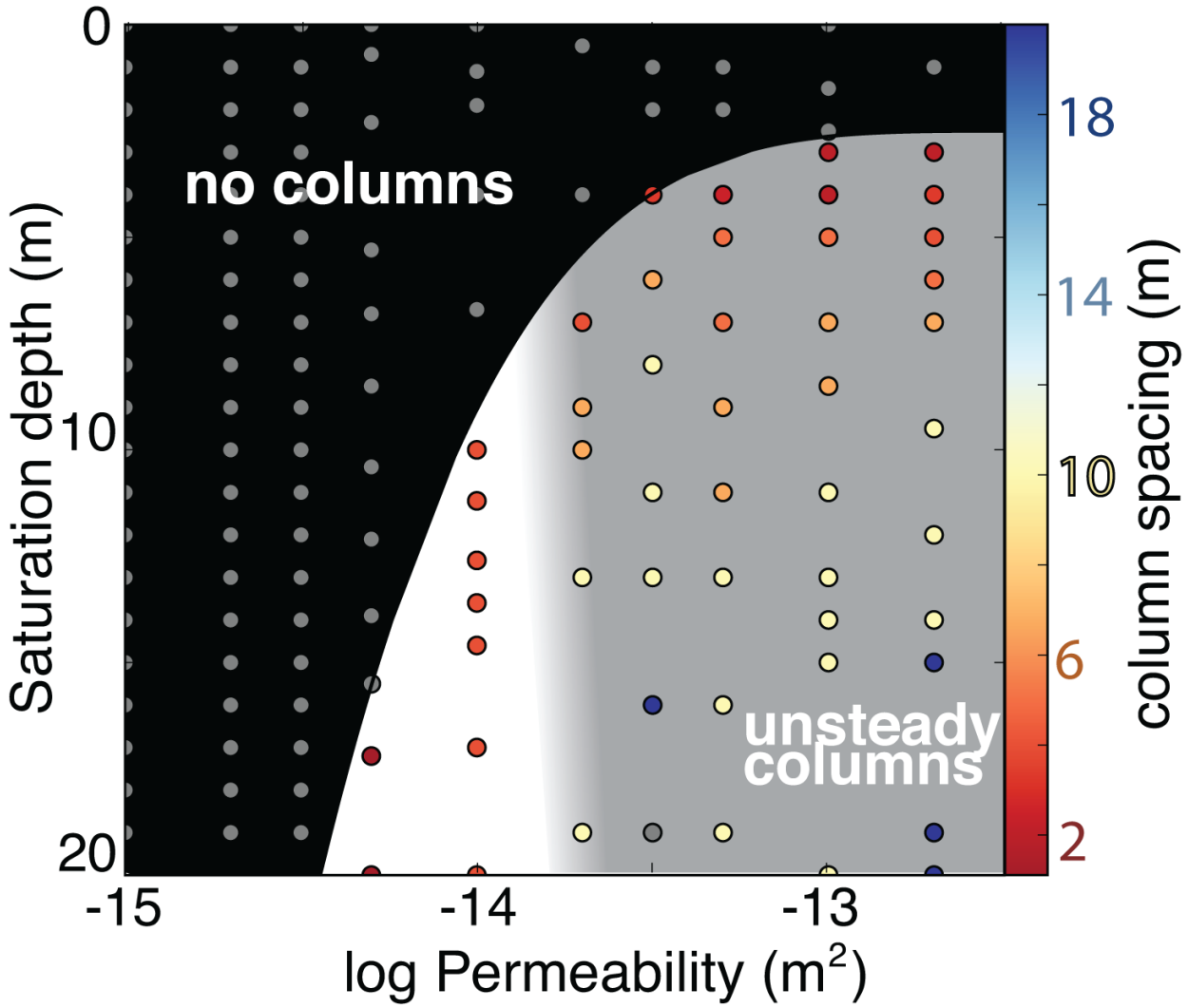

Figure 2.4: Regime diagram for simulations. Each vertical line of points shows a single simulation that progresses from 0 to 20 m in saturation depth. Gray circles show no columns. Colors show column spacing in meters. White background shows range with persistent columns, gray background shows unsteady columns, and black shows no columns.

2.8 Results

Geometry of Flow

At low permeabilities, $<10^{-15}$m^2, liquid water infiltrates the tuff with a narrow, <1 m multiphase boiling zone. Temperature, pressure, and phase do not vary laterally. For slightly higher permeabilities (10^{-14}m^2), the cooling path is the same until periodic undulations begin at $\sim$12 m depth. These undulations form at the boundaries of a thickening, isothermal, two-

phase zone. Within this two-phase zone, periodic fingers of saturation (0.1–1) correspond to undulations in the two phase–single phase interfaces. Fingers remain at a constant ∼3 m spacing until the first finger reaches the bottom boundary. Upon reaching this lower boundary, water condenses and flows along the base. At higher permeability ($>10^{-13}$m^2), unsteady fingers form immediately in the two-phase zone. These fingers coalesce into a single downwelling, which sweeps across the domain. Unlike the lower permeability simulations, the downwelling fingers remain largely steam dominated (0.3 saturation) until they reach the base of domain (Figure 2.4).

Topography greater than the liquid water thickness at the onset of fingering appears to set the wavelength of fingering; i.e., one large swale creates two large downwellings and a single large upwelling (*e.g.*, Supplemental Figure 2.14). Relative permeability functions that produce sharper saturation gradients have more stable fingers. The geometry of flow does not appear to be sensitive to changes in initial temperature between 200 and 800 °C, although these changes do affect the rate of cooling. Finally, higher vertical permeability seems to increase the stability of fingers while higher horizontal permeability increases the unstable cannibalization of fingers (Supplemental Figure 2.15).

Rate of Cooling

At low permeabilities, $<10^{-15}$m^2, cooling follows the conductive cooling path, requiring ∼40 yr to cool 20 m of tuff (assuming a thermal diffusivity of 10^{-6} m^2/s). At higher permeabilities, 10^{-14}m^2, liquid water infiltrates the tuff at the rate of conductive cooling until fingering begins. Once fingering begins, the tuff cools at the rate of advective cooling to 100 °C. At even higher permeabilities, 10^{-13}m^2, fingering begins immediately with many small downwellings. However, as the fingers coalesce they advance at a slower rate than the advective cooling rate, cooling 20 m of tuff to ∼100 °C in only 4 yr (Figure 2.5).

2.9 Discussion and Conclusions

Low-temperature hydrothermal alteration in the Bishop Tuff cements evenly spaced columns. This alteration pervades at least a few square kilometers of Bishop Tuff and appears to form in very different lithofacies with different hydrologic properties (*e.g.*, units Ig1Ea and Ig2E). We show that liquid water infiltrating tuff from above can produce evenly spaced gravitational fingers. Scaling shows that the liquid water–steam interface probably is the source of the instability that generates columnar flow. At high permeabilities, numerous downwellings quickly coalesce into a large downwelling, which migrates laterally across the domain. Only for intermediate permeabilities are numerous downwellings stable in time and space. These stable downwellings advance into the tuff at the rate of fluid advection. The spacing of these columns in simulations is, in order of magnitude, similar to the spacing we observe in the field and similar to linear stability analysis (Woods, 1999). The intermediate

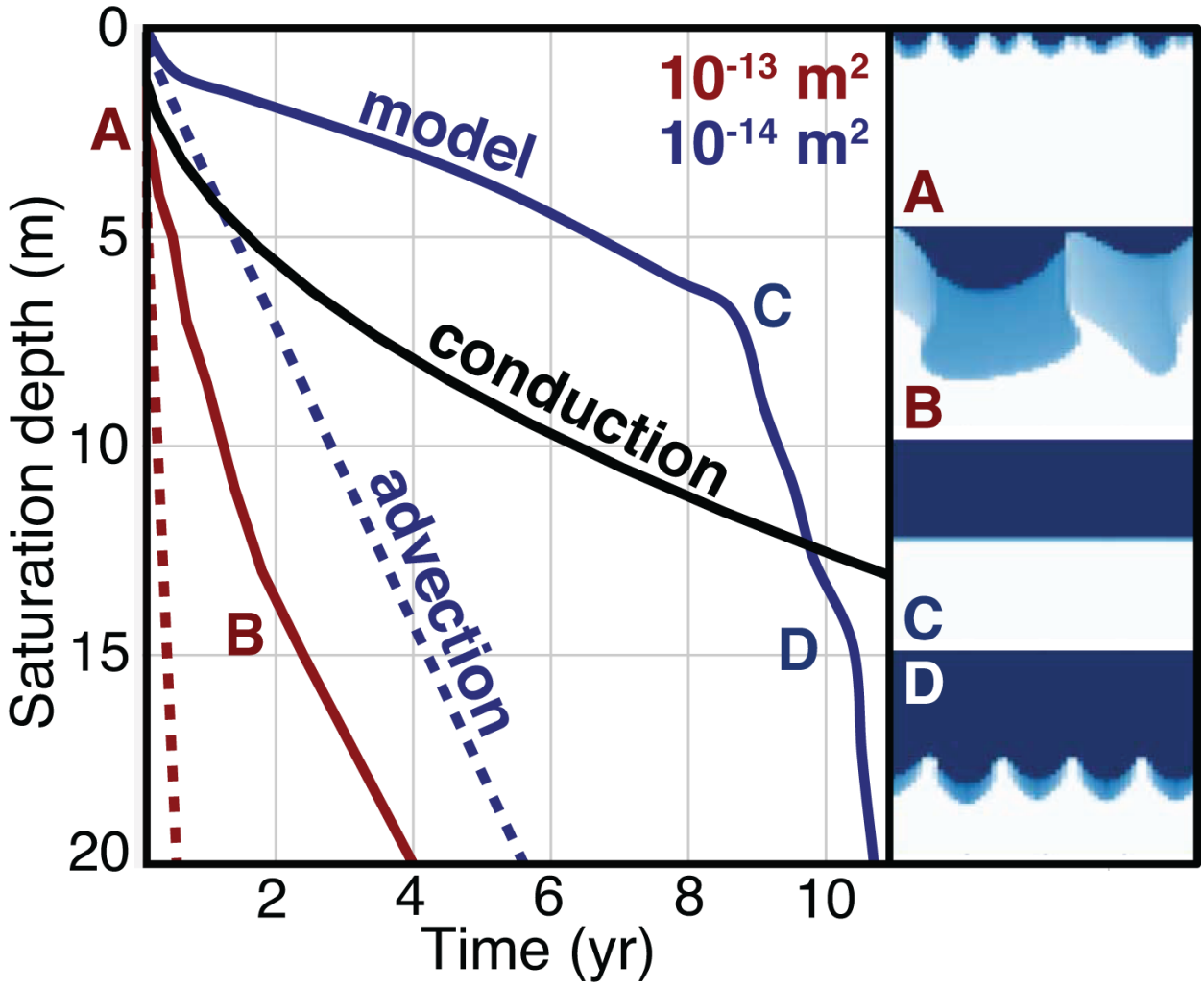

Figure 2.5: Black line shows tuff cooling by conduction. Red is 10^{-14} m^2permeability and blue is 10^{-13} m^2 permeability. Dotted lines show advective cooling assuming no vaporization. Solid lines show numerical model results. Boxes show 20 $\times$ 20 m simulations where dark blue is liquid water saturated and white is steam saturated tuff.

permeability simulations may be stabilized due to saturation gradients between upwelling and downwelling fluid (e.g., Coumou et al., 2008).

Our two-dimensional flow simulations roughly capture the spacing of the observed columns. Although we do not explicitly model mineral precipitation, changes in effective permeability for different phases are captured by relative permeability functions. Mordenite crystals are small relative to pore size (Figure 2.2A and B), and in X-ray computed microtomography scans are not large enough to be seen or to change the pore network (Supplemental Figure 2.16). The high porosity of the tuff and fibrous mineral structure of mordenite imply

that precipitation and dissolution may have relatively small effects on permeability and large effects on strength. Future laboratory experiments may contribute a new understanding to the kinetics of mordenite precipitation and the mechanical consequences of these reactions. Although dominantly columns, mordenite alteration in the Bishop Tuff is diverse (Supplemental Figure 2.8A), including rolls, hexagonal cells, and tilted columns all with meter-scale spacing and patterns analogous to those in three-dimensional Rayleigh-Bénard convection. Extension of our model to reactive three-dimensional flow may offer new insights into the rates and patterns of hydrothermal flow.

If our hypothesis is correct, the Bishop Tuff columns are a rare window into the geometry and rates of flow in many geothermal systems, fumarolic areas, and caldera lakes. This model also implies that water pooled in and near the SE sector of Long Valley caldera soon after the Bishop Tuff eruption and caldera formation.

2.10 Acknowledgements

I would like to acknowledge my collaborators on this study S. Self, M. Manga, S. Breen, A. Hernandez. We are grateful to S. Barker, J. Vandemeulebrouck, and two anonymous reviewers for helpful reviews, and to W. Hildreth, T. Driesner, and S. Ingebritsen for helpful comments on the manuscript. Randolph-Flagg was supported by the National Science Foundation Graduate Research Fellowship (DGE 1106400), while other authors were supported by the National Science Foundation (NSF-1521855) and the University of California Berkeley Larsen grant. X-ray microtomography was enabled by access to the Lawrence Berkeley National Lab Advanced light source on beamline 8.3.2. We thank Dula Parkinson for guidance with μXRT imaging and image processing.

2.11 Supplemental Information

Table 2.1: Constants used for scaling analysis.

acceleration due to gravity	$\mathbf{g}$	9.81	m/s^2
column spacing	λ	0.5-2	m
convective layer thickness	h	0.1-100	m
change in density	$\Delta\rho$	994	kg/m^2
permeability	k	10^{-11}-10^{-15}	m^2
porosity	φ	0.1-0.7	
latent heat of vaporization	L	2,260	kJ/kg
thermal diffusivity	κ	10^{-6}	m^2/s
viscosity liquid water	μ	10^{-3}	Pas
viscosity of steam	μ	10^{-5}	Pas

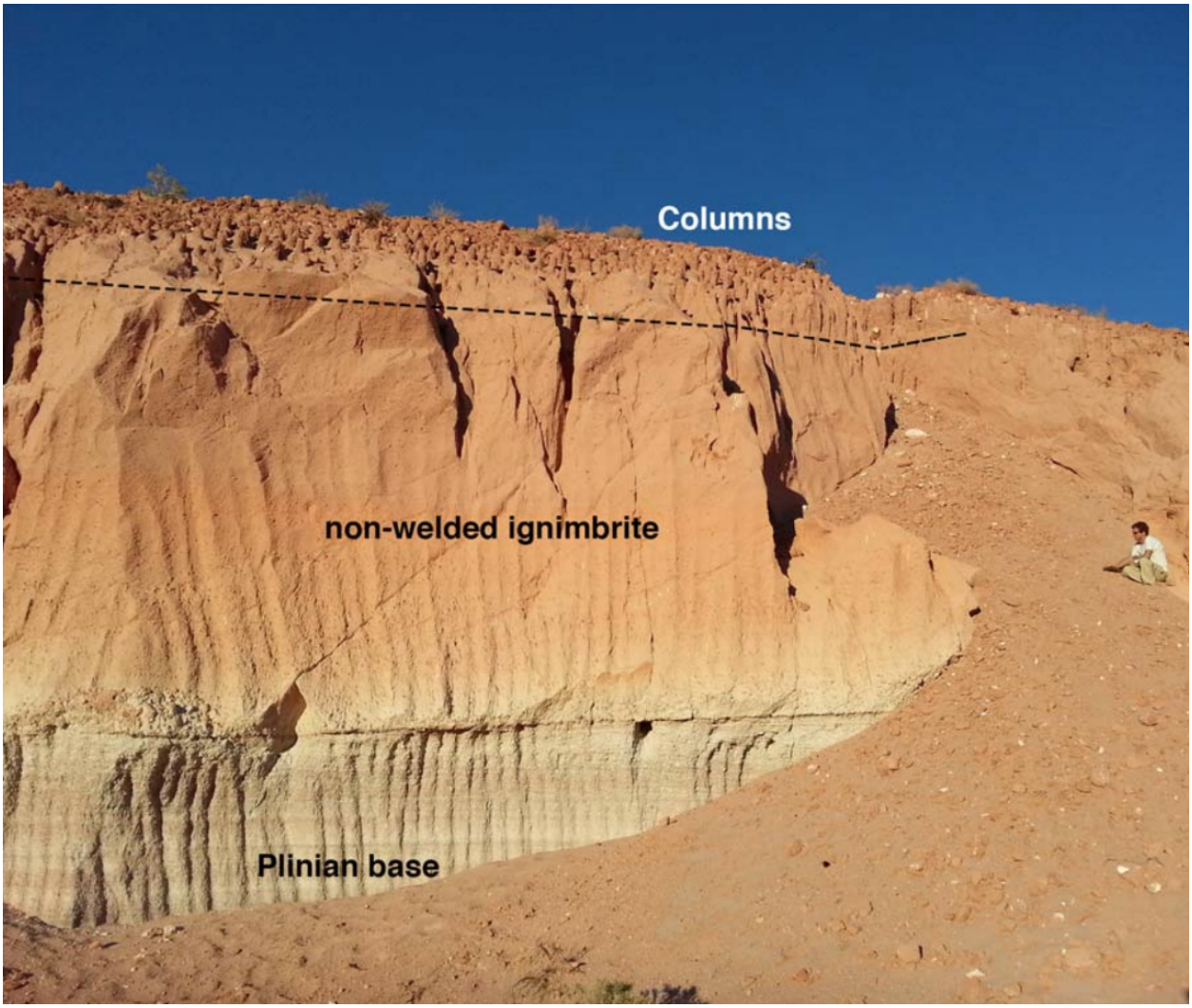

Figure 2.6: Base of Bishop Tuff showing pinkish tuff overlying the white plinian airfall deposit. Dotted line shows where columns start. Note that runnels in the plinian base and tuff are due to the mining process and are unrelated to composition changes in the tuff.

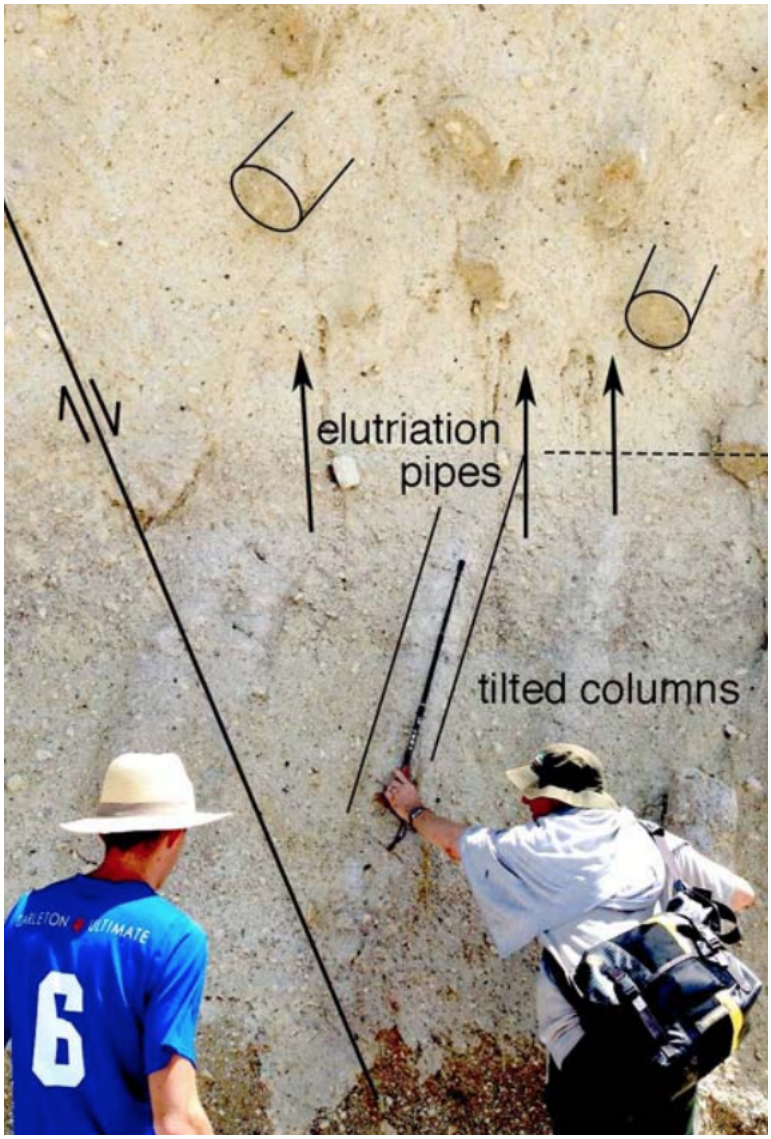

Figure 2.7: Figure showing tilted columns and elutriation pipes. Elutriation pipes form vertically in hot tuff and show that, despite faulting, columns probably formed in their current orientation after the elutriation pipes formed.

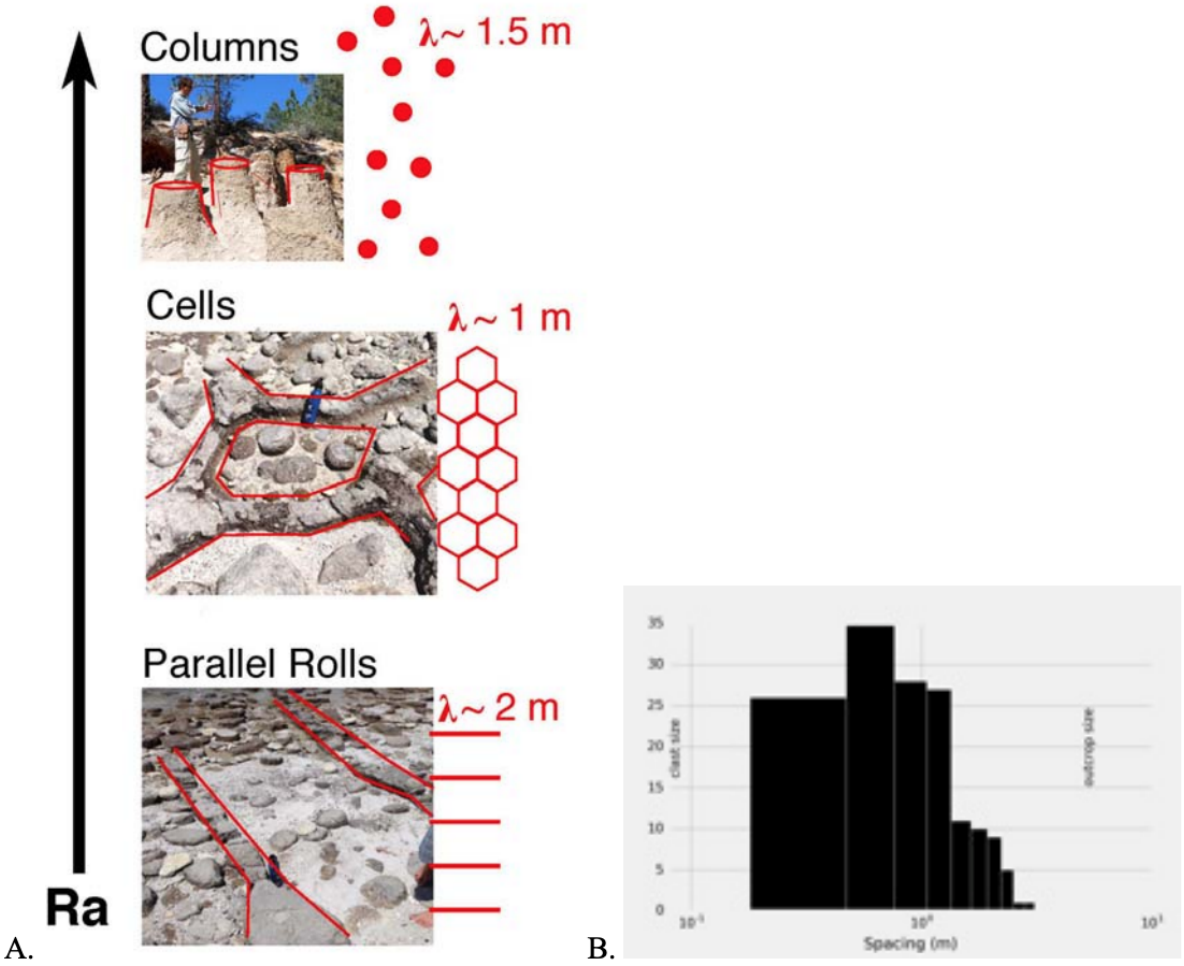

Figure 2.8: **A**. Range of 3D geometries observable in the Bishop Tuff. Red schematic drawings show idealized plan-views of the outcrops. In single phase convection these patterns are anticipated at different Rayleigh numbers. **B.** Histogram of column spacing along beach outcrops.

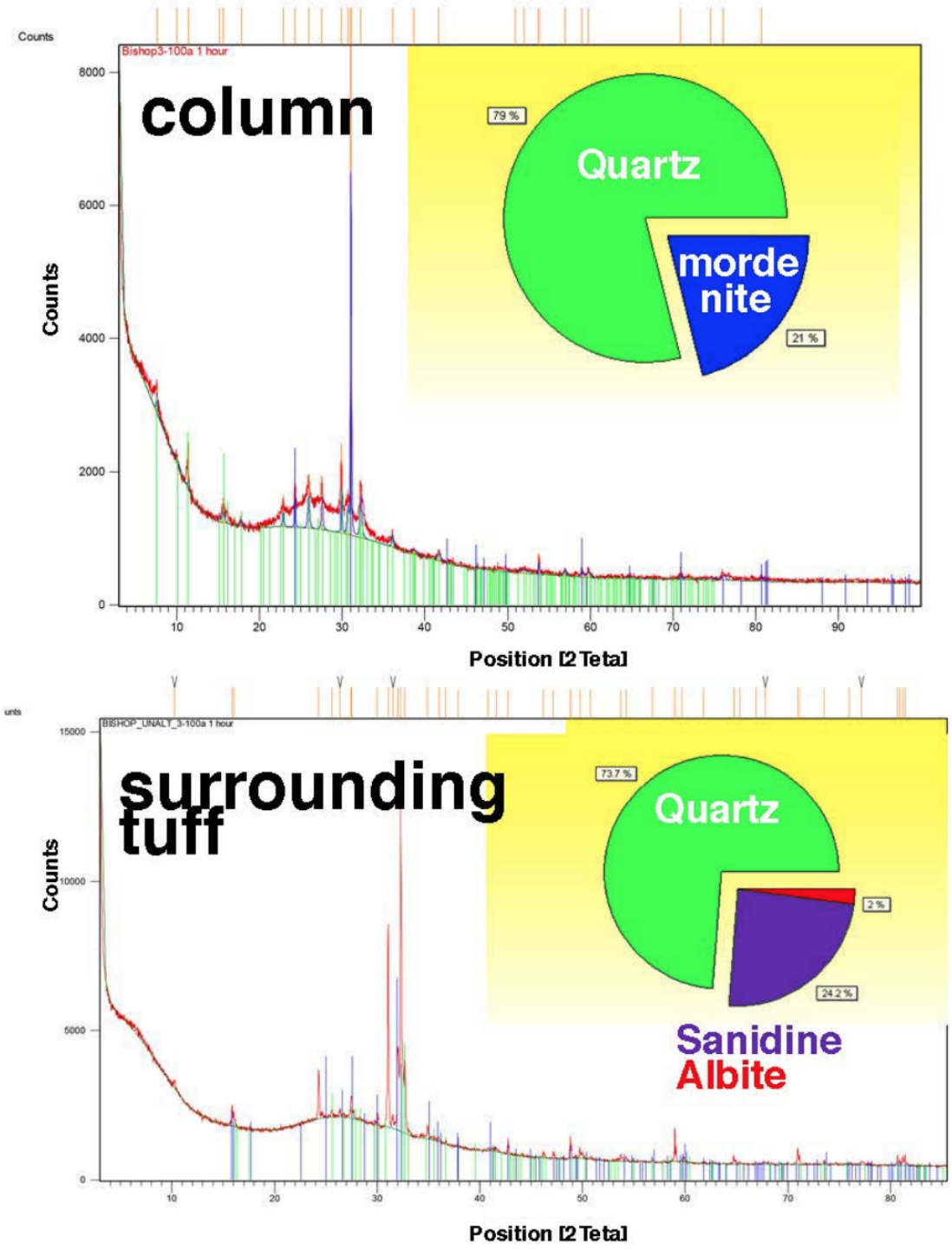

Figure 2.9: 1 hour x-ray diffraction spectrum for columns and unaltered tuff surrounding a column. Green lines show peaks best explained by quartz while blue, purple, and red lines show peaks best explained by mordenite, sanidine, and albite respectively. Inset shows relative spectral strength of each mineral species. (37.47º N, 118.73º W)

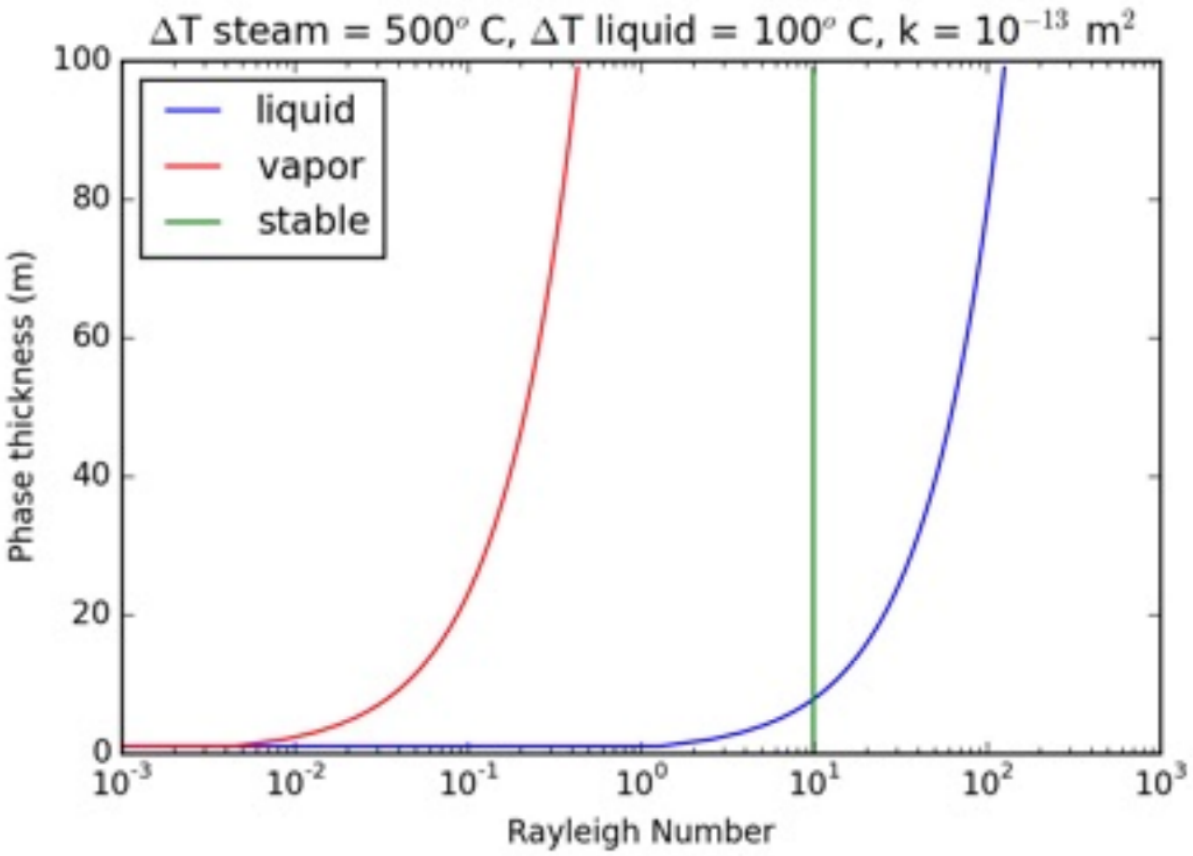

Figure 2.10: Rayleigh number as a function of phase thickness. The vertical green line shows the critical Rayleigh number for porous media. This means when the liquid water (blue) extends beyond this critical Rayleigh number it is prone to thermal convection. In a porous medium, a measure of the gravitational instability is given by the ratio advective and diffusion timescales called the Rayleigh-Darcy number (Ra). $Ra = \frac{\rho g \Delta T \alpha k h}{\mu \kappa}$ whereρ is the density, g is the acceleration due to gravity, α is the thermal expansivity, ΔT is the change in temperature across the convective layer, k is the permeability, h is the convective layer thickness, μ is the viscosity of water, and κ is the thermal diffusivity. The most variable of these quantities is the permeability, which in tuffs ranges from 10^{-14} to 10^{-11} m^2 (Wright and Cashman, 2014).

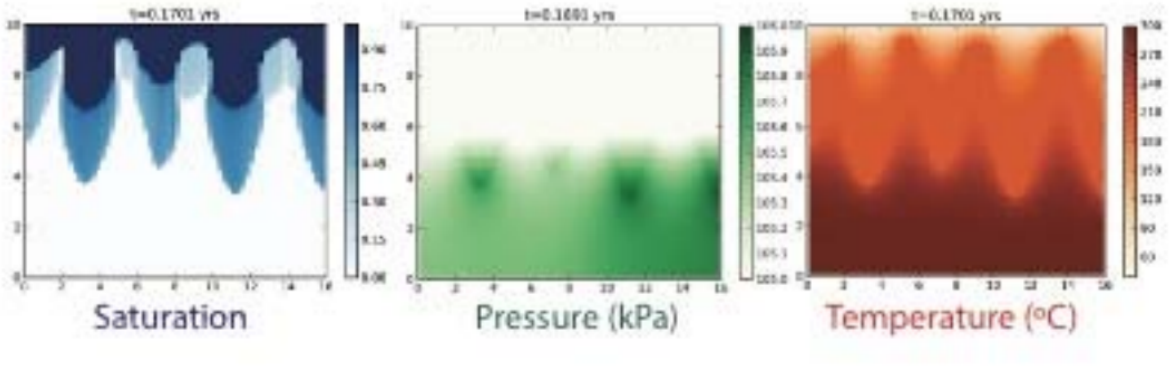

Figure 2.11: Saturation (blue,) pressure (green) and temperature (red) for columns in 10-14 m2isotropic permeability 10 m x 16 m simulation. Upper boundary condition is 10 atm otherboundaries are closed to fluid and energy flow.

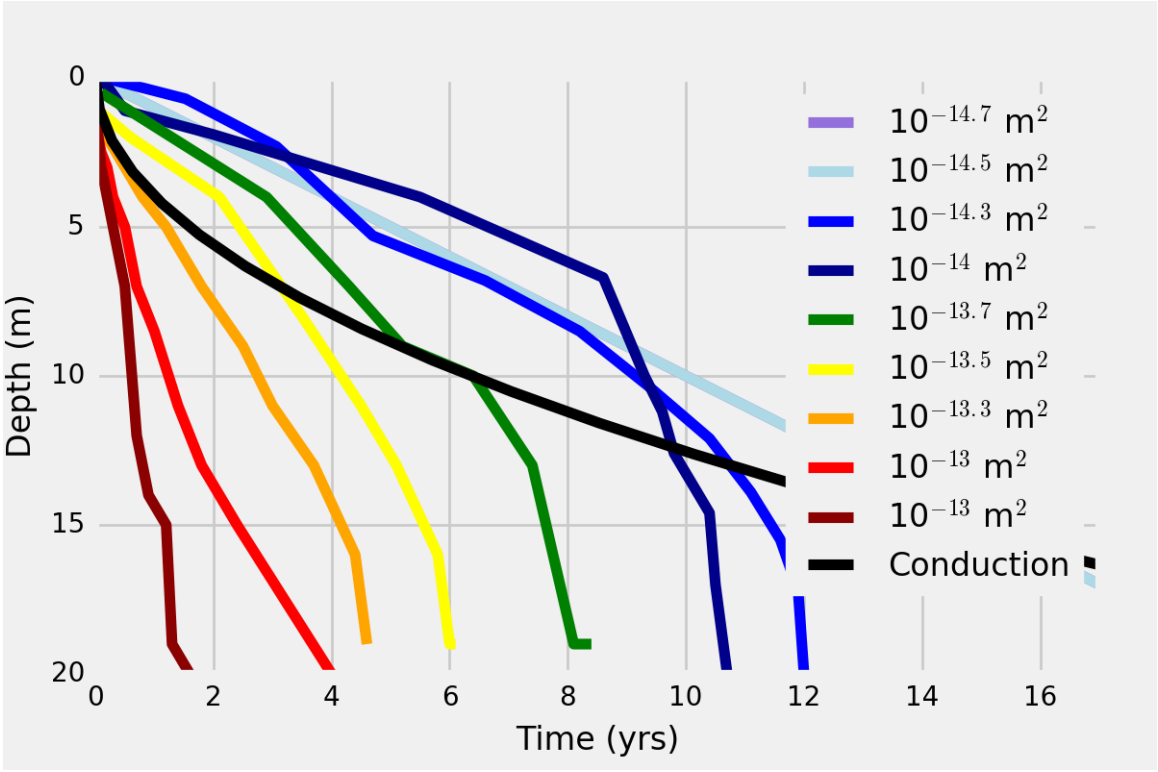

Figure 2.12: Saturation depth through time for a range of permeabilities. From left to right: $10^{-12.5}$ m^2, $10^{-12.7}$m^2, 10^{-13}m^2, $10^{-13.3}$ m^2, $10^{-13.5}$ m^2, $10^{-13.7}$ m^2, 10^{-14}m^2, $10^{-14.3}$ m^2. Black shows the conductive cooling profile.

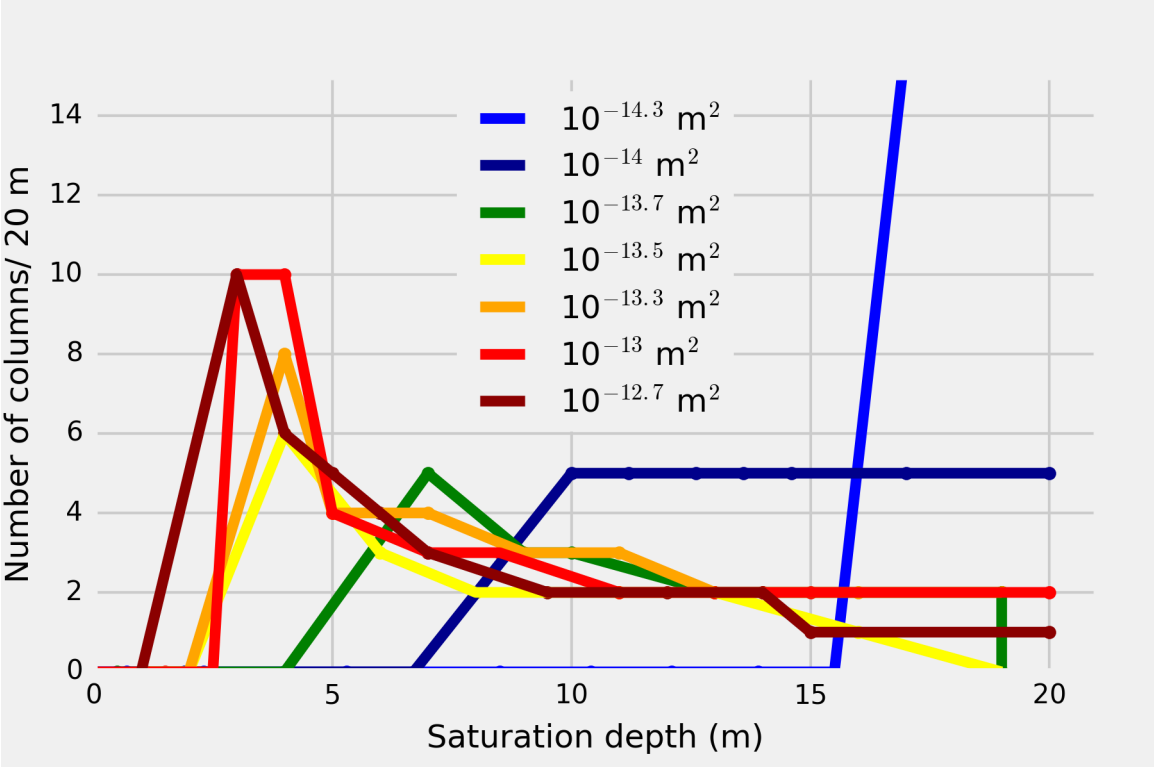

Figure 2.13: Number of columns in 20 m simulations for a range of permeabilities. From left to right: $10^{-12.5}$ m^2, $10^{-12.7}$m^2, 10^{-13}m^2, $10^{-13.3}$ m^2, $10^{-13.5}$ m^2, $10^{-13.7}$ m^2, 10^{-14}m^2, $10^{-14.3}$ m^2.

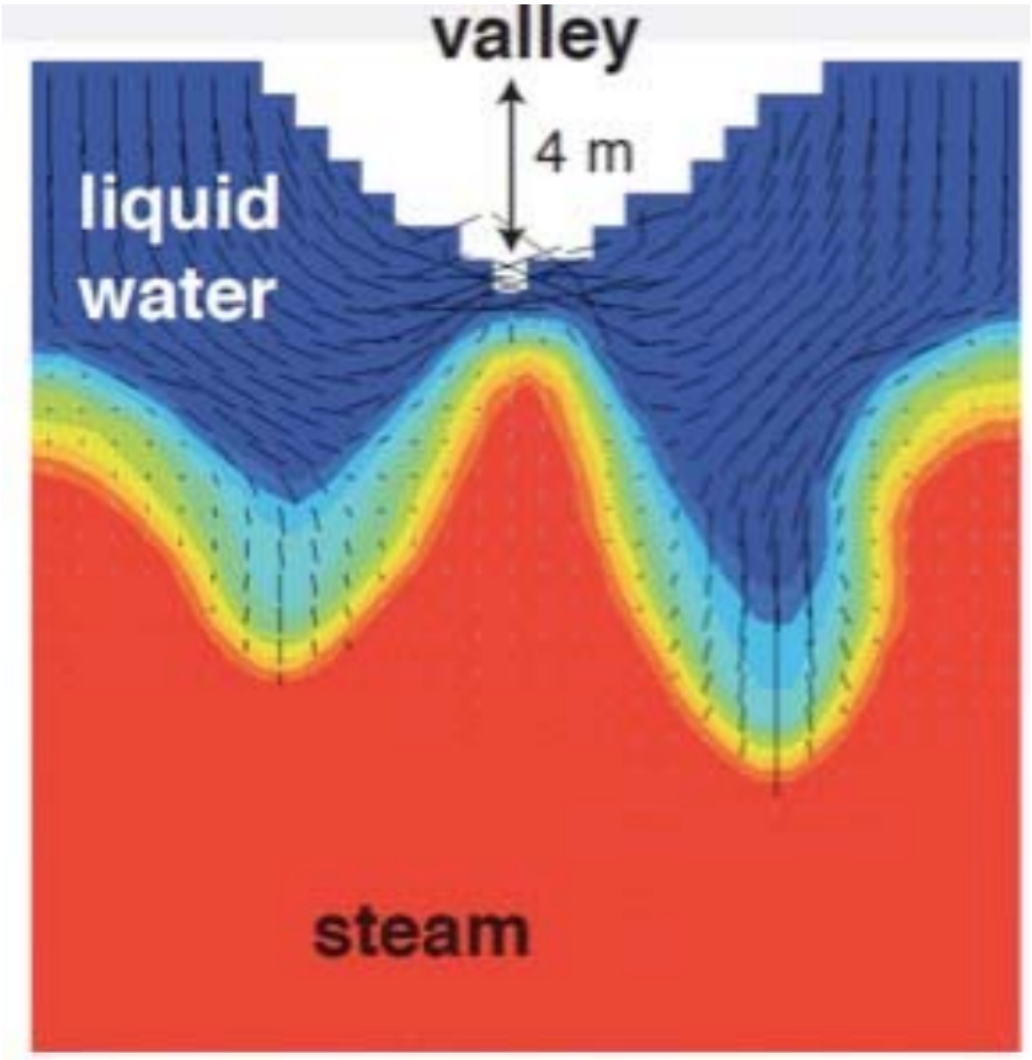

Figure 2.14: Simulation of 10^{-13} m^2 domain including a 6 m x 4 m triangular drainage to drive topographic flow. Red is 100^{o} C and blue is 30^{o} C while black line lengths are proportional to liquid water velocities.

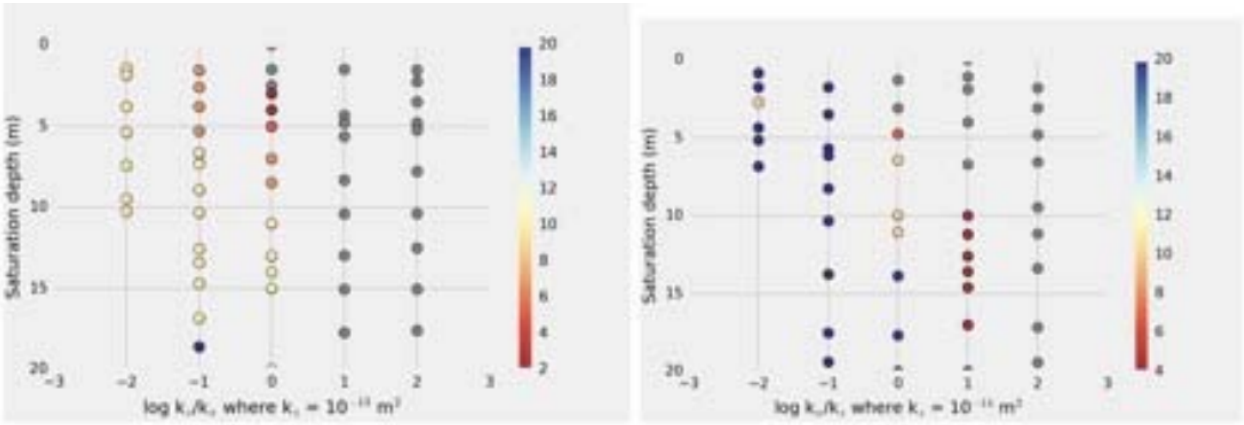

Figure 2.15: Phase space of columnar flow for anisotropic permeabilities. Each vertical line of points shows a single simulation which progresses from 0 to 20 m in saturation depth. Gray circles show no columns. Colors show column spacing in meters.

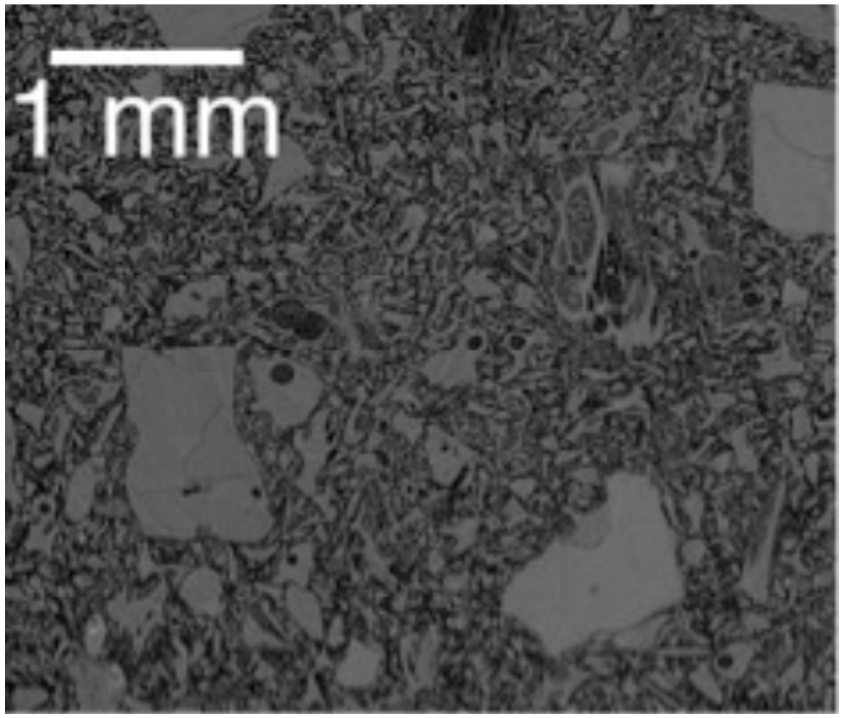

Figure 2.16: X-ray computed microtomography scans of column tuff. Gray blocks are crystals and volcanic glass. Circular features are vesicles. Fine fabric are ash shards. Note that mordenite crystals are not large enough to be seen. (37.47º N, 118.73º W)

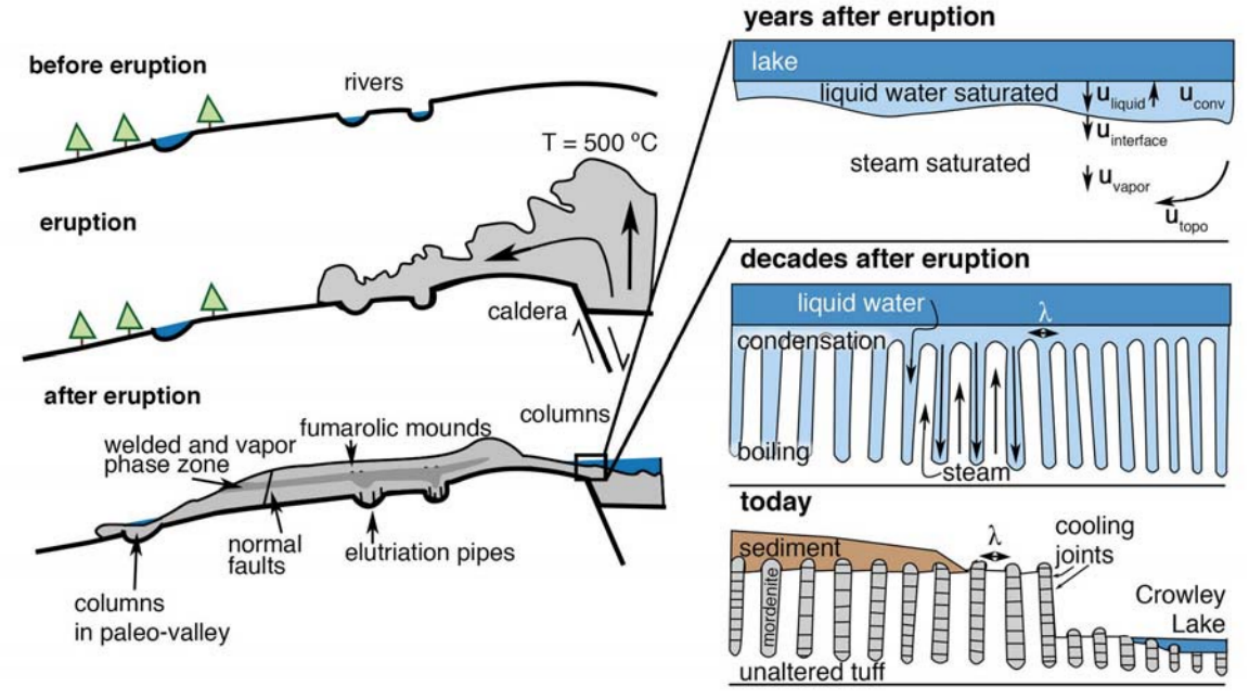

Figure 2.17: Extended cartoon of cooling Bishop Tuff.

Chapter 3

Water level changes and triggered seismicity at Long Valley Caldera, California, USA

3.1 Abstract

Long Valley caldera, in eastern California, has some of the best-documented water level changes and dynamically triggered earthquakes in response to the passage of teleseismic waves. We compare high-frequency (up to 0.2 Hz) water level and temperature data from well CH-10B with waveforms from several broadband stations within the caldera for hundreds of global and local earthquakes. Water levels in the well always drop during the passage of Rayleigh waves, by as much as 1.2 m. These water level drops persist for up to a few hours and then fully recover to pre-earthquake levels. The magnitude of the changes is strongly dependent on peak ground velocity of surface waves. We introduce a quantitative model for water flow into fractures caused by changes in permeability from passing seismic waves. This model replicates water level changes in the well drilled into fractured crystalline rock and may be applicable for explaining pore pressure increases within permeable fault zones. Coincident with the water-level drops, we also identify small, triggered earthquakes by filtering the waveforms from several stations in and around Long Valley and by examining seismicity rates in local catalogs.

3.2 Introduction

Water levels in wells can rise or fall in response to the passing of surface waves from large, distant earthquakes (*e.g.*, Blanchard and Byerly, 1935; Rexin et al., 1962; Cooper et al., 1965). Early studies have related the largest water level fluctuations to long-period Rayleigh waves and showed that water level response to seismic waves diminishes rapidly as wave length decreases (*e.g.*, Eaton and Takasaki, 1959). These water level changes can be tran-

sient, prolonged or permanent due to permeability variations and/or pore pressure transients (*e.g.*, Roeloffs, 1996; Manga et al., 2012; Manga and Wang, 2015).

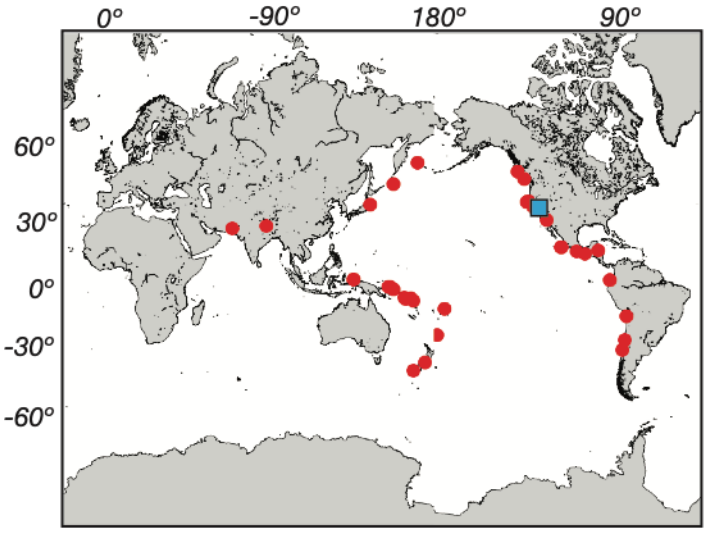

Figure 3.1: Map of earthquake epicenters with M>6.0 from 2008-2018 that caused > 2 cm drop in water level at CH 10B (red) and earthquakes with the largest peak ground velocity. Long Valley Caldera is shown with the blue square and Fig. 3.2 is a detailed map of this region.

The amplitude and sign (rise or drop) of water-level change in a well in response to seismic waves depends on the characteristics of seismic waves, the properties of the surrounding rocks, and geometrical dimensions of the well (*e.g.*, Cooper *et al.* 1965, Liu et al., 1989; Roeloffs, 1996). The availability of data from broadband seismometers that are located in close proximity to wells with high frequency of water level data permits a more detailed study of the relation between long-period seismic waves and coincident water level response (*e.g.*, Brodsky et al., 2003; Kitagawa et al., 2011; Shalev et al., 2015; Liu et al., 2018). Nevertheless, several fundamental processes are yet not well understood. How small symmetric strains induced by passing seismic waves are amplified to produce large asymmetric changes in water level appears to vary with tectonic setting and lithology and remains an area of active research and debate (for a review see Manga et al., 2012). More specifically, do the Love or Rayleigh waves, each generating a different stress field (Hill, 2012) induce water level changes? Why do water level changes in some wells always have the same response (either drop or rise)? What are the timescales for water levels to recover to pre-earthquake values? To address these questions and probe the mechanisms for water level changes, we use new, high-resolution water level and temperature data collected between 2008 and 2018 from well CH-10B in Long Valley caldera in eastern California (Figs. 3.1 and 3.2).

Long Valley caldera is an ideal setting to study the interactions between seismic waves

and crustal fluids because it is both seismically active and densely monitored (*e.g.*, Hill, 2017). In part because of this monitoring, Long Valley caldera was one of the first places where dynamically triggered earthquakes were documented (*e.g.*, Hill et al., 1993; Prejean et al., 2004; Brodsky and Prejean, 2005). Additionally, water levels in several wells were shown to have prolonged changes after nine large earthquakes in California between 1989 and 1999 (Roeloffs et al., 2003). However, the response to these earthquakes was analyzed using water level data that was sampled only every 10 to 20 minutes which is much longer than the period of seismic waves.

The new analysis we present here is based on water level and temperature data that was sampled at five second intervals (Clor et al., 2018), which is shorter than the period of teleseismic seismic surface waves. Combining the water level data with data from a nearby broadband seismometer, we examine water level response to global earthquakes with moment magnitude >M6. We examine what aspects of seismicity (amplitude, frequency and azimuth) may cause changes in water levels. We also document coincident increases in local seismicity rate triggered by those same earthquakes that induced water level changes. Finally, we introduce a new one-dimensional model that describes changes in groundwater flow into and out of dilating fractures as a possible mechanism that can explain the observations.

3.3 Hydrothermal flow and seismicity in Long Valley Caldera

Long Valley caldera in eastern California formed after a large explosive eruption ~767 ka that produced the ~650 km^3 rhyolitic Bishop Tuff (*e.g.,* Hildreth, 2017). Active deformation and earthquake swarms prompted dense seismic, geodetic, and hydrologic monitoring systems partly to disentangle the magmatic and hydrothermal signals at Long Valley (*e.g.*, Hildreth et al., 2017; Hill, 2017). Drilling within the caldera revealed relatively low temperatures (<180 °C) to depths of ~3 km (*e.g.,* Hurwitz et al., 2010).

Deep water recharge on the western caldera rim is heated from the system that had eruptions in the Holocene along the Inyo chain (review by Evans, 2017). The ascending thermal water with a maximum measured temperature of 220° C is focused in permeable units that channel groundwater flow eastward to lower elevations. Some of this thermal water is tapped along the flow path at Casa Diablo (Fig. 3.2 and 3.3) for geothermal energy production. The rest of the thermal water discharges through springs at the Hot Creek Geologic Site (Fig. 3. 2). Along this flow path, the water degasses CO_2 as pressure decreases and, thus, dissolved CO_2 concentrations in CH-10B are relatively low (Brown et al, 2013). Well CH-10B is located 0.5 km from Hot Creek and the bottom of the well is at approximately the same elevation as the springs in Hot Creek. Onset of geysering in Hot Creek in May 2006 was coincident with temperature at the top of the water column in CH-10B attaining the local boiling temperature (Evans et al., 2018).

Dynamically triggered earthquakes were first described in Long Valley caldera and nearby

Table 3.1: Properties for 11 earthquakes analyzed in this study and the water level Response in CH-10B

Date and time	Earthquake Location	Water level Drop (m)	Duration (min)1	EQ Mag2	BA (º)3	Depth (km)4	PGV (m/s)5
12/8/16 17:38	70km WSW of Kirakira, Solomon Islands	1.10 (0.15)6	80 (90)	7.8	255	41	0.63
11/13/16 11:02	54km NNE of Amberley, New Zealand	0.90 (0.09)	160 (105)	7.8	224	15	0.337
7/17/17 23:34	198km ESE of Nikol'skoye, Russia	0.53 (0.05)	40 (60)	7.7	314	11	0.351
1/22/17 04:30	41km WNW of Panguna, Papua New Guinea	0.48 (0.03)	35 (60)	7.9	263	136	0.180
12/8/16 14:49	160 km W of Ferndale, California	0.40 (0.02)	10 (15)	6.6	298	8	0.385
12/17/16 10:51	46km E of Taron, Papua New Guinea	0.25 (0.02)	70 (60)	7.9	265	103	0.145
4/4/10 22:40	12km SW of Delta, B.C., MX	(1.27)	(30)	7.2	150	10	6.290
9/8/17 04:49	87km SW of Pijijiapan, Mexico	(0.89)	(45)	8.1	128	70	5.346
4/16/16 23:58	27km SSE of Muisne, Ecuador	(0.37)	(45)	7.8	21	16.6	0.160
3/10/14 05:18	78km WNW of Ferndale, California	(0.22)	(30)	6.8	305	17	0.835
9/29/09 17:48	Samoa Islands region	(0.13)	(60)	8.1	234	18	0.947

1 – duration of water level response relative to 5 minutes priorto earthquake
2 – earthquake magnitude
3 - the back azimuth of the earthquake relative to LongValley caldera
4 – earthquake depth
5 - peak ground velocity for the vertical component of theseismic waveform recorded at the MCB broadband seismometer
6 - data in parentheses are from 15 min data

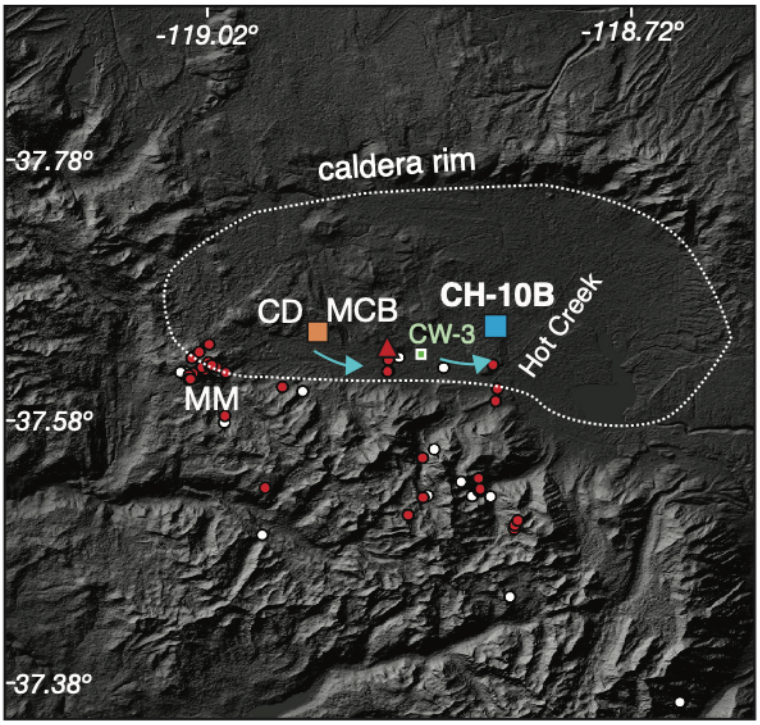

Figure 3.2: Topographic map of the Long Valley Caldera with blue arrows showing hydrothermal flow across the caldera. The blue square shows Core Hole10-B (CH-10B), the orange square is the Casa Diablo geothermal plant (CD), red triangle is the MCB broadband seismometer. MM is Mammoth Mountain. The topographic rim of the caldera is highlighted with the dotted line. Circles show earthquakes from the NCDC catalog that occur 12 hours before (white) and 12 hours after (red) for the two earthquakes that produced the largest water level changes, the April 2010 and September 2017 Mexico earthquakes (Table 3.1).

Mammoth Mountain after the M7.2 Landers, California earthquake in 1992 (Hill et al., 1993). Subsequent studies have identified small triggered earthquakes predominantly in the shallow crust (< 8 km) within the caldera after other large earthquakes (*e.g.*, Prejean et al., 2004; Brodsky and Prejean, 2005; Aiken and Peng, 2014). Shallow (5-7 km) earthquake swarms in Long Valley caldera in 1997 and in 2014 were inferred to be associated with hydrothermal fluid circulation (Dreger et al., 2000, Shelly et al., 2016), but neither swarm corresponded to measurable water level changes at CH-10B.

3.4 Well CH10-B

Well CH-10B is 96 m deep with a 10 cm diameter casing and 5 m of screens at its bottom that allow for water to flow into and out of the well (Fig. 3.2). The top 30 m of the

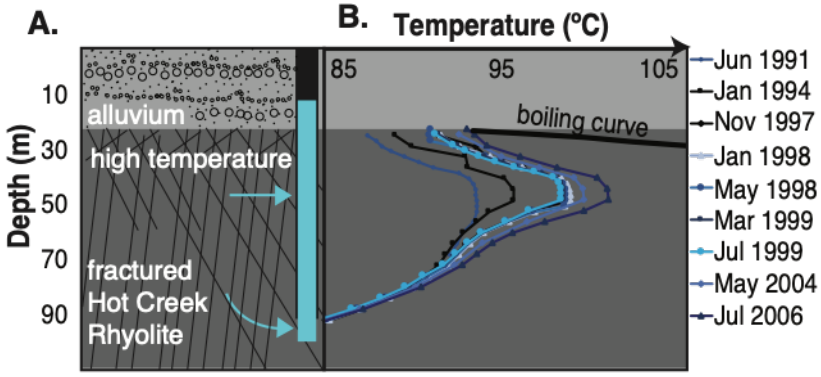

Figure 3.3: Schematic cross section of CH-10B. The well casing diameter is 10 cm and the bottom 5 m is screened allowing water to flow into and out of the well. B) Representative Temperature profiles measured in the well during period of record (data from Farrar et al., 2010).

well were drilled in alluvium while the bottom ~ 70 m were drilled through a rhyolite flow (Fig 3.2). Water levels in CH-10B have been measured and recorded by the U.S. Geological Survey (USGS) every 10 to 20 minutes intermittently since 1989 with a precision of 0.3 cm (https://waterdata.usgs.gov/ca/nwis/inventory/?site_no=373930118491602&agency_cd=USGS). The bubbler system used for measuring water pressure consists of a nitrogen tank, a pressure regulator, tubing, a pressure transducer and a datalogger. The pressure data were converted to water levels using manual measurements of water depths with a precise electronic tape several times per year (Howle and Farrar, 1996). We also record temperature continuously at depths of 36 m and 56 m below the land surface using insulated resistance temperature detector (RTD) sensors with a resolution of 0.1 °C. Annual temperature measurements spanning the full well depth (Supplemental Fig. 3.3) show systematic changes in water temperature with near-boiling temperature near the contact between the alluvium and the rhyolite flow with lower temperatures above and below (Evans et al., 2018). Deeper in the well, water remains significantly colder than the boiling temperature for the corresponding pressure.

For our study, water level and temperature data have been sampled and recorded every five seconds since 2008 (Clor et al., 2018). Due to instrument malfunctions, five second water level and temperature data at the time of several large earthquakes were not recorded. For these earthquakes, 10 to 20-minute data was available for the analysis. We find that the 10 to 20 minute data underestimates the amplitude of water level oscillations by a factor of approximately seven (R^2 = 0.91; Supplemental Fig. 3.11), suggesting that the amplitudes of the largest water level changes observed with the low-frequency water level data may be significant underestimates.

There are long term trends in water level and temperature following the onset of geothermal energy production at Casa Diablo in 1984 (*e.g.,* Roeloffs et al., 2003; Clor et al., 2018).

There are also water level changes related to seasonal and long-term climate variability (Supplemental Fig. 3.12). Our analysis suggests that water levels are only slightly sensitive to Earth tides, consistent with the previous analysis of Roeloffs et al. (2003). The semidiurnal water level oscillations are more consistent with changes in barometric pressure (Supplemental Fig. 3.13), suggesting that CH-10B taps an unconfined aquifer (*e.g.*, Rojstaczer and Riley, 1990; Quilty and Roeloffs, 1991).

3.5 Results

Relating water level changes to global earthquakes

We identify all earthquakes with >M6.0 between 2008 and 2018 in the USGS catalog of global earthquakes (https://earthquake.usgs.gov/earthquakes/search/) to examine if they induced a measurable water level response in CH-10B. We also use all recorded earthquakes (M>0.1) within a 500 km radius of Long Valley caldera using data from the Northern California Earthquake Data Center (NCEDC - ncedc.org). There are large water level drops (and never a rise) in CH-10B after many global earthquakes. Fig. 3.1 shows a map of earthquakes that induced water level drops > 2 cm between 2008 and 2018. These earthquakes include strike-slip and dip-slip events from a range of magnitudes (M6-M9), a range of distances (500 -19,300 km), a range of depths (8-150 km) and back azimuths of 120°-360° (Fig. 3.6c).

Some of the large earthquakes analyzed did not induce detectable water level changes; these include the April 12, 2012 M7.0 Baja California (Mexico) and the January 5, 2013 M7.5 Queen Charlotte Fault in southeastern Alaska earthquakes (Fig. 3.1; white circles). The largest measured water level drop we analyzed was in response to the April 4, 2010 M7.2 Baja California (El Mayor–Cucapah) earthquake and the September 8, 2017 M8.2 Mexico City earthquake for which five-second data was not available. The temporal pattern of water level changes in response to global earthquakes is very similar for all events, with a rapid (tens of minutes) drop followed by a gradual recovery over a few hours (Fig. 3.2C). The maximum volume of water displaced from the well is ~40 L for a water level drop of 1.27 m (0.1 m casing diameter) during the 2010 M7.2 earthquake in Mexico. This water level drop occurred over 30 minutes, corresponding to a flux of 5.7 x 10^{-5} m/s from the well into the surroundings. After water levels recover to approximate pre-earthquake levels, the well appears to be equally sensitive to distant earthquakes. For example, two hours after the December 2016, M6.6 Ferndale, California earthquake, water level dropped by more than one meter following the M7.8 Solomon Islands earthquake (Supplemental Fig. 3.4).

The largest water level drops follow earthquakes in North and South America that also induced the largest peak ground velocities for example events 2010 (M7.4 in the USA), 2012 (M7.2 in the USA), 2017 (M8.1 in Mexico), 2012 (M6.8 in Canada) and the 2010 (M8.8 Maule Earthquake in Chile). Earthquakes from the South Pacific also cause detectable changes in water level, but there were no detectable water level changes following earthquakes to the east of Long Valley caldera during the period of record.

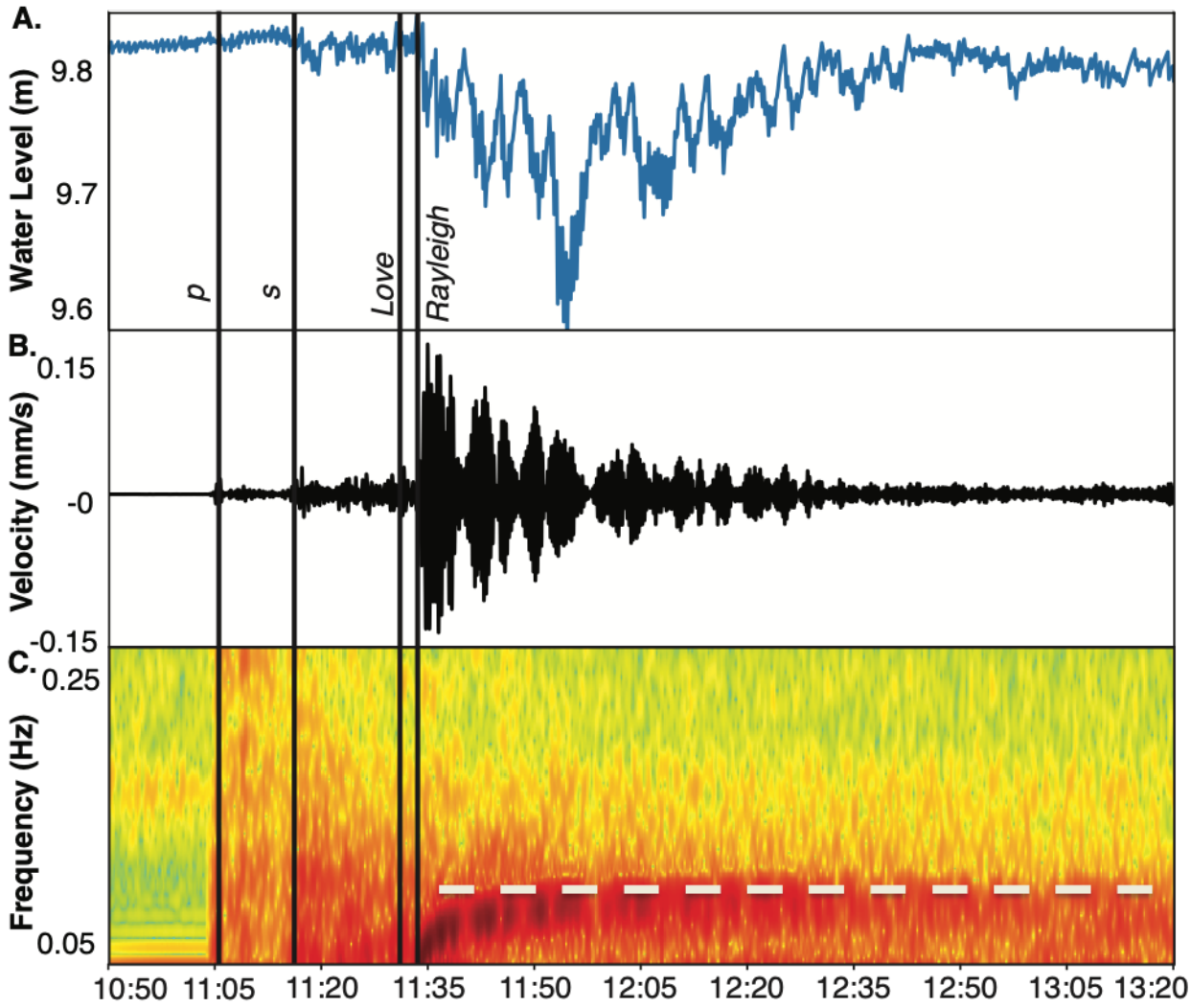

Figure 3.4: Representative 5-second water level record from CH-10B during the passage of seismic waves from the December 12, 2016 M7.9 Papua New Guinea earthquake. B) Seismic vertical velocity record from the MCB broadband station for the same earthquake C) Spectrogram of the vertical velocity recorded at the MCB broadband station. Warm colors show more spectral power. The dashed white horizontal line shows the frequency with the highest spectral power during the teleseismic wave train. Vertical lines show the arrival of the p, s, Love and Rayleigh waves.

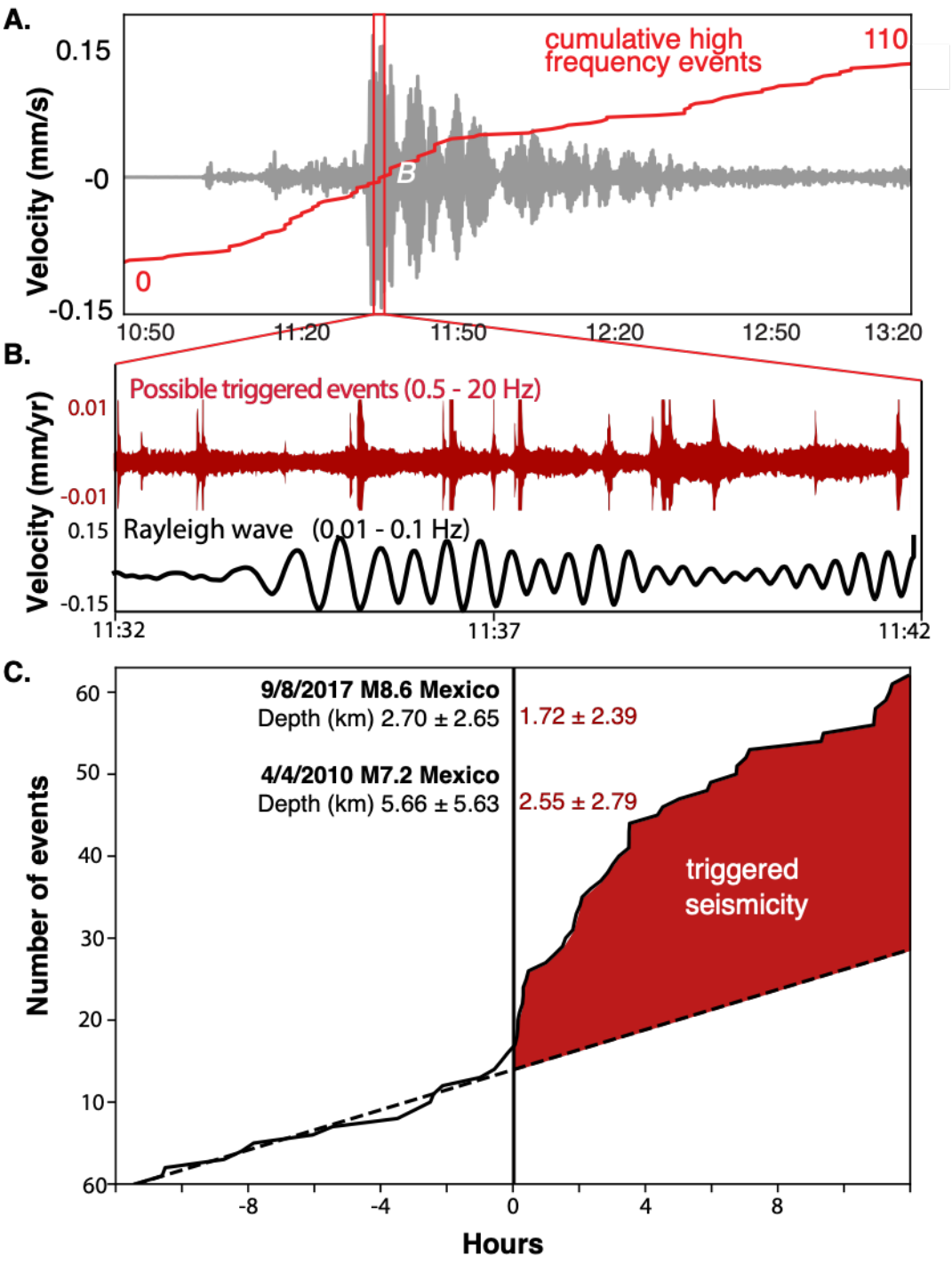

Figure 3.5: Bandpass filtered seismic waveform (0.01-0.1 Hz) from the vertical component recorded at the MCB broadband station. Red curve shows the cumulative number of high frequency (0.5-20 Hz) events that appear as peaks in the seismic trace shown in panel B. B. Close up of seismic waveform from boxed region in panel A. Red curve shows bandpass filtered waveform (0.5-20 Hz) and black curve shows the waveform in the 0.1-0.01 Hz in the vertical component of MCB. C. Cumulative number of earthquakes is the USGS catalog (M>0.1) before and after the two earthquakes with the largest change in water level. The dashed line is a linear regression of background seismicity rate from the preceding 12 hours.

Water level drops after global earthquakes

We compare the new high frequency water level data from CH-10B with data from a 100 Hz broadband station (MCB) located ~5 km to the northeast (Fig. 3.2; ncedc.org) and process this data using the Obspy python package (*Beyreuther*, 2010[HS1]). The P-wave and S-wave arrivals from all analyzed earthquakes produce small water level oscillations that are amplified after the arrival of the surface waves (Fig. 3.4). Love waves generally travel faster and have shear strains of larger magnitude whereas Rayleigh waves arrive later and have a dilatational component. We observe that the large drops in water level coincide with the arrival of Rayleigh waves (Fig. 4). Water level oscillations typically persist for the duration of measurable surface waves (and longer period signals within the coda) in broadband station MCB. No measurable water temperature changes (precision of 0.1 °C) was observed in response to any of the large earthquakes (Supplemental Fig. 3.12).

We quantified the peak ground velocity (PGV) for each earthquake using data from the MCB broadband station (Table 1). Both the 10 minute and 5 second water level data are highly correlated with peak ground velocity of the filtered (0.01 and 0.1 Hz) Rayleigh wave (r^2 = 0.90 and 0.74 respectively; Fig. 3.4). For earthquakes where both 10-minute and 5-second data are available, the amplitudes of water level drops are a factor of seven greater in the high frequency data compared with the low frequency data (n= 7; r^2 = 0.92).

We find that the water level oscillations at CH-10B can persist for up to an hour after the decay of measurable Rayleigh waves and we define water level "recovery" as the return to within 90% of the lowest value of the pre-earthquake period. We note that high background variability in water level biases these measurements for shorter durations. Water level recovery and the decay of Rayleigh wave amplitudes are correlated (r^2 = 0.71; Supplemental Fig. 3.15 and 3.16). The data is best fit by an exponential relation ($z = Ae^{Bt}+C$; where z is the water level drop, t is time, and A, B, and C are coefficients, r^2 = 0.913) or error function ((r^2 = 0.9132; z = Aerfc(Bt) + C, r^2 = 0.912) which is consistant with pore pressure diffusion (Supplemental Fig. 3.17).

Comparison between water level seismic data

We bandpass filtered the seismic waves to separate the low frequency teleseisms (0.01-0.1 Hz) and the high frequency peaks which may reflect triggered earthquakes (0.5-20 Hz). We were unable to correlate most of these high frequency peaks between stations (Supplemental Fig. 3.17), suggesting that the triggered earthquakes were very small and/or shallow. We calculated the total number of high frequency peaks which appeared to increase in number throughout the duration of the teleseisms (Supplemental Fig. 3.5A). We also search for a temporal association between the water levels in CH-10B and earthquakes in Long Valley caldera and the adjacent Mammoth Mountain (Latitude 37.3 to 37.9, Longitude -120 to -118, Fig. 3.1) that are in the NCDC catalog. For the two global earthquakes that induced the largest water level changes, the April 2010 M7.2 Baja California and 2017 M8.1 Pijijiapan events (both in Mexico), we plot the number of earthquakes for the 12 hours before and after

the passage of the seismic waves (Fig. 3.3). Seismicity rate following these two earthquakes increases substantially following the arrival of the surface waves and is also slightly shallower compared with the seismicity during the 12 hours before the arrival of the seismic waves, although this is within one standard deviation (Fig. 3.5C). Earthquakes locations before and after the arrival of surface waves (Fig. 3.2) are similar with most events occurring outside the Long Valley caldera. Other earthquakes that induced large water level changes did not induce enough detectable earthquakes in the vicinity of Long Valley caldera to determine a change in seismicity rate (Supplemental Fig. 3.18).

3.6 Discussion

We find that water levels in well CH-10B change in response to global earthquakes from a large range of depths, magnitudes, back azimuths, and distances (Fig. 3.1 and 3.6). The response always takes the form of a water level drop which begins after the arrival of Rayleigh waves (*e.g.,* Fig. 3.4). The peak ground velocity of the Rayleigh waves usually predicts the magnitude of water level drop (Fig. 3.6A; Supplemental Fig. 3.19 or Supplemental Fig. 3.20 $r^2 = 0.90$). However, there is significant variability in responses for similar earthquakes. For example, the PGV of ~0.5 mm/s induced water level drops of 0 to 13 cm (Fig. 3.6A). Variations are not clearly explained by back azimuth; the April 2012 M7.8 earthquake in Mexico induced no water level change while the April 2010 M7.2 earthquake in Mexico induced the largest response on record. Low frequency water level data (10-20 minute sampling) underestimates the amplitude of water level changes by almost an order of magnitude (Supplemental Fig. 3.11), yet the overall response is similar regardless of sampling rate. Water levels in CH-10B are sensitive to strains induced by seismic waves but are not sensitive to comparable strains induced by Earth tides (Supplemental Fig. 3.13). We also find a temporal correlation between earthquake-induced water level changes and triggered seismicity in Long Valley caldera and its vicinity (Fig. 3.2 and 3.5).

Water Level Responses to Teleseismic events

Water level response in wells near earthquake epicenters (within 1-2 fault lengths) are sometimes linked to static stress changes (*e.g.,* Jønsson et al., 2003), but static stress changes are infinitesimal in the far field. Water level changes are thus attributed to dynamic stresses from seismic waves when the earthquakes are distant (*e.g.,* Roeloffs, 1998; Brodsky et al., 2003; Shalev et al., 2016). Water levels in wells that are distant from the earthquake source have been observed to oscillate forming hydroseismograms (*e.g.*, Blanchard and Byerly, 1935; Cooper et al., 1965, Weingarten and Ge, 2014) which are explained by poroelastic processes due to dilatational Rayleigh waves (Hsieh et al., 1980). Water level oscillations in CH-10B are asymmetric where the rate of co-seismic drop is higher than the rise and water level recovery persists for up to an hour after shaking. A nearby well (CW-3, Fig. 3.2) appears to always experience water level rises which led Roeloffs et al. (2003) to attribute changes in

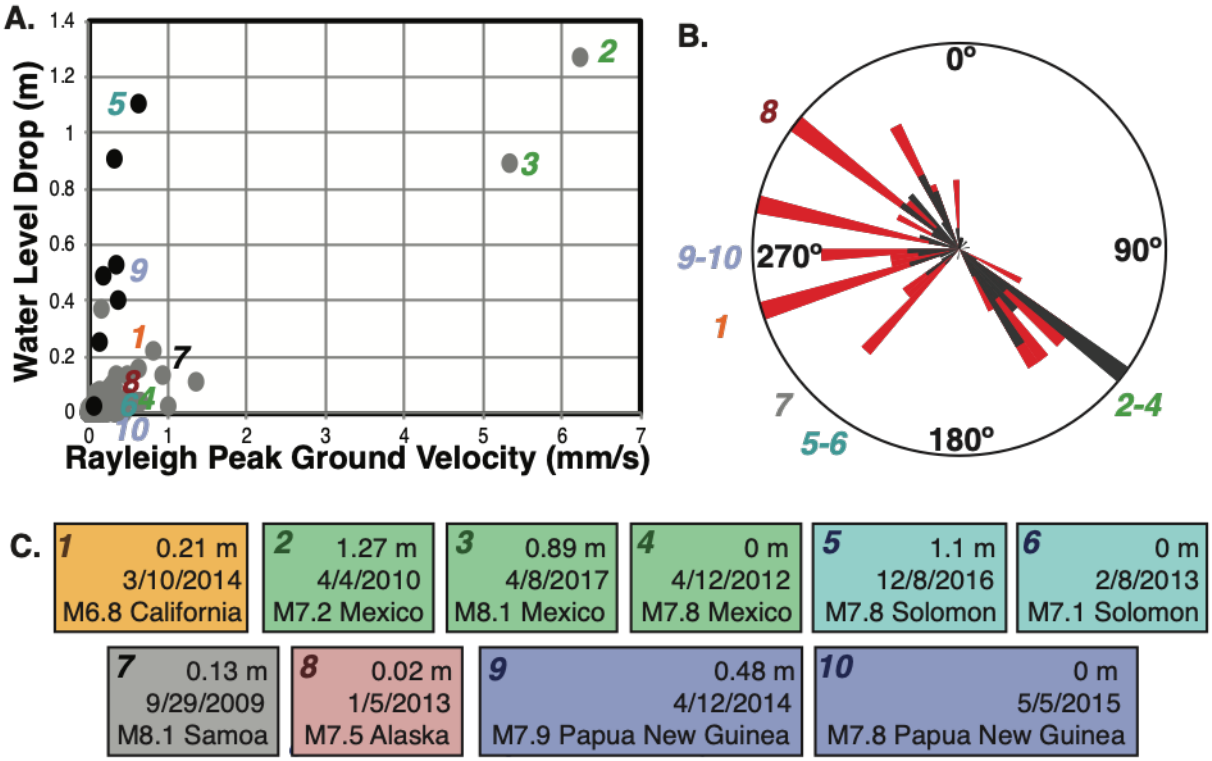

Figure 3.6: Relationship between water level drop and peak vertical ground velocity of the surface waves (bandpass filtered between 0.01-0.1 Hz.). The gray dots show the water level change from the 10-minute record for approximately 400 events. The black dots show water level change for the 5-second data (earthquakes are numbered in panel C). Because the 10-minute record is averaged over many oscillations, the water level changes are 7 times smaller (ratio of slopes on left). B) Rose diagram showing back azimuth of earthquakes shown in Figure 3.1A that induced water level changes (in red; n = 33) and all M>7.0 global earthquakes during period of record (2008-2017; n=143) in black. C. Co-seismic water level drop (top row), date (middle row) and magnitude and location (bottom row) of earthquakes presented in panels A and B.

water levels in Long Valley to regional hydrothermal flow. However, this model was invoked to explain permanent changes in water levels while we found transient changes that decayed after a few hours.

We find that water level drops correlate with the arrival of Rayleigh waves which is in contrast to other settings where the Love waves correlate with permanent changes in water level (*e.g.,* Brodsky et al., 2003; Wang et al., 2009; Shalev et al., 2016a). Shalev et al. (2016a) relate the response to both dilatational waves and Love waves to highly fractured rock being sensitive to deviatoric stresses.

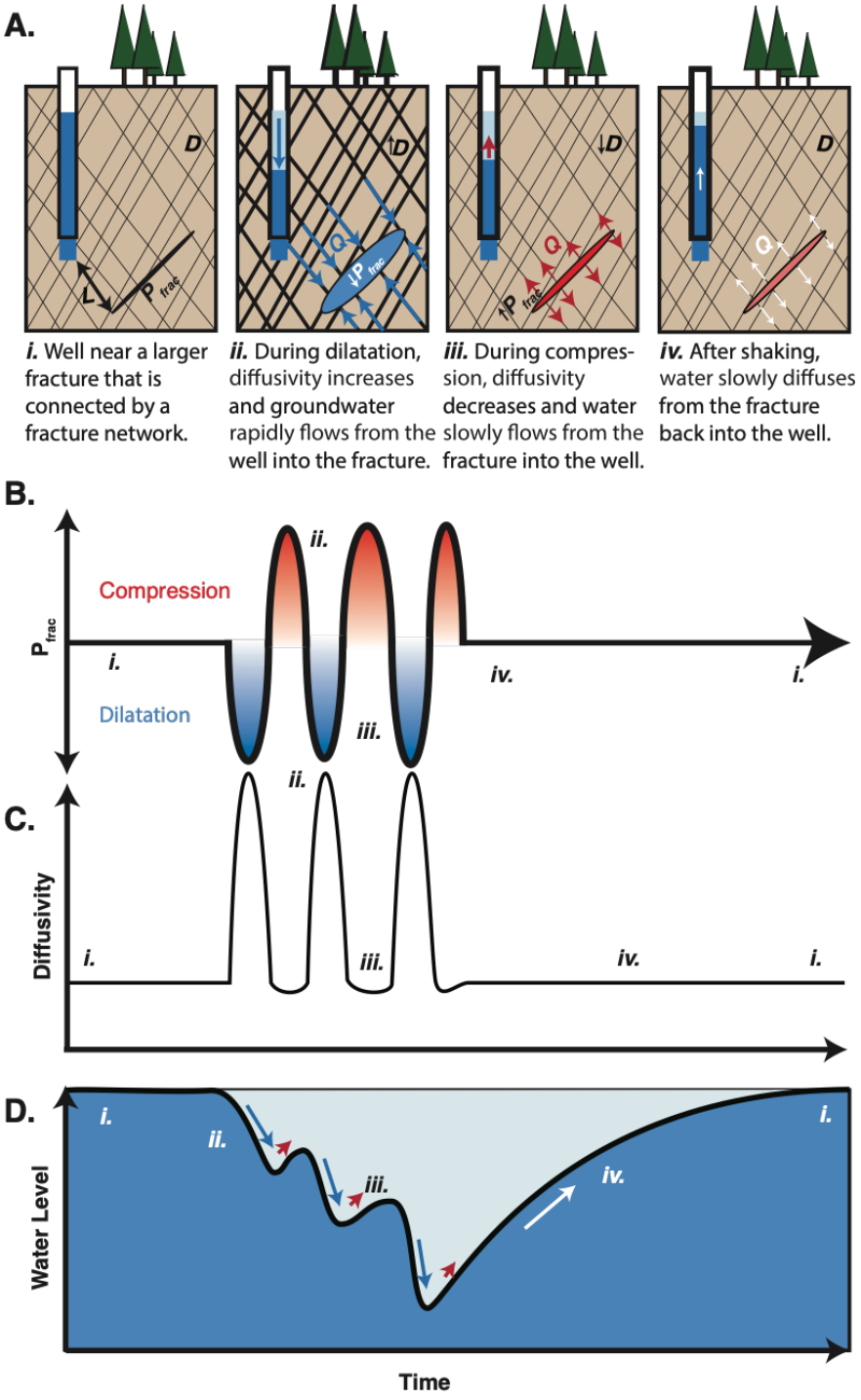

Figure 3.7: Schematic illustration of the controlling processes in the proposed model. B) pressure within a fracture near the well, C) hydraulic diffusivity changes during fracture dilatation, and D) shows water level changes resulting from these two changes. i.-iv. show the initial conditions (i), effect of dilation (ii), compression (iii), and the relaxation after shaking ends (iv).

Proposed quantitative model

Several physical models have previously been invoked to explain a causal relation between stresses induced by long-period seismic surface waves from large and distant earthquakes and water level changes in wells. Such models require water level data sampled at frequencies higher than those of the seismic surface waves. Models that relied on data sampled at frequencies lower than those of seismic surface waves were unable to determine which part of the seismic wave train induced the change and whether the change resulted from volumetric deformation induced by P and Rayleigh waves, or by deviatoric strain induced by S and Love waves (*e.g.*, Matsumoto and Roeloffs, 2003; Shi et al., 2015; Zhang et al., 2015).

Similar to the water level response in CH-10B, in nearly all wells drilled into volcanic or crystalline rocks water level changes have the same sign (co-seismic drop) following passage of the surface waves. However, in contrast to water level changes in CH-10B, in most documented cases water level drops were sustained, and the proposed models mainly accounted for the rapid co-seismic water level drops, but not for the recovery (*e.g.*, Geballe et al., 2011; Shalev et al., 2016). The previous model proposed for water level changes in Long Valley Caldera following large regional and distant earthquakes was based on data that was sampled only every 10 to 20 minutes and, thus, unable to directly relate seismic waves to water level drops in CH-10B (Roeloffs et al., 2003).

Brodsky et al. (2003) proposed a model for co-seismic water level drops induced by long-period seismic waves in a well drilled into a fractured granodiorite confined aquifer at Grants Pass Oregon. They attributed water level drops to unclogging of colloidal clay particles that block fractures. However, since water level drop implies that water flows from the well into the surrounding rocks, removal of colloidal clay from the fractures would imply that water pressure in the well prior to barrier removal was higher than in the surrounding rocks, which is an unstable and highly unlikely situation.

Models that propose nucleation, growth and transport of steam or gas bubbles (*e.g.,* Crews et al., 2014) are not applicable for explaining water level drops at CH-10 because dissolved CO_2 concentrations in the well are low (Brown et al., 2013) and the temperatures are below boiling for the local pressure (Fig. 3.3; Clor et al., 2018). Bubbles formed by cavitation would increase the volume of fluid (liquid + gas) within the well and cause water levels to increase.

We present a new quantitative model to explain the rapid co-seismic water level drop and the gradual, exponential recovery in CH-10B. The model is inspired by the fault valve model proposed by Sibson (1980) and models of dilatation (*e.g.*, Nur, 1972; Bower and Heaton, 1978).

We use a one-dimensional pressure diffusion model to explain how Rayleigh waves induce water level drops in fractured crystalline rock. We *a priori* assume that large fractures amplify dilatational stresses (*e.g.*, Chouet, 1985; Zheng, 2017) and dilated fractures increase hydraulic diffusivity (*e.g.*, Sibson, 1985; Lei et al., 2017). Our idealized model captures the hydraulic consequences of these two reasonable assumptions. The purpose of this model is to understand the flow into and out of the well without modeling the mechanical coupling,

turbulence within the well bore, the geometry of fractures, or any other second order effects. We refer to the process as "pumping" since there is a net transfer of fluid from large fractures caused by the time-varying permeability which leads to asymmetric flow out of and into fractures from an otherwise symmetric expansion and contraction during the passage of seismic wave.

We model pore pressure (P_f) diffusion (M L t^{-2}) away from a large fracture that amplifies dilatational strains into the surrounding fractured rock (Fig. 3.6A). Pore pressure within the fracture is given by:

$$P_{fr}(t) = P_0 + \Delta P sin(t\omega), \tag{3.1}$$

where is the initial pressure in the fracture, ΔP is the amplitude of the pressure change, is the frequency of the seismic wave (t^{-1}), and t is time (t) (Fig. 3.5B). Hydraulic diffusivity of the surrounding rock ($D = K/S_s$ where K is the hydraulic conductivity (L t^{-1}) and S_s is the specific storage (L^{-1}) also changes during the passage of seismic waves:

$$D(t) = D_0 e^{\alpha sin(t\omega)}, \tag{3.2}$$

where is the initial diffusivity (L^2 t^{-1}) and is the dimensionless scaling factor for diffusivity enhancement which is proportional to ΔP. The diffusion of pore pressure away from the fracture is given by:

$$\frac{\partial P}{\partial t} = D(t)\frac{\partial^2 P}{\partial x^2} \tag{3.3}$$

where x is distance from the fracture. Note that D in this model is a function of time rather than pressure and is described in equation (2), and hence fracture dilatation rather than the diffusion of pore pressure controls changes in diffusivity. The volume flux of water into the fracture is given by Darcy's Law:

$$Q = -A\frac{D(t)S_s}{\rho g}\nabla P \tag{3.4}$$

where is the surface area of the fracture (L^2), S_s is the specific storage of the fractured rock surrounding the well (L^{-1}), ρ is the density of water (M•L^{-3}), g is the gravitational acceleration (L t^{-2}), and ∇P is determined from equation (3). In turn, this flow of water into or out of the fracture (Q) affects the pore pressure at the boundary condition where $\frac{dP_{fr}}{dt} = \beta\frac{Q}{V_{fr}}$ where β is the bulk modulus of the fracture (M•L•t^{-2}), is the volume flux (L^3 t), and $V_{fr}$is the water volume within the fracture (L^3). This ensures mass conservation during dilatation and allows for pressure to relax after the last teleseismic wave (Fig. 3.4) without the assumptions required for full mechanical coupling (*e.g.,* Berryman et al., 2007). CH-10B then samples this pressure field at an unknown distance L from the fracture.

We non-dimensionalize these equations to highlight the relationship between physical properties and to generalize beyond the particular features we observe at CH-10B. The following scales are used to non-dimensionalize the variables:

$$P = P*/\Delta P; D = D^*/D_0; x = x^*\sqrt{D_0/\omega}; t = t^*/\omega \tag{3.5}$$

With * indicates a dimensionless variable: pressure is normalized by the amplitude of the pressure changes ΔP , diffusivity is normalized by the initial diffusivity D_0, length is normalized by the diffusive length scale $\sqrt{D_0/\omega}$ and time is normalized by the frequency of teleseismic waves ω.

During the dilatational portion of the Rayleigh wave, the fracture widens producing low pore pressure which diffuses through the rock (Fig. 3.7). During the compressional portion of the Rayleigh wave, the fracture contracts producing high pressure within the fracture (Fig. 3.7). However, because the diffusivity also drops, high pore pressure diffuses away from the fracture more slowly. This change in diffusivity during dilatation produces a net pumping effect where water moves from the crystalline matrix into the fracture (Fig. 3.7D). During the earthquake, pressure increases within the fracture and decreases at the well. After the earthquake, pressure slowly equilibrates between the fracture and surrounding medium (Fig. 3.7i).

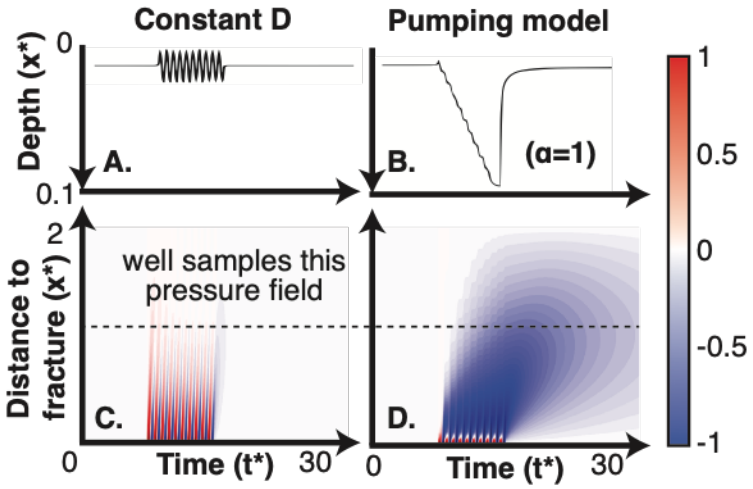

Figure 3.8: Water level (A and B) and water pressure (C and D) response to pore pressure diffusion away from a fracture. Color scale shows pressure where blue is dilatational and red is compressional. The dotted horizontal line in C and D show an example well sampling the pressure field while A and B show example water level for wells. Water level drop and the distance from the fracture is given for dimensionless distance $L/\sqrt{(D_0/\omega)}$ and time is given for a Rayleigh wave period of ω. We show two end member cases where diffusivity does not change with time (A and C) and one where permeability is amplified by a factor of two during the passage of dilatational seismic waves (B and D).

To highlight these processes, we show the pore pressure fields produced for a few seismic waves for constant diffusivity (Fig. 3.8A) and a factor of two increase in diffusivity (Fig. 3.8B). In the constant diffusivity case, both high and low pressure diffuse away from the crack producing symmetrical flow into and out of the well. However, even relatively modest

($\alpha < 2$) permeability enhancement produces a large pumping effect from the asymmetry in the flow (Fig. 3.6). Model results are most sensitive to the amplification of permeability due to passing seismic waves (α) as well as to the length and time scales for pressure diffusion. The closer the fracture is to the well the larger the maximum drop in water level (Fig. 3.9). Similarly, lower frequency seismic waves produce pressure perturbations that diffuse farther away from the fracture. The recovery of water level after dilatation ends is controlled by the degree of amplification (α) or the change in diffusivity during the earthquake. While the present model explains water level changes conceptually, we can apply this idealized model to observations, using the seismic wave as a proxy for the pressure within the fracture (P_{frac}). This produces behavior similar to that observed for relatively brief ($<$ 30 minute duration) water level changes (Fig. 3.10) but diverges significantly for longer events. This suggests that the complexity of the waveform, the geometry of fractures, and the feedbacks between dilatation and changing diffusivity are not fully captured in the idealized model presented here.

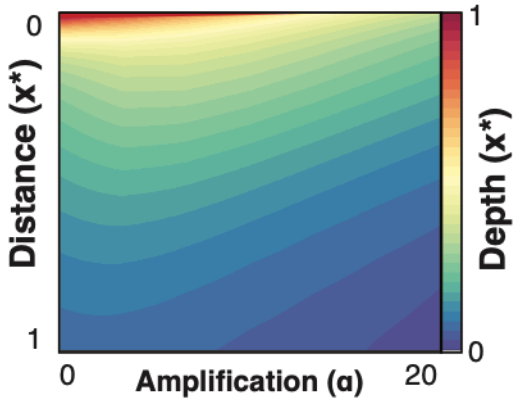

Figure 3.9: Model result showing the solution to equation 4. showing the sensitivity of water level drop (color) to diffusivity amplification (on the x-axis) and distance between well and fracture (on the y-axis) for 10 sinusoidal Rayleigh waves.

Our idealized model replicates several features of the observations from CH-10B: why the water level always drops, the dependence on peak ground velocity, the asymmetrical flow into and out of the well (Fig 4), and the recovery after Rayleigh waves decay (Figs. 3.4, 3.8 and 3.10).

5.3 Water level association with triggered seismicity

Dynamic triggering of earthquakes by seismic waves is well documented (*e.g.*, Hill et al., 1993), but the mechanisms by which teleseismic waves induce earthquakes are currently unknown, or not well understood (*e.g.,* Brodsky and van der Elst, 2014; Hill and Prejean, 2015). The temporal association between water level changes in CH-10B and triggered seismicity in Long Valley caldera suggests similar mechanisms might cause both responses. Indeed,

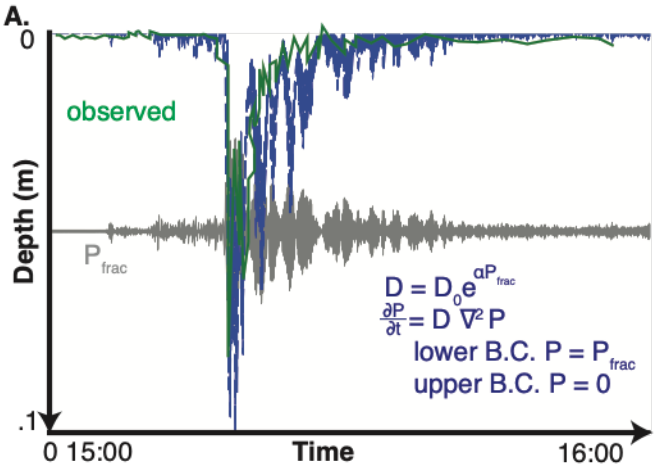

Figure 3.10: Measured water level change following the 2016 M6.6 Ferndale, California Earthquake (black curve) and the modeled (equations 1-4) water level change for the event (blue curve) using the vertical component of the surface waves from broadband station MCB (gray curve). This model assumes the distance from fracture is 3 m, α =20, and D_0 = .01 m2/s

Brodsky et al. (2003) suggest changing permeability may explain triggered in geothermal settings. Parsons et al. (2017) found the temporal evolution of triggered earthquakes to be consistent with the diffusion of pore pressure along a fault. In addition to our observation of triggered seismicity, past occurrences in Long Valley caldera also appear to have caused changes in water level at CH-10B (Roeloffs et al., 2003). At Yellowstone National Park, the November 2002 Denali earthquake 3000 km away triggered earthquakes and changed geyser eruption rates (Husen et al., 2004). The model we propose to explain water level changes in CH-10B may also be relevant at seismogenic depths and provide a mechanism to explain why seismicity can continue after teleseismic waves have passed. The effects of Rayleigh waves attenuate with depth, yet at 5 km (Fig. 3.4) these dilatational stresses can still be substantial (~90 kPa; Hill, 2012). These dilatational stresses may drive water from a fracture zone near to the fault into the fault increasing pressure. However, to expand our proposed model to seismogenic depths would require detailed information about the fault architecture and the locations of triggered events.

3.7 Conclusion

In this study, we presented new observations of water level changes in a well in Long Valley caldera in response to large global earthquakes. We present a physical model to explain how Rayleigh waves propagating through fractured crystalline rock induce water level changes. The main conclusions are:

1. Water levels in well CH-10B in Long Valley caldera drop by as much as 1.2 m during the passage of Rayleigh waves. The magnitude of water level change is correlated with the peak ground velocity of Rayleigh waves. Back azimuth, earthquake magnitude, earthquake depth, and the central frequency of seismic waves appear to minimally affect groundwater levels.

2. No measurable water temperature changes (precision of 0.1 °C) were recorded by two sensors in response to any of the large earthquakes.

3. Water levels gradually recover exponentially to pre-earthquake levels within a few hours following the expression z = Ae

4. For earthquakes where both 10-minute and 5-second data are available, the amplitudes of water level drops are a factor of seven greater in the high frequency data compared with the low frequency data.

5. We present a new quantitative physical model in which permeability is a function of strain. This leads to a net transfer of fluid from fractures owing to the asymmetry of flow entering and leaving fractures. This model replicate observed water level changes in response to the passage of teleseismic waves.

6. Some distant earthquakes that induced large water level changes at CH-10B also triggered micro-earthquakes in Long Valley caldera.

3.8 Acknowledgements

I would like to acknowledge my collaborators on this study S. Hurwitz, M. Manga, T. Mittal, L. Clor, and J. Howle. We dedicate this chapter to the late Dave Hill, the founder and former scientist-in-charge of the Long Valley Volcano Observatory who was essential in raising earthquake and volcano hazard awareness in the Long Valley and Mammoth Lakes area and was one of the initiators of studies on triggered seismicity. We thank Fred Murphy for his help designing and operating the high-frequency measurements at CH-10B. N. Randolph-Flagg was supported by the National Science Foundation Graduate Research Fellowship (DGE 1106400). MM and NRF were further supported by NSF awards 1334424 and 1521855. S. Hurwitz and L. Clor were supported by the USGS Volcano Hazards Program and J. Howle by the USGS California Water Science Center. Authors are not aware of any conflicts of interest. Data used within this study is all publicly available via USGS and IRIS archives. Any use of trade, firm, or product names is for descriptive purposes and does not imply endorsement by the U.S. Government.

3.9 Supplemental Information

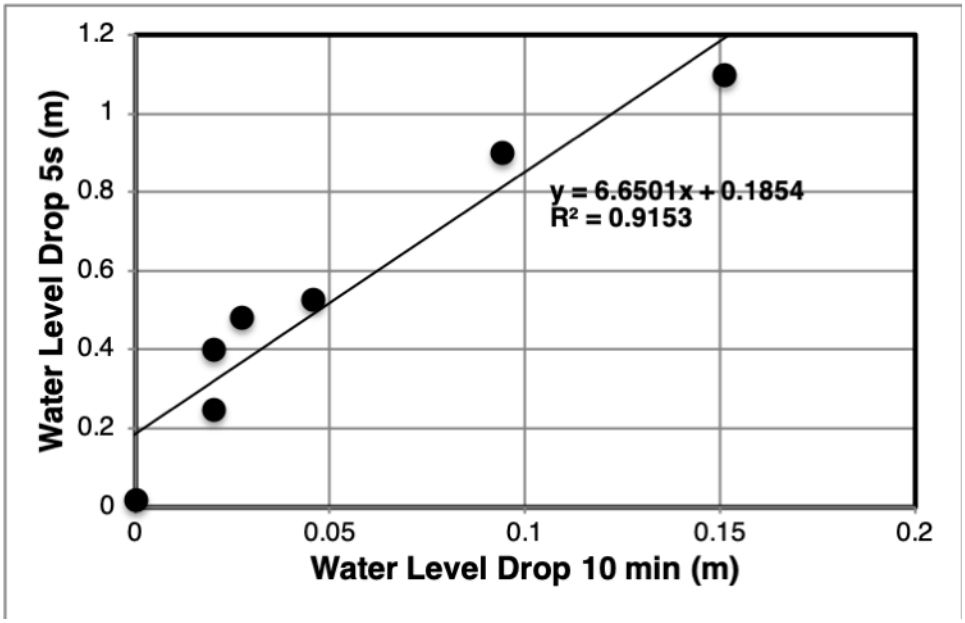

Figure 3.11: Comparison between water level change recorded using 10 min data and 5 second data.

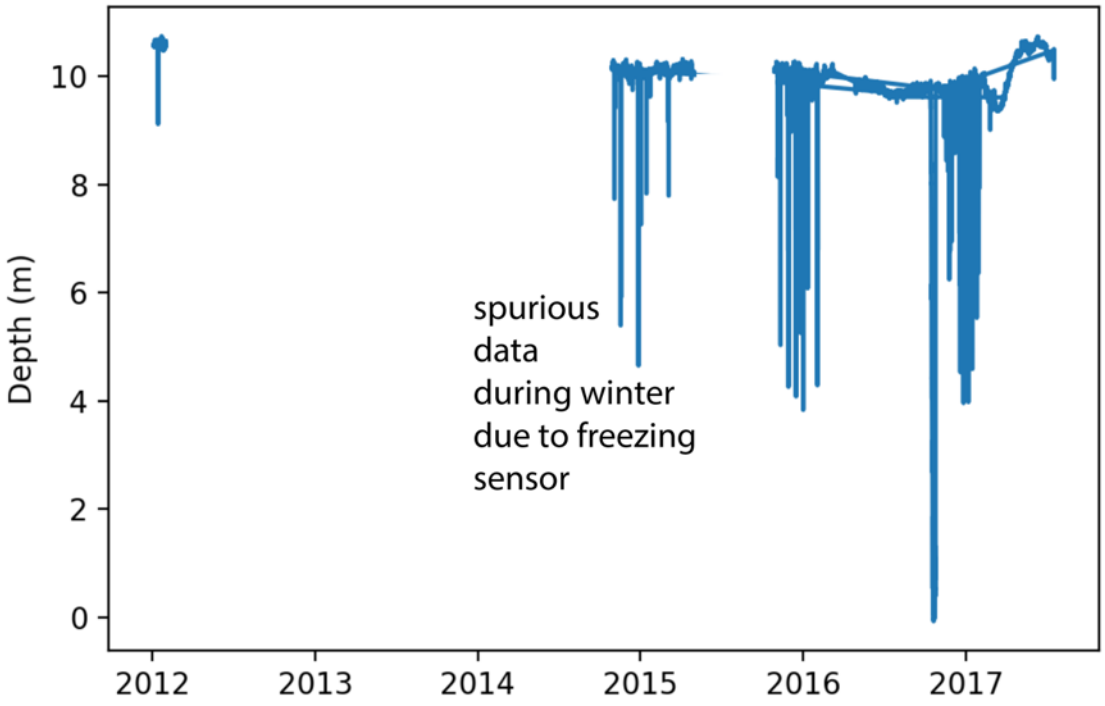

Figure 3.12: Intermittent 5-second water level records. Large drops in water level are due to freezing sensor. These changes due to equipment failure have diagnostic features and are not correlated with any earthquakes.

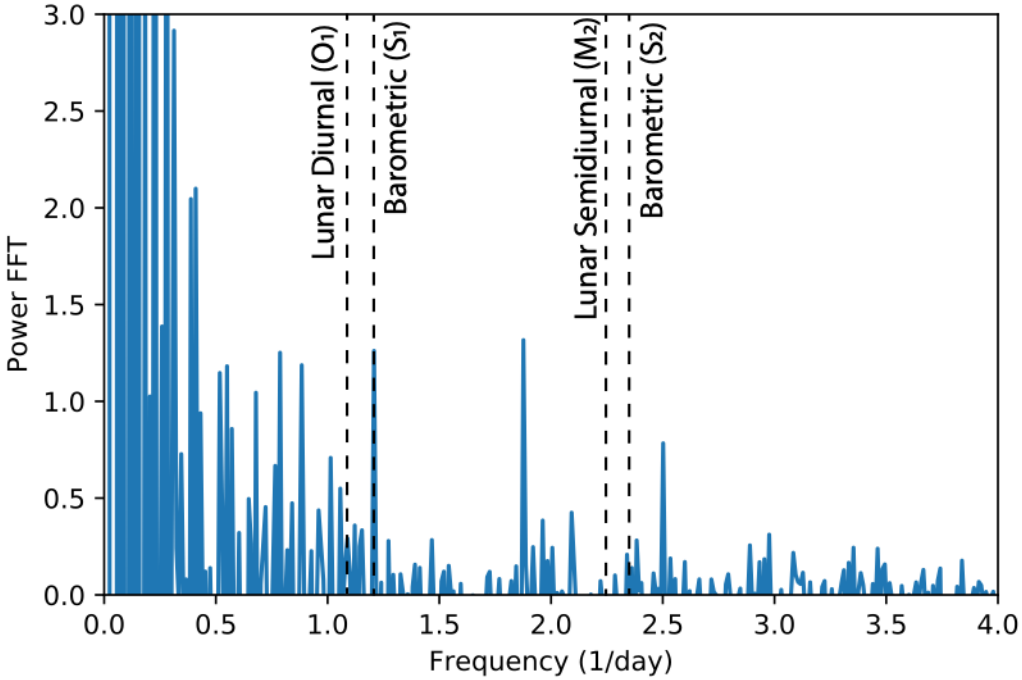

Figure 3.13: Periodogram of water level changes at CH10-B. Frequency of solid Earth tides and barometric pressure calculated from SPOTL (https://igppweb.ucsd.edu/~agnew/Spotl/spotlmain.html) are marked as vertical lines.

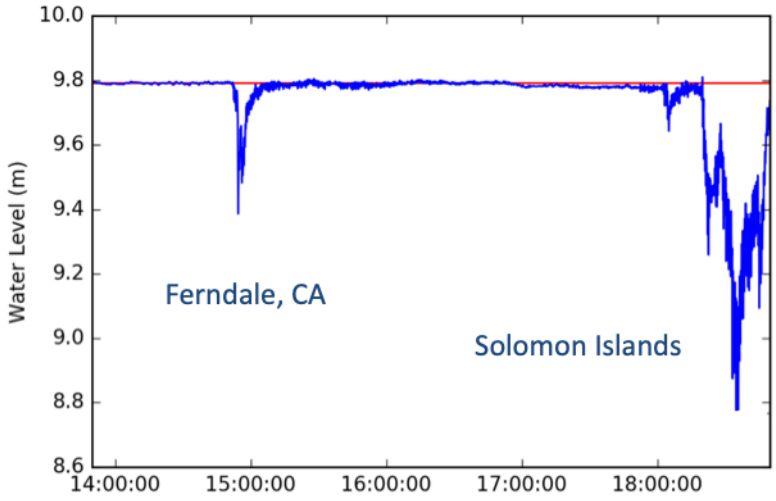

Figure 3.14: Time series of water level changes for two earthquakes that occurred within 2 hours of each other on 08 December, 2016.

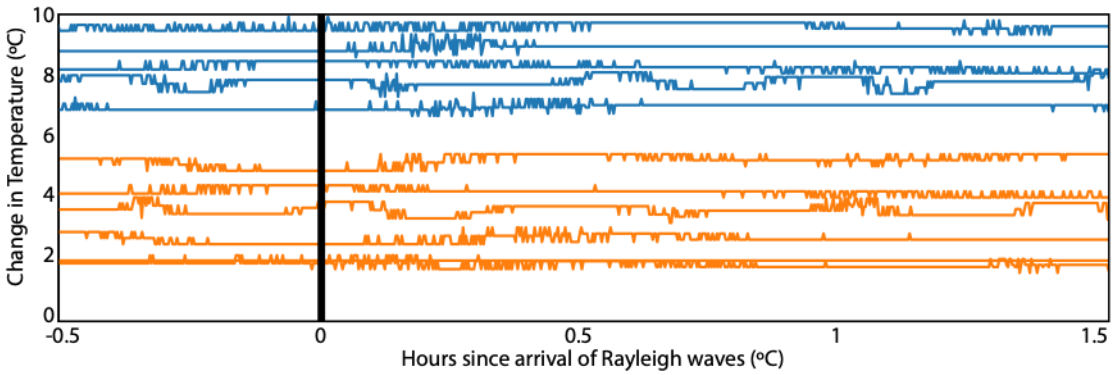

Figure 3.15: Time series of temperature at a depth of 43 m (blue) and 49 m (orange) sampled at five seconds after 5 earthquakes detailed in Table 3.1 that had 5 second data available. Black vertical line is the arrival of the earthquake. Blue data is for 43 m and orange data is from 49 m depth. Data are offset from so that curves are distinguishable all 43 m is ~98^{o}C and all 49 m data is ~95^{o}C.

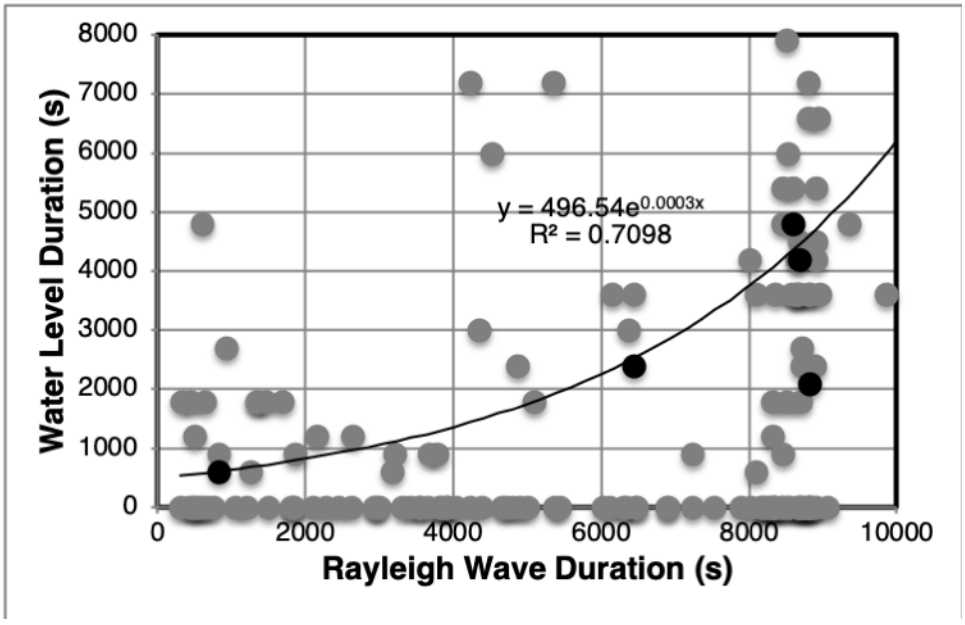

Figure 3.16: Duration of water level change and Rayleigh wave where duration is calculated as the return time after the earthquake to within 90% of variability for 15 minutes prior to the earthquake. Gray dots show 10 and 15 minute data while black dots show 5 second data.

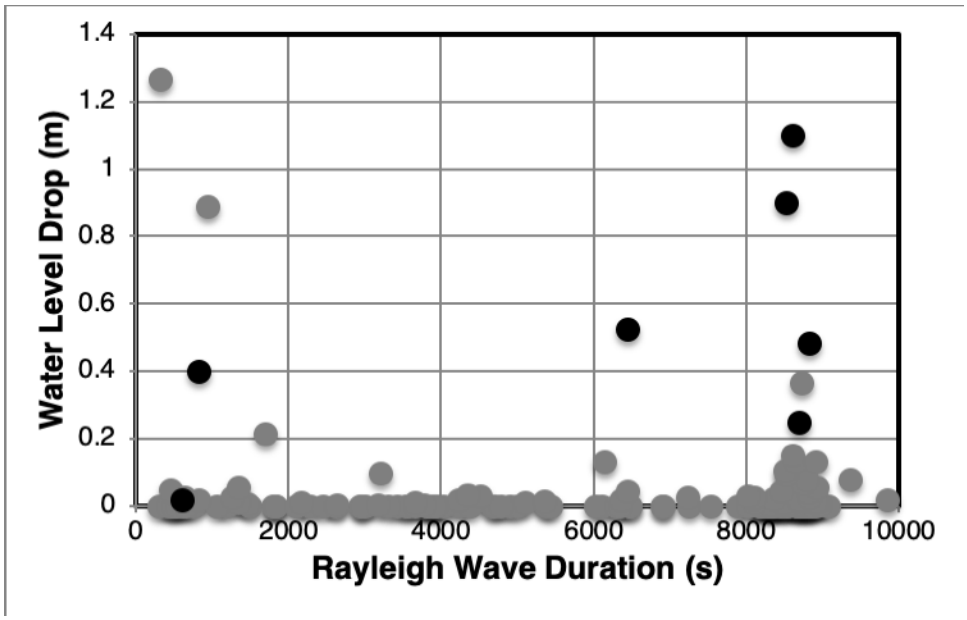

Figure 3.17: Duration of water level change and Rayleigh wave where duration is calculated based on deviation from 90% of variability for 15 minutes prior to the earthquake. Gray dots show 10 and 15 minute data while black dots show 5 second data.

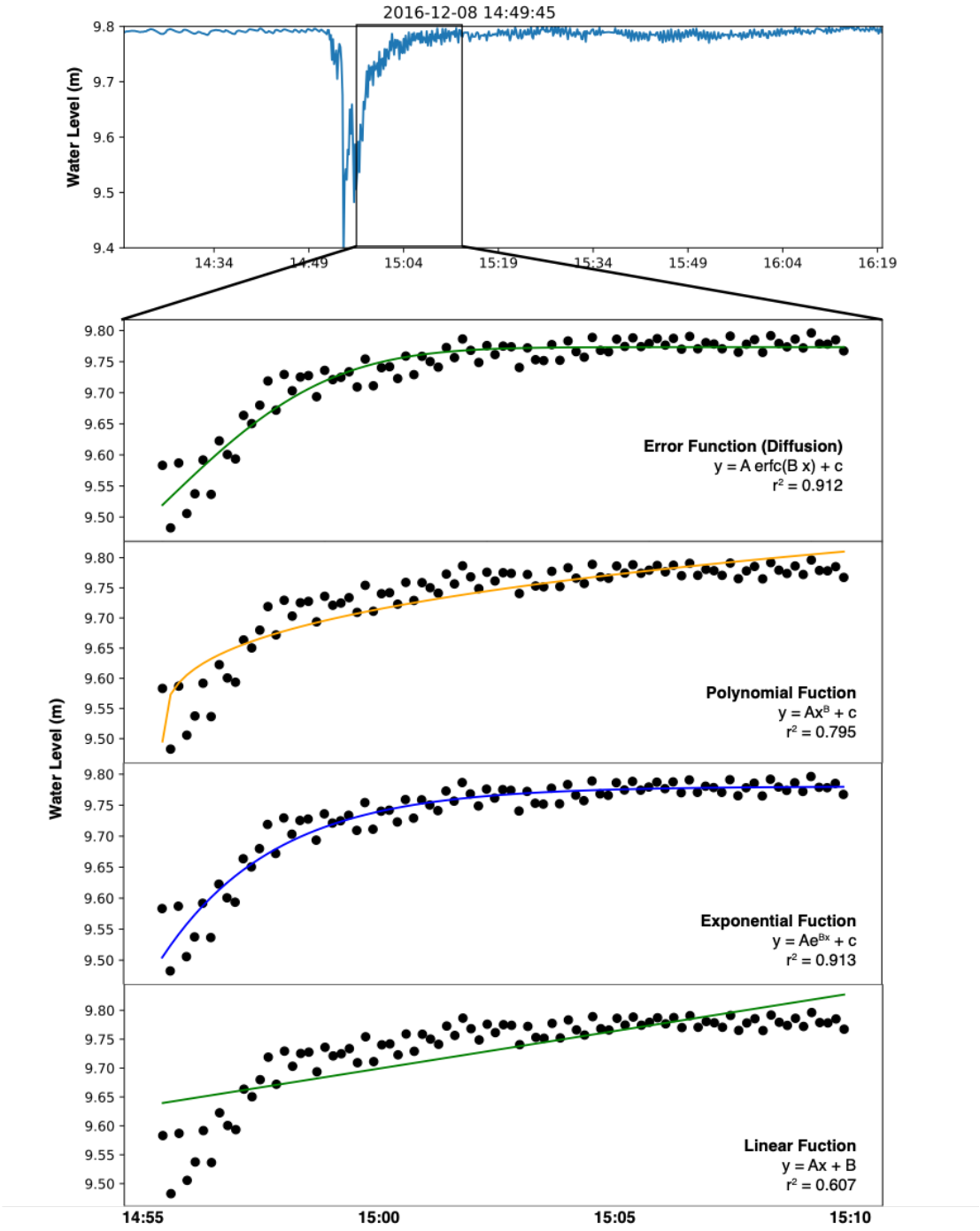

Figure 3.18: Comparison between linear, exponential, polynomial, and diffusive recovery fits to water level change for 12/08/2016 M6.6 Ferndale, California earthquake.

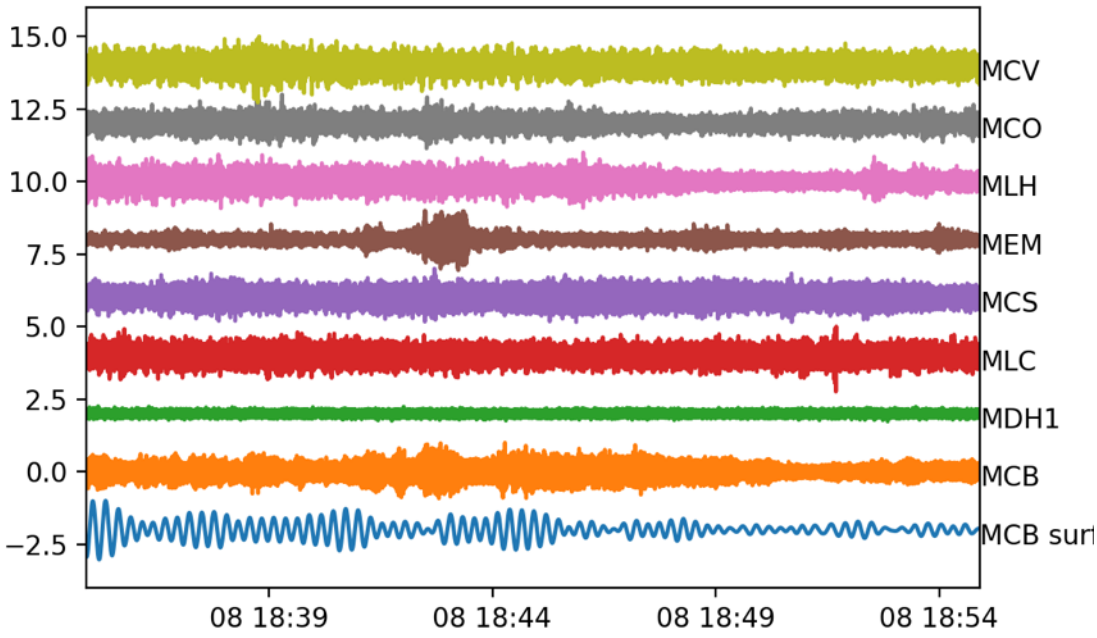

Figure 3.19: Bandpass filtered broadband data for the 12/8/2016 M7.8 Solomon Islands earthquake. The bottom curve (MCB surf) is the low frequency surface waves (0.01-0.1 Hz) recorded by the vertical component at MCB. The other curves are the high frequency vertical component (0.5-20 Hz) recorded at nearby broadband seismometers (all available at IRIS.org). Highlights difficulty in correlating high frequency peaks among stations.

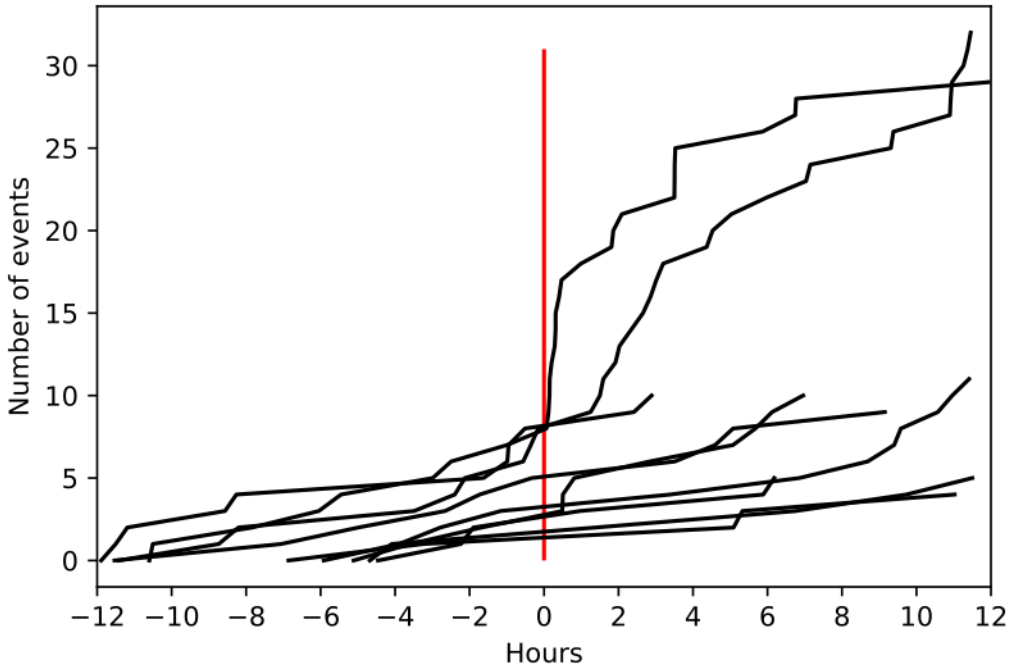

Figure 3.20: Cumulative number of earthquakes is the USGS catalog (M>0.1) before and after the two earthquakes with the largest change in water level for each earthquakes in Table 3.1. Red line shows the arrival of the Rayleigh wave for each earthquake.

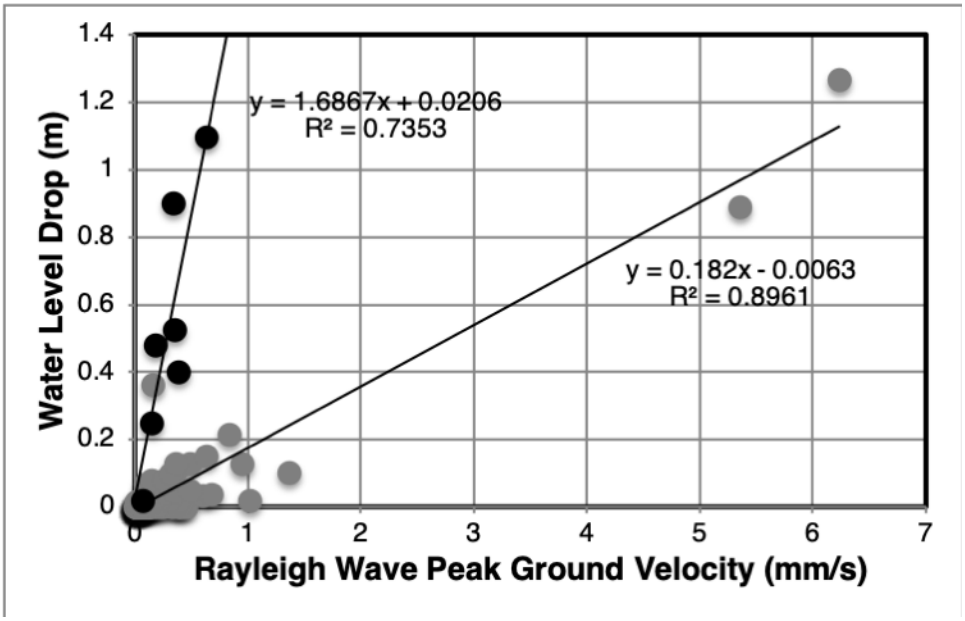

Figure 3.21: Comparison of water level drop with Rayleigh wave central frequency. Gray dots show 15 minute data and black dots show 5 second data.

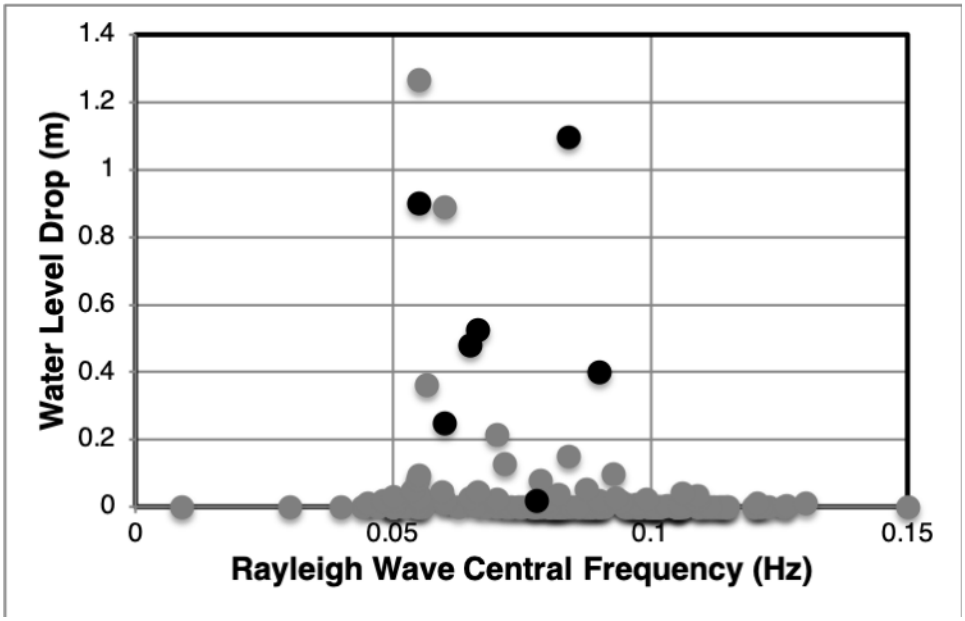

Figure 3.22: Comparison of water level drop with Rayleigh wave central frequency. Gray dots show 15 minute data and black dots show 5 second data.

Chapter 4

Hydrologic responses to the M6.4 2016 Meinong Earthquake, Taiwan

4.1 Abstract

The 2016 M6 Meinong earthquake in southern Taiwan produced hydrologic responses as much as 100 km away from the earthquake epicenter. These responses include liquefaction, mud volcano eruptions, increased discharge in streams, and water-level changes in 270 wells. These hydrologic observations were accompanied changes in mud volcano chemistry and changes in seismic velocity all of which suggest that the Meinong earthquake caused mixing between deep and shallow groundwater systems.

4.2 Introduction

Earthquakes cause a variety of hydrological responses including liquefaction, water level changes in wells, and mud volcano eruptions (for reviews see Wang and Manga, 2010). Most studies of these responses have been explained by the enhanced permeability of aquifers (*e.g.*, Manga et al., 2012). Recent studies (*e.g.*, Wang et al., 2012; Rutter et al., 2016; Liao et al., 2015; Wang et al., 2016; Zhang et al., 2019) suggests that, in addition to permeability enhancement, earthquakes can also breach aquitards between aquifers, change groundwater flow patterns, and thereby disrupt groundwater systems. This disruption can impact water resources and subsurface infrastructure. Hazardous waste is often stored in deep aquifers under the assumption that it will not mix with more shallow drinking water supplies. Much of the damage after the 2015 M6 Danfield/Christchurch earthquakes was due to liquefaction when highly pressurized aquifers equilibrated with shallow soils causing liquefaction (Rutter et al., 2016).

Due to the ongoing collision between the Eurasian Plate and the Philippine Sea Plate, the island of Taiwan is one of the most seismically active areas on Earth. This convergence has been foundational in our understanding of accretionary wedges and fold thrust belts

(*e.g.,* Suppe et al., 1990) where a series of parallel N-S trending faults produce earthquakes, aseismic slip, folds, and mud volcanoes. The 1999 M7.6 ChiChi earthquake in central Taiwan produced the most thoroughly studied groundwater response to a large local earthquake (*e.g.,* Wang et al., 2001; Chia et al., 2001; Lee et al., 2002; Wang et al., 2004; Wang et al., 2012; Huang et al, *in prep*) and gave rise to testable predictions about how fluid reservoirs may be disrupted after a large local earthquake.

At 2 am on February 7, 2016 the M6.4 Meinong earthquake struck the southern part of this island (Fig. 1a), killing more than 100 people and causing property damage. The hypocenter was 15-20 km deep on a 25-30° NE dipping fault while >10 cm of occurred at the surface more than 10 km to the west suggesting shallow faults were activated (*e.g.*, Le Beon et al., 2016; Huang et al., 2016).This tragedy is a timely opportunity to study how earthquakes may disrupt groundwater systems. The Meinong event occurred near to ~500 groundwater wells (Fig. 1) that have continuous hourly data, more than two dozen mud volcanoes (You et al., 2004; Yang et al., 2004; Chao et al., 2010), and broadband seismometers to record ground motion. Many of the water wells host a cluster of wells drilled to different depths and opened to different aquifers. This dense, continuous network of wells sampling at a range of depths is ideal for examining how earthquakes may breach aquitards and disrupt groundwater systems.

Enhanced permeability was first proposed to explain changes in stream discharge after 1992 Landers Earthquake (Rojstaczer et al., 1995). Subsequent analyses of the tidal response of water level in wells confirm that large earthquakes can locally change the permeability of aquifers (*e.g.*, Elkhoury et al., 2006; Xue et al., 2013; Shi et al., 2015). Wang et al. (2004a) showed that the increased stream flow after the 1999 Chi-Chi earthquake in Taiwan could be due to an increase in the vertical permeability of the crystalline Central Range. Studies on increased stream flow after several other large earthquakes (*e.g.*, M6.9 Loma Prieta earthquake, Rojstaczer and Wolf, 1992; M7.9 Chi-Chi earthquake, Wang et al., 2004b; M5.5 Alum Rock earthquake, Manga and Rowland, 2009; earthquake in Chile, Mohr et al., 2016), on basin-scale changes of groundwater temperature (Wang et al., 2013), and on the composition of water that emerged to the surface after the 2014 Napa earthquake in California (Wang and Manga, 2015) are consistent with this model. Liao et al. (2015) studied the tidal response of water level in a deep (~4 km) well in western China and showed that large earthquakes can also increase the vertical permeability of groundwater systems to depths of several km.

There are numerous mud volcanoes in the accretionary wedge of western Taiwan (Fig 1) which taken together emit ~40,000 tons of methane into the atmosphere (Chao et al, 2010). Mud volcanoes are caused by overpressured muds rising kilometers through the crust. Similar to groundwater in artesian wells, mud volcanoes sometimes respond to earthquakes (*e.g.*, Mellors et al., 2006; Maestrelli et al., 2017) and, in Taiwan, have responded to past similarly sized earthquakes (Jiang et al., 2006). These responses are proposed to be caused by the same mechanisms that change groundwater levels, i.e. dynamic or static stress changes that change horizontal or vertical permeability (*e.g.,* Rudolph et al., 2015). Unlike wells, mud volcanoes sample deeper fluids and may provide insight into fault zone processes and deeper

hydrologic responses.

This densely monitored area with numerous wells and mud volcanoes is an ideal location to address three questions: Did the hydrologic system change after the earthquake occur? How and why did these changes occur? Did the earthquake create new hydrologic connections between deep fluids and the shallow groundwater system? The 2016 Meinong earthquake in Taiwan caused liquefaction and mud volcano eruptions and as such is a new opportunity to collect additional data and test hypotheses. To answer these questions and test hypotheses we collected water samples, recorded responses at mud volcanoes, recorded water temperature and collaborated with local scientists to determine the location and magnitude of liquefaction, well responses, and ground accelerations. We also compare coseismic strain from geodetic measurements and map ground motion to compare to interpret the spatial distribution of responses. We analyze water sample hydrogen and oxygen isotopes at mud volcanoes to look for changes in water source and whether the Meinong earthquake caused connections between shallow and deep fluids. In particular, we would like to quantify the depth of disruption after a moderately sized earthquake. While the magnitude of the Meinong event is not unusual, the large number of monitoring wells and mud volcanoes that have responded make this an uncommon opportunity to study the disruption of groundwater systems, the coseismic increase of vertical permeability, and the possible coseismic connection between the deep and shallow hydrologic systems.

4.3 Data

Taiwan has a dense hydrologic monitoring network. The Central Weather Bureau (http://gic.wra.gov.tw) collects hourly stream discharge, water levels in groundwater wells, and precipitation throughout the country. Mapped liquefaction, distributed mud volcanoes, and broadband seismometers provide information about the hydrologic system through a few kilometers of the crust.

Streams: At the surface, we use stream discharge which, in most cases, flow east and west from the Central Range to the ocean. We look at stream gauges for 32 streams that use rating curves to convert water level to volumetric discharge (Fig. 1, diamonds).

Liquefaction: The shallowest groundwater may contribute to liquefaction. We combine the mapped incidences of liquefaction (Fig 1, crosses) from two geotechnical surveys conducted shortly after the Meinong earthquake (Lu et al., 2017; Tsai et al., 2018).

Mud volcanoes: Mud volcanoes are common in accretionary wedges. In June 2016, four months after the Meinong Earthquake, we sampled four mud volcanoes near to the earthquake epicenter (Fig 1, triangles). We collected 500 ml jars of mud, allowed the mud to settle, extracted and filtered the water, and finally performed the isotope analysis of this water at the Center for Stable Isotope Biogeochemistry, UC Berkeley. We also use some publicly available Google Earth images to estimate the eruptive surface area in the days after the earthquake.

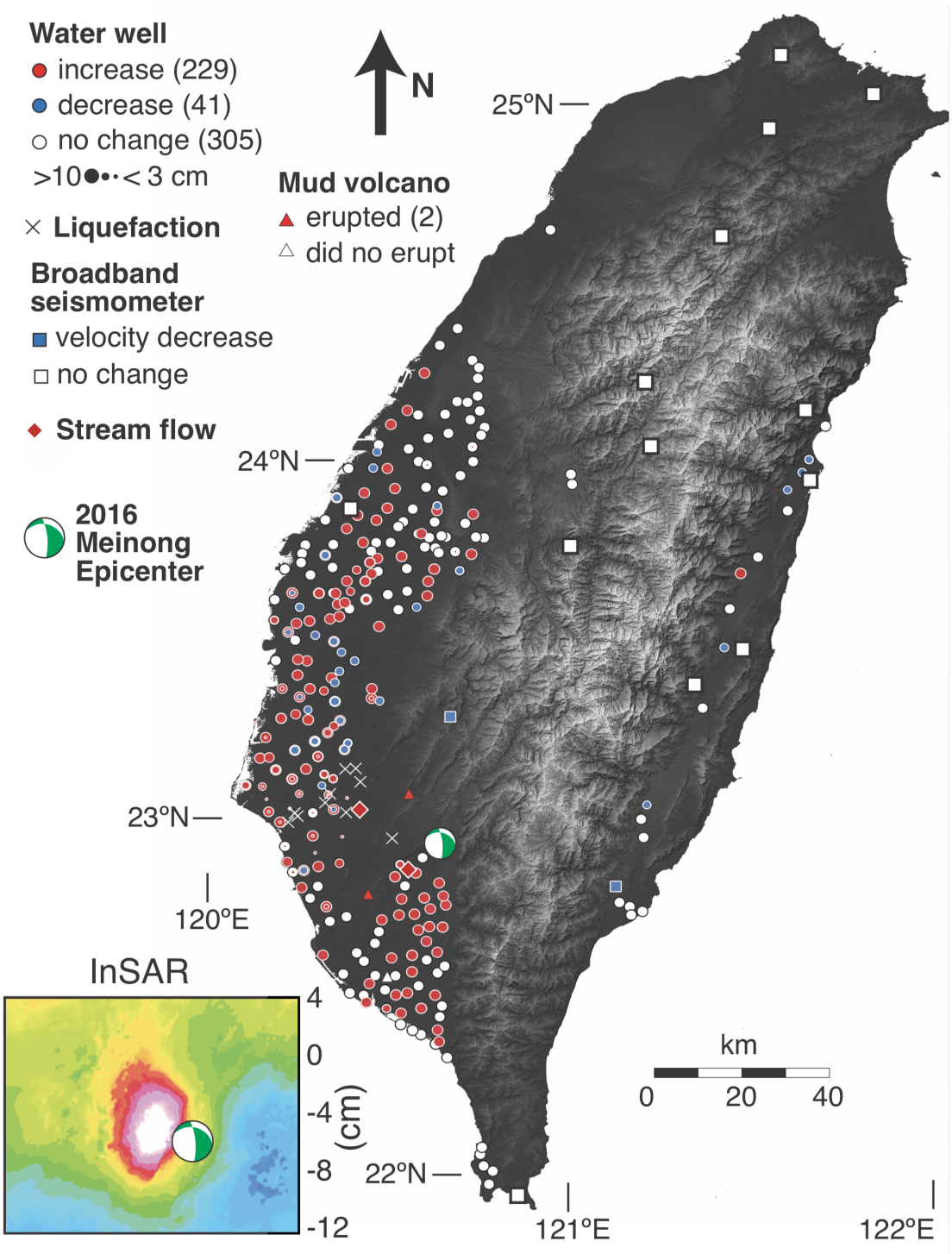

Figure 4.1: Map of Taiwan showing groundwater wells (circles) that rose (red), dropped (blue), or remained unchanged (white) after the 2016 Meinong Earthquake. The circle size reflects the magnitude of this change. White x's show documented liquefaction while red diamonds show streams that had an increase in discharge. Squares show broadband seismometers that experienced decreases in seismicvelocity (blue) or no change (white.) Triangles show mud volcano that eyewitnesses found erupted or increased eruption rate (red) and those that did notchange in (white.) Inset shows vertical deformation from ALOS InSAR for the samemap scale.

Seismometers: Broadband seismometers may record even deeper changes in rock properties. We use 17 broadband seismometer records (Fig. 1, squares) available via IRIS (iris.edu) to find changes in seismic velocity before and after the earthquake. We use single station cross correlations to reduce the effect of clock errors and to determine the relative change in seismic velocity (see Huang et al., *in prep.* for full methodology).

4.4 Results and Discussion

Of the 32 streams that had continuous discharge measurements only two show a dramatic increase in discharge after the earthquake. Both records are within 20 kilometers of the earthquake epicenter and are close to the most significant surface deformation reported by Huang et al. (2016) (Fig. 1). These findings are consistent with Mohr et al. (2018) who found that streams in Chile require larger peak ground acceleration than wells to produce changes in discharge. While it is possible that local rain storms may affect stream flow, nearby rain gauges show that there was relatively little rain in February of 2016 ($<$ 10 mm over the month) and that the two small (1 mm) rainfall events that occurred a few days after the earthquake would not be sufficient to explain the observed changes in water discharge. Some stream gauges closer to the earthquake epicenter and to the most dramatic deformation had no measurable change in discharge (*e.g.,* Shanlin Bridge). Both streams that responded are upstream from urban and agricultural centers. The change in discharge is similar to that observed after other earthquakes (see Manga and Wang, 2009). These observations suggest that changes in stream flow are likely related to changes in permeability allowing for increased groundwater supply into the stream (*e.g.,* Rojcatzer et al., 1996) rather than due to precipitation or breached irrigation channels or levees.

Similar to the changes in stream flow, liquefaction after the earthquake was concentrated directly west of the earthquake epicenter (Fig. 1; Lu et al., 2017; Tsai et al., 2018). This is partly due to the distribution of developed population centers but also related to the strong directivity of shaking and possibly the activation of faults within the Tainan tableland (Huang et al., 2016). Le Béon et al. (2017) conducted field surveys within the hills close to the epicenter and found no evidence of liquefaction although other types of damage were observed (Le Béon et al., 2017). Documented instances of liquefaction all occur in sedimentary basins which are largely composed of interlayered high and low permeability sediments. Liquefaction in these settings sometimes is the result of breaching aquitards such that high pore fluid pressures fluidize shallow sediments (*e.g.*, Rutter et al., 2015).

We surveyed water level records at 575 groundwater wells in southern Taiwan (Fig. 1). The average water level change after the Meinong earthquake was 8 $\pm$ 27 cm with 229 wells showing an increase in water level, 41 wells showing a decrease in water level, and 305 wells showing no change. At wells where we have records from multiple depths, we observe that deeper wells have drops in water level and shallower wells have rises in water level (Fig. 4.1). The largest rise in water level was observed at Wujia (depth 46 m) where the water level rose by 3.03 m while the largest drop in water level occurred at Pingxi (depth 248 m) where

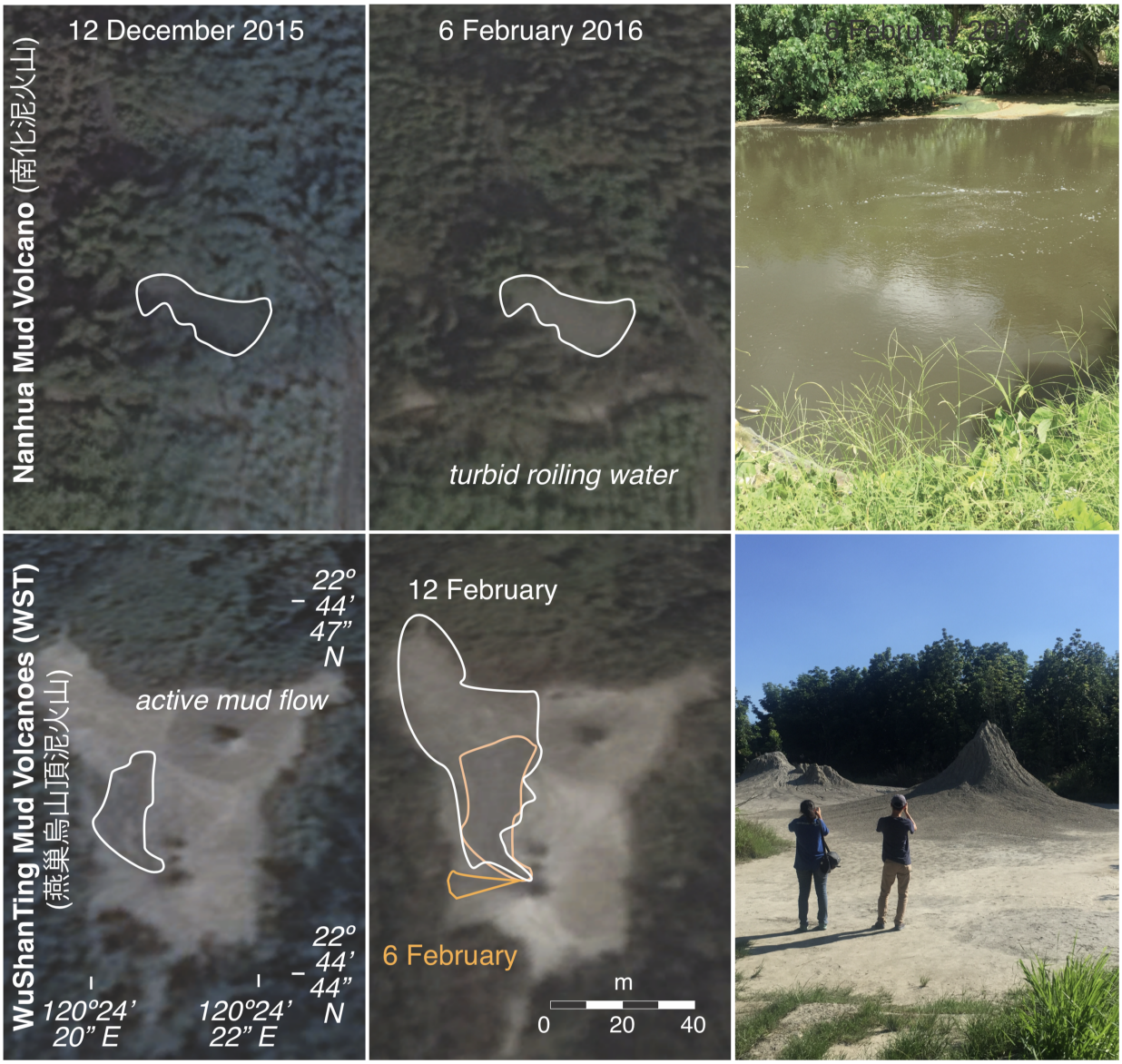

Figure 4.2: Nanhua mud volcano (top) and WuShanTing mud volcanoes (bottom). Left column shows Google Earth satellite image two months before the Meinong Earthquake. Middle column shows Google Earth satellite 15 hours after the Meinong Earthquake with active mud flow area highlighted in orange. The area of active mud flow six days after the earthquake is highlighted in white. The right column shows photos of both sites in June, 5 months after the Meinong Earthquake.

the water level dropped 1.92 m. The most distant well where we observed a groundwater response was ~100 kilometers from the epicenter and the largest responses were closer to the epicenter. Some studies found that the rise or fall of water level reflects changes in static stress after an earthquake (*e.g.*, Jønssen et al., 2003). In contrast, we observe changes in water level to be broadly similar throughout southern Taiwan suggesting that dynamic stresses may better explain the observed changes in water level. This is consistent with past studies in Taiwan (*e.g.*, Wang et al., 2004 or Manga et al., 2012 for global survey). These findings are consistent with a similar analysis by Feng et al. (2016).

After the Meinong earthquake, two relatively large and easily accessible mud volcanoes were observed to change. The most dramatic of these changes was at Nanhua mud volcano which was originally an oil and gas well during the Japanese occupation in the 1920s. After production ceased, the well filled with water, and mud and gas now vent into this pool. In the hours after the Meinong earthquake, Nanhua mud volcano erupted, causing water to launch over a meter into the air. During this time, the pond became more turbid (visible from satellite images) and roiling, and both observations persisted for a few days (Fig. 2). The other mud volcano where eyewitnesses observed changes, Wushanting, is a developed tourist attraction with about five mud vents. Two of these mud volcanoes have meter-scale edifices while the others are small bubbling pots. In the days after the Meinong earthquake the largest vent which had been erupting before the earthquake increased in eruptive volume (Fig. 2). This change was confirmed with satellite observations where the wet mud is visibly darker than the dry surrounding material. We observe an increase from ~100 m^2 to ~800 m^2 in the 48 hours after the Meinong earthquake. Most of Taiwan's mud volcanoes are small, not observable from space, and remote and hence unlikely to have eyewitness accounts of changes in eruption rate or style. The distance between these mud volcanoes which erupted and the earthquake epicenter is consistent with documented mud volcano eruptions globally where mud volcanoes erupt where seismic energy densities are greater than ~1 J/m^3 (Fig 3; Supplemental Table 4.1).

The Wandan mud volcano erupted within actively cultivated rice fields near a monastery and, consequently has had every eruption recorded for decades. Unlike most other mud volcanoes in southern Taiwan, Wandan has relatively high temperature (~80 ^{o}C) suggesting that mud traverses kilometers of the crust (average geotherm 10 ^{o}C/km; You et al., 2004) without losing heat. We witnessed the first eruption of 2016 during our fieldwork in June of 2016. Although Wandan is farther from the earthquake epicenter than the two mud volcanoes that erupted, it is at the southern terminus of the FengShan Fault it experienced ground motions that have triggered mud volcano eruptions in other settings. This may reflect that the Wandan mud volcano is connected to a deeper fluid reservoir and that there is simply a long lag between changes within this reservoir and mud eruption at the surface. While it is possible that the deeper fluid reservoir may have been affected by the earthquake, it seems unlikely that the eruption in June was triggered by the earthquake in February.

Finally, we use the geochemistry of mud volcanoes to identify both changes in water chemistry after the Meinong earthquake and to propose a mechanism for these changes. You et al. (2004) document the water chemistry of mud volcanoes throughout southern

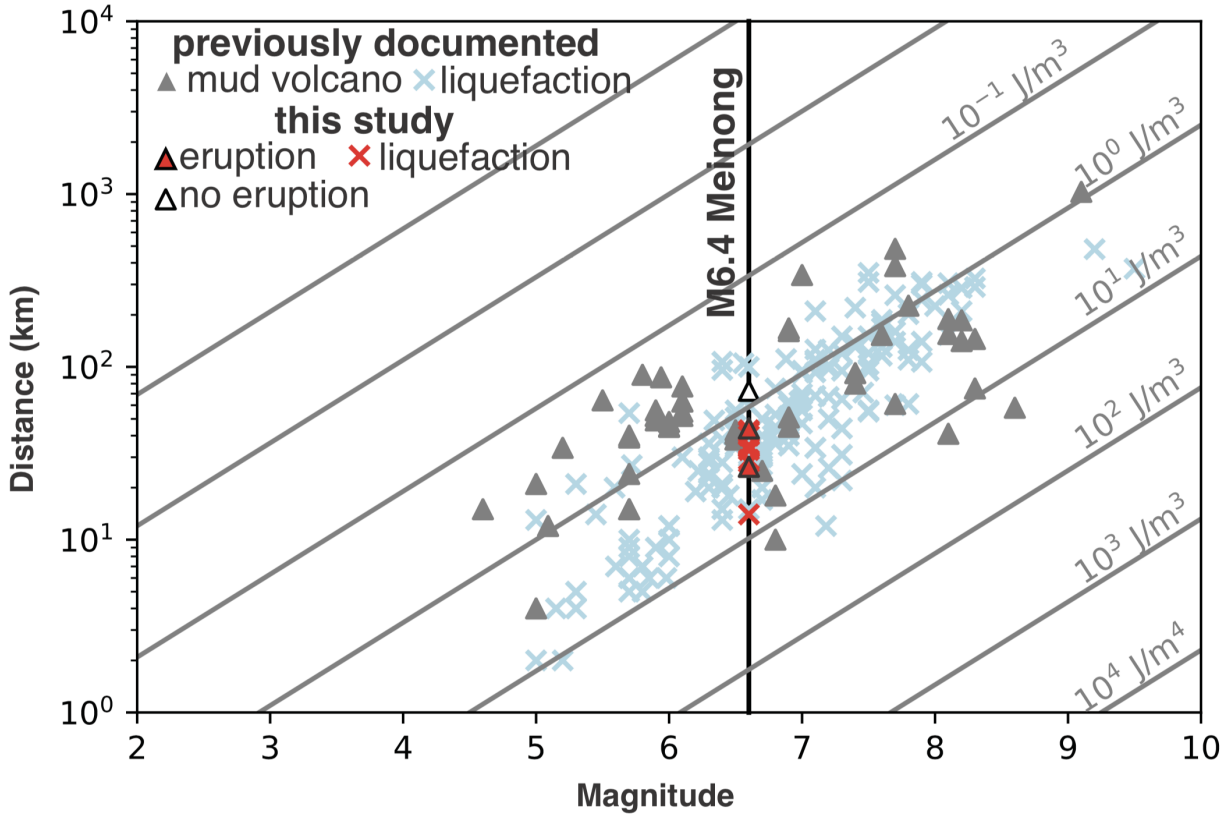

Figure 4.3: Epicentraldistance and magnitude for liquefaction and mud volcano eruptions compiled byWang and Manga (2010). Diagonal lines show energy density. Red crosses showobserved liquefaction from the Meinong Earthquake. Red triangles showdocumented mud volcano eruptions after the Meinong Earthquake. The WanDan mudvolcano, which did not erupt, is plotted as a white triangle.

Taiwan. We resampled three of these mud volcanoes in June of 2016 and found two to be more isotopically similar to shallow groundwater or meteoric water than when You et al. (2004) sampled the same mud volcanoes (arrows from right to left in Fig. 4). One of these mud volcanoes, Wushanting (WST), also had eyewitness-documented changes while the other, Kunshuiping (KSP), may have had more subtle changes in eruption rate to explain the change in chemistry. We also found that the Nanhua mud volcano is largely fed by groundwater and is isotopically similar to groundwater in Taiwan and within the California coast range which has similar chemistry. Perhaps because of this, there was no significant change between our observations and those of You et al. (2004). An important caveat to interpreting mud volcano fluid chemistry, is that some mud volcanoes have changes in water chemistry through time suggesting that separate fluid reservoirs mix unpredictably even without earthquakes (Chao et al., 2015). That said, in the broader context of the Meinong

responses, the change in isotopic chemistry is remarkably consistent between the two mud volcanoes where we are able to make a direct comparison between published data and data collected after the Meinong earthquake. One explanation for both the increased eruption rate and the changing chemistry is that the Meinong allowed for shallow groundwater mix with the deeper mud, lowering the viscosity and increasing the overall eruption rate. This is consistent with observed changes in water chemistry observed in other settings (Skelton et al., 2014; 2019).

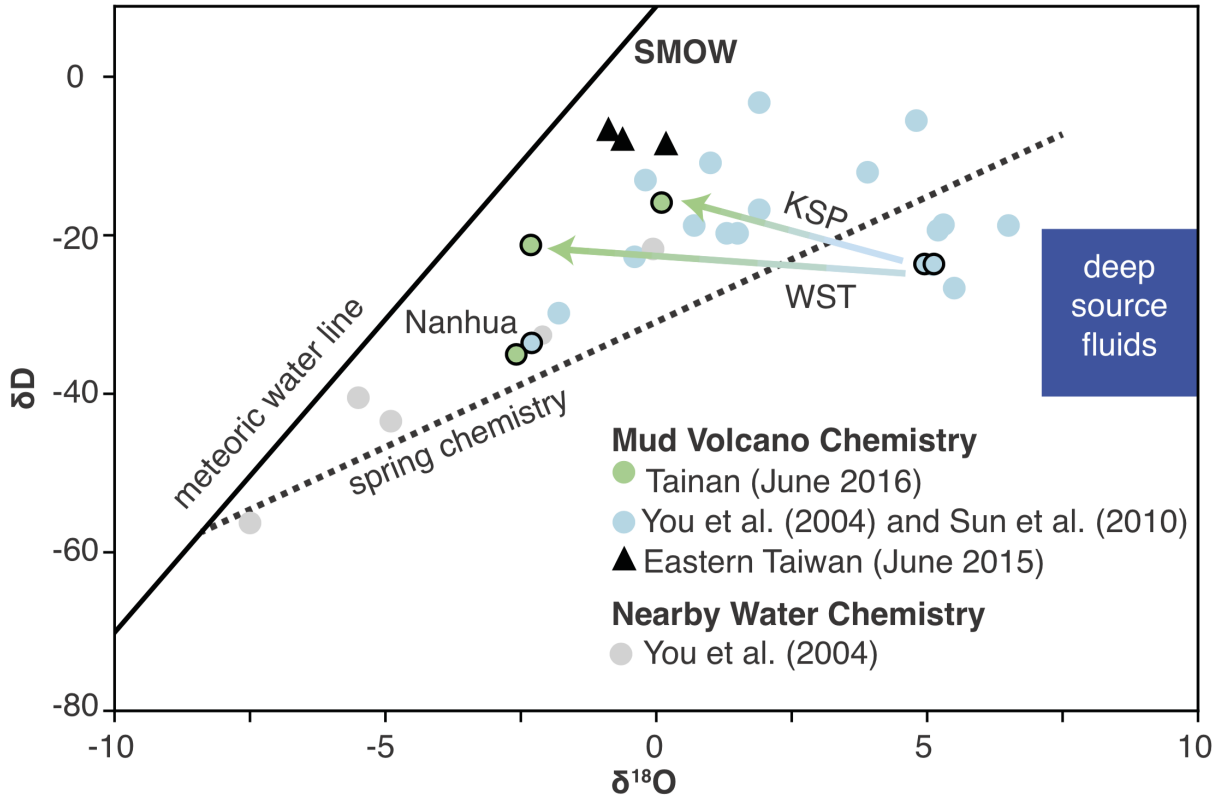

Figure 4.4: Hydrogen and oxygen isotopes for mud volcanoes sampled 5 months after the MeinongEarthquake (green) and those previously published (blue). Arrows between black highlighted points show difference in chemistry between our measurements and those of You et al. (2004). Solid line shows the meteoric water line and the dashed line shows the chemistry of springs in a similar geologic setting in California. Gray circles show groundwater chemistry from Taiwan (You et al.,2004). The blue box shows the deep fluid source proposed by You et al. (2004).

Changes in seismic velocity may also reflect changes in hydrologic properties and these changes appear to be broadly consistent with observations of hydrologic responses to earthquakes. We document studies that have both changes in seismic velocity and changes in hydrologic properties (Supplemental Table 4.2). Two broadband seismometers, both close

to the Meinong epicenter, may show changes in seismic velocity. However, these changes are an order of magnitude less than those observed after similarly sized earthquakes such as the 2015 M6 Napa earthquake (Taira et al., 2016). This may suggest depth dependence of these measurements. These observations may suggest changes in hydrologic properties within the deep crust although future work is needed to clarify the link between relative velocity changes from ambient noise with these varied hydrologic observations.

4.5 Conclusions

We examined changes in streams, groundwater, mud volcanoes, and seismic velocity to answer two questions posed in the introduction.

Did the hydrologic system change after the earthquake? We observed changes in over 500 wells, in streams, in mud volcanoes, and in seismic velocity. Some of these changes occurred as far as 100 kilometers from the Meinong epicenter and provide an unusually rich data set to understand these changes.

Did the earthquake cause a hydrologic connection between deep fluids and the shallow groundwater system? All of the changes we observed suggest mixing between shallow and deep fluid reservoirs. Where multiple depths are sampled within a well, water level changes appear to be due to breached aquifers causing reservoirs . The chemistry of mud volcanoes even four months after the earthquake have a high proportion of meteoric water.

Taken together, these diverse observations suggest that the M6.4 Meinong earthquake caused mixing between deep and shallow fluid reservoirs. Stream flow shows that some streams near to the earthquake epicenter had increases in discharge suggesting increased permeability and increased flow from groundwater into springs. Liquefaction shows the effect of seismic waves on some of the shallowest groundwater in the crust. Changes in water levels at groundwater wells show that dynamic shaking can cause water levels to drop (mostly in deeper wells) and rise (mostly in shallow wells) due to mixing between deep and shallow confined aquifers. These groundwater changes occurred as far as 100 km from the epicenter and cause meters of water level change. Mud volcanoes erupted after the Meinong earthquake suggesting that changes in the hydrologic system may extend much deeper into the crust. Isotopic evidence suggests that the Meinong earthquake may have caused mixing between shallow groundwater and deeper mud possibly lowering its viscosity and allowing for increased eruption rates. Finally, changes in seismic velocity may also suggest changes in pore pressure in the deeper crust. Overall, these disparate observations suggest that the 2016 M6.4 Meinong earthquake, despite its moderate magnitude, was able to cause mixing between deep and shallow fluid reservoirs throughout a large region in southern Taiwan.

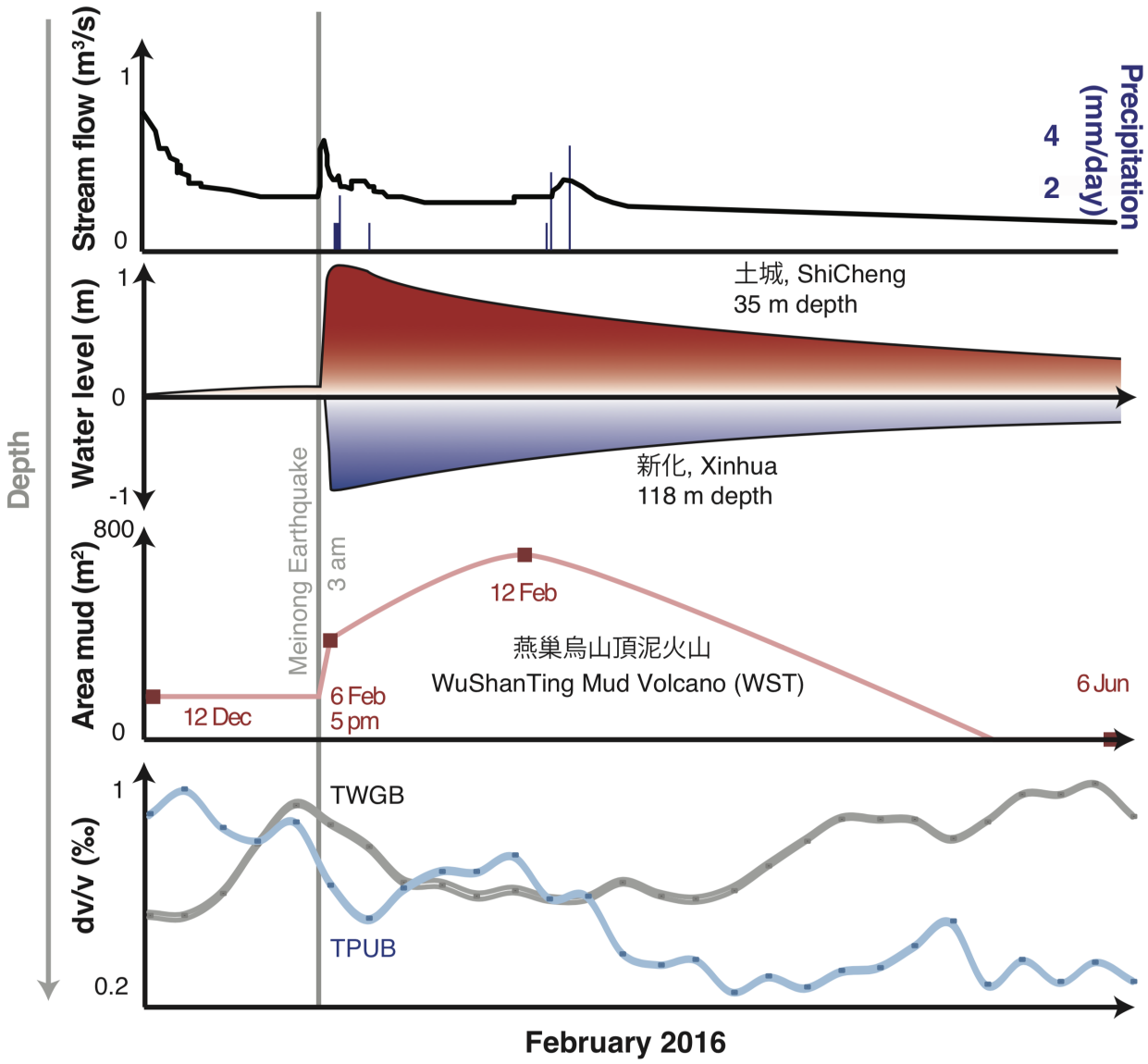

Figure 4.5: (from top to bottom). Example time series for stream flow, precipitation, a shallow water well (red) a deeper water well (blue,) the area of active mud flow from Google Earth satellite images at WuShanTing mud volcano (WST), and seismicvelocity from the nearby TWGB broadband station.

4.6 Acknowledgements

I would like to acknowledge my collaborators on this study J.C. Lee, C.Y. Wang, M.H. Huang, and M. Manga. N. Randolph-Flagg was supported by the National Science Foundation Graduate Research Fellowship (DGE 1106400). MM and NRF were further supported by NSF awards 1334424 and 1521855.

4.7 Supplemental Information

Table 4.1: Global compilation of mud volcano responses.

Date	Location	Magnitude	Distance (km)	Source
-91	Nirano, Italy	5.7	15	Bonini (2009)
-91	Montegibbio	5.7	15	Bonini (2009)
1781-04-05	Montegibbio	5.94	87	Bonini (2009)
1828-05-05	Caltanizetta, Italy	5.9	56	Bonini (2009)
1848-09-24	Marazy, AZ	4.6	15	Mellors et al. (2007)
1872-01-28	Kalamaddyn, AZ	5.7	24	Mellors et al. (2007)
1872-01-28	Shikhzairli, AZ	5.7	40	Mellors et al. (2007)
1873-05-16	Montegibbio	5.09	12	Bonini et al. (2016)
1895-07-08	Livanoca, South Caspaun	8.2	141	Mellors et al. (2007)
1895-09-04	Portico di Romagna, Italy	5	4	Bonini (2009)
1935-05-30	Thok, Baluchistan	7.7	61	Snead (1964)
1945-11-28	Ormara, Makran	8.1	41	Delisle (2005)
1945-11-28	Hingol, Makran	8.1	189	Delisle (2005)
1945-11-28	Gwadar, Makran	8.1	155	Delisle (2005)
1952-03-04	Niikappu	8.6	58	Chigira and Tanaka (1997) with PGV from Manga et al. (2009)
1957-12-04	Gobi Altay, Mongolia	8.3	75	Rukavickova and Hanzl (2008)
1968-05-16	Niikappu	8.2	186	Chigira and Tanaka (1997) with PGV from Manga et al. (2009)
1977-03-	Beciu	7.4	92	Mellors et al.

Table 4.2: Global compilation of changes in seismic velocity after earthquake where changes in hydrologic diffusivity is also estimated.

Location	**dv/v (%)**	**D/Do**	**dv/v source**	**dD source**
2014 M6.0 Napa, CA, USA	0.08	10	Taira et al., GRL, 2015	Wang and Manga, 2015
1999 M7.6 ChiChi, Taiwan	0.5	10^3	Huang et al., 2019	Wang et al., 2012
2003 M6.8 Chengkung, Taiwan	0.02	10	Chapter 4	Chapter 4
2011 M9 Tohoku, Japan	1.5	2	Minato et al., GRL, 2012	Kinoshita et a, 2015
2016 M6.4 Meinong, Taiwan	0.006	2	this study	this study

Chapter 5

Changes in seasonal aseismic slip after the M6.8 2003 Chengkung Earthquake, Taiwan

5.1 Abstract

The Longitudinal Valley Fault in eastern Taiwan aseismically creeps more rapidly during the wet season and this seasonal modulation increased by a factor of three after the M6.8 Chengkung Earthquake. We document a simultaneous drop in seismic velocity of ~0.08%, an increase in the depth of seasonal deformation on the fault inferred from GPS, and a more rapid response to hydrologic loads. We propose that the earthquake increased the hydraulic diffusivity of the fault zone and present an idealized 1D pore pressure diffusion model and with the depth of fluid circulation suggested by water isotope data. We show that some frictional changes on faults following earthquakes are due to changes in hydrologic properties and suggest that there is a shallow slip deficit on the Longitudinal Valley Fault.

5.2 Introduction

Long term motion between tectonic plates is accommodated by seismic slip (earthquakes) and aseismic slip (creep). The partitioning, in space and time, of plate motion between these two regimes is crucial to understanding earthquakes and assessing earthquake hazards (for a review see Avouac, 2015). The recurrence (Reid, 1910) and depth (*e.g.*, Savage, 1983) of earthquakes along faults can be attributed to the accumulation of elastic strain or the slip deficit between plate motion and aseismic slip. Modern seismic and geodetic observations provide an unprecedented window into elastic strain accumulation along the fault interface (*e.g.*, Schmidt et al., 2005; Thomas et al., 2014b), the evolution of the fault properties during and after earthquakes (*e.g.*, Avouac, 2015; Fukuda et al., 2013; Lee et al., 2018) and the propagation of slip (*e.g.*, Ishii et al., 2005).

While most fault motion is driven by tectonics, slip can also be initiated or accelerated by hydrologic loads. For example, some creeping segments of the San Andreas Fault in California (Roeloffs, 2001) and the Longitudinal Valley Fault in Taiwan (Lee et al., 2003) have different slip rates during the rainy and dry seasons. Some earthquakes may be triggered by seasonal hydrologic loads (*e.g.*, Saar and Manga, 2003; Christiansen et al., 2005; Hainzl et al., 2006; 2013; Johnson et al., 2016; Montgomery-Brown et al., 2019; Chapter 6). Whether this seasonal slip is due to the elastic stresses applied to the surface (*e.g.*, Heki, 2003; Johnson et al., 2017) or the diffusion of pore pressure into the fault zone (*e.g.*, Hainzl et al., 2006; Montgomery-Brown et al., 2019) remains an area of active research.

Seismic waves also change the hydrologic properties of rocks and fault zones. Changes in groundwater properties after earthquakes have been observed for millennia (*e.g.*, Pliny, 79). These hydrologic changes have often been linked to temporarily increased permeability inferred from increased stream discharge (Rojstaczer and Wolf, 1992), changes in water temperature (Wang et al., 2012), changes in water chemistry (*e.g.*, Wang et al., 2015, Chapter 4), and changes in water level response to solid earth tides (*e.g.*, Hsieh et al., 1988; Elkhoury et al., 2006). Decreased seismic velocity after earthquakes, as monitored with ambient seismic noise, are colocated with, and have a similar recovery time to, changed hydrologic properties after the M9.0 Tohoku (Minato et al., 2012; Kinoshita et al., 2015), M6.0 Napa (Taira et al., 2014; Wang et al; 2015), M6.0 Meinong (Chapter 4), and M7.9 Chi-Chi (Wang et al., 2004; Huang et al., in review) earthquakes. A change in permeability has also been documented by drilling into fault zones immediately after the 2008 M7.9 Wenchuan earthquake (Xue et al., 2013) and the 2011 M9.0 Tohoku earthquake (Fulton et al., 2013).

Here we seek to probe how faults respond to hydrologic loads and earthquakes by examining the Longitudinal Valley fault in eastern Taiwan. The change in seasonal creep after the 2003 Chengkung earthquake is an unusual example of how permeability and pore- pressure diffusion change fault behavior and suggest a shallow strain deficit in Longitudinal Valley Fault.

Geologic Setting

Taiwan is an ideal setting to study the interactions among hydrology, seismic waves, and aseismic slip. Taiwan is tectonically active (convergence rate of ~9 mm/yr), has large changes in hydrologic loads, and is densely monitored. The Philippine Sea Plate subducts beneath the Eurasian plate to the north-east of the island and the Eurasian plate subducts beneath the Philippine Sea Plate along the eastern edge of the island (Fig. 1A). The convergence rate of these plates is more than twice that of the San Andreas Fault in California and the slip is distributed across the island and is focused on several N-S trending faults.

The Longitudinal Valley Fault or ChihShang Fault is the plate boundary between the Eurasian and Philippine Sea Plate. An oblique thrust fault, the southern half of the fault aseismically slips in the shallow crust where serpentinite mélange outcrops along the hanging wall (Wang, 1976; Lee et al., 1998; Thomas et al., 2014) while the footwall throughout the valley is composed of ~ 1 km of interleaving gravels and other Central Range sourced

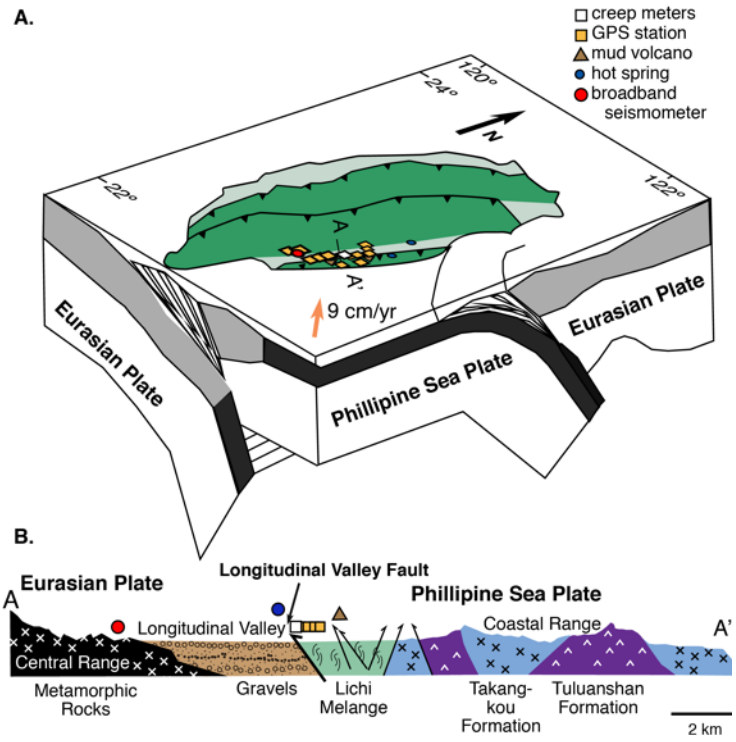

Figure 5.1: **A.** Tectonic block diagram of Taiwan modified from Angelier (1986). Transect A-A' is shown in panel B. **B.** Geologic cross section of eastern Taiwan showing the geologic units modified from Mu et al. (2011). On both figures, the white square shows the creep meter, orange squares show nearby GPS stations, the red circle shows the broadband seismometer in Fig. 4.2, brown triangles show mud volcanoes, and blue circle shows hot springs.

sediments (Fig.1B; Mu et al., 2011). Beneath this valley fill, seismically reflective dense material is interpreted to be high-grade metamorphic rocks connected to the Central Range (Fig. 1B). The mélange is locally highly deformed (Thomas et al., 2014a) consistent with geodetic observations of distinct faults. The fault is steeply dipping at the surface with multiple splay faults and dips more shallowly with depth. The 1951 M7. 1 ChihShang Earthquake and 2003 M6.8 both ruptured in the deeper listric fault zone with coseismic slip and afterslip propagating to the aseismic portions of the fault. The Longitudinal Valley Fault also appears to shorten seasonally according to creep meter data (*e.g.*, Lee et al., 1998; Chang et al., 2009) similar to some portions of the San Andreas Fault (Roeloffs et al., 2001). Repeating earthquakes at ~ 5 km depth show a slip rate of ~3 cm/yr suggesting most slip at depth is expressed at the surface. In the deeper portion of the fault, at repeating earthquakes 15-40 km depth also appear to have strong seasonal and tidal modulation (Chen et al., 2018).

On December 11, 2003 the M6.8 Chengkung earthquake (epicenter: 23.11^{o}N, 121.32^{o}E) ruptured downdip from the aseismically creeping section of the Longitudinal Valley Fault. Aftershock sequences propagated north of the coseismic slip. Accelerated creep near the

surface was interpreted to reflect velocity strengthening (*e.g.*, Chen et al., 2006; Lee et al., 2006; Chin et al., 2006) that changes with depth (Lee et al., 2018). Afterslip models based on GPS (*e.g.*, Hu et al., 2006) and InSAR (*e.g.*, Thomas et al., 2014b) data found that the rupture at ~ 10 km propagated up dip and that moment released from the afterslip is comparable to that from earthquake itself.

5.3 Data

We use geophysical data recorded by the Institute of Earth Sciences at Academia Sinica to examine the seasonal modulation of slip on the Longitudinal Fault before and after the 2003 Chengkung earthquake. The most direct record of aseismic slip at the surface is from rod-type creep meters installed across three discrete surface ruptures of the fault in Chinyuan, Taiwan. These sensors were installed in 1998 and have been calibrated to account for thermal expansion and contraction and validated with campaign-style leveling and Global Positioning System (GPS) surveys (Lee et al. 2003; Mu et al., 2011). In this study we use monthly averaged slip rates to highlight the annual trend.

Seismic velocity is from at TWGB broadband seismometer which is part of the BATS seismic network. This network is also maintained by Academia Sinica and data are available from the http://www.iris.org. Changes in seismic velocity are from a companion study and are determined by cross-correlating different components of seismic record (*e.g.*, EW-NS; for detailed methodology see Huang et al., *in prep*).

We also use daily precipitation records from the Central Weather Bureau as well as their Continuous GPS array. These stations record 1 Hz data in three components and are publicly available at http://gps.earth.sinica.edu.tw/. This GPS network has documented the convergence rate across the plate boundary (Yu et al., 1997) and as well as the co-and post-seismic deformation of the Chengkung earthquake (Ching et al., 2007; Hu et al., 2007; Cheng et al., 2009; Hsu et al., 2009; Thomas et al., 2014b). We also use all available interferometric synthetic aperture radar (InSAR) acquisitions from the ALOS (Japan Aerospace Exploration Agency) and Sentinel (European Space Agency) satellites.

Finally we collected 500 ml water and mud samples from hot springs and mud volcanoes in eastern Taiwan. We measured the hydrogen and oxygen isotopic composition of this water using Isotope Ratio Infrared Spectroscopy at the Center for Stable Isotope Biogeochemistry, UC Berkeley. The ratios and the sample temperature can be used to infer depth of fluid flow (*e.g.,* Wang et al., 2015).

5.4 Results

Total shortening at all three Chinyuan creep meters was 2.5 ± 1 cm/yr from 1998-2003. This slip rate accelerated to 20 cm/yr the month after the Chengkung earthquake and slowed to 3 ± 1 cm/yr for the period after 2005. Of this total slip ~40% occurs on C3, ~35% on C2,

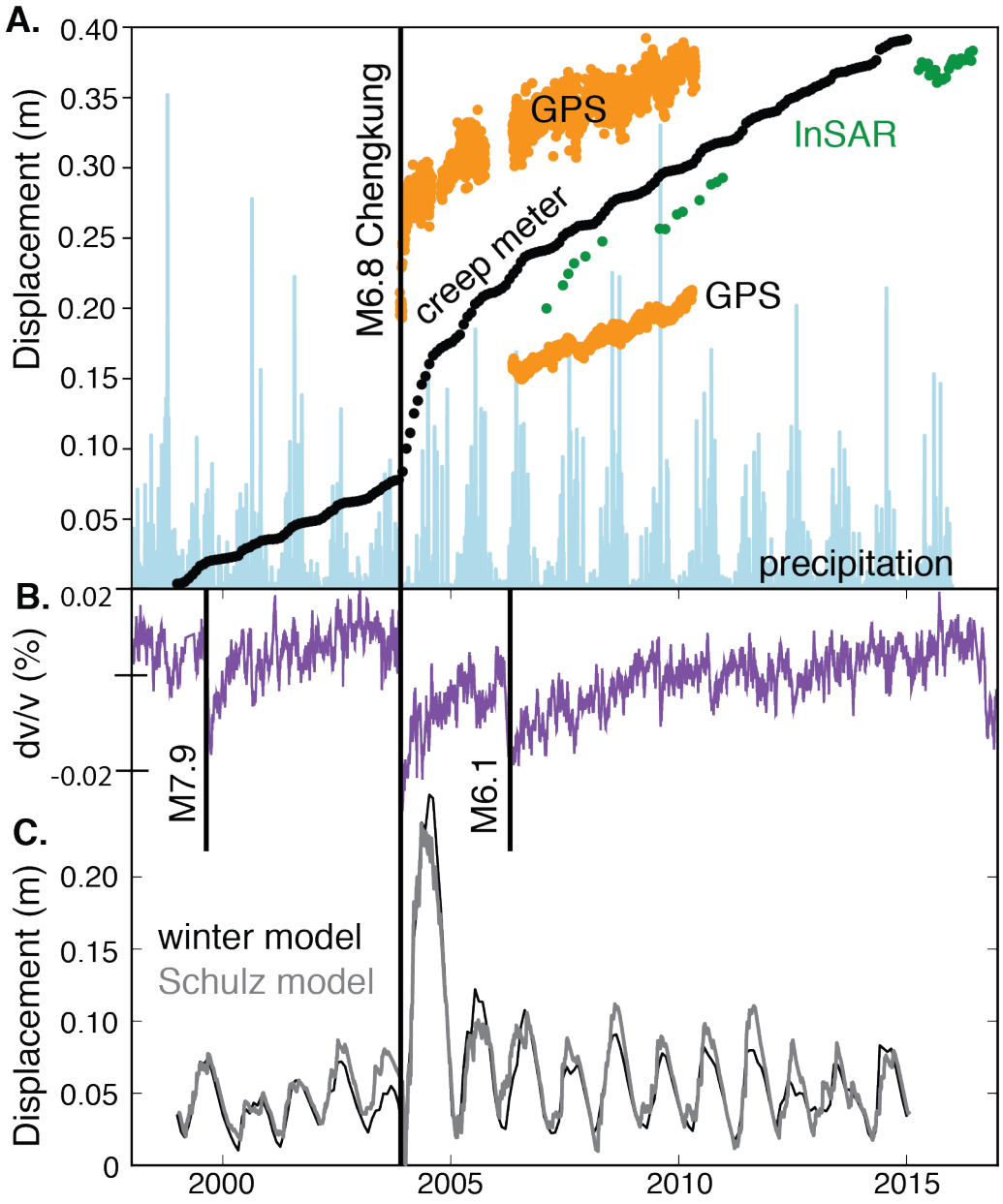

Figure 5.2: **A.** Geodetic and hydrologic observations at the Longitudinal ValleyFault from 1998-2015. Creep meter data is in black. Blue bars show thedaily precipitation rate in cm. Orange shows two representative time series for GPS stations T107 and T104. Green dots show displacement across the fault inferred from InSAR satellite measurements (ALOS from 2006-2012 and Sentinelstarting in 2015). Both InSAR and GPS are offset to arbitrary starting displacements so that curves are distinguishable from each other. **B.** Changes in seismic velocity inferred from ambient noise after large regional earthquakes. **C.** Detrended creep meter data for two afterslip models. The winter model assumes that the dry season slip rate is representative and the Schulz model fits overall slip on the fault.

and the remaining 25% occurs on C4 (Fig. S1). Almost all of this aseismic slip occurs from March to July when the slip rate accelerates up to ~ 8 cm/yr in 2015 (Fig. S2). All three creep meters show seasonal modulation of creep although ~50% of the seasonality is due to C3 (Fig. S3).

Seasonal deformation is visible at GPS stations across the Longitudinal Valley. To understand this seasonality as a function of depth on the fault we examine eight GPS stations on the hanging wall within 3 kilometers of actively creeping Longitudinal Valley Fault as inferred from InSAR (Fig. S1). Assuming a fault dip of 60^{o} as observed at the surface (Lee et al., 2003) this corresponds to the upper 5 km of the fault. To quantify seasonality, we first establish a baseline by comparing GPS stations on the hanging wall to a station on the footwall. These different baselines are broadly similar (Fig. S5) and we thus focus on data relative to station TAPE as it has a relatively long time series, and is only 100 m from the Longitudinal Valley Fault. We subtract the long term slip rate from the total slip as well as the vertical and horizontal components for windows of record greater than one year (Table S1). We fit this detrended slip with the equation $y = A\ \sin(\omega t + \psi\ )$ where y is the displacement, A is the amplitude of differential seasonality, ω is the frequency, t is time, and ψ is the phase lag.

Most relative motion across the fault is not seasonally modulated with the average non-seasonal slip of 1.8 ± 1.3 cm/yr and the average seasonal modulation of 0.3 ± 0.2 cm/yr. Most of this overall slip is vertical (3.7 ± 6.7 cm/yr) rather than horizontal (0.7 ± 0.8 cm/yr). The largest detrended slip was for the period immediately after the 2003 Chengkung Earthquake. The amplitude of seasonal deformation is most similar to the footwall near to the fault and most different far from the fault (Fig. S6).

Seasonal deformation integrates both tectonic and hydrologic signals. We have two constraints on the hydrologic forcing independent of tectonics. First, we cross-correlate daily precipitation and find that the peak precipitation precedes creep on the fault by about two months (Fig. 5.2; Supplemental Figure 5.11). Second, we measured the hydrogen and oxygen isotopes and water temperature for nearby hot springs and mud volcanoes (Supplemental Figure 5.12). While there is considerable uncertainty in the geotherm and source fluid chemistry both records diverge from the meteoric water line and from subduction fluid chemistry. This shows fluid flow and mixing through the upper few kilometers of the crust.

In GPS, creep meter, and leveling data, deformation accelerated after the 2003 Chengkung earthquake. This post seismic deformation has been well studied in general (*e.g.,* see review by Marone et al., 1991; Wang et al., 2012) and for the 2003 Chengkung earthquake in particular (*e.g.,* Chen et al., 2006; Lee et al., 2006; Chin et al., 2006; Hu et al., 2006; Thomas et al., 2015; Lee et al., 2018) using a variety of geophysical and modelling techniques. To understand seasonal deformation we subtract afterslip using an idealized physical model from Marone et al. (1991). We fit this model to both the overall slip rate ($r^2 = 0.98$; Supplemental Figure 5.13) and the winter slip rate ($r^2 = 0.97$; Supplemental Figure 5.13) and both produce very similar detrended slip (Fig 2C).

In addition to the increase in overall slip, the seasonal modulation of slip increased by a factor of three at the creep meters after the 2003 Chengkung earthquake (Figure 5.2C).

This change is relatively insensitive to which afterslip model is subtracted from the overall slip rate (Figure 5.2C). In addition to the change in overall amplitude of slip, the timing of slip changed after the earthquake. We find that for the 5 years before the Chengkung earthquake, half of the annual slip occurred by June while in 2004, half of the annual slip occurred two months earlier (Figure 5.14). This change is also reflected by cross correlating precipitation and creep for every year (Supplemental Figure 5.11). Seasonal deformation from leveling and GPS both show increased seasonal deformation farther from the fault for the year after the earthquake. Seismic velocity at the TWGB broadband seismometer show a drop is seismic velocity of ~0.03% which appears to logarithmically approach the pre-Chengkung value until the M6.1 2006 Tainan earthquake which again changed the seismic velocity without noticeably changing creep rate (Fig. 2B).

5.5 Discussion

Seasonal hydrologic loads can cause deformation by elastically loading the crust (*e.g.*, Heki, 2003; Johnson et al., 2016) or by increasing pore pressure within permeable fault zones (*e.g.*, Saar et al., 2003; Montgomery-Brown et al., 2019). In both cases the background stress field is modulated by seasonal changes in the effective stress. The effect of each is shown in Coulomb's failure stress (CFS)

$$CFS = \tau - \mu(\sigma_n - p_f)$$

where τ is the shear stress, μ is the coefficient of friction, σ_n is the normal stress, and p_f is the pore pressure. Groundwater produces a 'hydrologic ratchet' effect where motion on the shallow fault is suppressed when the hydrologic load disfavors slip and this slip deficit is recovered when the load is removed. Of course, fluid flow and elastic stresses are coupled and sensitive to the geometry of faults and hydrologic loads. That said, it is instructive to consider three end-member cases considering the relative importance of elastic loads and pore pressure diffusion to explain seasonal deformation (Fig. 5.3 A-C). These models in turn, predict diagnostically different behavior after the 2003 Chengkung earthquake (Fig. 5.3 D-F).

Seasonal Loading Models

Spatially uniform seasonal elastic loads contribute positively to the normal stress (σ_n) on thrust and strike slip faults and negatively in the case of normal faults. Elastic loads may also compress pores and thereby increasing fluid pressure (p_f).

$$p_f = \frac{B}{3}\sigma_n$$

where B is the Skempton coefficient which is always less than one (Roeloffs, 1996). This means that the net effect of elastic loads on thrust faults is always suppresses slip. If

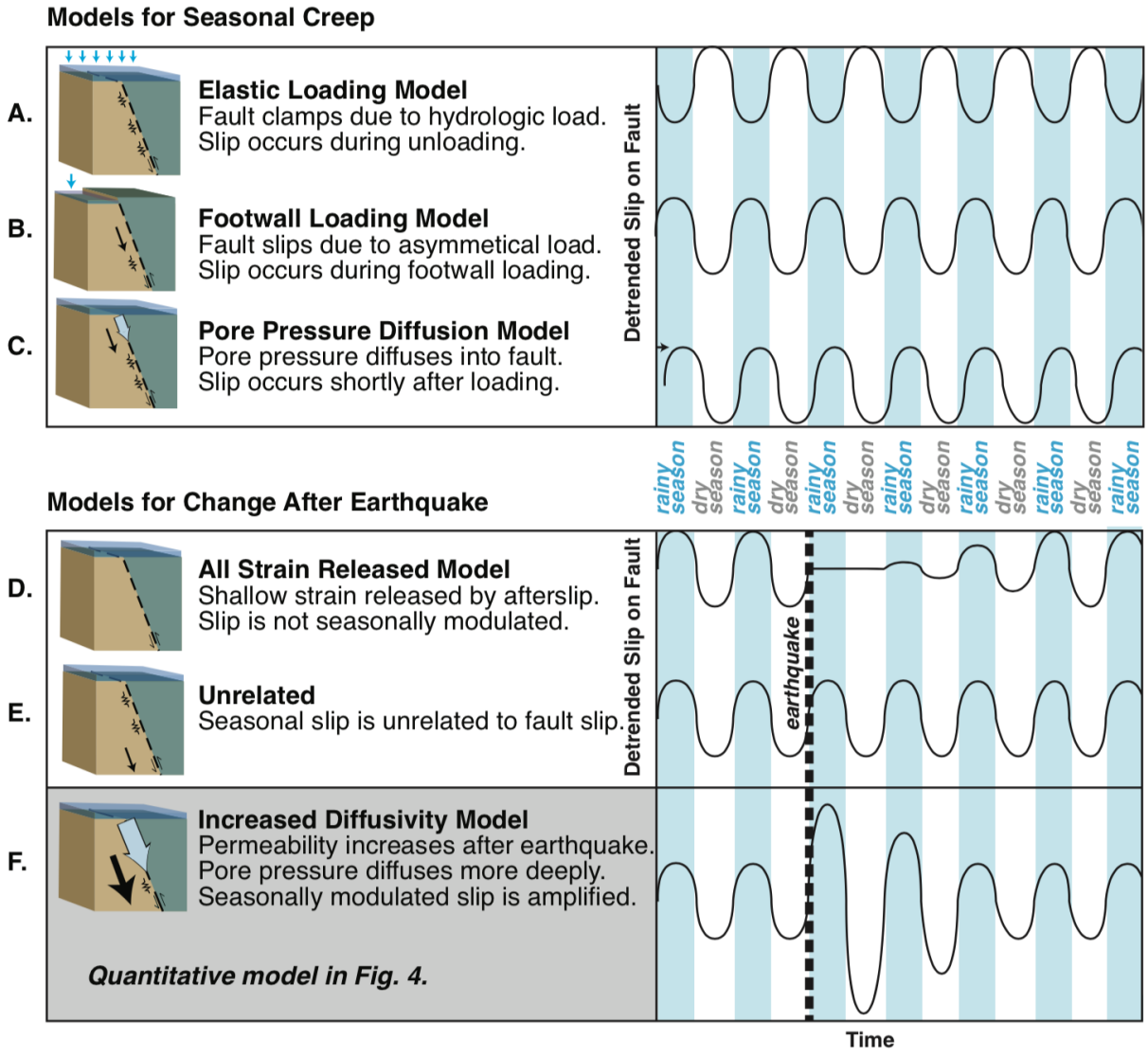

Figure 5.3: Predicted deformation for the six conceptual models discussed within the text.

uniform elastic loads produced seasonal creep on the Longitudinal Valley Fault we would expect loading to anti-correlate with deformation (Fig. 5.3A). This is in striking contrast to our observations from creep meters and GPS (Fig. 5.2) where the hydrologic load precedes aseismic slip by about a month (Fig. 5.3).

However, hydrologic loads are concentrated within the valley while the Longitudinal Valley Fault is near to the valley's eastern margin. This means that the cyclic hydrologic loads are concentrated on the footwall of the fault and predict that hydrologic loads would correlate with slip on the fault (Fig. 5.3B). The complex geometry of the hydrologic load is mirrored by complexity within the shallow fault where leveling data shows a shallow pop-

up structure along the splays of the fault (Mu et al., 2011). How these structures would respond to spatially heterogeneous loads is unknown. Roeloffs et al. (1988) examined the poroelastic effects of seasonal loading for reservoirs situated close to faults and found that thrust faults were most sensitive to cyclic hydrologic loads on the footwall. Despite this complexity, observations of seasonal creep on the Longitudinal Valley Fault (Fig. 5.2) are broadly consistent with seasonal loads concentrated on the footwall (Fig. 5.3B).

Pore Pressure Diffusion Models

The other conceptual framework that has been used to explain seasonal slip is pore pressure diffusion. This idea was influenced by pioneering work on induced seismicity at Lake Mead and Rocky Mountain Arsenal in the American west which found a clear relationship between seismicity and the diffusion of pore pressure from injection sites and reservoirs (*e.g.*, Hsieh and Bredehoeft, 1981; Roeloffs, 1988; Simpson et al., 1988). When applied to seasonal slip on faults, pore pressure is thought to propagate into the fault causing elastic stresses that built up during the dry season to release, "unzipping" the fault downwards. This predicts a similar phase and style of deformation as loading on the footwall of the fault with a time lag. (Fig. 5.3C).

Unlike elastic loads which propagate near instantaneously, pore pressure diffusion is controlled by rock properties and can produce substantial phase lags between loads and pore pressure at different depths. The one-dimensional diffusion of pore pressure is given by

$$\frac{\partial p_f}{\partial t} = \frac{\partial}{\partial z}[D(t,z)\frac{\partial}{\partial z}p_f]$$

where t is time, D is the diffusivity which can be a function of time, and z is the depth. Diffusivity is equal to the permeability (k) divided by the specific storage (S_s). The Longitudinal Valley Fault has extremely different hydrologic properties on the foot and hanging walls. The valley fill sediments are highly permeable ($> 10^{-11}$ m^2) with correspondingly high diffusivity (Mu et al., 2011) while the hanging wall is effectively impermeable ($< 10^{-21}$ m^2). Chang et al. (2009) modeled the one-dimensional diffusion of pore pressure for an assumed diffusivity of 10^{-4} m^2/s to fit creep on the Longitudinal Valley Fault. They found this value to fit well with a rate-state friction model proposed by Perfetinni et al. (2007).

Isotopic ratios from groundwater springs and mud volcanoes along the fault suggest that fluids are traversing the upper kilometer of the crust sufficiently quickly to remain hot (up to 60 ^{o}C) and unmixed with meteoric water (Supplemental Fig. 5.6). Using the estimated depth of seasonal creep (L) from GPS of ~1 km (Supplemental Fig. 5.7) and the average 10-week lag time (τ) between precipitation and the onset of annual creep we can estimate the diffusivity of the shallow Longitudinal Valley Fault$D \sim \frac{L^2}{\tau} \sim 10^{-1} m^2$ which can be a function of time (t), and z is the depth. Diffusivity is equal to the permeability (k) divided by the specific storage (S_s). The Longitudinal Valley Fault has extremely different hydrologic properties on the foot and hanging walls. The valley fill sediments are highly permeable ($> 10^{-11}$ m^2) and correspondingly high diffusivity (Mu et al., 2011) while the

hanging wall is effectively impermeable ($< 10^{-21}$ m^2). Chang et al. (2009) modeled the one-dimensional diffusion of pore pressure for an assumed diffusivity of 10^{-4} m^2/s to fit creep on the Longitudinal Valley Fault. They found this value to fit well with a rate-state friction model proposed by Perfetinni et al. (2007).

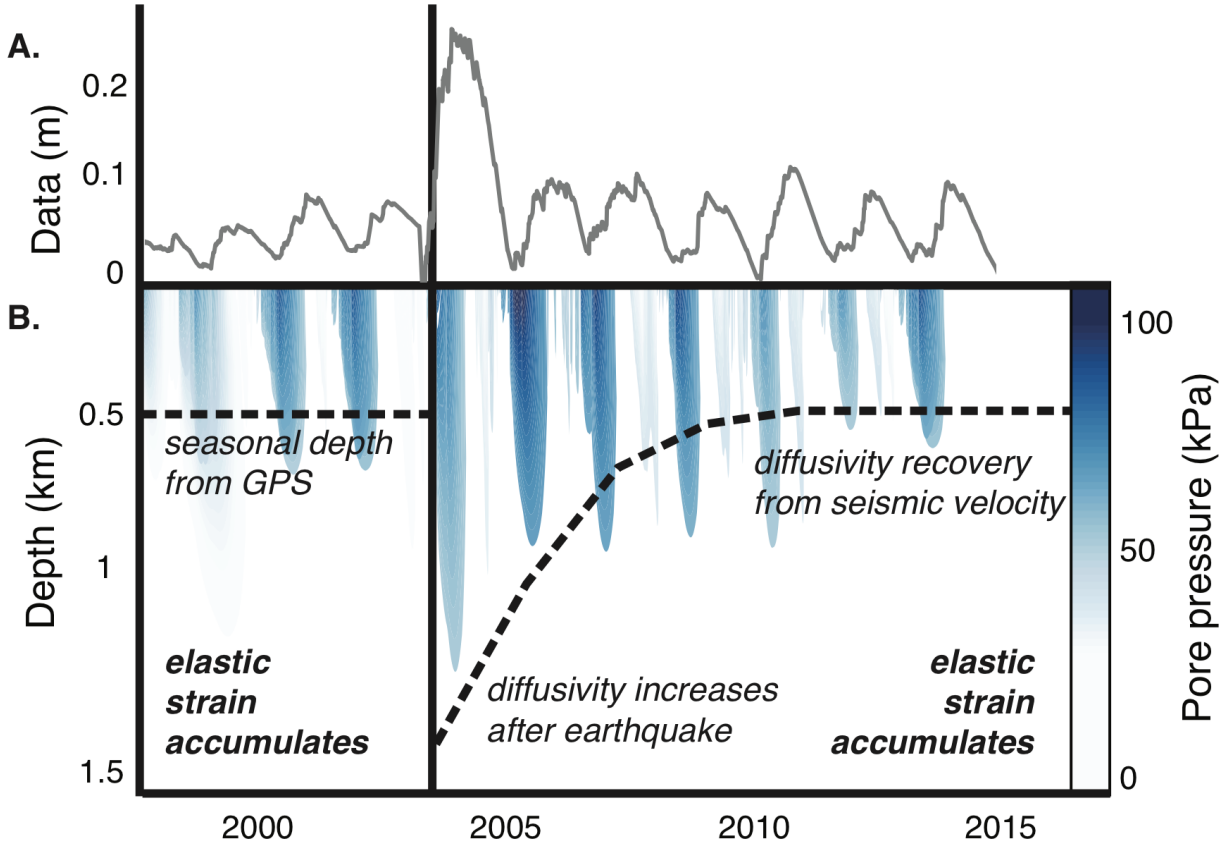

Figure 5.4: **A.** Detrended creep meter data from Fig. 5.3. **B.** Quantitative pore pressure diffusion model for a hydrologic diffusivity of m. Blue shows pore pressure in kPa. The dotted line until 2004 shows the depth of seasonal deformation inferred from GPS and water chemistry while after 2004, shows the modeled depth of the same pore pressure given the increased diffusivity. The time to return to the initial diffusivity is inferred from seismic velocity.

Afterslip of the 2003 Chengkung earthquake

Aseismic slip on the Longitudinal Valley Fault increased after the 2003 M6.8 Chengkung Earthquake. This constrains the mechanism of seasonal loading more broadly and the effect of the Chengkung earthquake on the fault. Afterslip has been observed to change the re-

currence interval of creep events (*e.g.*, Belardinelli, 1996; Boettcher and Marone, 2004; Wei et al., 2013) or even stop aseismic slip entirely (Burford, 1988). This is because the elastic strain that normally accumulates during the dry season continuously releases during afterslip (Fig. 5.3D).

In fact, for afterslip to be seasonally modulated, elastic strain accumulation in the shallow crust must not be affected by afterslip. One possibility is that seasonal behavior that we observe in the creep meter is due to poroelastic effects that are not related to the fault zone (Fig. 3E). Displacement from GPS stations on the hanging wall and leveling data (Supplemental Fig. 5.8) suggest that this seasonal deformation likely propagates within the upper kilometer of the crust and, therefore, into the fault zone. That said, if seasonal deformation were unrelated to the fault, it unlikely that seasonal modulation would be unlikely to increase during a relatively dry year.

Our observations are in strong contrast to both of these predictions. Seasonal behavior continues after the earthquake showing that elastic strains do not relax during afterslip. Seasonal modulation also amplifies after the earthquake suggesting that the earthquake changed some frictional or fault properties. We propose a simple model to explain these changes. Fault slip increased by factor of three in 2004 (Fig. 5.2C) and the increased seasonal modulation persists for ~ 3 years after the earthquake, similar to in situ permeability measurements after the 2008 Wenchuan Earthquake (Xue et al., 2013). We propose that the Chengkung earthquake increased the permeability of the fault by an order of magnitude. This is consistent with observations made on other faults (Xue et al., 2013; Fulton et al., 2013) and with the change in seismic velocity that we observed (Fig. 2B). We model the diffusion of pore pressure for this permeability change and show an increased depth of high pore pressures. We suggest that elastic strain is stored in the upper kilometer of the Longitudinal Valley Fault (Supplemental Fig. 5.9) and that the magnitude of seasonal slip after the 2003 Chengkung earthquake reflects deeper penetration of these fluid pressures into the fault.

5.6 6. Conclusions

Seasonal slip on the Longitudinal Fault is a rare window into fault process in response to two different stimuli— seasonal hydrologic loads and the M6.8 Chengkung earthquake. We find that seasonal deformation on the fault is consistent with other geodetic observations including GPS, leveling, and InSAR (Fig. 2). We also find that this seasonal modulation persisted and even amplified during afterslip. This is in contrast to observations at other faults where afterslip suppresses overall slip and slip transients (Buford et al., 1988). We also find that GPS stations on the hanging wall had greater seasonality near the fault and that this seasonality decayed at ~1 km depth. This is similar to depth of fluid circulation inferred from isotopic measurements made at nearby hot springs and mud volcanoes. The time lag between precipitation and slip is about 10 weeks and this lag decreased after the earthquake (Supplemental Fig. 5.11). We argue that these observations are consistent with

either loading on the footwall or pore pressure diffusion into the fault. After the Chengkung earthquake, we observe a large drop in seismic velocity at a nearby broadband seismometer. These changes are often inferred to reflect increased permeability. We argue that increased permeability after the earthquake allows high pore pressures to propagate more deeply into the fault releasing elastic strain on more of the fault. We model the diffusion of pore pressure after the earthquake (Fig. 5.4) to show that an increase of an order of magnitude in the diffusivity is sufficient increase the depth of pore pressure diffusion by a factor of three. These observations also imply elastic strain storage in the very shallow crust and may affect our understand of earthquake hazard in the Longitudinal Valley.

5.7 Acknowledgements

I would like to acknowledge my collaborators on this study J.C. Lee, M.-H. Huang, M. Manga, R. Bürgmann, C.H. Mu., A. Nayak, and T. Taira. N. Randolph-Flagg was supported by the National Science Foundation Graduate Research Fellowship (DGE 1106400) and East Asia Pacific Summer Institute (No. 1515635). MM and NRF were further supported by NSF awards 1334424 and 1521855.

5.8 Supplemental Information

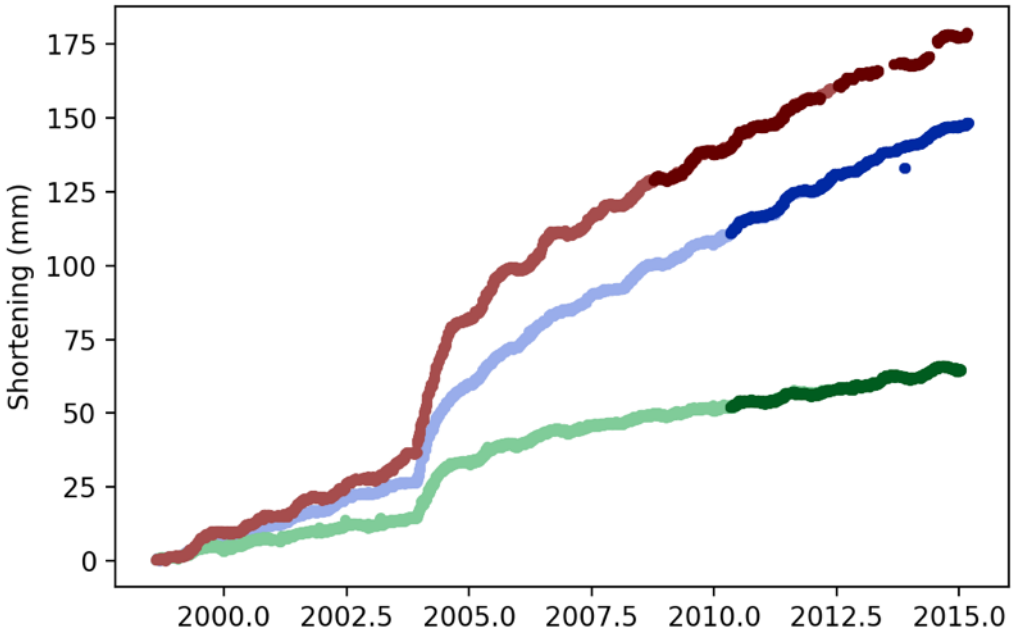

Figure 5.5: Daily creep meter data from C3 (red), C2 (blue), and C4 (green) creep meters at Chinyuan. Light colors and dark colors are for different data collections methods. This data is totaled and averaged over each month to produce Fig. 5.2.

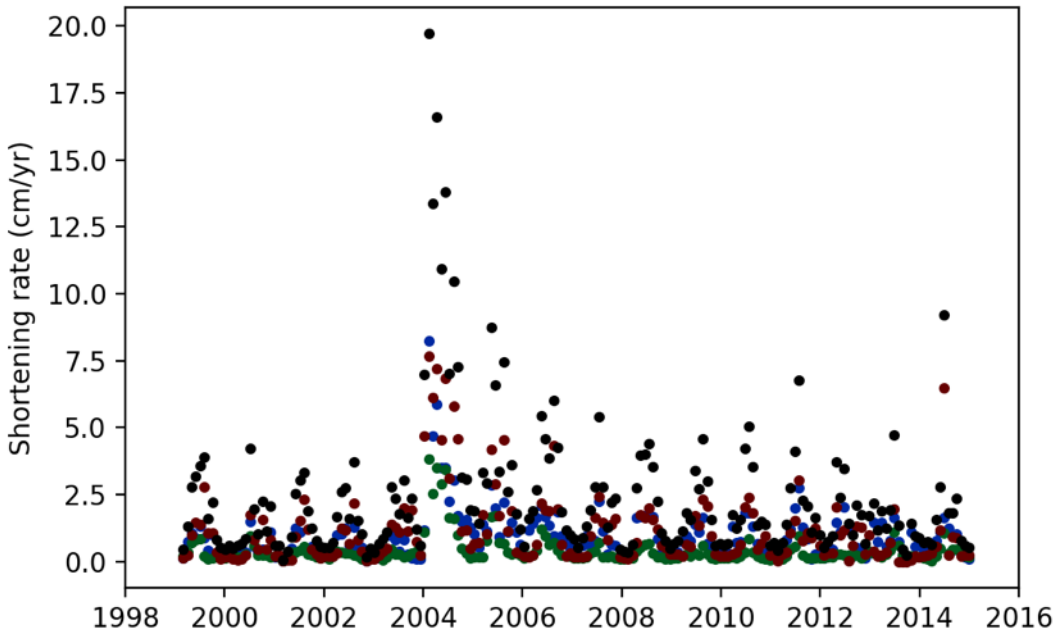

Figure 5.6: Shortening rate per month for all three creep meters (black) and each creep meter separately where C3 (red), C4 (blue), and C5 (green).

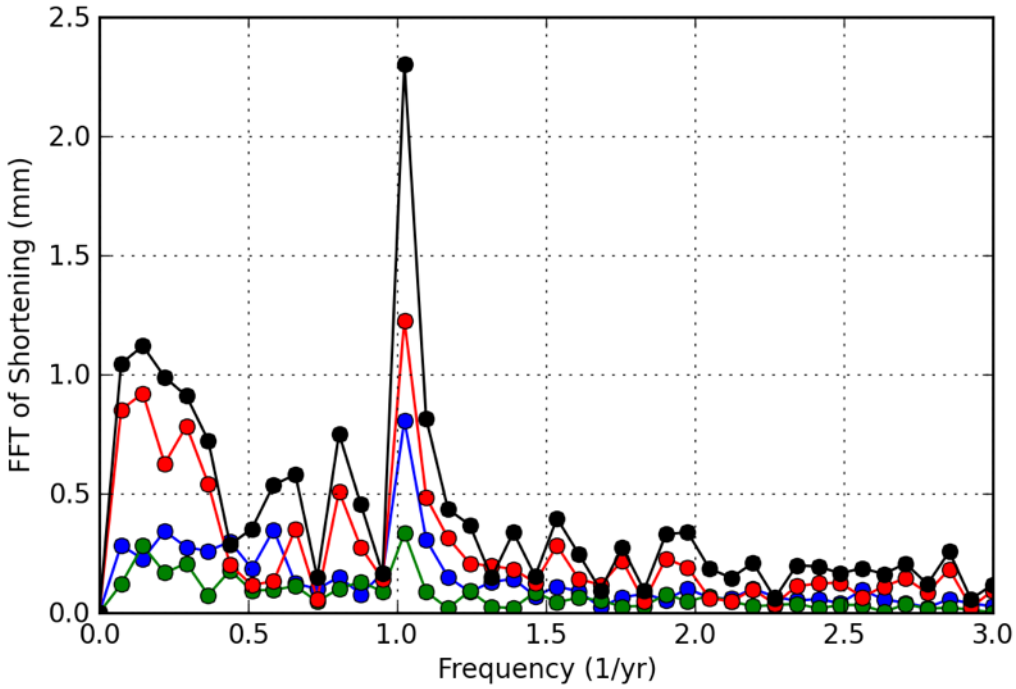

Figure 5.7: Fast Fourier Transform (FFT) of monthly aseismicslip record. Black is for the total creep, red is for C3, blue is for C4, andgreen is for C5. Frequency peak at 1 year visible for all records.

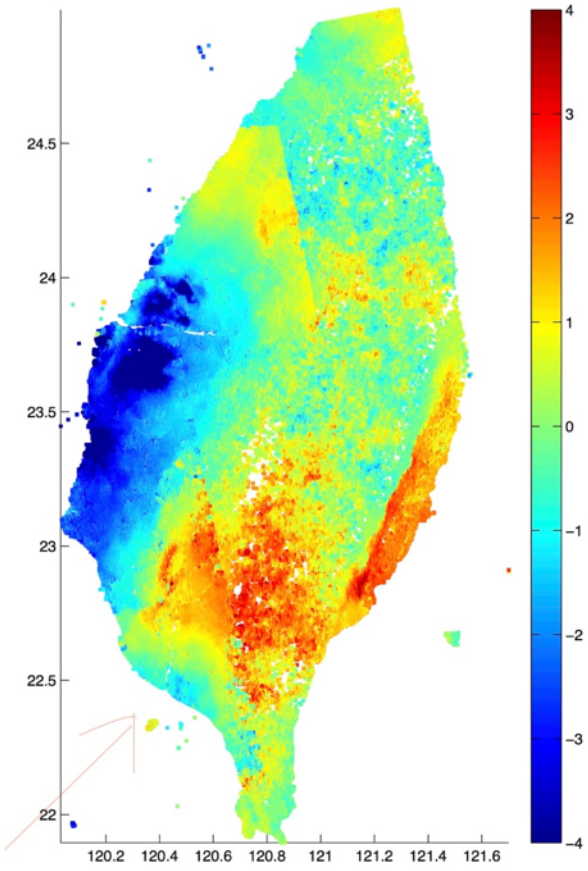

Figure 5.8: Ascending line-of-sight InSAR image from ALOS from2006-2011. Red shows motion toward and blue away in cm/yr.

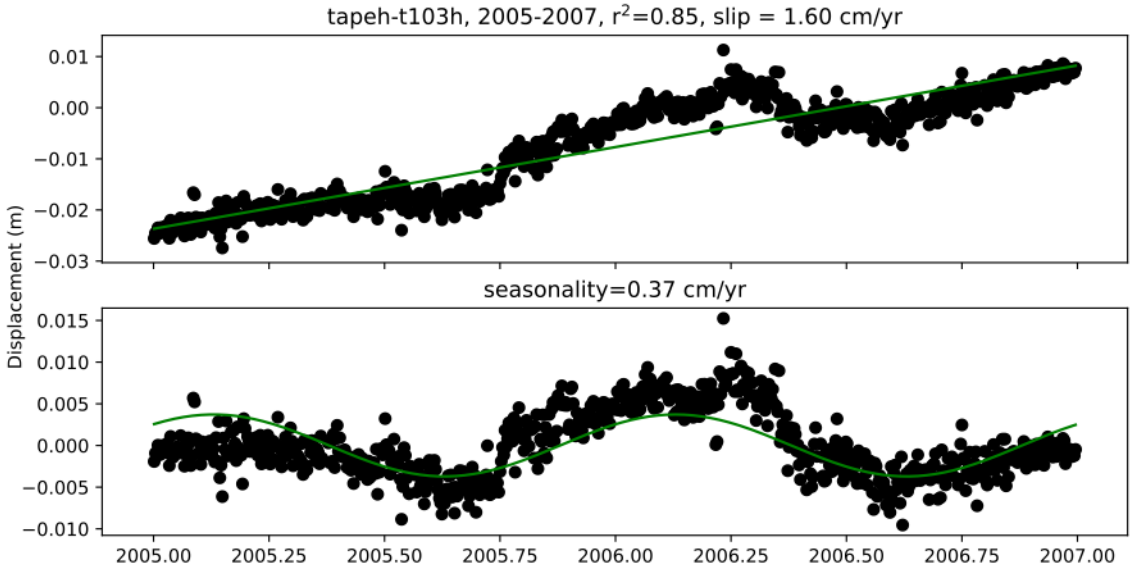

Figure 5.9: Example of GPS signal processing comparing stationsTAPE and t103.

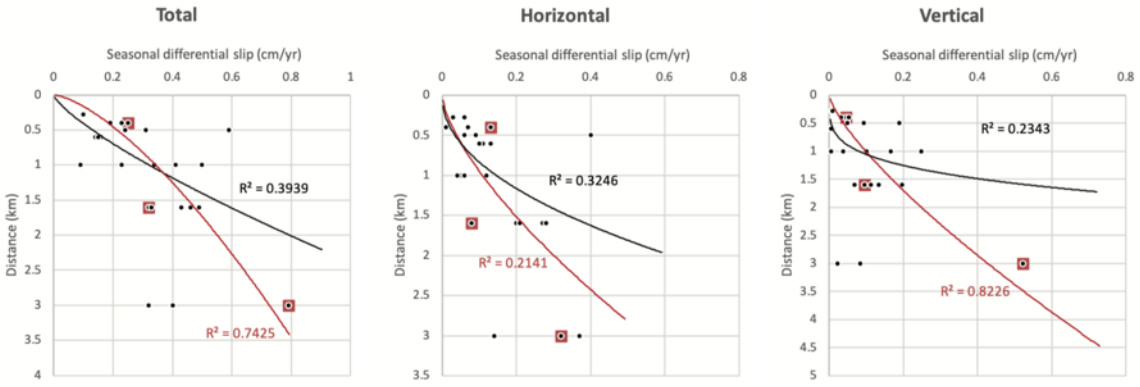

Figure 5.10: Difference in seasonal slip between hanging wall and footwall inferred from eight GPS stations. Low differential slip show that the seasonality in the footwall is mirrored in the hanging wall while larger differential slip show that they are uncoupled. Red points are for the period immediately after the 2003 Chengkung earthquake. Trend lines are power law fit for a fixed y intercept of 0.

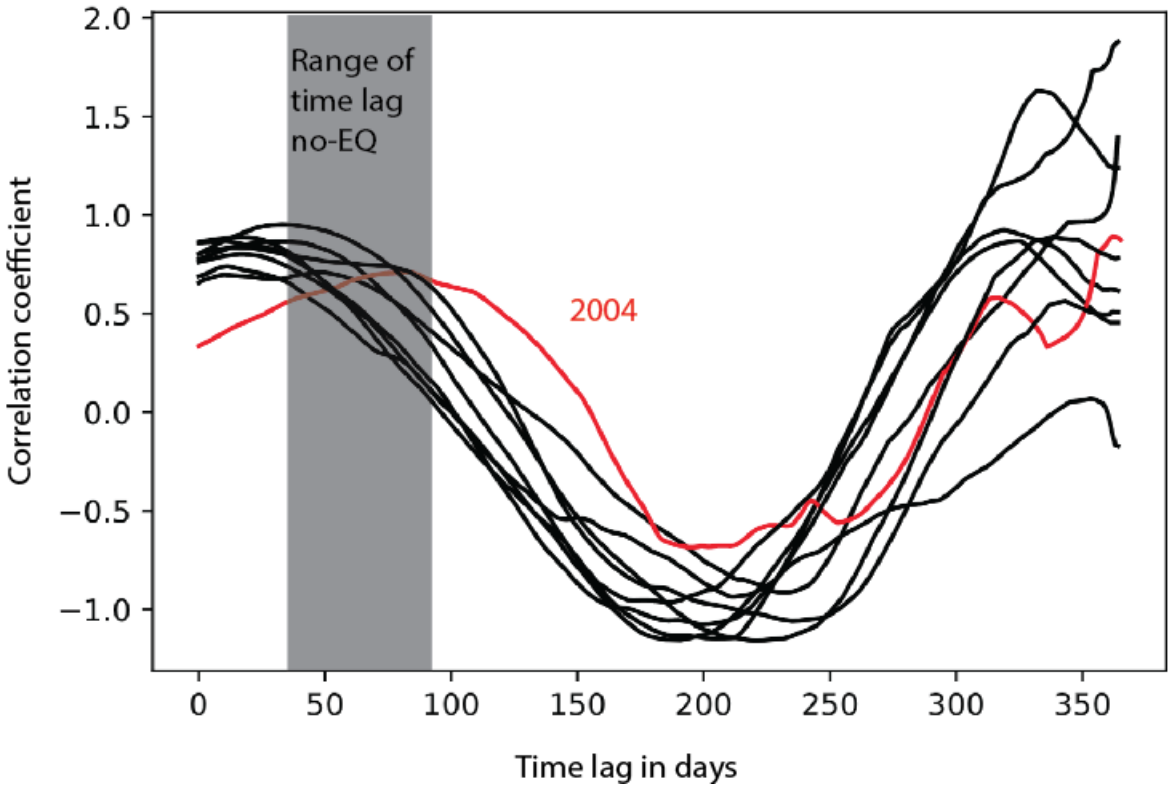

Figure 5.11: Cross correlation function between precipitation and creep meter data. Gray box shows range of phase lag between creep and precipitation for all years other than 2004. The cross correlation for 2004 is highlighted in red.

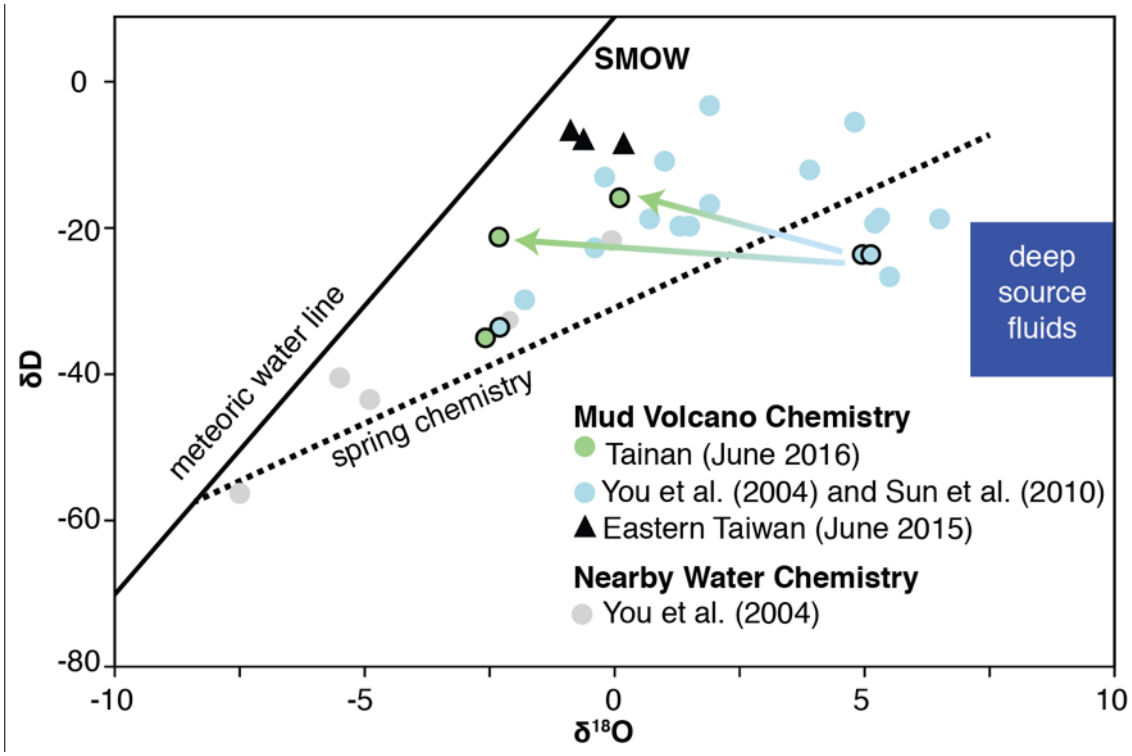

Figure 5.12: Hydrogen and oxygen isotopes for mud volcanoes and hot springs sampled in Taiwan. Black triangles show samples taken at two mud volcanoes and one hot spring in eastern Taiwan mapped on Fig. 1. Circles show samples from 5 months after the Meinong Earthquake (green) and those previously published (blue). Arrows between black highlighted points show difference in chemistry between our measurements and those of You et al. (2004). Solid line shows the meteoric water line and the dashed line shows the chemistry of springs in a similar geologic setting in California. Gray circles show groundwater chemistry from Taiwan (You et al., 2004). The blue box shows the deep fluid source proposed by You et al. (2004).

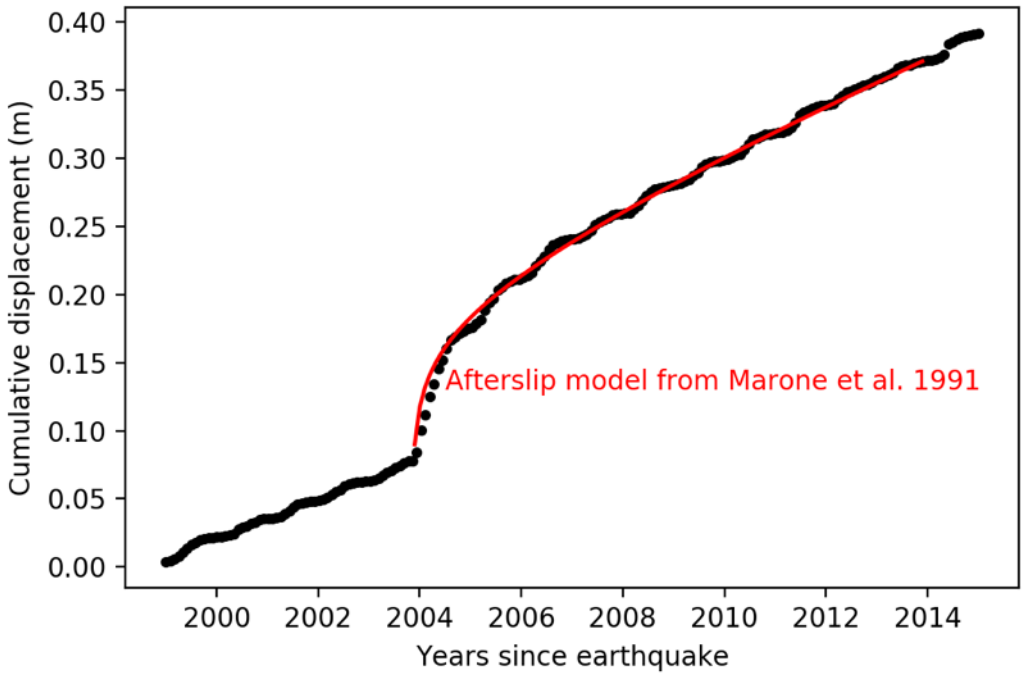

Figure 5.13: Best fit afterslip model from Marone et al. (1991).No afterslip model has seasonal slip so the subtracted signal in Fig. 5.2C is largely independent from which modle is chosen. This curve was found by solving Y = (a - b) σ_n /k and u = Y *log((V_{cs}/Y)t + 1) + (V_o t) for the best fit parameters of a = .5, b = -1.5, k = 790, σ_n = 10, V_{cs} = .45, V_o= .015.

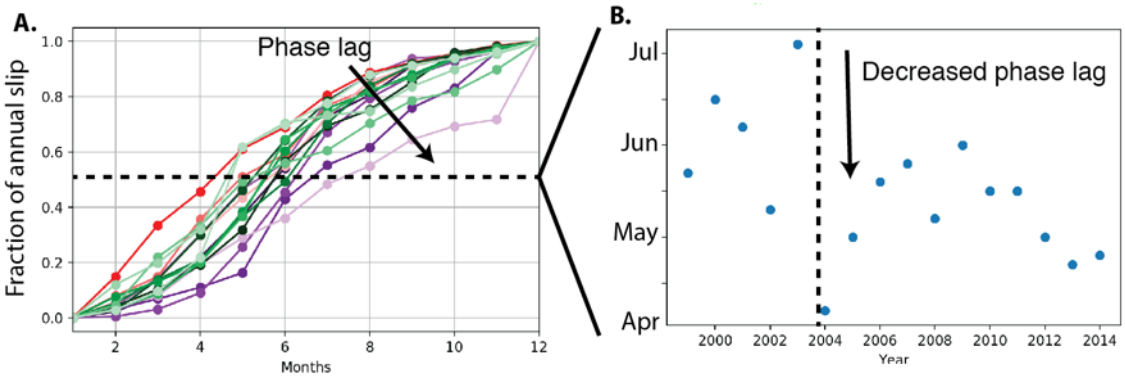

Figure 5.14: **A.** Fraction of annual shortening from 1998-2014. The more convex curves show less lag between hydrologic loads and slip while the more concave curves show lower phase lags. **B.** Month at which 50% of annual slip has occurred. Lower values shows a lower phase lag.

Chapter 6

Hydrologic modulation of seismicity near the Tibetan Plateau from 1985 to 2015

6.1 Abstract

Hydrologic loading, changes in pore fluid pressure, solid earth tidal stresses, and stresses due to thermoelastic expansion have all been proposed to modulate seismicity in a range of tectonic and climatic settings. A minority of seismicity from 1985-2015 (14,416 events) near the Tibetan Plateau, between 20º and 60º N and between 70º and 105º E, appears to be seasonally modulated with, at most, 10-40% more shallow events (<30 km depth) in the spring or fall than the summer or winter. We show that this modulation is statistically significant using Schuster tests, analysis of variance tests, and the multifrequential periodogram statistic on complete, repeating earthquake, and declustered catalogs. The tectonic and climatic heterogeneity in our study region shows that the spatial variation of modulation correlates with the spatial variation in hydrologic loading as measured by the GRACE satellites. We also document a downward migration in seismicity rate suggesting diffusion of pore pressure through fractured crystalline rock.

6.2 Introduction

Deep drilling projects and induced and triggered seismicity suggest that much of the Earth's crust, even far within continental interiors, is near critically stressed (Zoback et al., 2002). These faults are prone to fail after small stress changes that occur disproportionately on hydraulically conductive faults (Zoback and Townend, 2001). Changes in stress of only a few kilopascals due to hydrologic loading from rain and snow (*e.g.*, Heki, 2003), changes in pore fluid pressure from precipitation (*e.g.*, Hainzle et al., 2006) or snowmelt (*e.g.*, Saar and Manga, 2003), solid earth tides (e.g. Cochran et al., 2004), changes in ocean tides (*e.g.*, Tanaka, 2012), and thermal expansion of the Earth's surface (*e.g.*, Ben-Zion and Leary, 1986) may be sufficient to generate earthquakes. Because many of these stresses are periodic

or quasi-periodic, periodicity in seismicity may be widespread and show which processes modulate seismicity and lead to earthquake nucleation.

The idea that earthquakes could be modulated by hydrology is not new (*e.g.*, Pliny, 79 CE. More recent interest is due, in part, to innovations in geodesy that allow both the Earth's hydrologic cycle and surface deformation to be measured and correlated. Measurements of annual peak-to-trough changes in surface elevation on the order of a few centimeters in northern India (Chanard et al., 2014, Fu and Freymueller, 2012; Bettinelli et al., 2008), California, and globally are well explained by seasonal changes in mass loading (*e.g.*, Amos et al., 2014; Argus et al., 2014).

Periodic modulation of earthquakes at annual periods has been observed in the High Himalaya in Nepal (Bollinger et al., 2007; Bettinelli et al., 2008; Ader and Avouac, 2013), the San Andreas fault near Parkfield, CA (Christiansen et al., 2007), Mt. Hochstaufen in Germany (Hainzl et al., 2006, 2013), intraplate reverse earthquakes in mountainous regions in Japan (Heki, 2003), Bangladesh (Steckler et al., 2010), and some hydrothermal systems (Braunmiller et al., 2014; Christiansen et al., 2005; Saar and Manga, 2003; Wilcock, 2001; Gao et al., 2000; Rydelek et al., 1992). All of these studies focus on smaller areas; here, in contrast, we examine apparently similar modulation in seismicity from 1991-2015 throughout an ~100,000 km^2 area including the Tibetan Plateau, Altyn Tagh, Tarim Basin, and Tien Shan (Figure 6.1). This diversity of tectonic and climatic settings allows us to assess proposed causes for earthquake modulation as well as the suite of statistical tools used in past analyses.

6.3 Data

We analyze earthquakes between 20º and 60º N and between 105ºand 70º E (Figure 6.1) from three catalogs: the Annual Bulletin of Chinese Earthquakes (ABCE) from 1991 to 2005 (22,513 events, magnitude of completeness (Mc) = 4.5, Supplemental Figure 6.1, Schaff and Richards (2004)), the China Earthquake Networks Center Catalog (CENC) from 2006 to 2014 (5,162 events, Mc = 4, http://www.csndmc.ac.cn/, Supplemental Figure 6.2), and from 1980 to 2014 focal mechanisms from the Global Centroid-Moment-Tensor (CMT) catalog (638 events, Mc = 5, http://www.globalcmt.org). Data from November 2004 is missing from ABCE, so we use the average of October and December 2004 for the time series analysis. We also compare background seismicity in the ABCE catalog to repeating earthquakes in the ABCE catalog (2,379 events) as identified by (Schaff and Richards, 2004). Repeating earthquakes are often associated with faults experiencing aseismic slip and may be more sensitive to small stress changes (Liu et al., 2009), although (Thomas et al., 2009) found no statistically significant periodicity in San Andreas Fault repeating earthquakes. Using the Gutenberg-Richter relationship between earthquake occurrence and magnitude we assess catalog completeness for 1991-2005 and 2009-2014 after the 2008 Mw 7.9 Wenchuan earthquake and aftershock sequence. Although seismic catalogs are incomplete for Mw $\leq$ 5 the catalog completeness does not change seasonally (Figures S6.9 and S6.10}) implying that

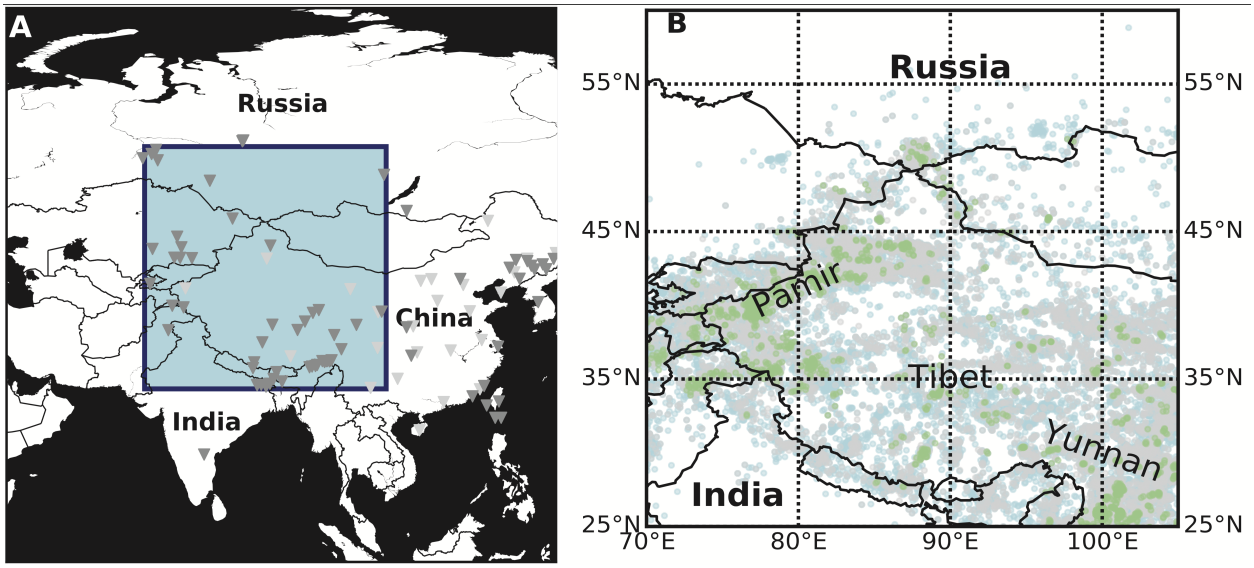

Figure 6.1: A. Map of Asia and seismic networks. Dark gray triangles are approximate locations for Annual Bulletin of Chinese Earth-quakes (ABCE) seismometers from (Schaff and Richards, 2004) while light gray triangles show China Earthquake Networks Center (CENC) seismometers. B. Map of seismicity. Gray points are ABCE events(1985-2005), blue dots are CENC events (1970-2015), and green dots are multiplets in the ABCE data as identified by Schaff and Richards(2004). Because of overlapping time series, many events are covered. See Supplemental Figs. 6.8 for non-overlapping maps and Supplemental Figs. 6.11-13 for Global Centroid-Moment-Tensor (CMT) and declustered catalogs.

the seasonal modulation we observe is not simply due to changes in instrument sensitivity and, therefore, Mw < 5 earthquakes are not discarded for the analyses.

We compare these earthquake catalogs to records of water storage, precipitation, and atmospheric pressure as potential sources of stress that might modulate seismicity. The Gravity Recovery and Climate Experiment (GRACE) has recorded changes in mass since 2002 by measuring changes in the Earth's gravity field (Landerer and Sensen, 2012). Rainfall data from 1991 to 2013 are from the Global Precipitation Climatology Project data set (Adler et al., 2003) while atmospheric pressure is from the National Oceanic and Atmospheric Administration (NOAA) Global Surface Summary of the Day database (https://data.noaa.gov/dataset/global-surface-summary-of-the-day-gsod).

6.4 Methods

The statistical tests that evaluate periodicities in data could be biased by a few large events that trigger a large number of smaller events. We use three methods to distinguish background seismicity from clusters of foreshocks and aftershocks. First, we compare our cata-

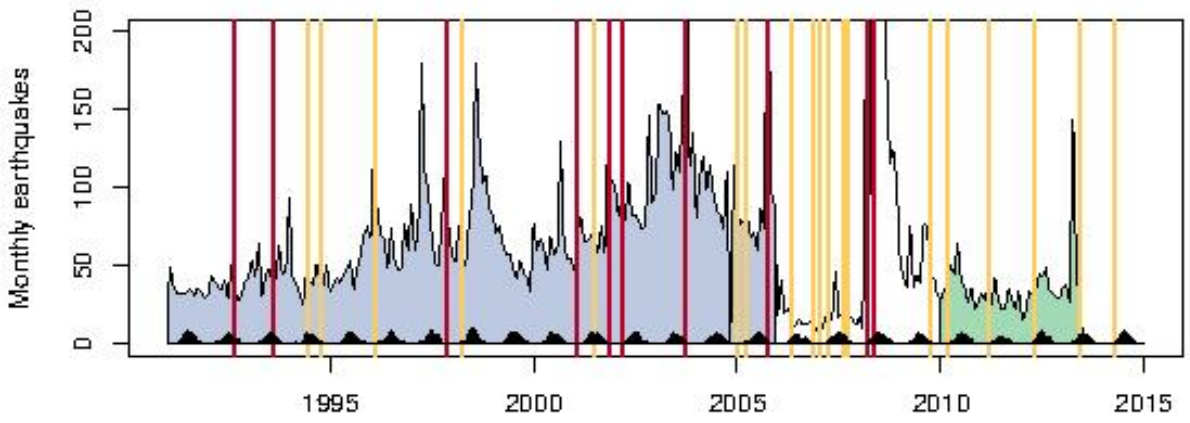

Figure 6.2: Histogram of monthly earthquakes. Blue shaded area is theAnnual Bulletin of Chinese Earthquakes (ABCE) catalog 1991-2005.White and green shaded areas are the China Earthquake Networks Center Catalog (CENC) 2006 to 2014. White areas are excluded from statistical analysis either because of incomplete station coverage (2006-2008)or Wenchuan earthquake aftershocks (2008-2010.) Vertical yellow lines show global seismicity $\geq$M8 and vertical red lines show seismicity $\geq$M7within the study area. Black curve at the base is annual rainfall in Yunnan Province (in southwestern China) in mm.

logs to the times of global Mw $\geq$ 8 events and local Mw $\geq$ 7 events (Figure 6.2) to see if events are related to dynamic triggering by teleseismic surface waves or large regional aftershock sequences (*e.g.*, Wenchuan 2008 in Figure 6.2). Second, we compare two declustering methods. (For a more thorough discussion see van Stiphout et al. (2012).) The Reasenberg (1985) link-based method identifies the likelihood that earthquakes are related in a spatial-temporal window based on Omori's Law. This widely used method builds families of earthquakes, which could be related to an original earthquake or any of its aftershocks. In contrast, the stochastic epidemic-type aftershock sequence (ETAS) method, first proposed by Ogata (1988) and extended by Zhuang et al. (2012) calculates the likelihood that each earthquake is a background event. By comparing event probability to a uniform distribution of random probabilities, the catalog is declustered and characterizes the background seismicity (Zhuang et al., 2012). Two concerns with both methods are the possibility of removing background events and discarding so many, particularly low magnitude, events that later statistical analysis becomes unreliable. Another concern is that ETAS assumes catalog completeness, possibly generating a spurious signal of opposite sign, i.e. periods that once had more events due to aftershock sequences then would have fewer events because more back-

ground events were mistaken for aftershocks. A final concern, is that swarm-type clusters may introduce correlated events even in declusterd catalogs.

Moving from point process statistics to continuous time series, we compare monthly seismicity. Determining the statistical significance of periodicity in seismicity has been contentious from the outset— Schuster (1897) developed his eponymous random walk test to disprove tidal modulation of earthquakes proposed by Knott (1897). Schuster's uni-frequential approach first assesses the degree to which a single frequency correlates with seismicity and then computes a statistical significance (p-value). One limitation of the Schuster test is that two or more similar frequencies could be convolved into a single broad peak in the obtained spectrum obtained from applying this test to a range of frequencies Ader and Avouac (2013). To address this concern, Dutilleul et al., (2015) used a multi-frequential periodogram analysis (MFPA) to separate sunspot frequencies into components with 9-month and 13-month periods. MFPA tests the superposition of up to 10 different frequencies simultaneously to find the combination of frequencies that produce the best fit to the observed data; this is analogous to the fitting of different trigonometric function used to assess causal mechanisms in Hainzl et al. (2013). In its first application to seismicity, Dutilleul et al., (2015) used the MFPA to test for periodicity in California seismicity, finding significant modulation at annual period and its harmonics. In addition to Schuster spectra and MFPA, we use analysis of variance (ANOVA) and Kruskal-Wallis (KW) tests as used in Christiansen et al., (2005). The ANOVA test compares the means populations. This is equivalent to a t-test for more than two groups. The more general KW tests the similarity between the ranked data of different populations. Table 6.1 compares the means of monthly bins while the supplemental code include three and six month bins.

6.5 Observation and Results

Most seismicity near the Tibetan Plateau has no obvious modulation (Figure 6.4) with an average seismicity rate of 67 $\pm$ 66 events per month. Yet there are significant deviations from this average rate particularly at shallow depths. In the ABCE catalog from 1985-2005, from 0-15 km there are ~40% and ~25% more events in the fall than the summer and winter respectively. From 20-30 km there are ~10% -20% more events in the fall and spring than the summer and winter (Figure 6.4). When considering the seasonal distribution of individual catalog years, eight years show peak seismicity during spring or fall over 2 σ, where σ= variance$^{1/2}$, with almost all years showing some seasonal change in total seismicity. This variation is not simply artifact of a single year or aftershock sequence but rather a majority of years with often similar amplitude changes in seismicity (Figure S6.18). Similar peaks in the spring and fall are apparent in the catalog of repeating earthquakes as well as the declustered catalogs although the total number of events in declustered and repeating catalogs is about an order of magnitude smaller than the total catalog (Figure 6.3).

Table 6.1 shows the statistical significance of periodicity (p-values) from Schuster tests and analysis of variance (ANOVA) and the statistically significant annual period (in months)

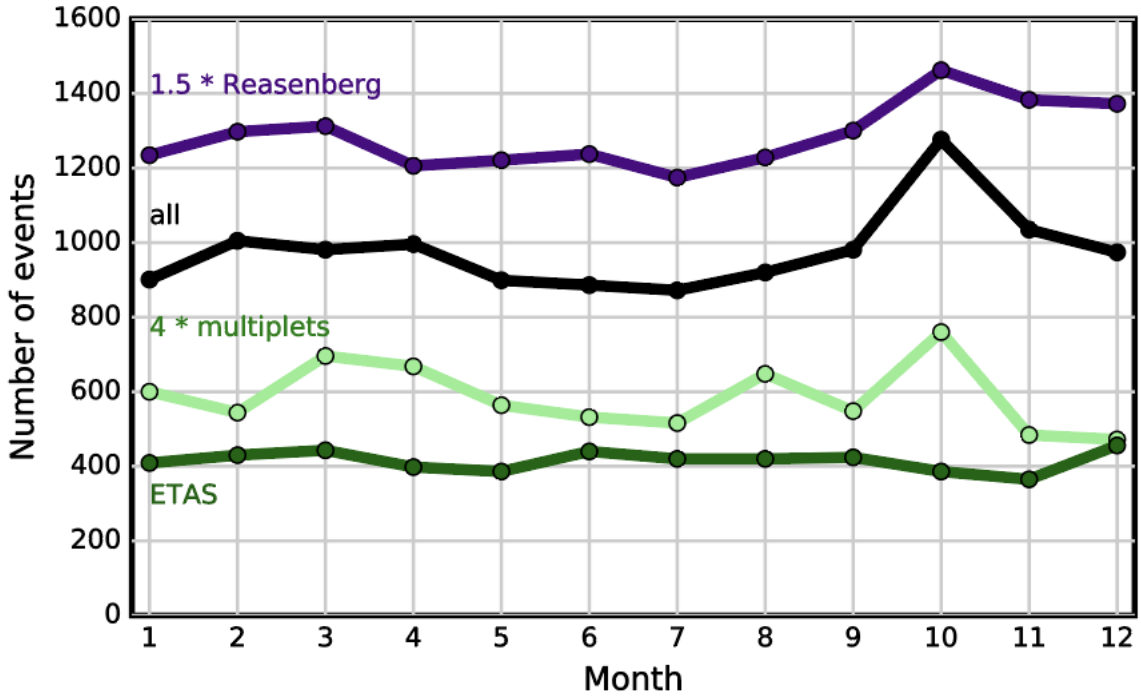

Figure 6.3: Figure 3: Cumulative monthly seismicity for all earthquakes (black), five times the repeating earthquakes as identified by Schaff and Richards, 2011 (blue), and two times the Reasenberg declustered catalog (gray).

of the multifrequential periodogram approach (MFPA). In the MFPA and Schuster test, harmonics of the ~12 month signal (*e.g.*, 24, 12, 6, or 3 months) have significant p-values. We show statistical analyses for the complete dataset, rather than selectively windowing places or times with more statistically significant modulation but fewer events (Shearer and Stark, 2012). Unsurprisingly, given the low amplitude signal there is significant noise in the data, yet there is a trend towards 12 month harmonics in MFPA tests for all data, even strongly declustered catalogs. This trend is less obvious in the Schuster spectra suggesting that some overlapping periodicities identified in the MFPA may be convolved into broad or spurious peaks in the Schuster test. (For a thorough discussion of differences between MFPA and Schuster spectra see Dutilleul et al. (2015).) These results are similar in both tests for downsampled data where arbitrary years are removed.

In addition to the annual modulation, the time series have a strong interannual structure. The late 1990's show approximately annual broad peaks of ~100 events per month (Figure 6.2). The early 2000's appear to have more total earthquakes with, if present, weak seasonal change superimposed on a broad multiyear trend peaking in 2004. The early 1990's have fewer total events and weaker seasonal changes. Starting in 2009, the CENC had ~25

Table 6.1: Table of statistical test results. ABCE 1991-2005 is the Annual Bulletin of Chinese Earthquakes catalog. The first column contains the complete catalog and the catalog divided by minimum moment magnitude, and declustering method. Average, strong, and weak Reasenberg declustering are the range of values from southern Californian seismicity (Reasenberg, 1988.) The second column shows the number of events for each. The third and fourth column shows the Schuster Test statistical peaks closest to 6 or 12 months with their corresponding p-values. For complete Schuster spectra see Supplemental Fig. S6.8. The Multifrequential Periodogram Approach periods (MFPA) show the periods (often harmonics of 12 mo) that add together to reproduce the time series. Analysis of variance (ANOVA) and Kruskal-Wallis (KW) are comparable to the Schuster p-values where 0.05 corresponds to 95% confidence.

ABCE 1991-2005	# of events	MFPA T (mo)	Schuster T (mo)	p-value	ANOVA	KW
Complete	10,259	2.6, **6.1**, 23.2, 9.6, **12.2**	6.6, 13	0.005, 0.05	$\ll$0.001	$\ll$0.001
M$\geq$3	10,168	**24, 11.9**	**6.5**, 13	$<$0.01, 0.2	0.478	0.997
M$\geq$4	3,657	**11.9, 24**	20, 10.9	$<$0.01	0.075	0.986
Depth $\leq$ 15 km	4,162	**24, 12**	14, 25	0.08, $<$0.01	0.245	0.951
Reasenberg	9,189	2.7, **6.1**, 9.7, 31.9, **12.1**	11, 14	0.14, 0.17	$\ll$0.001	$\ll$0.001
Reasenberg-Weak	9,513	2.6, **6**, 10.5, **12.2**	14.5	0.08	$\ll$0.001	$\ll$0.001
Reasenberg-Strong	7,815	2.4, 3.4, 8.9, 10.2	16	0.09	$\ll$0.001	$\ll$0.001
ETAS	5,007	2.6, 26.1, 64.6, **6.5**	**24**, 3, **6, 12**	0.8, 0.7	$\ll$0.001	$\ll$0.001

events per month, also showing apparent seasonal modulation. With the exception of the 2004 M9.1 Sumatra and 2008 M7.9 Wenchuan earthquake, the peaks in the catalog are not obviously related to global M $\geq$ 8 events (Figure 6.2 red vertical bars) or local M$\geq$ 7 events (Figure 6.2 blue vertical bars.) Some of these long-term trends in seismicity may be related to changes in station coverage although general agreement between ABCE and CENC in overlapping years suggest some of the long-term trends are real.

6.6 Discussion

Seasonality in the shallow seismicity may be due to hydrologic loading, barometric pressure, pore fluid pressure changes, tides, and thermo-elastic expansion. Each process produces a

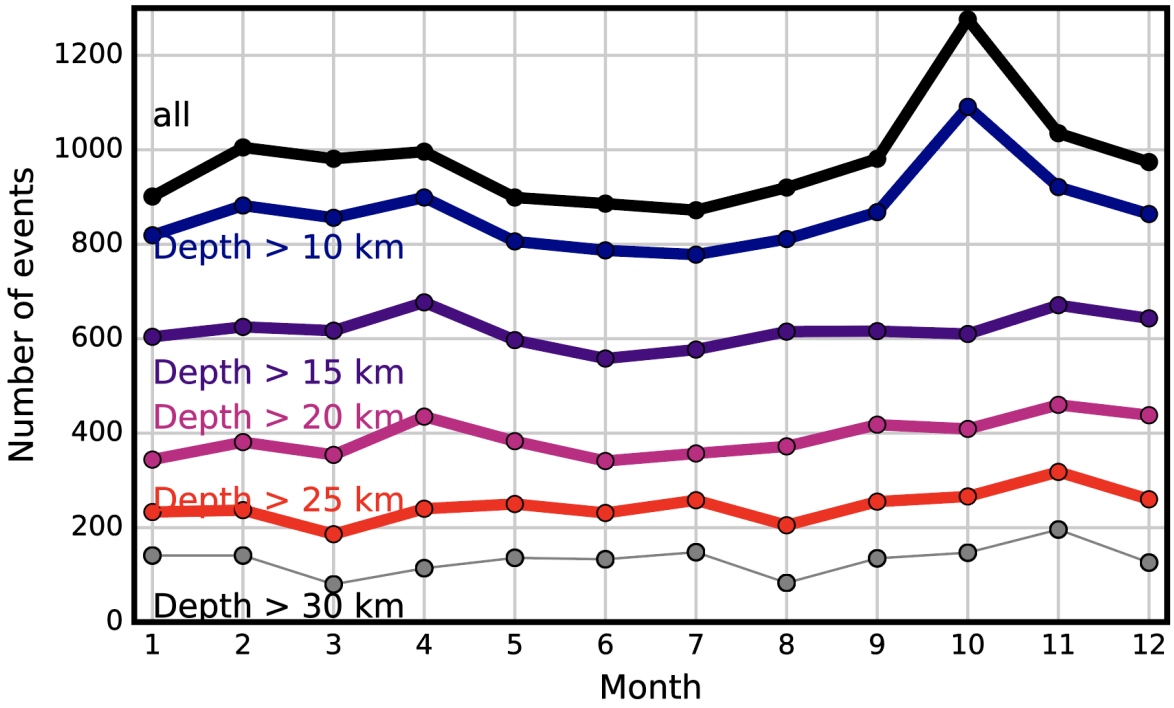

Figure 6.4: Total monthly seismicity for different depths. Seasonal 203modulation is strongest near the surface.

few kPa stress change in the shallow crust (Hainzl et al., 2013; Ben-Zion and Leary, 1986) and each makes specific predictions about the location, depth, focal mechanism, and phase of seasonal earthquakes. Unlike past studies which focus on much smaller areas and relatively few events, whenever possible, we aggregate many earthquakes from a large, diverse region. This leads to more noise but reduces the potential for local biases. The diversity of tectonic and climatic settings has the added benefit of testing the many mechanisms proposed to modulate seismicity.

Proposed Mechanisms

We assume modulation occurs on a population of critically stressed faults sensitive to very small changes in stress. Failure on such faults is governed by Coulomb's law

$$\sigma_s = \tau - \mu(\sigma_n - p_f)$$

where σ_s is the Coulomb stress, τ is the shear stress, μ is the coefficient of friction, σ_n is the normal stress, and p_f is the pore fluid pressure.

Hydrologic loading due to water or snow would cause a local increase in normal stress (σ_n), independent of faulting style. Because the vertical load also increases shear stress (τ) on steeply dipping normal faults, surface loading should encourage normal events. Shallowly dipping thrust and vertical strike-slip events, in contrast, would 'clamp' thus suppressing earthquakes during loading. In 2D and 3D this simple conceptual model breaks down– loading far from faults generates shear stresses on favorably oriented faults regardless of fault type. Accounting for the full complexity of the loading problem is nontrivial requiring knowledge of fault-type, crustal properties, and probably finer resolution loading data than GRACE. As a first order test of loading, we compare the prediction from the 1D loading model to the relatively small CMT catalog.

Atmospheric pressure variations also produces stresses on the order of a few kPa with similar seasonal amplitudes (*e.g.*, Gao et al., 2000). Unlike the hydrologic cycle, atmospheric pressure can fluctuate over much shorter time scales. Liu et al. (2009) observed eleven slow-slip events that coincided with typhoons in Taiwan although this correlation has been since been disputed Hsu et al. (2015). They explained this signal by arguing that a reduction of up to 2 kPa of normal stress over the course of about a day would be sufficient to unclamp the fault and initiate slip.

Pore fluid pressure increases (p_f) associated with surface waters can propagate into fault zones, lowering the effective normal stress by a few kPa (*e.g.*, Christiansen et al., 2007; Roeloffs, 1996)) and thus increasing the likelihood of slip on all fault types. Because, permeability is highly scale-dependent, fault zones may allow pore fluid pressures to propagate deep into the earth and (Zoback et al., 2002) argue that critically stressed faults tend to be hydraulically conductive. In particular, steeply dipping faults (*e.g.*, strike-slip and normal faults) may allow fluid pressures to efficiently propagate to seismogenic depths (Hainzl et al., 2006). Additionally, because pore pressures will reach different depths at different times, if pore fluid pressures were the dominant cause of seasonality we would expect systematic changes in peak seismicity with depth (*e.g.*, Hainzl et al., 2006). Braunmiller et al. (2014) argue that surface loads indirectly modulate pore fluid pressures at seismogenic depths although permeability (and thus water content) at these depths may be quite low (Ingebritsen and Manning, 1999).

Spatial heterogeneity in the thermoelastic expansion of rocks may also produce systematic increases and decreases of Coulomb stress with depth (*e.g.*, Ben-Zion and Leary, 1986). These stresses, also a few kPa, penetrate to depths proportional to the topographic wavelength of the landscape. Similar to pore pressure, this process predicts systematic changes in the depth of seismicity, in this case, simultaneously suppressing and promoting earthquakes at different depth of each fault (*e.g.*, Ben-Zion and Leary, 1986).

Spatial variations in seasonally modulated seismicity

Spatial variation in tectonics and climate around the Tibetan Plateau test some of the causal mechanisms proposed to modulate seismicity. Surface loading is documented by Gravity Recovery and Climate Experiment (GRACE) satellite measurements of seasonal changes in

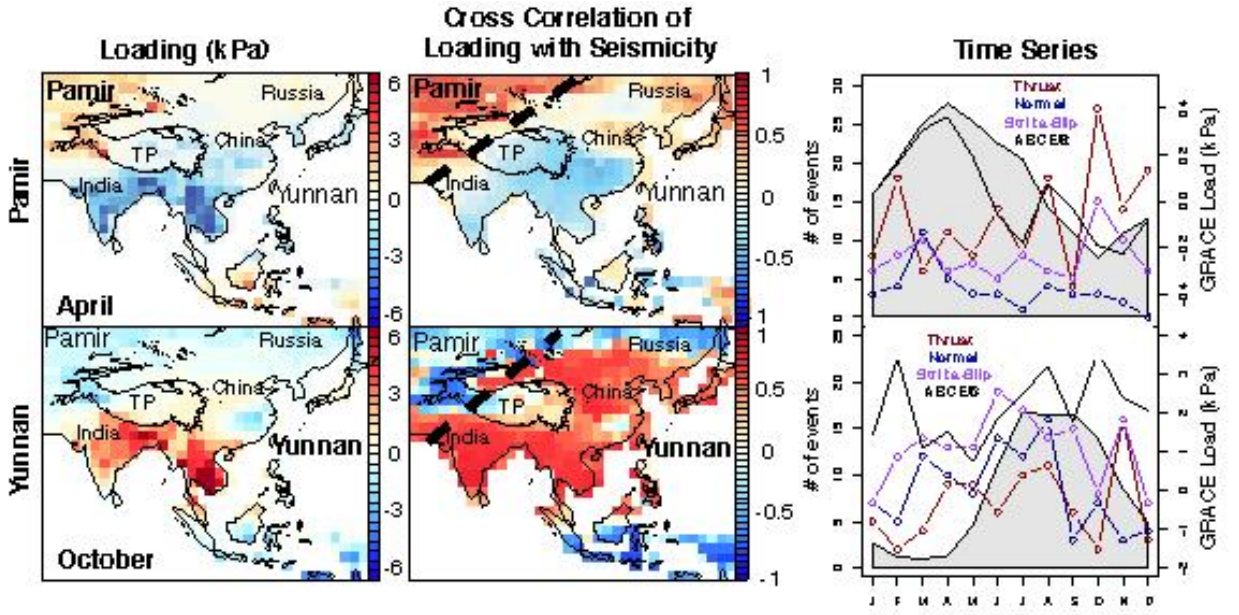

Figure 6.5: Maps and time series showing the relationship between hydrologic loading and seismicity from two different climate regions. The top row focuses on the climate in to northwest of the plateau labeled Pamir while the bottom row focuses on the more monsoon climate labeled Yunnan. The first column shows estimated average load at the surface from GRACE gravity satellites for April, the month of peak loading in Pamir, and October, the month of peak loading in Yunnan. The second column shows the Pearson product-moment cross correlation coefficient of GRACE data with seismicity above and below the dotted line. Red regions have an annual loading cycle that correlates with the seismicity in Pamir (top middle) or Yunnan (bottom middle.) The final column shows monthly time series of earthquakes with different focal mechanisms from the Global CMT Catalog (1980-2015, depth <30km,) Annual Bulletin of Chinese Earthquakes (1991-2005, depth <30km.) The gray shaded curve is a representative GRACE load for Pamir and Yunnan respectively.

the Earth's gravitational field. Seasonal loading around the Tibetan Plateau can be over a meter of water equivalent thickness (10 kPa) and peak loading occurs at different times in different regions (Figure 6.5.) An important caveat is that the resolution of GRACE is on the order of a hundred kilometers while the aquifers are a few kilometers is width. This means that tens of meter changes in water level (100 kPa, *e.g.*, Bettinelli et al., 2008) can appear as only a few kPa when smeared over a larger regional scale. This suggests GRACE is a measure of the phase (within a few days) but not necessarily amplitude of stress changes experienced by faults across the area. We use this spatial heterogeneity to show that the phase of hydrologic loading, as recorded in GRACE, matches the phase of seismic modulation. In other words, regions with positive correlation coefficients have more seismicity coincident with loading while those with negative correlation coefficients have less

seismicity during times of peak loading. In other words, we compare the phase of loading for each pixel of GRACE data with the with regional seismicity above and below the dashed line to show that climate and seismicity co-vary at the largest spatial scales. The signal above the dashed line is dominated by the Pamir thrust belt which has both peak loading and seismicity in the spring while the signal below the dashed line is dominated by the SE borderland of Tibet in Yunnan which has both peak loading and seismicity in the late fall.

If surface loading directly modulates seismicity, in 1D, loading should suppress thrust and strike-slip faulting and therefore negatively correlate with nearby seismicity. In contrast, if pore fluid pressures rather than loading modulate seismicity, earthquakes should positively correlate with GRACE data. In a more complex geometry seasonal loading along the footwall, but not the hanging wall, of thrust faults may also positively correlate with seismicity (*e.g.*, Roeloffs, 1988). Both regions in Figure 6.5 contain dominantly thrust and strike slip faults although small normal faults pervade the region. It is worth noting that these two regions have extremely high rates of seasonal loading (left-most graphs in Figure 6.5), seismicity (Figure 6.1B), and are particularly well captured by the ABCE seismic network (Figure 6.1A). To understand this loading we use focal mechanisms from the Global CMT catalog from 1981-2013 for both Pamir and Yunnan (right-most graphs in Figure 6.5). The data is sparse but all types of seismicity appear to peak during peak loading. The strength of the correlation between loading and seismicity suggests some causal link yet the phase may be more consistent with other mechanisms like the diffusion of pore fluid pressures or may reflect the limitations of our simplistic 1D loading model or the Global CMT catalog.

Annual changes in temperature and atmospheric pressure also vary regionally. However, the annual changes in atmospheric pressure (up to a few kPa) are dwarfed by smaller time scale changes in atmospheric pressure and synchronous changes in hydraulic loading. Supplemental Figure 6.10 which shows the combined effect of hydraulic loading recorded by GRACE and atmospheric pressures recorded by the National Oceanic and Atmospheric Administration (NOAA) Global Surface Summary of the Day database (https://data.noaa.gov/dataset/global-surface-summary-of-the-day-gsod.) These plots are equivalent and nearly identical to the first two columns of Figure 6.5. Unsurprisingly, changes in annual surface temperature appear to vary strongly with latitude (Figure S6.10) but show no obvious relationship to the phase of seismic modulation.

Depth variations in seasonal modulation of seismicity

Pore fluid pressures and thermoelastic expansion of rocks predict systematic changes of seismicity with depth. Hainzl et al. (2006) found a downward propagation in earthquake rate within a few days or rain. This propagation was consistent with a hydraulic diffusivity of 3.3 m^2/s, which is reasonable for faulted crystalline rock which range from ~10^{-1}–10^4 m^2/s (Roeloffs, 1996). Figure 6.6 shows the density of seismicity from 5 – 10 km for the entire study area. Unlike Hainzl et al. (2006) our catalogs are incomplete at low magnitudes and have considerable uncertainty with depth. Horizontal lines correspond to rounding of depth data and the stronger signals at 10 km intervals are likely related to these rounding errors.

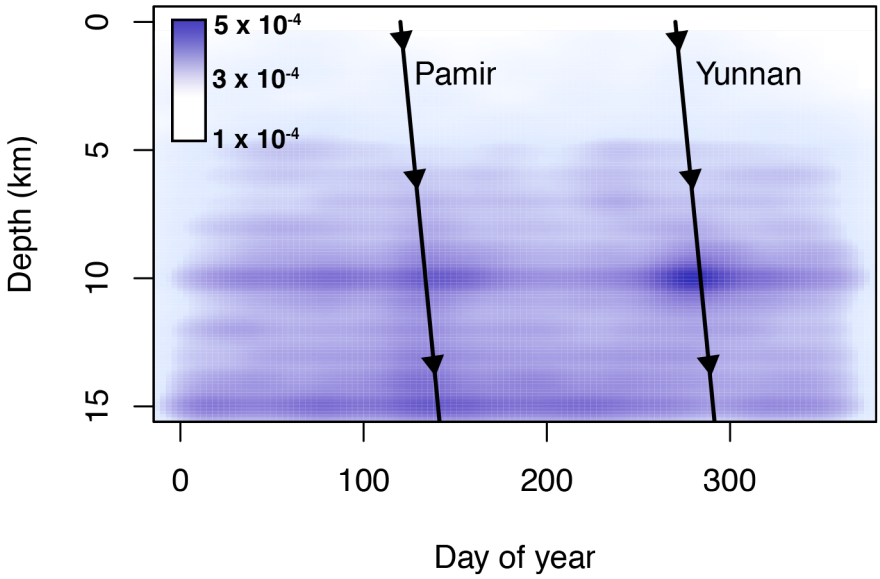

Figure 6.6: Heat map of seismicity from including ABCE events from1991-2005 and CENC events from 2009-2014. Dark purple is equivalent 4 x 10^{-4} events per day while white is equivalent to 1 x 10^{-4} events per day. Black lines show the propagation of pore pressures calculated from peak loading in Pamir and Yunnan for reasonable diffusivity of fractured crystalline rock (Roeloffs, 1996).

However, there is a suggestive downward propagation of seismicity from the time of the surface load in Pamir and Yunnan down to 15 km (Figure S6.6). For an annual sinusoidal load at the surface, in one-dimension, the time lag between peak loading at the surface and peak pore pressure at depth is given by

$$\Delta t = \frac{y}{\sqrt{2D\omega}}$$

where Δt is the time lag, y is the depth, D hydraulic diffusivity, and ω is the angular frequency of the load (Todd, 1961). In Figure 6.6 we overlay seismicity with the timing of peak loading predicted for Yunnan and Pamir, as measured by GRACE satellites. We bracket the range of hydraulic diffusivities for fractured crystalline rock given by (Roeloffs, 1996) and plot the envelope of this independent data for the range of shallow depths. We find good agreement between the timing of peak seismicity and peak pore pressure for shallow seismicity implying relatively high hydraulic diffusivities (Fig. 6.6). However, at 5 km depth, even with the high hydraulic diffusivity implied by the changes in pore pressure are small, about 2 kPa, and the decrease in permeability with depth (Ingebritsen and Manning, 1999) may mean that the hydraulic diffusivities implied by Figure 6.6 are unreasonably high

or that conductive, critically stressed faults maintain upper crustal permeabilities even at seismogenic depths.

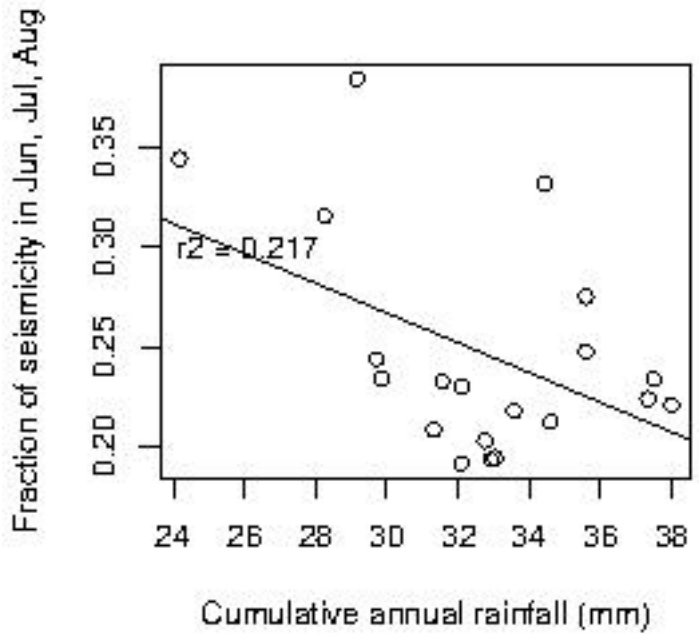

Figure 6.7: Fraction of total annual seismicity in the summer months compared to annual rainfall from Adler et al. (2003).

Interannual changes in seismicity

There is also a weak correlation between cumulative rainfall and seasonal modulation. There is weak anticorrelation between total rainfall and summer seismicity (Figure 6.7) and a weak positive correlation between total rainfall and fall and spring seismicity (Figure S6.5) This is broadly consistent with the idea of fault clamping due to loading first proposed by (Bettinelli et al., 2008). There are several complications to comparing interannual variability of seismicity with annual rainfall not least that loading and rainfall are different properties; we use rainfall because the GRACE gravity satellites launched in 2002. However, GRACE records changes in mass storage which could be dominated by snow pack, groundwater withdrawal, or for example in a river delta) rainfall many kilometers away.

If these interannual correlations are real, long-term changes in water storage and Tibetan hydrology (Tiwari et al., 2009) may also have tectonic implications. This intriguing

observation poses a number of questions. How will climate change affect seismicity and tectonics (Luttrell and Sandwell, 2010)? How does the shorter term seismic modulation relate to the longer-term climatic influence that erosion and isostatic rebound (*e.g.*, Molnar and England, 1990) impose on the region? How are large ≥M7 earthquakes affected by weak but widespread seasonal modulation?

6.7 Conclusions

Most seismicity is not seasonality modulated. However, summer and fall months in our study area have up to 20% more events than summer or winter and these variations (Figure 6.3), though variable year to year, strongly correlate with the timing of regional hydraulic loading (Figure 6.5.) Statistically significant annual modulation of seismicity appears in complete, declustered, and repeating earthquake catalogs. Annual modulation positively correlates with GRACE gravity measurements implying that seismicity is related to hydrologic loading. The spatial variation of this loading also correlates the spatial variation in the phase of modulated seismicity; that is, places that have more loading in the fall have more seismicity in the fall and those that have more loading in the spring have more seismicity in the spring. We also show that the timing of seismicity propagates downward at reasonable hydraulic diffusivities suggesting that seismicity may be triggered by changes in pore fluid pressures. Finally, we find a weak correlation between the magnitude of annual rainfall and seasonal seismicity.

The seasonal and interannual signals we observe are imperfectly explained by any of the proposed mechanisms. Simple hydrologic loading does not explain modulation by focal mechanism. The phase and downward migration of seismicity Figure 6.6 is most consistent with the idea of diffusing pore fluid pressure. Improved seismic network coverage and longer time series will increase the resolution of the suggested temporal signals and may clarify their underlying processes.

6.8 Acknowledgements

I would like to acknowledge my collaborators on this study C. Johnson, J. Day, R. Bürgmann, and M. Manga. We are grateful to P. Dutilleul (McGill University) and two anonymous reviewers for helpful comments. J. Seeley and M.H. Huang also helped with figures. N. Randolph-Flagg was supported by the National Science Foundation Graduate Research Fellowship (DGE 1106400) and Fulbright Research Grant. MM and NRF were further supported by NSF awards 1334424 and 1521855.

6.9 Supplemental Information

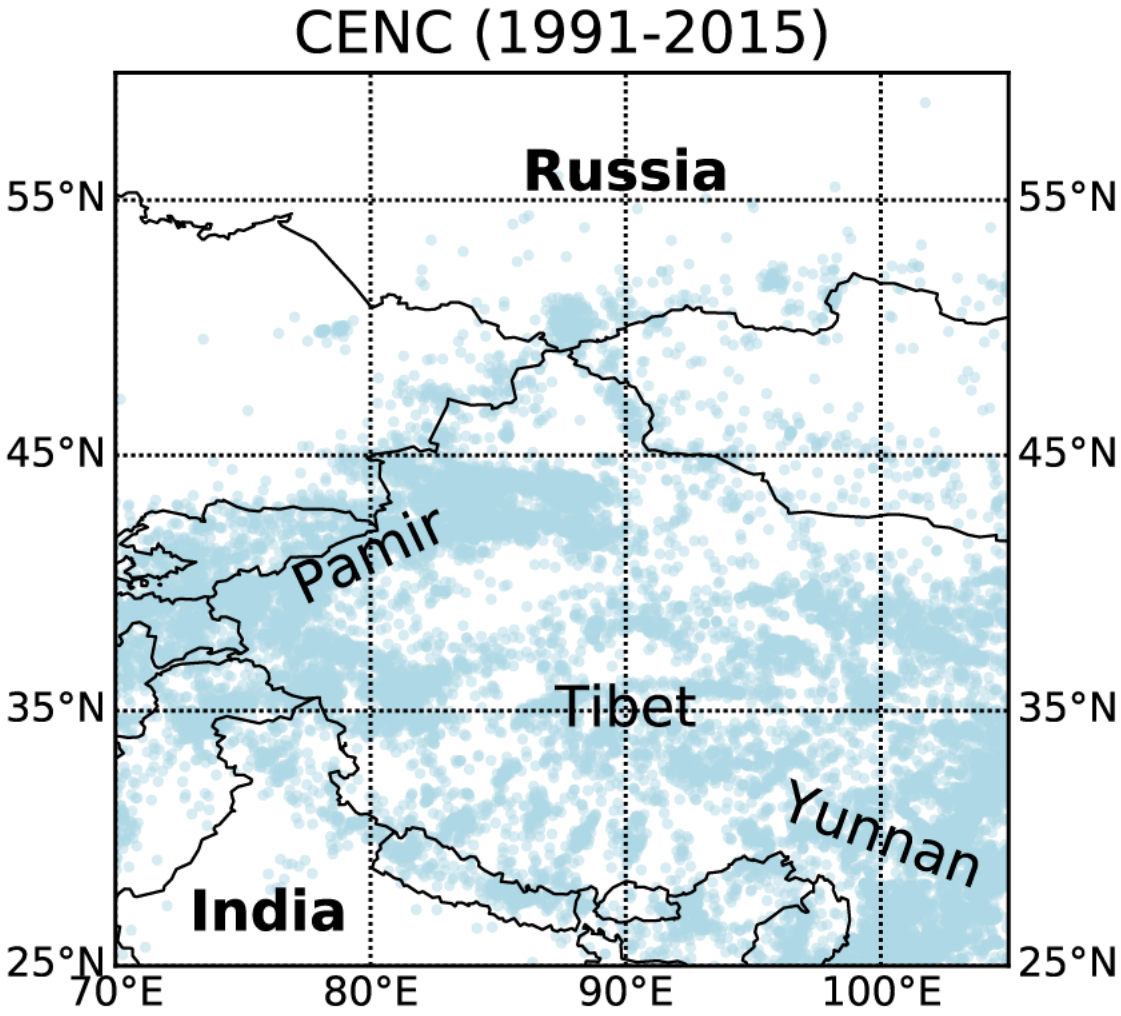

Figure 6.8: Map of China Earthquake Networks Center (CENC) events (1970-2015).

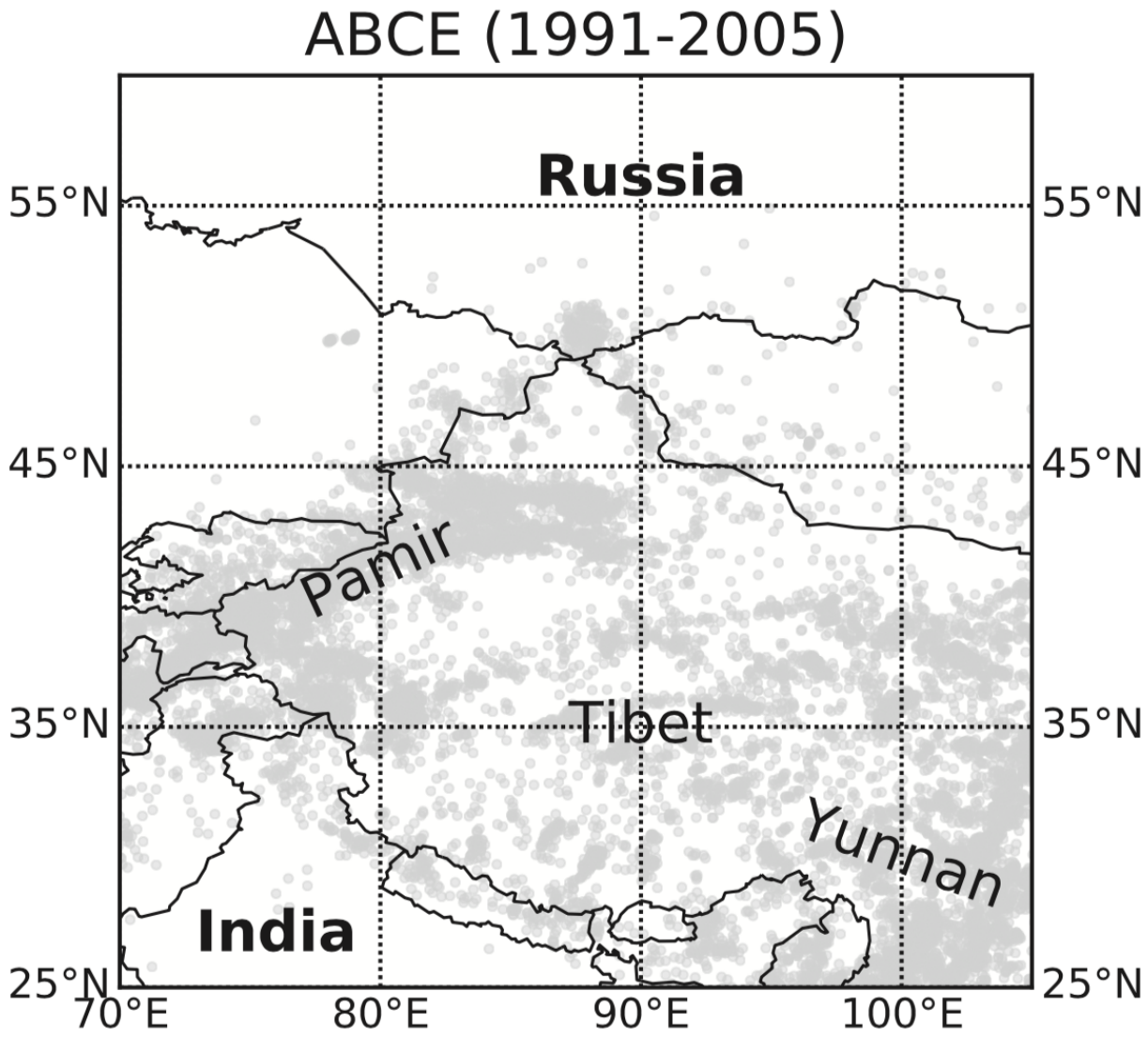

Figure 6.9: Map of Annual Bulletin of Chinese Earthquakes (ABCE) events (1985-2005).

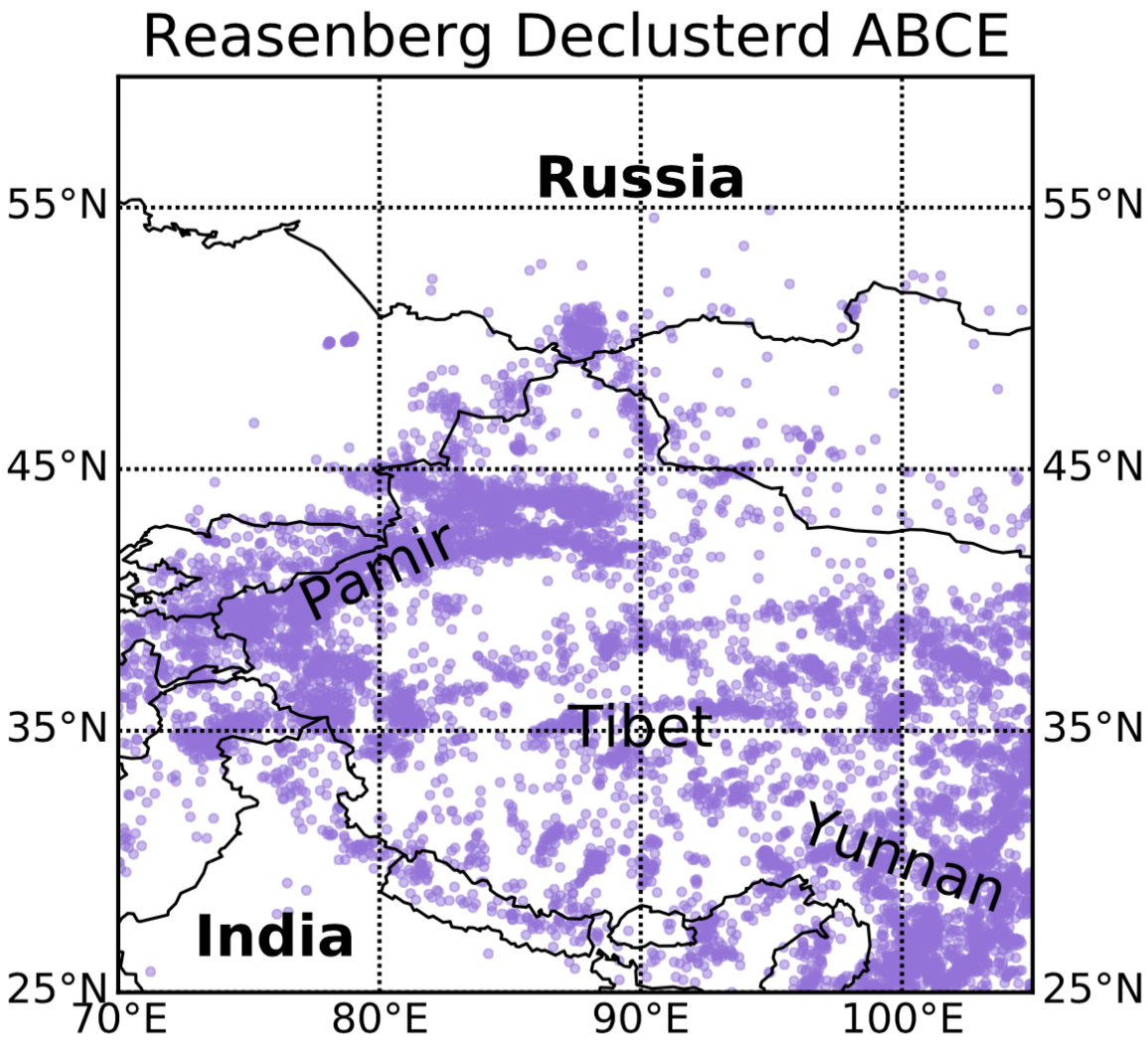

Figure 6.10: Map of Reasenberg declustered ABCE events (1985-2005).

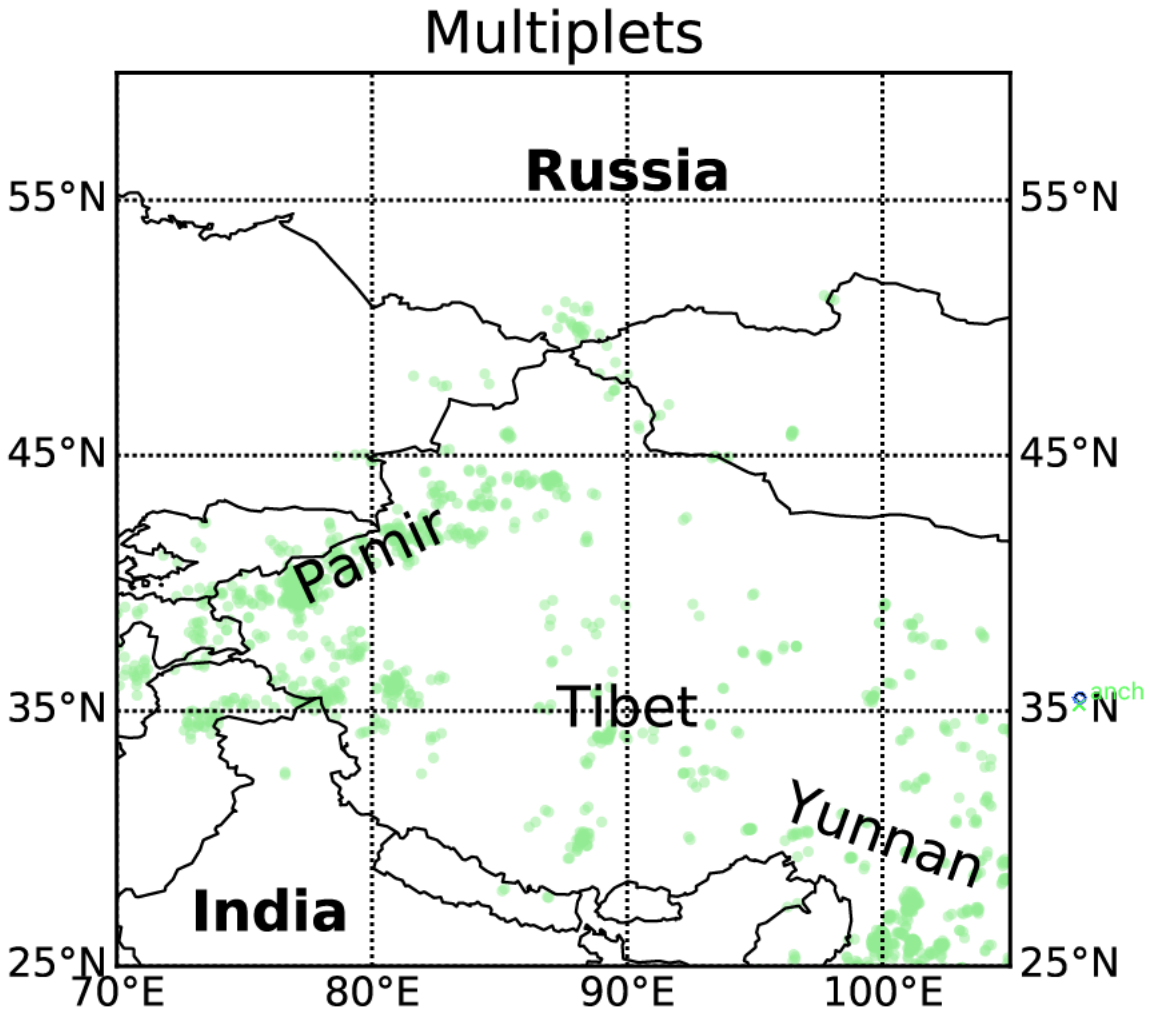

Figure 6.11: Map of Annual Bulletin of Chinese Earthquakes (ABCE) multiplets identified by Schaff and Richards (2004).

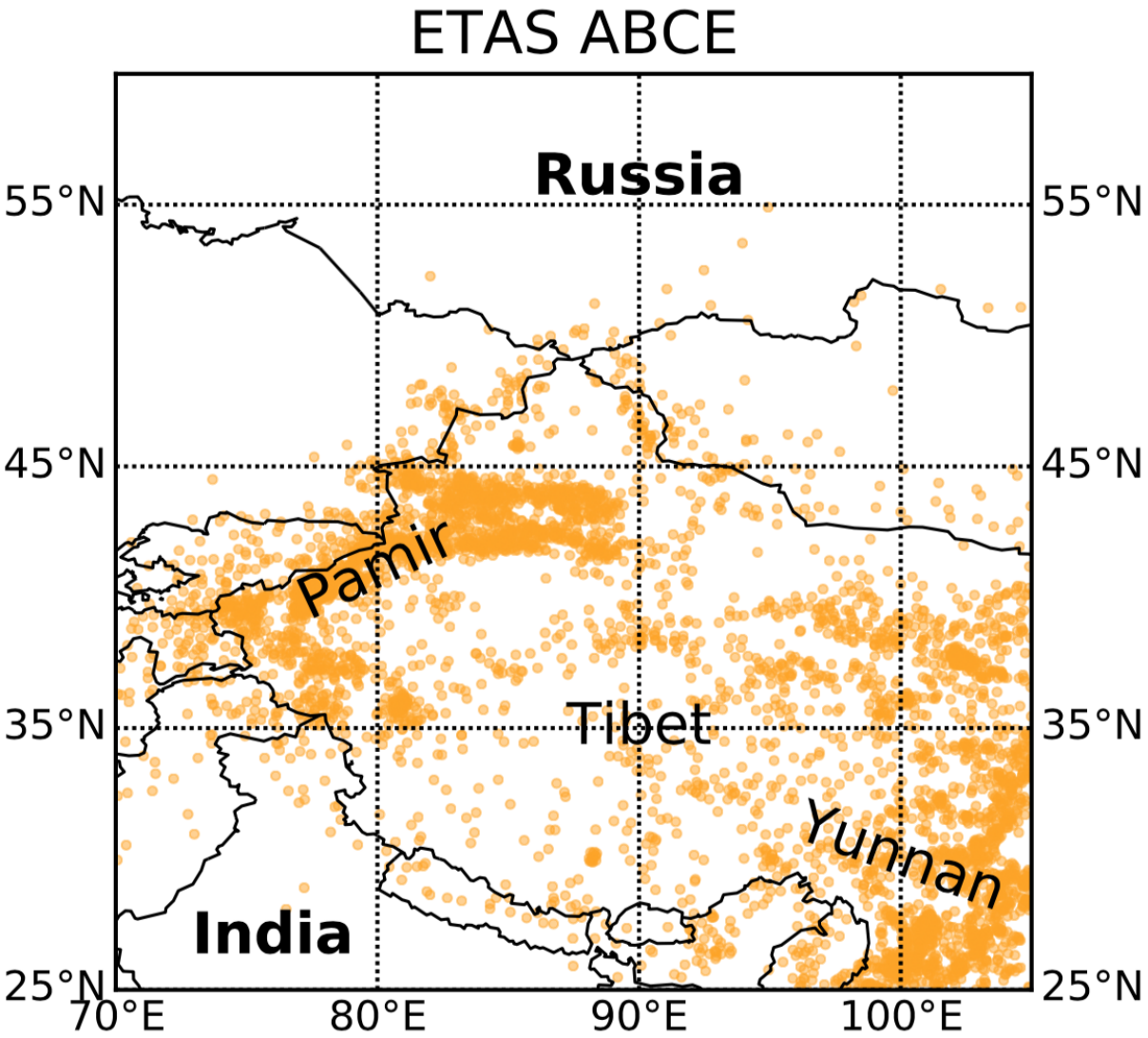

Figure 6.12: Map of ETAS declustered ABCE events (1985-2005).

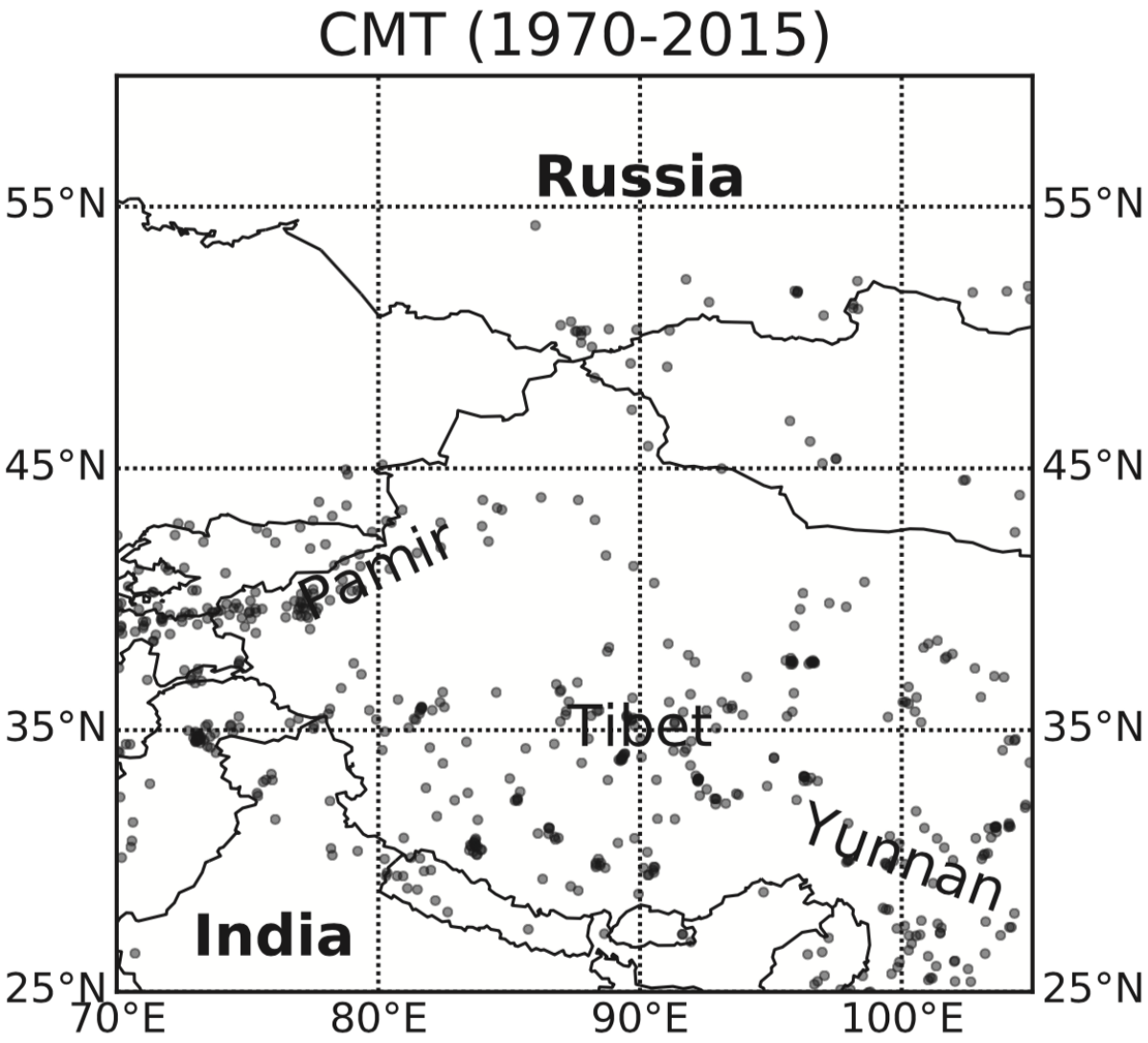

Figure 6.13: Map of Global Centroid-Moment-Tensor(CMT) events (1980-2015).

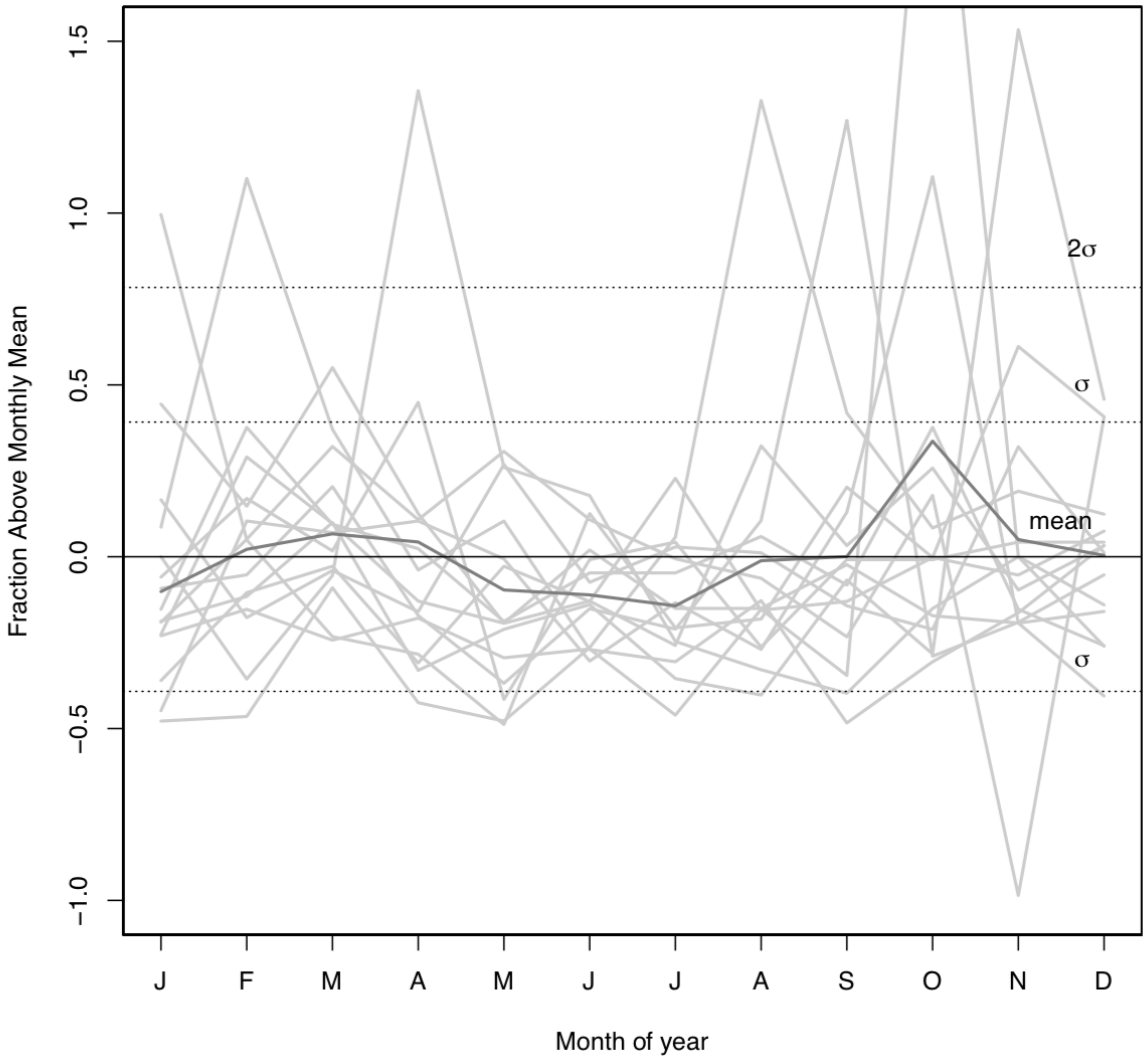

Figure 6.14: Monthly seismicity normalized by the annual average. Light gray lines are 1991-2005 while the dark gray line shows the monthly mean seismicity. The solid horizontal line shows the mean value for all years and dashed lines show standard deviations above and below the mean.

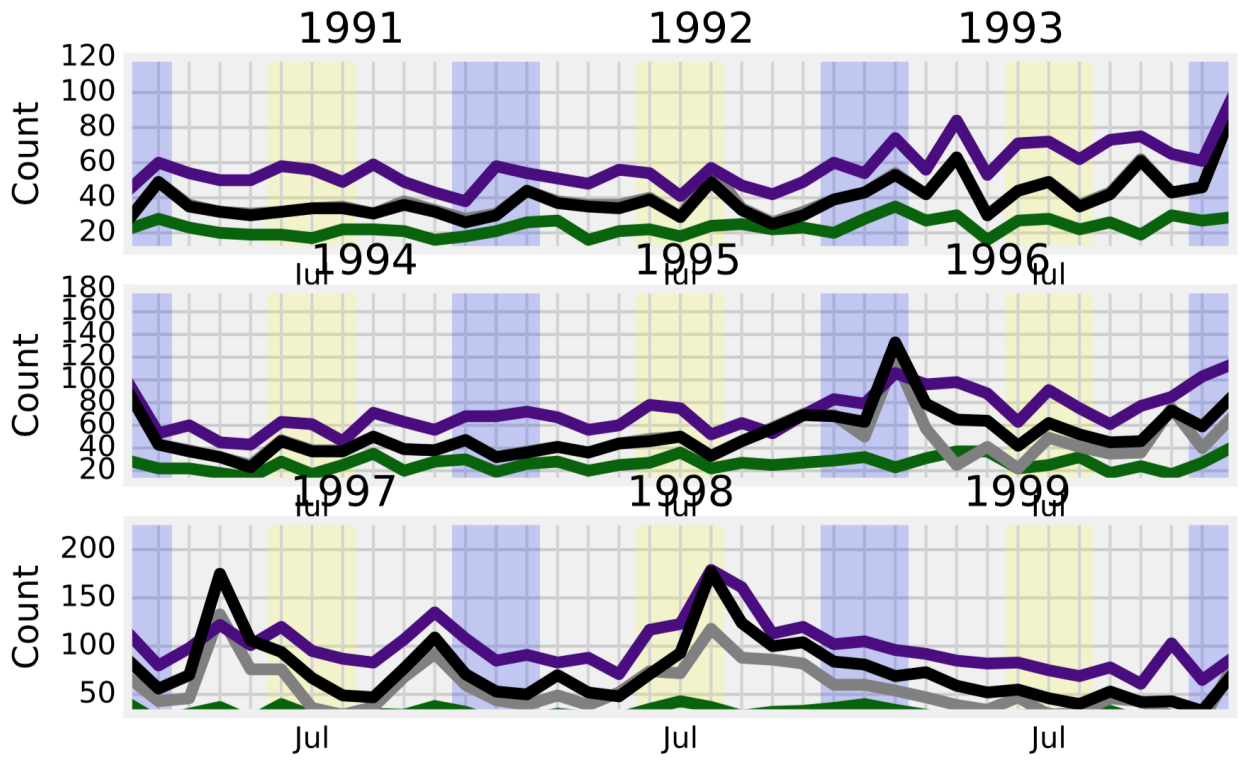

Figure 6.15: Monthly seismicity from 1991-1999. Gray line shows CENC seismicity, black line shows ABCE seismicity, dark green line shows ETAS declustered catalog, dark purple shows Reasenberg declustered catalog using the 'average' values in Supplemental Table 6.2. Blue and yellow vertical lines show winter and summer months respectively.

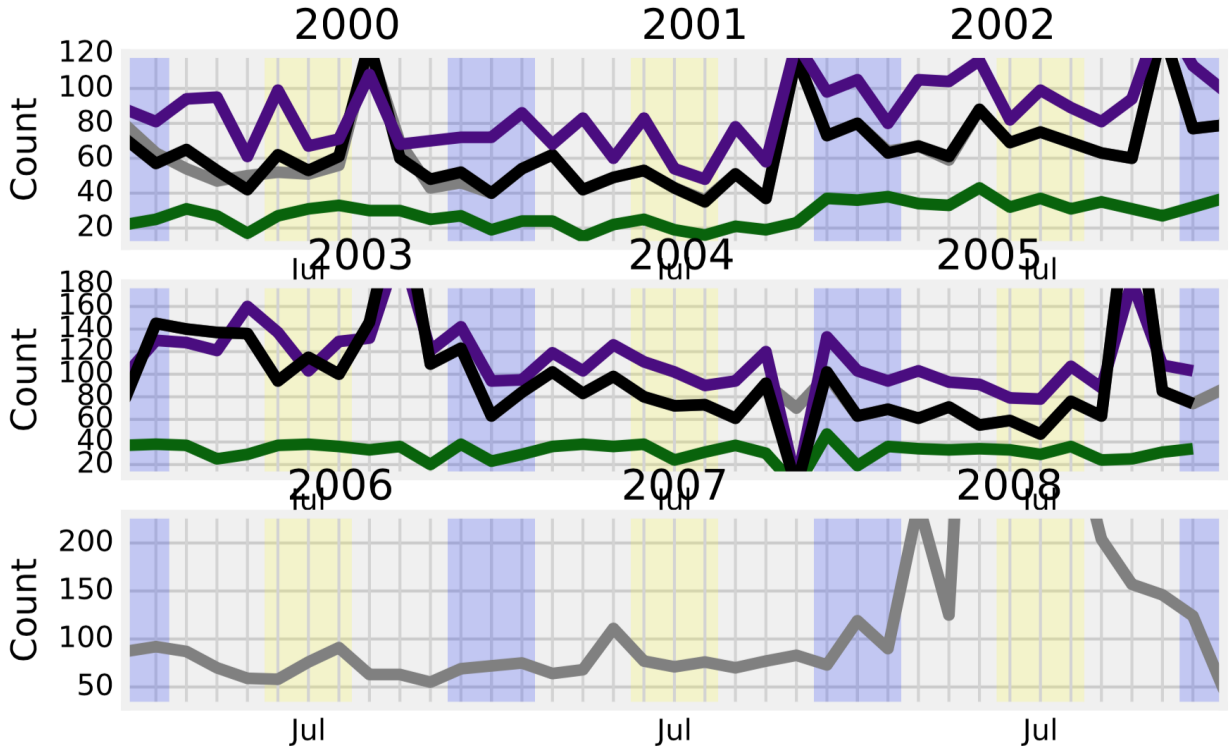

Figure 6.16: Monthly seismicity from 2000-2008. Gray line shows CENC seismicity, black line shows ABCE seismicity, dark green line shows ETAS declustered catalog, dark purple shows Reasenberg declustered catalog using the 'average' values in Supplemental Table 6.2. Blue and yellow vertical lines show winter and summer months respectively.

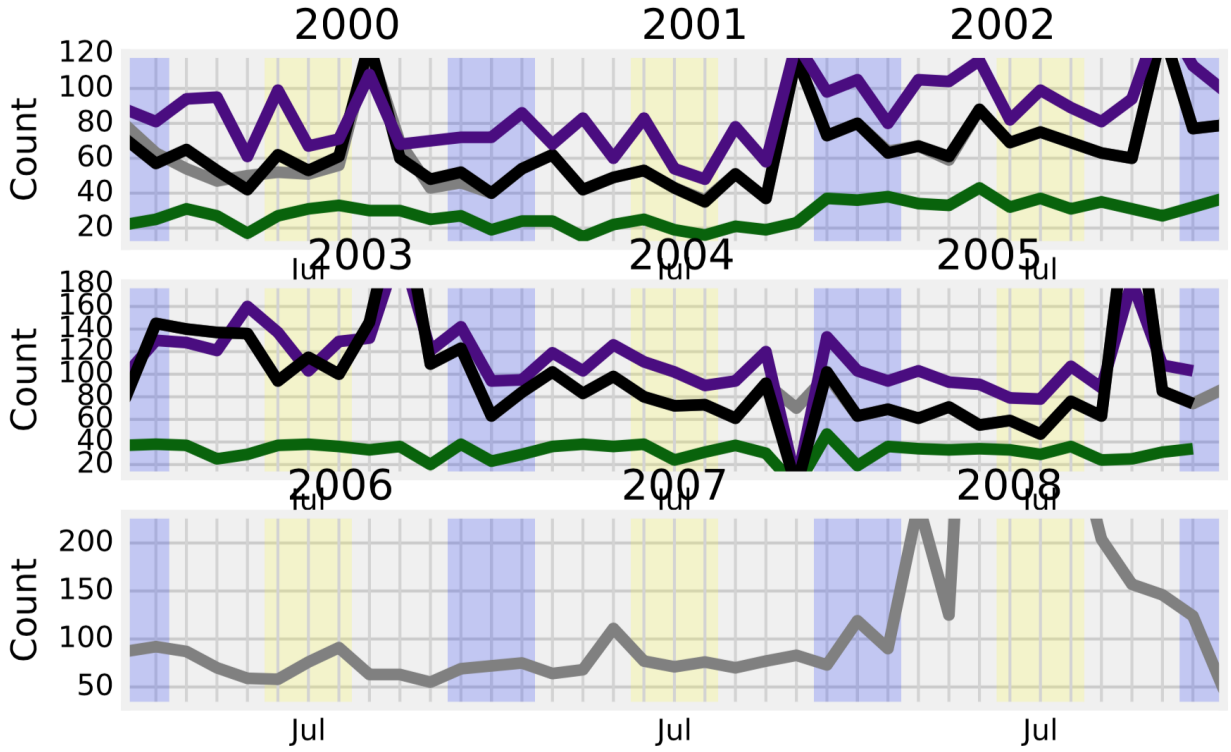

Figure 6.17: Monthly seismicity from 2000-2008. Gray line shows CENC seismicity, black line shows ABCE seismicity, dark green line shows ETAS declustered catalog, dark purple shows Reasenberg declustered catalog using the 'average' values in Supplemental Table 6.2. Blue and yellow vertical lines show winter and summer months respectively.

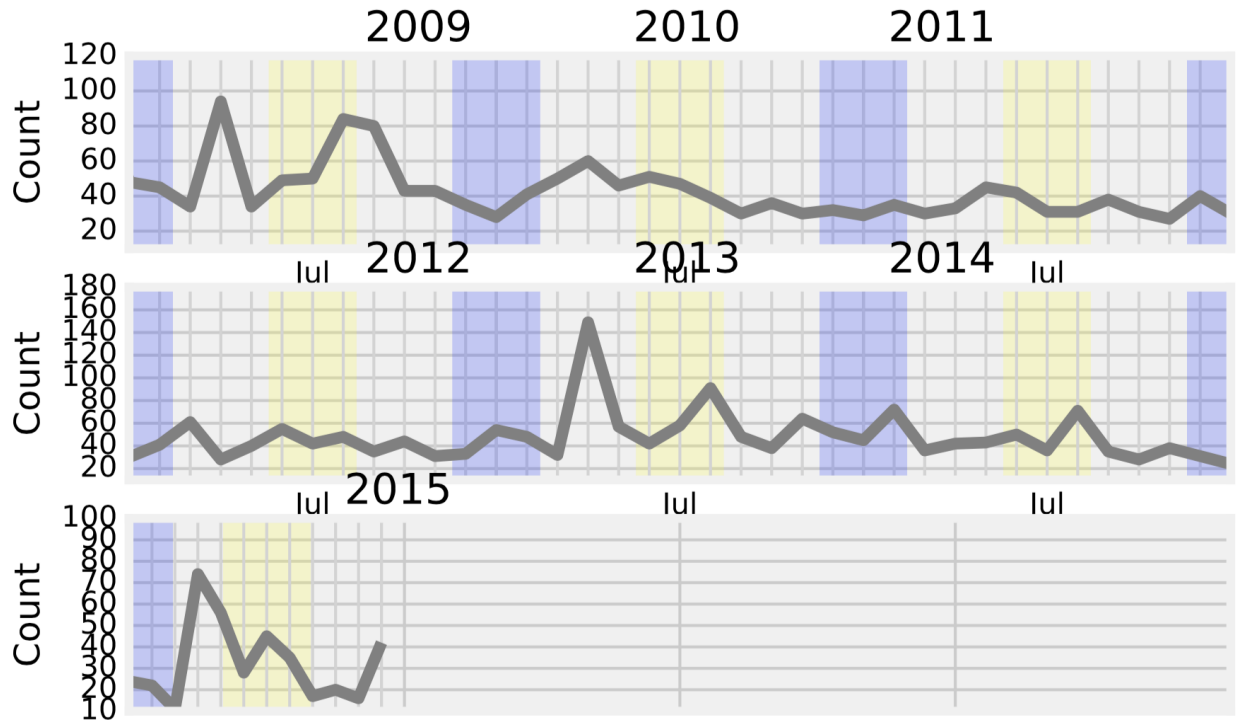

Figure 6.18: Monthly seismicity from 2009-2015. Gray line shows CENC seismicity, black line shows ABCE seismicity, dark green line shows ETAS declustered catalog, dark purple shows Reasenberg declustered catalog using the 'average' values in Supplemental Table 6.2. Blue and yellow vertical lines show winter and summer months respectively.

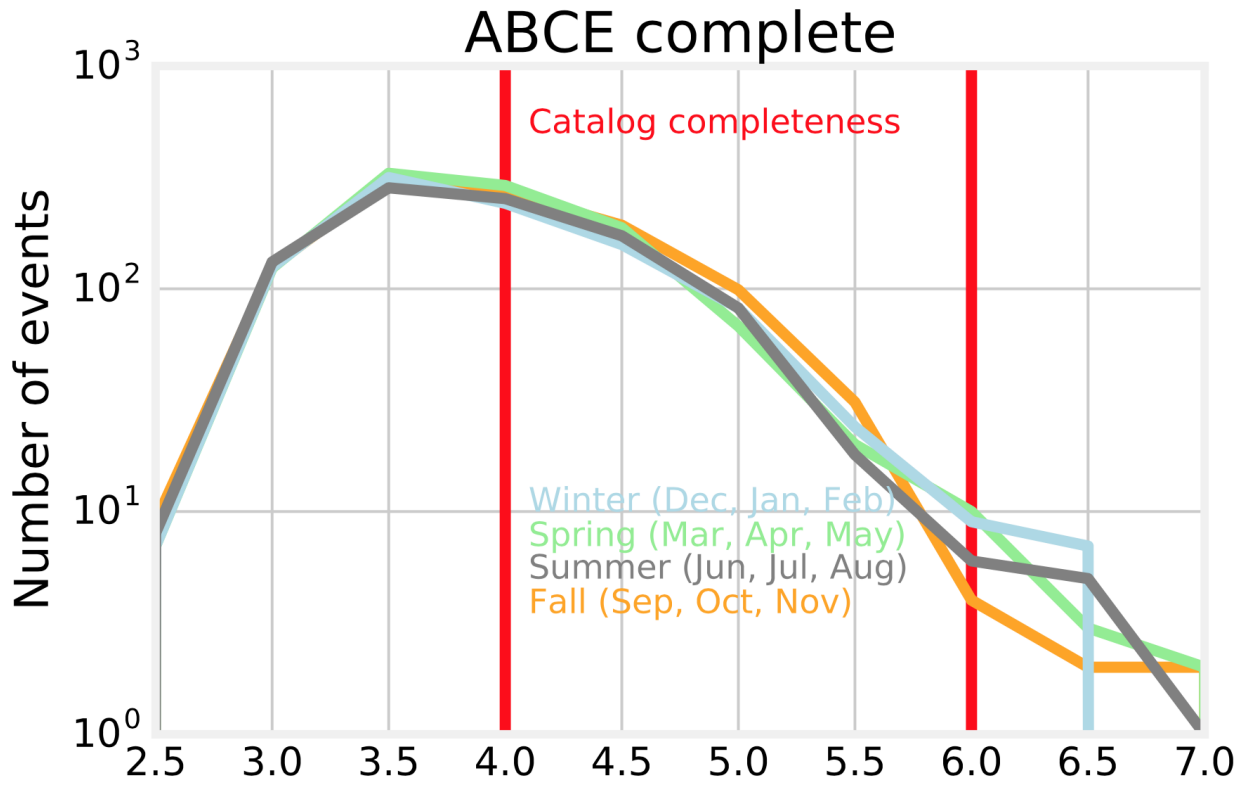

Figure 6.19: Gutenberg-Richter plot for ABCE catalog 1985-2005. Spring is a bin of March, April, May; Summer is a bin of May, June, Jul, Fall is a bin of August, September, October; and Winter is a bin of December, January, February.

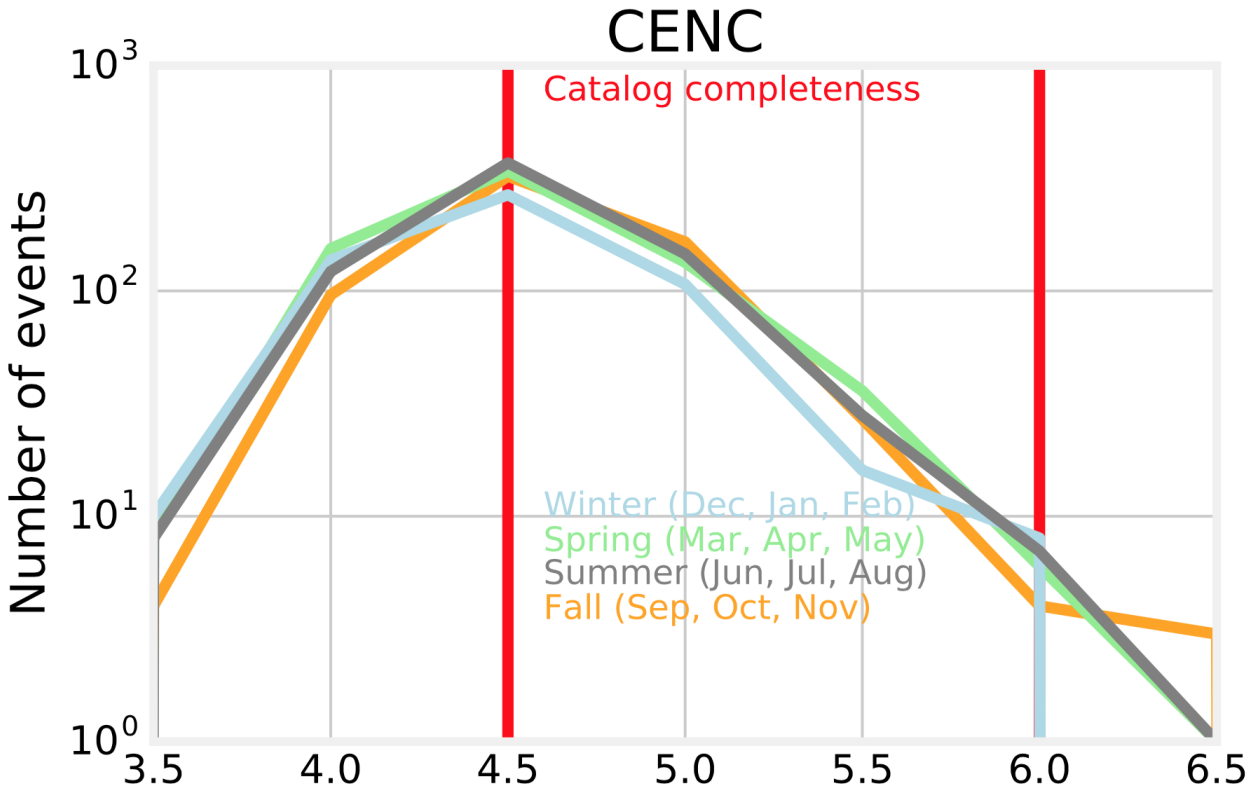

Figure 6.20: Gutenberg-Richter plot for CENC catalog 1970-2015. Spring is a bin of March, April, May; Summer is a bin of May, June, Jul, Fall is a bin of August, September, October; and Winter is a bin of December, January, February.

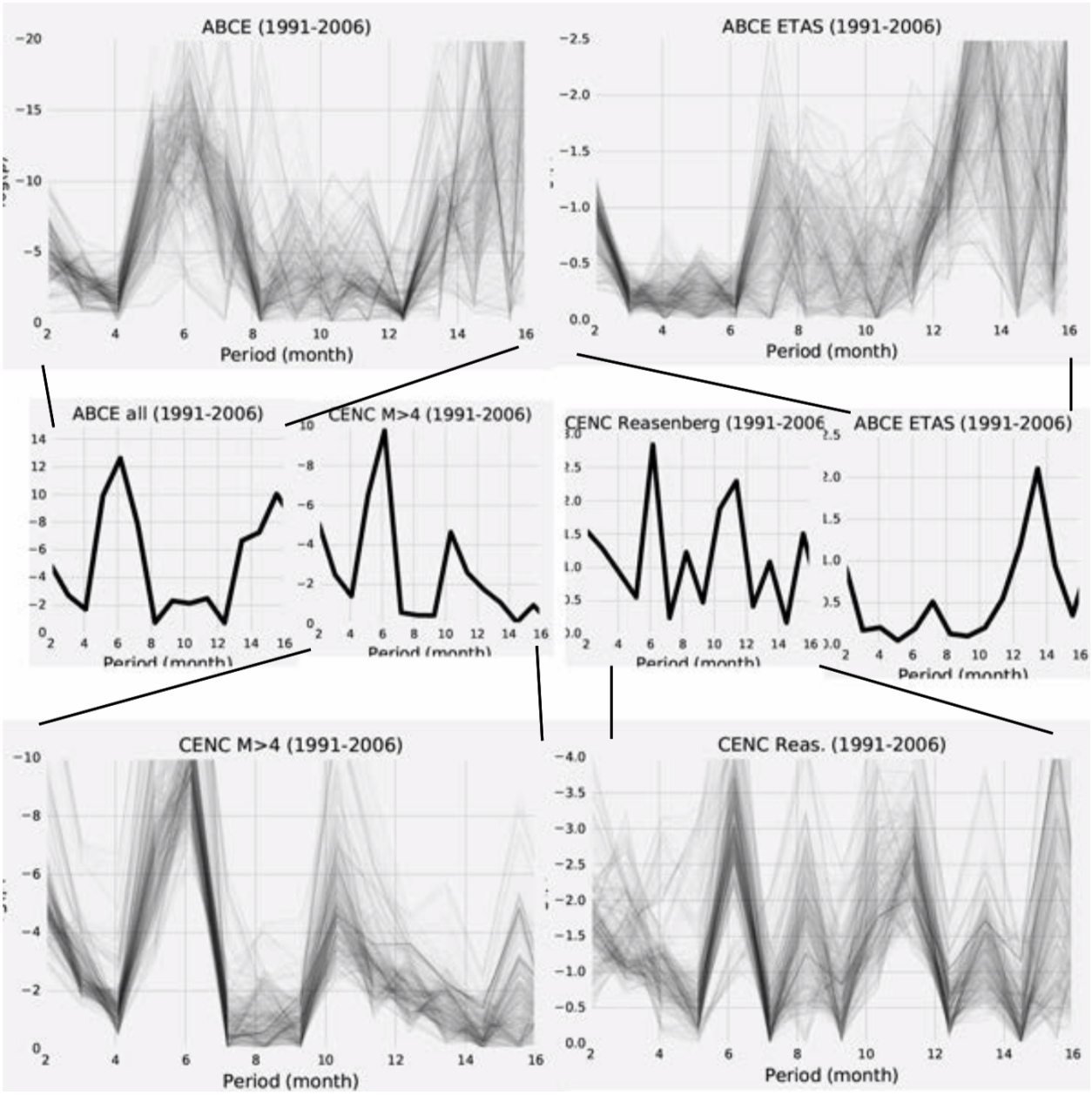

Figure 6.21: Central plots show schuster spectra for complete and declustered catalogs. The robustness of these spectra is shown by bootstrapping one thousand times through the time series by arbitrarily removing 1 or 2 months from the time series.

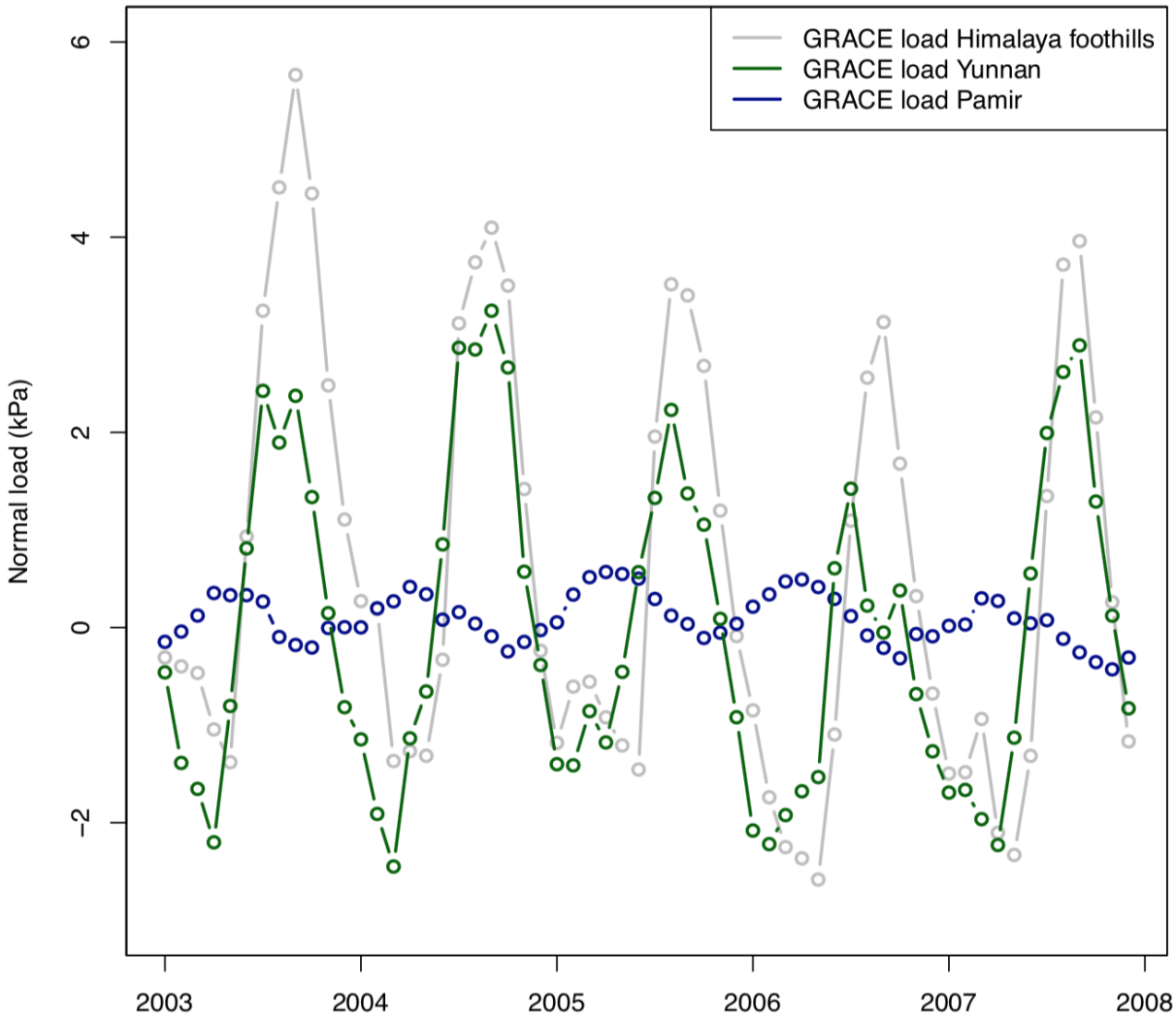

Figure 6.22: Monthly water load from GRACE for the Himalayan foothills, Yunnan, and the Pamir.

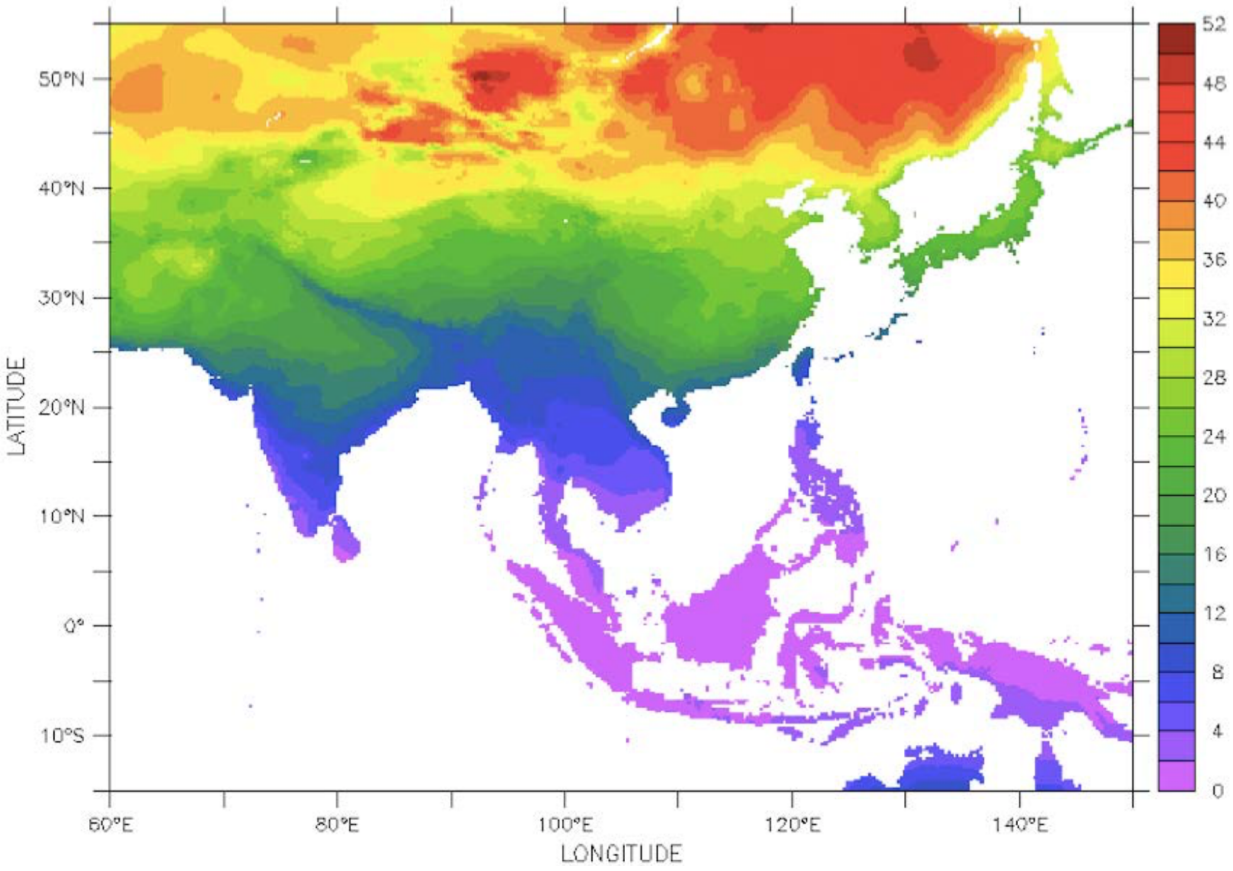

Figure 6.23: Annual changes in surface temperature recorded by NOAA GSOD.

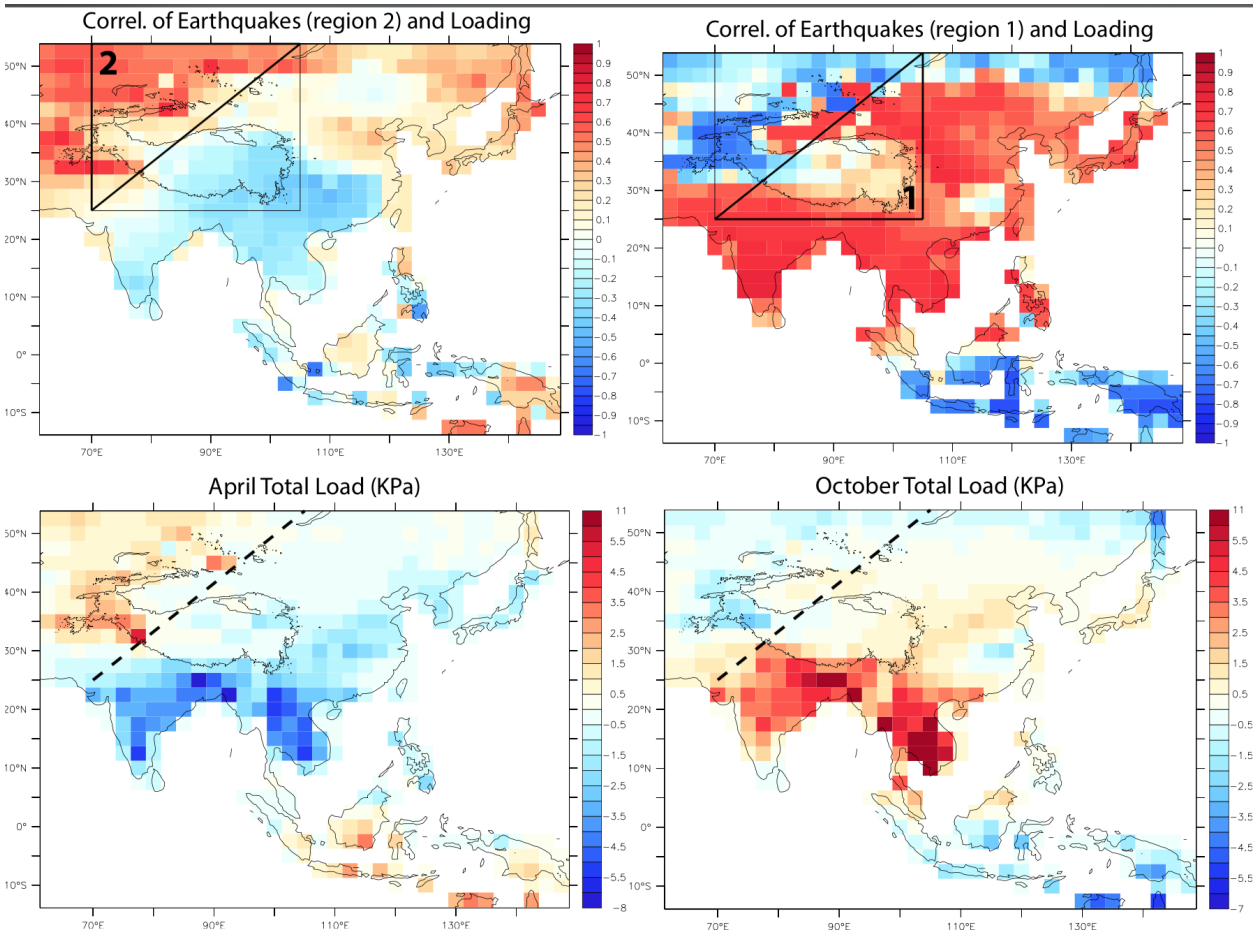

Figure 6.24: Annual changes in atmospheric pressure as recorded by NOAA GSOD added to annual changes in GRACE load. The top row focuses on the climate in to northwest of the plateau labeled Pamir while the bottom row focuses on the more monsoon climate labeled Yunnan. The first column shows estimated average surface load from GRACE load and atmospheric pressure for April, the month of peak loading in Pamir, and October, the month of peak loading in Yunnan. The second column shows the Pearson product-moment cross correlation coefficient of atmospheric pressure and GRACE data with seismicity above and below the solid line. Red regions have an annual loading cycle that correlates with the seismicity in Pamir (top middle)or Yunnan (bottom middle.)

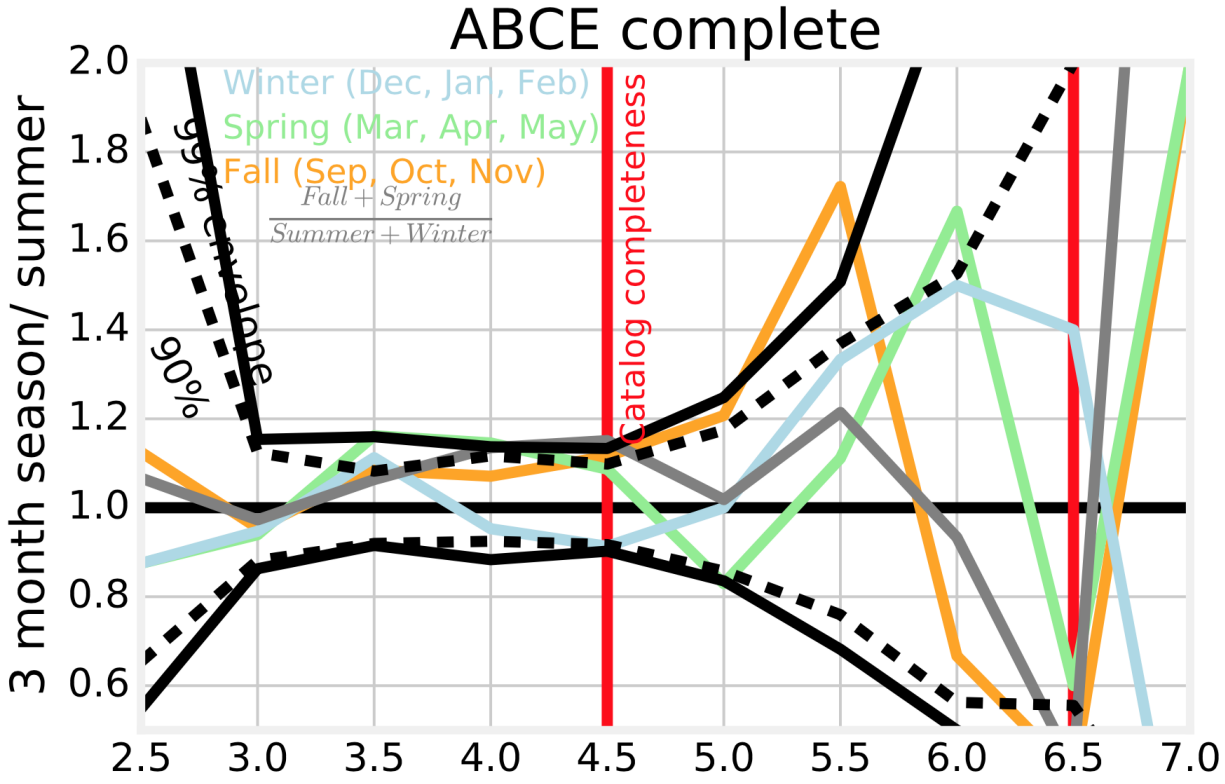

Figure 6.25: After Bollinger et al. (2007) Fig. 3b for the complete ABCE catalog (1985-2005). Red ver- tical lines show catalog completeness. The solid curves are the fall/summer ratios that contain 99% of the fall/summer ratios derived from 1000 random catalogs with an identical range of magnitudes. The solid curves are the fall/summer ratios that contain 90% of the fall/summer ratios derived from 1000 random cat- alogs with an identical range of magnitudes. Curves are normalized to summer seismicity. Suggesting that modulation of higher magnitude events in the fall is most likely to be a true signal for larger magnitude events.

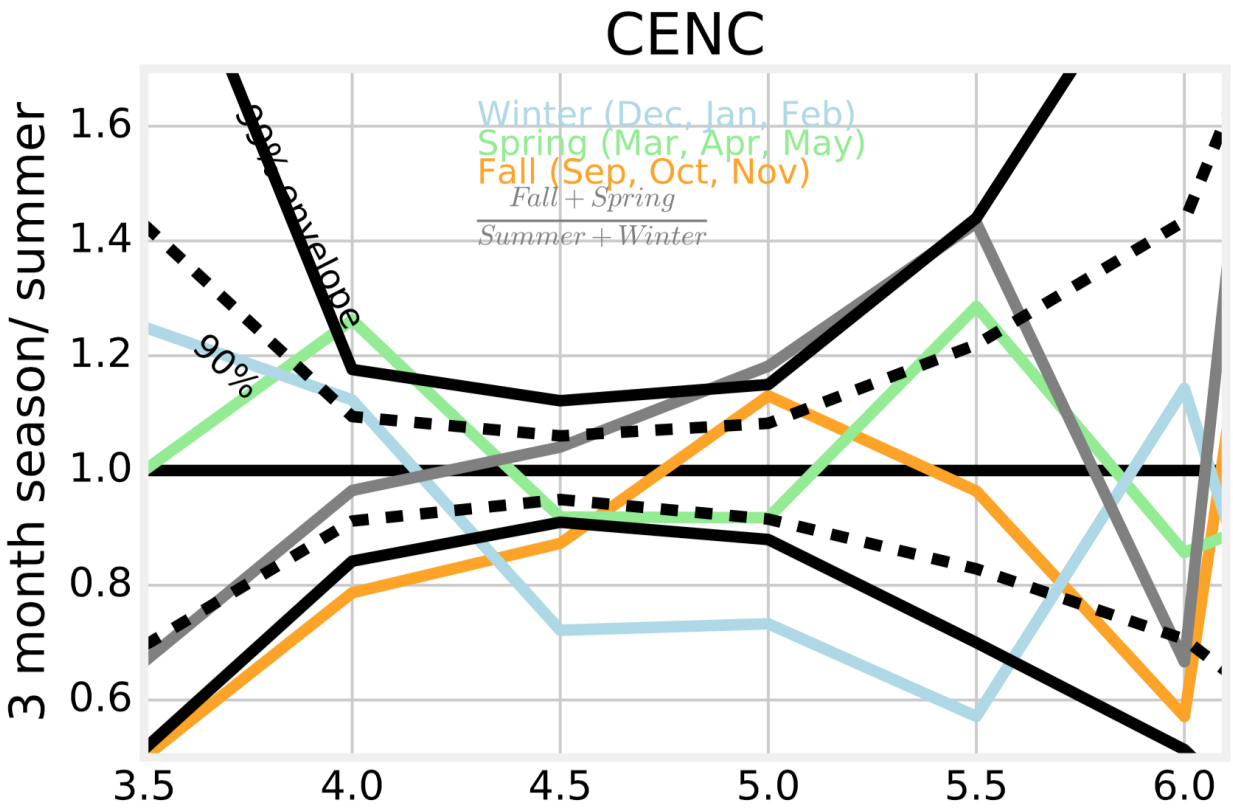

Figure 6.26: After Bollinger et al. (2007) Fig. 3b for the complete CENC catalog (1970-2015). Red ver- tical lines show catalog completeness. The solid curves are the fall/summer ratios that contain 99% of the fall/summer ratios derived from 1000 random catalogs with an identical range of magnitudes. The solid curves are the fall/summer ratios that contain 90% of the fall/summer ratios derived from 1000 random cat- alogs with an identical range of magnitudes. Curves are normalized to summer seismicity. Suggesting that modulation of lower magnitude events in the spring and winter are more likely to be significant..

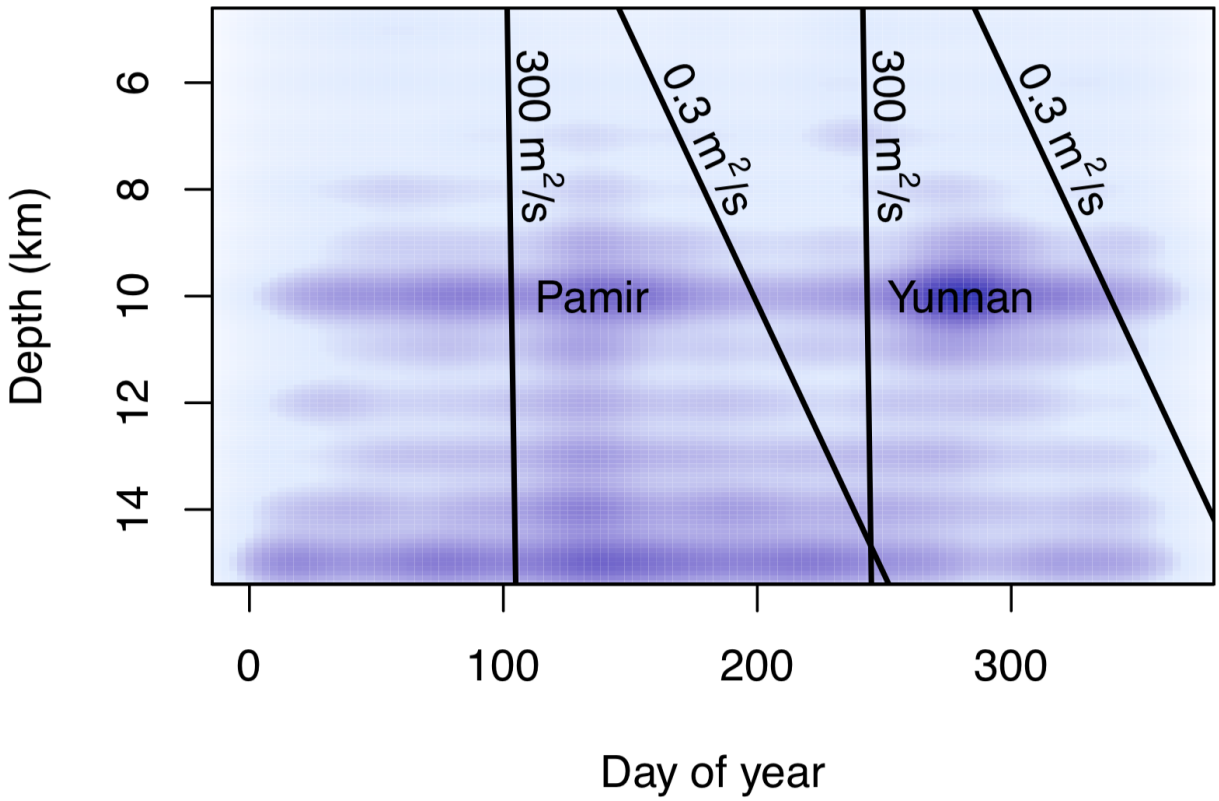

Figure 6.27: Heat map of seismicity from including ABCE events from1991-2005 and CENC events from 2009-2014. Dark purple is equivalent 4 x 10^{-4} events per day while white is equivalent to 1 x 10^{-4} events per day. Black lines show the propagation of pore pressures calculated from peak loading in Pamir and Yunnan for the range of hydraulic diffusivities for fractured crystalline rock (Roeloffs, 1996).

Table 6.2: Table of values used for Reasenberg declustering from van Stiphout et al. (2012).

Parameter	Standard	Weak	Strong	Description
τ_{min}	1	0.5	2.5	the minimum look-ahead time in days for building clusters
τ_{max}	10	3	15	the maximum value of the look-ahead time for building clusters
p1	0.95	0.9	0.99	probability of detecting the next clustered event used to compute M
x_k	0.5	0	1	increase in the lower cut-off magnitude during clusters
x_{meff}	1.5	1.6	1.8	cutoff magnitude (effective magnitude)
r_{fact}	10	5	20	number of crack radii from an EQ for an event to be considered part of the cluster

Chapter 7

Conclusions

Groundwater regulates the transmission of energy and mass through the shallow crust. Understanding tectonic processes is, in part, the understanding of this groundwater regulation– its ability to cause or suppress slip on faults or volcanic eruptions. To illustrate the opportunities for groundwater to regulate tectonics, consider a single volcanic eruption. As magma accumulates it heats groundwater increasing the pore pressure triggering a flank collapse and an eruption. Alternatively, the magma loses its volatiles to the groundwater system, suppressing that eruption. Superimposed on these internal processes, rain and snow cyclically change the pore pressure within the volcano and distant earthquakes change groundwater pressure triggering other earthquakes and possible eruptions.

In this dissertation, I examine both how groundwater can cause these changes in tectonic systems and how tectonic processes affect groundwater. This dissertation comprises five studies at three field sites where, motivated by new observations, I developed quantitative models of how groundwater and tectonics interact. In particular, I have focused on the response of coupled tectonic-hydrologic systems to periodic forcings such as the hydrologic cycle (Chapters 5 and 6) or seismic waves (Chapters 3, 4, and 5) and the emergent patterns that reflect physical processes. This work has been enabled by the development of new tools including 1) data from satellites which provide unprecedented statiotemporal resolution of earth processes, 2) signal processing methods identify previously invisible changes in time series, particularly seismic data, 3) dense hydrologic monitoring networks, and 4) advances in computation to numerically test hypotheses.

Below I briefly return to the overarching questions of this dissertation before discussing unanswered questions that persist and future directions for this work.

How do tectonic processes affect distant groundwater? Earthquakes sometimes increase permeability (Chapter 4 and 5) mixing water between deep and shallow reservoirs (Chapter 4). Rayleigh waves can dilate fractures pumping water into faults or fractures and away from wells (Chapter 3). These interactions can extend thousands of kilometers from earthquake epicenters and require mechanisms for small stresses to resonate and amplify. We find resonances form between tectonic forces and hydrologic systems by changing pore pressure in dilating fractures (Chapter 3), boiling fronts (Chapter 4), and fault zones (Chapter

5 and 6).

How are volcanic eruptions and earthquakes triggered? The resonances between tectonics and hydrology also cause changes on faults and in volcanoes. I found that patterns due to boiling regulate volcanic cooling and, possibly, hydrothermal explosions (Chapter 2). I also found that coincindent with changes in groundwater wells, faults within Long Valley Caldera and Mammoth Mountain appeared to slip. I suggest that earthquakes may also be triggered by Rayleigh waves pumping water from reservoirs into dilated fractures (Chapter 3). Seasonal loads modulate seismicity and aseismic slip and we suggest that the new observations we provide are most consistent with pore pressure diffusion rather than simply elastic loading of the crust (Chapters 5 and 6). Because slip is modulated by pore pressure, depth of this modulation is partly controlled by the fault zone permeability which, in turn, changes after earthquakes (Chapter 5).

Each quantitative model proposed within these case studies should be testable both in other tectonic settings and controlled lab and numerical experiments. While each study site considered in the thesis was chosen to best illustrate and constrain processes that are widespread, questions remain as to why the features we observe are not more common or more easily observed at other settings. For example, why are columns of hydrothermal alteration rare in volcanic deposits and why is dynamically triggered seismicity only observed in geothermal settings? In many cases, future work on these questions will require dense monitoring of hydrologic and tectonic systems and longer time series to understand the diversity of responses. In some cases, additional earthquakes or actively cooling volcanic settings will produce useful future tests of hypotheses and models proposed herein. While each chapter raises its own narrow questions, these studies raise four broader questions on the interaction between hydrology and tectonics.

How do shallow groundwater systems reflect deeper tectonic systems? As with many Earth systems, direct observations of tectonic hydrology are largely limited to the surface. How do these surficial systems reflect deeper processes? We find that at a few kilometers depth triggered earthquakes are coincident with large water level changes and speculate that these phenomena may be due to related underlying processes at different depths. How do changes in geothermal systems reflect intrinsic instability of systems (*e.g.*, Chapter 2 and 3) or more fundamental changes in underlying fault zones or magmatic systems.

How do tectonics and groundwater interact without gravity or seasons driving flow? Much of the groundwater flow considered in this dissertation is driven largely by gravity and seasonal cycles. How do groundwater systems operate on small icy satellites where tides dominate seasons and gravity is low (*e.g.*, Roberts et al., 2015; Choblet et al., 2017)? How do these processes extend to submarine volcanoes and earthquakes where there flow is not driven by gravity and pore pressures are generally high (*e.g.*, Baker et al., 1999; Lauer et al., 2018).

How does tectonics change climate? Volcanic eruptions and fault driven changes in topography also affect climate and the hydrologic cycle (*e.g.*, Molnar and England, 1990). In this dissertation, climate is treated as largely independent modulating slip on faults or

cooling volcanic deposits. However, how do volcanic eruptions change climate and over what time scale (*e.g.*, Robock, 2000; Black et al., 2017)? What role does climate change have in tectonic processes?

What role does tectonic hydrology have on chemical and biological processes? In these studies, chemistry and biology are unlikely to modulate tectonic hydrology at the time scales considered. However, the effects of tectonic hydrology on chemistry and biology may be profound. For example, this dissertation show mixing between deep and shallow fluid reservoirs after earthquakes. How do these transient changes in groundwater chemistry affect larger chemical weathering rates or the habitability of the deep crust?

In conclusion, this dissertation produces rich new datasets including hydrologic responses to earthquakes (Chapters 3, 4, and 5), modulated fault motion (Chapter 3, 5, and 6), and new geologic and geochemical measurements (Chapter 2, 4, and 5). These studies compare these new datasets with recent constraints on hydrologic loads (Chapters 5 and 6) and the broader deformation of the earth's crust (Chapters 3, 4, 5, and 6). I integrate these observations to contribute quantitative models of the tectonic hydrology which focus on the ability of pore pressure diffusion and permeability to change the flow of mass and energy through the crust. This work suggests some ways in which seismic waves can induce changes in water wells or trigger slip on faults. Conversely, this works show some cases in which seasonal hydrologic loads also trigger aseismic and seismic slip. In this chapter, I have also highlighted some broad outstanding questions in the physical processes linking hydrology, volcanism, and fault zones.

Chapter 8

Bibliography

Ader, T. J., Avouac, J.-P. (2013) Detecting periodicities and declustering in earthquake catalogs using the Schuster spectrum, application to Himalayan seismicity. Earth and Planetary Science Letters 377, 97–105.

Adler, R.F., G. H. A. C. R. F. P. X. J. J. B. R. U. S. S. C., Bolvin, D., Gruber, A., Susskind, J., Arkin, P. (2003) The version-2 global precipitation climatology project (GPCP) monthly precipitation analysis (1979-present). J. Hydrometeor. 4, 1147–1167.

Aiken, C. and Peng, Z. (2014). Dynamic triggering of microearthquakes in three geothermal/volcanic regions of California. Journal of Geophysical Research, 119, 6992-7009.

Amos, C., Audet, P., Hammond, W., Bürgmann, R., Johanson, I., Blewitt, G. (2014) Uplift and seismicity driven by groundwater depletion in central California. Nature 509 (7501), 483–486.

Angelier, J. (1986). Geodynamics of Eurasia-Philippine Sea plate boundary: Preface: Tectonophysics, 125.

Argus, D., Fu, Y., Landerer, F. (2014) The global positioning system as a high-resolution technique for evaluating water resources in California. Geophys. Res. Lett. 41, 1971–1980.

Avouac, J. P. (2015). From geodetic imaging of seismic and aseismic fault slip to dynamic modeling of the seismic cycle. Annual Review of Earth and Planetary Sciences, 43, 233-271.

Bai, T., Pollard, D.D., and Gao, H. (2000) Explanation for fracture spacing in layered materials: Nature , v. 403, p. 753–756, https://doi.org/10.1038/35001550.

Bailey, J.E., and Self, S. (2010) The properties and formation of erosional pipe-shaped structures in ignimbrites around the Valles Caldera: Geological Society of America Abstracts

with Programs , v. 42, no. 5, p. 51.

Bailey, R.A., Dalrymple, G.B., and Lanphere, M.A. (1976) Volcanism, structure, and geochronology of Long Valley Caldera, Mono County, California: Journal of Geophysical Research , v. 81, p. 725–744, https://doi.org/10.1029/JB081i005p00725.

Ben-Zion, Y., Leary, P. (1986) Thermoelastic strain in a half-space covered by unconsolidated material. Bulletin of the Seismological Society of America 76 (5), 1447– 1460.

Berryman, J.G. (2007) Seismic waves in rocks with fluids and fractures. Geophysical Journal International, 171, 954-974.

Bettinelli, P., Avouac, J.-P., Flouzat, M., Bollinger, L., Ramillien, G., Rajaure, S., Sapkota, S. (2008) Seasonal variations of seismicity and geodetic strain in the Himalaya induced by surface hydrology. Earth and Planetary Science Letters 266 (3), 332–344.

Bish, D.L., and Aronson, J.L. (1993) Paleogeothermal and paleohydrologic conditions in silicic tuff from Yucca Mountain, Nevada: Clays and Clay Minerals , v. 41, p. 148–161.

Blanchard, F.B. and Byerly, P. (1935). A study of a well gauge as a seismograph. Bulletin of the Seismological Society of America, 25, 313-321.

Bollinger, L., Perrier, F., Avouac, J., Sapkota, S., Gautam, U., Tiwari, D. (2007) Seasonal modulation of seismicity in the himalaya of nepal. Geophys. Res. Lett. 34 (8), L08304–L08304.

Bower, D.R. and Heaton, K.C. (1978). Response of an aquifer near Ottawa to tidal forcing and the Alaskan earthquake of 1964. Canadian Journal of Earth Sciences, 15, 331-340.

Braunmiller, J., Nábêlek, J., Tréhu (2014) A seasonally modulated earthquake swarm near Maupin, Oregon. Geophys. J. Int. 197 (3), 1736–1743.

Brodsky, E.E. and Prejean, S.G. (2005) New constraints on mechanisms of remotely triggered seismicity at Long Valley Caldera. Journal of Geophysical Research, 110(B4).

Brodsky, E.E., Roeloffs, E., Woodcock, D., Gall, I. and Manga, M. (2003) A mechanism for sustained groundwater pressure changes induced by distant earthquakes. Journal of Geophysical Research, 108 (B8).

Candela, T., Brodsky, E.E., Marone, C. and Ellsworth, D. (2014) Laboratory evidence for particle mobilization as a mechanism for permeability enhancement via dynamic stressing. Earth and Planetary Science Letters, 392, 279-291.

Champenois, J., Fruneau, B., Pathier, E., Deffontaines, B., Lin, K. C., & Hu, J. C. (2012). Monitoring of active tectonic deformations in the Longitudinal Valley (Eastern Taiwan) using Persistent Scatterer InSAR method with ALOS PALSAR data. Earth and Planetary Science Letters, 337, 144-155.

Chanard, K., Avouac, J., Ramillien, G., Genrich, J., 2014. Modeling deformation induced by seasonal variations of continental water in the himalaya region:sensitivity to earth elastic structure. J. Geophys. Res. Solid Earth 119 (6), 5097–5113.

Chang, S. H., Wang, W. H., & Lee, J. C. (2009). Modelling temporal variation of surface creep on the Chihshang fault in eastern Taiwan with velocity-strengthening friction. Geophysical Journal International, 176(2), 601-613.

Chao, H. C., You, C. F., & Sun, C. H. (2010). Gases in Taiwan mud volcanoes: chemical composition, methane carbon isotopes, and gas fluxes. Applied Geochemistry, 25(3), 428-436.

Chen, K. H., Nadeau, R. M., & Rau, R. J. (2008). Characteristic repeating earthquakes in an arc-continent collision boundary zone: The Chihshang fault of eastern Taiwan. Earth and Planetary Science Letters, 276(3-4), 262-272.

Cheng, L. W., Lee, J. C., Hu, J. C., & Chen, H. Y. (2009). Coseismic and postseismic slip distribution of the 2003 Mw= 6.5 Chengkung earthquake in eastern Taiwan: Elastic modeling from inversion of GPS data. Tectonophysics, 466(3-4), 335-343.

Ching, K. E., Rau, R. J., & Zeng, Y. (2007). Coseismic source model of the 2003 Mw 6.8 Chengkung earthquake, Taiwan, determined from GPS measurements. Journal of Geophysical Research: Solid Earth, 112(B6).

Choblet, G., Tobie, G., Sotin, C., Běhounková, M., Čadek, O., Postberg, F., & Souček, O. (2017). Powering prolonged hydrothermal activity inside Enceladus. Nature Astronomy, 1(12), 841.

Christiansen, L. B., Hurwitz, S., & Ingebritsen, S. E. (2007). Annual modulation of seismicity along the San Andreas Fault near Parkfield, CA. Geophysical Research Letters, 34(4).

Christiansen, L., Hurwitz, S., Saar, M., Ingebritsen, S., Hsieh, P. (2005) Seasonal seismicity at western united states volcanic centers. Earth and Planetary Science Letters 240 (2), 307–321.

Cochran, E., Vidale, J., Tanaka, S. (2004) Earth tides can trigger shallow thrust fault earthquakes. Science 306, 1164–1166.

Cooper, H.H., Bredehoeft, J.D., Papadopulos, I.S. and Bennett, R.R. (1965). The response of well-aquifer systems to seismic waves. Journal of Geophysical Research, 70, 3915-3926.

Coumou, D., Driesner, T., and Heinrich, C.A. (2008) Heat transport at boiling, near-critical conditions: Geofluids , v. 8, p. 208–215, https://doi.org/10.1111/j.1468-8123.2008.00218.x.

Crews, J. B., & Cooper, C. A. (2014). Experimental evidence for seismically initiated gas bubble nucleation and growth in groundwater as a mechanism for coseismic borehole water level rise and remotely triggered seismicity. Journal of Geophysical Research: Solid Earth, 119(9), 7079-7091.

Crews, J. B., & Rybarski, S. (2017). The role of seismically initiated CO_2 gas bubble growth in groundwater. USGS Final Technical Report, USGS NEHRP G15AP00058.

Davis, J., Elósegui, P., Mitrovica, J., Tamisiea, M. (2004) Climate-driven deformation of the solid earth from grace and gps. Geophysical Research Letters 31 (24).

Dutilleul, P., Johnson, C. W., Bürgmann, R., Wan, Y., Shen, Z.-K. (2015) Multi- frequential periodogram analysis of earthquake occurrence: An alternative approach to the schuster spectrum, with two examples in central california. Journal of Geophysical Research: Solid Earth.

Elkhoury, J.E., Brodsky, E.E. and Agnew, D.C. (2006). Seismic waves increase permeability. Nature, 441, 1135-1138.

Evans, W.C., Hurwitz, S., Bergfeld, D., Howle, J.F. (2018). Hot water in the Long Valley Caldera - The benefits and hazards of this large natural resource, U.S. Geological Survey Fact Sheet, 2018-3009, doi: 10.3133/fs20183009.

Feng, H., Liu, C. Y., Chuang, P. Y., & Chia, Y. (2016, December). Groundwater Level Changes Induced by the 2016 Meinong Earthquake. In AGU Fall Meeting Abstracts.

Fu, Y., Freymueller, J., 2012. Seasonal and long-term verical deformation in nepal himalaya constrained by gps and grace measurements. J. Geophys. Res. 117, B03407– B03407.

Fukuda, J. I., Kato, A., Kato, N., & Aoki, Y. (2013). Are the frictional properties of creeping faults persistent? Evidence from rapid afterslip following the 2011 Tohoku-oki earthquake. Geophysical Research Letters, 40 (14), 3613-3617.

Fulton, P. M., Brodsky, E. E., Kano, Y., Mori, J., Chester, F., Ishikawa, T., ... & Toczko, S. (2013). Low coseismic friction on the Tohoku-Oki fault determined from temperature measurements. Science, 342(6163), 1214-1217.

Gao, S. S., Silver, P. G., Linde, A. T., Sacks, I. S. (2000) Annual modulation of triggered seismicity following the 1992 landers earthquake in california. Nature 406 (6795), 500–504.

Geballe, Z.M., Wang, C.Y. and Manga, M. (2011). A permeability-change model for water-level changes triggered by teleseismic waves. Geofluids, 11, 302-308.

Hainzl, S., Ben-Zion, Y., Cattania, C., & Wassermann, J. (2013). Testing atmospheric and tidal earthquake triggering at Mt. Hochstaufen, Germany. Journal of Geophysical Research: Solid Earth, 118(10), 5442-5452.

Hainzl, S., Kraft, T., Wassermann, J., Igel, H., & Schmedes, E. (2006). Evidence for rainfall-triggered earthquake activity. Geophysical Research Letters, 33(19).

Hainzl, S., Kraft, T., Wassermann, J., Igel, H., Schmedes, E. (2006) Evidence for rainfall-triggered earthquake activity. Geophys. Res. Lett. 33, L19303–L19303.

Heki, K. (2003). Snow load and seasonal variation of earthquake occurrence in Japan. Earth and Planetary Science Letters, 207(1-4), 159-164.

Heki, K. (2003) Snow load and seasonal variation of earthquake occurrence in Japan. Earth Planet. Sci. Lett 207 (10), 159–164.

Hildreth, W. (2017). Fluid-driven uplift at Long Valley Caldera, California: geologic perspectives. Journal of Volcanology and Geothermal Research, 341, pp.269-286.

Hildreth, W. and Fierstein, J. (2017). Geologic field-trip guide to Long Valley Caldera, California (No. 2017-5022-L). US Geological Survey.

Hildreth, W., and Wilson, C.J., 2007, Compositional zoning of the Bishop Tuff: Journal of Petrology , v. 48, p. 951–999, https://doi.org/10.1093/petrology/egm007.

Hildreth, W., Fierstein, J. and Calvert, A. (2017). Early postcaldera rhyolite and structural resurgence at Long Valley Caldera, California. Journal of Volcanology and Geothermal Research, 335, pp.1-34.

Hill, D.P. (2012). Dynamic stresses, Coulomb failure, and remote triggering—Corrected. Bulletin of the Seismological Society of America, 102, 2313-2336.

Hill, D.P. (2017). Long Valley Caldera-Mammoth Mountain Unrest: The Knowns and The Unknowns. Elements, 13, 8-9.

Hill, D.P., et al. (1993). Seismicity remotely triggered by the magnitude 7.3 Landers, California earthquake. Science, 1617-1623.

Hill, D.P., Johnston, M.J., Langbein, J.O. and Bilham, R. (1995). Response of Long Valley caldera to the Mw= 7.3 Landers, California, earthquake. Journal of Geophysical Research, 100, 12985-13005.

Hogeweg, N., Keith, T.E.C., Colvard, E.M., and Ingebritsen, S.E. (2005) Ongoing hydrothermal heat loss from the 1912 ash-flow sheet, Valley of Ten Thousand Smokes, Alaska: Journal of Volcanology and Geothermal Research , v. 143, p. 279–291, https://doi.org/10.1016/j.jvolgeores.2004.12.003.

Holt, E.W., and Taylor, H.P., 1998, 18O/16O mapping and hydrogeology of a short-lived ($\approx$ 10 years) fumarolic ($>$ 500° C) meteoric-hydrothermal event in the upper part of the 0.76 Ma Bishop Tuff outflow sheet, California: Journal of Volcanology and Geothermal Research , v. 83, p. 115–139, https://doi.org/10.1016/S0377-0273(98)00014-6.

Howell Jr, B. F. (2005). An introduction to seismological research: History and development. Cambridge University Press.

Howle, J.F. and Farrar, C.D. (1996). Hydrologic Data for Long Valley Caldera, Mono County, California, 1987-93 (No. 96-382). US Geological Survey; Open-File Report, 96-382, doi: 10.3133/ofr96382.

Hsieh, P. A., Bredehoeft, J. D., & Rojstaczer, S. A. (1988). Response of well aquifer systems to earth tides: Problem revisited. Water Resources Research, 24(3), 468-472.

Hsu, L., & Bürgmann, R. (2006). Surface creep along the Longitudinal Valley fault, Taiwan from InSAR measurements. Geophysical research letters, 33(6).

Hsu, Y. J., Yu, S. B., & Chen, H. Y. (2009). Coseismic and postseismic deformation associated with the 2003 Chengkung, Taiwan, earthquake. Geophysical Journal International, 176(2), 420-430.

Hsu, Y.-J., Chang, Y.-S., Liu, C.-C., Lee, H.-M., Linde, A. T., Sacks, S., Kitagawa, G., Chen, Y., 2015. Revisiting borehole strain, typhoons and slow earthquakes using quantitative estimates of precipitation induced strain changes. Journal of Geophysi- cal Research: Solid Earth.

Hu, J. C., Angelier, J., Lee, J. C., Chu, H. T., & Byrne, D. (1996). Kinematics of convergence, deformation and stress distribution in the Taiwan collision area: 2-D finite-element

numerical modelling. Tectonophysics, 255(3-4), 243-268.

Hu, J. C., Cheng, L. W., Chen, H. Y., Wu, Y. M., Lee, J. C., Chen, Y. G., ... & Yu, S. B. (2007). Coseismic deformation revealed by inversion of strong motion and GPS data: the 2003 Chengkung earthquake in eastern Taiwan. Geophysical Journal International, 169(2), 667-674.

Huang, B. S., Huang, W. G., Huang, Y. L., Kuo, L. C., Chen, K. C., & Angelier, J. (2009). Complex fault rupture during the 2003 Chengkung, Taiwan earthquake sequence from dense seismic array and GPS observations. Tectonophysics, 466(3-4), 184-204.

Hurwitz, S. and Johnston, M.J. (2003). Groundwater level changes in a deep well in response to a magma intrusion event on Kilauea Volcano, Hawai'i. Geophysical Research Letters, 30(22).

Hurwitz, S., Farrar, C.D., Williams, C.F. (2010). The Thermal regime in the Resurgent Dome of Long Valley Caldera, California, Inferences from precision temperature logs in deep wells, Journal of Volcanology and Geothermal Research, 198, 233-240.

Husen, S., Taylor, R., Smith, R. B., & Healser, H. (2004). Changes in geyser eruption behavior and remotely triggered seismicity in Yellowstone National Park produced by the 2002 M 7.9 Denali fault earthquake, Alaska. Geology, 32(6), 537-540.

Ingebritsen, S. E., Shelly, D. R., Hsieh, P. A., Clor, L. E., Seward, P. H., & Evans, W. C. (2015). Hydrothermal response to a volcano-tectonic earthquake swarm, Lassen, California. Geophysical Research Letters, 42(21), 9223-9230.

Ingebritsen, S., Manning, C. E. (1999) Geological implications of a permeability-depth curve for the continental crust. Geology 27 (12), 1107–1110.

Ishii, M., Shearer, P. M., Houston, H., & Vidale, J. E. (2005). Extent, duration and speed of the 2004 Sumatra–Andaman earthquake imaged by the Hi-Net array. Nature, 435(7044), 933.

Jiang, G. J., Angelier, J., Lee, J. C., Chu, H. T., Hu, J. C., & Mu, C. H. (2011) Faulting and Mud Volcano Eruptions Inside of the Coastal Range During the 2003 M w= 6.8 Chengkung Earthquake in Eastern Taiwan. Terrestrial, Atmospheric & Oceanic Sciences, 22(5).

Johnson, C. W., Fu, Y., & Bürgmann, R. (2017). Seasonal water storage, stress modulation, and California seismicity. Science, 356(6343), 1161-1164.

Johnston, M.J.S., Hill, D.P., Linde, A.T., Langbein, J. and Bilham, R. (1995). Transient deformation during triggered seismicity from the 28 June 1992 Mw= 7.3 Landers earthquake at Long Valley volcanic caldera, California. Bulletin of the Seismological Society of America, 85, 787-795.

Jønsson, S., Segall, P., Pedersen, R. and Björnsson, G. (2003). Post-earthquake ground movements correlated to pore-pressure transients. Nature, 424, 179-.

Keating, G.N. (2005) The role of water in cooling ignimbrites: Journal of Volcanology and Geothermal Research , v. 142, p. 145–171, https://doi.org/10.1016/j.jvolgeores.2004.10.019.

Kinoshita, C., Kano, Y., & Ito, H. (2015). Shallow crustal permeability enhancement in central Japan due to the 2011 Tohoku earthquake. Geophysical Research Letters, 42(3), 773-780.

Kipp, K.L., Jr.,Hsieh, P.A., and Charlton, S.R. (2008) Guide to the revised ground-water flow and heat transport simulator: HYDROTHERM—Version 3: U.S. Geological Survey Techniques and Methods 6–A25, 160 p.

Knott, C. (1897) On lunar periodicities in earthquake frequency. Proceedings of the Royal Society of London 60, 457–466.

Landerer, F., Swenson, S. (2012) Accuracy of scaled grace terrestrial water storage estimates. Water Resources Research 48 (4).

Lauer, R. M., Fisher, A. T., & Winslow, D. M. (2018). Three-dimensional models of hydrothermal circulation through a seamount network on fast-spreading crust. Earth and Planetary Science Letters, 501, 138-151.

Le Béon, M., Huang, M. H., Suppe, J., Huang, S. T., Pathier, E., Huang, W. J., ... & Hu, J. C. (2017). Shallow geological structures triggered during the Mw 6.4 Meinong earthquake, southwestern Taiwan. Terr. Atmos. Ocean. Sci, 28, 663-681.

Lee, J. C., Angelier, J., Chu, H. T., Hu, J. C., & Jeng, F. S. (2001). Continuous monitoring of an active fault in a plate suture zone: a creepmeter study of the Chihshang Fault, eastern Taiwan. Tectonophysics, 333(1-2), 219-240.

Lee, J. C., Angelier, J., Chu, H. T., Yu, S. B., & Hu, J. C. (1998). Plate-boundary strain partitioning along the sinistral collision suture of the Philippine and Eurasian plates: Analysis of geodetic data and geological observation in southeastern Taiwan. Tectonics, 17(6), 859-871.

Lee, J. C., Chu, H. T., Angelier, J., Hu, J. C., Chen, H. Y., & Yu, S. B. (2006). Quantitative analysis of surface coseismic faulting and postseismic creep accompanying the 2003, Mw= 6.5, Chengkung earthquake in eastern Taiwan. Journal of Geophysical Research: Solid Earth, 111(B2).

Lee, J. C., Jeng, F. S., Chu, H. T., Angelier, J., & Hu, J. C. (2000). A rod-type creepmeter for measurement of displacement in active fault zone. Earth, Planets and Space, 52(5), 321-328.

Lee, J. C., Liu, Z. Y. C., & Shirzaei, M. (2018, December). Depth variations of fault friction parameter derived from dynamic modeling of GPS afterslip associated with the 2003 Mw 6.5 Chengkung earthquake in eastern Taiwan. In AGU Fall Meeting Abstracts.

Lee, M., Liu, T. K., Ma, K. F., & Chang, Y. M. (2002). Coseismic hydrological changes associated with dislocation of the September 21, 1999 Chichi earthquake, Taiwan. Geophysical Research Letters, 29(17), 5-1.

Liao, X., Wang, C. Y., & Liu, C. P. (2015). Disruption of groundwater systems by earthquakes. Geophysical Research Letters, 42(22), 9758-9763.

Linde, A.T., Sacks, I.S., Johnston, M.J., Hill, D.P. and Bilham, R.G. (1994). Increased pressure from rising bubbles as a mechanism for remotely triggered seismicity. Nature, 371, 408-410.

Liu, C., Linde, A. T., Sacks, I. S., 2009. Slow earthquakes triggered by typhoons. Nature 459 (7248), 833–836.

Liu, L.B., Roeloffs, E. and Zheng, X.Y. (1989). Seismically induced water level fluctuations in the Wali well, Beijing, China. Journal of Geophysical Research, 94, 9453-9462.

Lu, C. C., Hwang, J. H., & Hsu, S. Y. (2017). The impact evaluation of soil liquefaction on low-rise building in the Meinong earthquake. Earth, Planets and Space, 69(1), 109.

Luttrell, K., Sandwell, D., 2010. Ocean loading effects on stress at near shore plate boundary fault systems. Journal of Geophysical Research: Solid Earth (1978–2012) 115 (B8).

Maestrelli, D., Bonini, M., Delle Donne, D., Manga, M., Piccardi, L., & Sani, F. (2017). Dynamic triggering of mud volcano eruptions during the 2016–2017 Central Italy seismic sequence. Journal of Geophysical Research: Solid Earth, 122(11), 9149-9165.

Manga, M. and Wang, C.-Y. (2015) Earthquake hydrology, Treatise of Geophysics, second edition.

Manga, M., & Rowland, J. C. (2009). Response of Alum Rock springs to the October 30, 2007 Alum Rock earthquake and implications for the origin of increased discharge after earthquakes. Geofluids, 9(3), 237-250.

Manga, M., Beresnev, I., Brodsky, E. E., Elkhoury, J. E., Elsworth, D., Ingebritsen, S. E., ... & Wang, C. Y. (2012). Changes in permeability caused by transient stresses: Field observations, experiments, and mechanisms. Reviews of Geophysics, 50(2).

Marone, C. J., Scholtz, C. H., & Bilham, R. (1991). On the mechanics of earthquake afterslip. Journal of Geophysical Research: Solid Earth, 96(B5), 8441-8452.

Matsumoto, N. and Roeloffs, E.A. (2003) Hydrological response to earthquakes in the Haibara well, central Japan–II. Possible mechanism inferred from time-varying hydraulic properties. Geophysical Journal International, 155, 899-913.

Matsumoto, N., Kitagawa, G. and Roeloffs, E.A. (2003) Hydrological response to earthquakes in the Haibara well, central Japan–I. Groundwater level changes revealed using state space decomposition of atmospheric pressure, rainfall and tidal responses. Geophysical Journal International, 155, 885-898.

Mazzini, A., & Etiope, G. (2017). Mud volcanism: an updated review. Earth-Science Reviews, 168, 81-112.

Mellors, R., Kilb, D., Aliyev, A., Gasanov, A., & Yetirmishli, G. (2007). Correlations between earthquakes and large mud volcano eruptions. Journal of Geophysical Research: Solid Earth, 112(B4).

Minato, S., Tsuji, T., Ohmi, S., & Matsuoka, T. (2012). Monitoring seismic velocity change caused by the 2011 Tohoku-oki earthquake using ambient noise records. Geophysical Research Letters, 39(9).

Mohr, C. H., Manga, M., Wang, C. Y., & Korup, O. (2017). Regional changes in streamflow after a megathrust earthquake. Earth and Planetary Science Letters, 458, 418-428.

Molnar, P., England, P., 1990. Late cenozoic uplift of mountain ranges and global climate change: chicken or egg? Nature 346 (6279), 29–34.

Montgomery-Brown, E. K., Shelly, D. R., & Hsieh, P. A. (2019). Snowmelt-triggered earthquake swarms at the margin of Long Valley Caldera, California. Geophysical Research

Letters.

Mu, C. H., Angelier, J., Lee, J. C., Chu, H. T., & Dong, J. J. (2011). Structure and Holocene evolution of an active creeping thrust fault: The Chihshang fault at Chinyuan (Taiwan). Journal of Structural Geology, 33(4), 743-755.

Nur, A. (1972). Dilatancy, pore fluids, and premonitory variations of ts/tp travel times. Bulletin of the Seismological society of America, 62, 1217-1222.

Ogata, Y., 1988. Statistical models for earthquake occurrences and residual analysis for point processes. J. Am. Stat. Assoc. 83, 9–27.
Parsons, T., Malagnini, L. and Akinci, A. (2017). Nucleation speed limit on remote fluid-induced earthquakes. Science Advances, 3, 1700660.

Phillips, O.M., 1991, Flow and Reactions in Permeable Rocks: Cambridge, UK, Cambridge University Press, 296 p.

Pliny (77) Pliny's natural history. in thirty-seven books. P. Holland, edited 1601 by the wernerian club., 720; http://www.biodiversitylibrary.org/bibliography/32799

Prejean, S.G., Hill, D.P., Brodsky, E.E., Hough, S.E., Johnston, M.J.S., Malone, S.D., Oppenheimer, D.H., Pitt, A.M. and Richards-Dinger, K.B. (2004). Remotely triggered seismicity on the United States west coast following the Mw 7.9 Denali fault earthquake. Bulletin of the Seismological Society of America, 94, S348-S359.

Reasenberg, P. (1985) Second-order moment of central california seismicity, 1969-82.

Reid, H. F. (1910) Elastic rebound theory, Univ. Calif. Publ. Bull. Dept. Geol. Sci., 6, 92-120.

Roberts, J. H. (2015). The fluffy core of Enceladus. Icarus, 258, 54-66.
Roeloffs, E. (1996). Poroelastic techniques in the study of earthquake-related hydrologic phenomena. Advances in Geophysics, 135–195.

Roeloffs, E. A. (2001). Creep rate changes at Parkfield, California 1966–1999: Seasonal, precipitation induced, and tectonic. Journal of Geophysical Research: Solid Earth, 106(B8), 16525-16547.

Roeloffs, E. A. (1988) Fault stability changes induced beneath a reservoir with cyclic variations in water level. Journal of Geophysical Research: Solid Earth (1978–2012) 93 (B3), 2107–2124.

Roeloffs, E., Sneed, M., Galloway, D.L., Sorey, M.L., Farrar, C.D., Howle, J.F. and Hughes, J. (2003). Water-level changes induced by local and distant earthquakes at Long Valley caldera, California. Journal of Volcanology and Geothermal Research, 127, 269-303.

Rojstaczer, S., & Wolf, S. (1992). Permeability changes associated with large earthquakes: An example from Loma Prieta, California. Geology, 20(3), 211-214.

Rojstaczer, S., Wolf, S., & Michel, R. (1995). Permeability enhancement in the shallow crust as a cause of earthquake-induced hydrological changes. Nature, 373(6511), 237.

Rudolph, M. L., Manga, M., Tingay, M., & Davies, R. J. (2015). Influence of seismicity on the Lusi mud eruption. Geophysical Research Letters, 42(18), 7436-7443.

Rutter, H. K., Cox, S. C., Ward, N. D., & Weir, J. J. (2016). Aquifer permeability change caused by a near-field earthquake, Canterbury, New Zealand. Water Resources Research, 52(11), 8861-8878.

Rydelek, P. A., Sacks, I. S., Scarpa, R., 1992. On tidal triggering of earthquakes at campi flegrei, italy. Geophysical journal international 109 (1), 125–137.

Saar, M. O., & Manga, M. (2003). Seismicity induced by seasonal groundwater recharge at Mt. Hood, Oregon. Earth and Planetary Science Letters, 214(3-4), 605-618.

Savage, J. C. (1983). A dislocation model of strain accumulation and release at a subduction zone. Journal of Geophysical Research: Solid Earth, 88(B6), 4984-4996.

Schaff, D. P., Richards, P. G., 2004. Repeating seismic events in china. Science 303 (5661), 1176–1178.

Schmidt, D. A., Bürgmann, R., Nadeau, R. M., & d'Alessio, M. (2005). Distribution of aseismic slip rate on the Hayward fault inferred from seismic and geodetic data. Journal of Geophysical Research: Solid Earth, 110(B8).

Schuster, A. (1897) On lunar and solar periodicities of earthquakes. Annalen der Physik 61, 455–465.

Shalev, E., Kurzon, I., Doan, M.L. and Lyakhovsky, V. (2016a). Water-level oscillations caused by volumetric and deviatoric dynamic strains. Geophysical Journal International, 204, 841-851.

Shalev, E., Kurzon, I., Doan, M.L. and Lyakhovsky, V. (2016b). Sustained water-level changes caused by damage and compaction induced by teleseismic earthquakes. Journal of

Geophysical Research, 121, 4943-4954.

Shearer, P., Stark, P., 2012. Global risk of big earthquakes has not recently increased. Proc. Nat. Acad. Sci. 109, 717–721.

Shelly, D.R., Elsworth, W.L. and Hill, D.P. (2016). Fluid-faulting evolution in high definition: Connecting fault structure and frequency-magnitude variations during the 2014 Long Valley Caldera, California, earthquake swarm. Journal of Geophysical Research, 121, 1776-1795.

Shi, Z., Wang, G., Manga, M., & Wang, C. Y. (2015). Mechanism of co-seismic water level change following four great earthquakes–insights from co-seismic responses throughout the Chinese mainland. Earth and Planetary Science Letters, 430, 66-74.

Sibson, R.H. (1990). Conditions for fault-valve behavior. Geological Society, London, Special Publications 54.1: 15-28.

Skelton, A., Andrén, M., Kristmannsdóttir, H., Stockmann, G., Mörth, C. M., Sveinbjörnsdóttir, Á., ... & Siegmund, H. (2014). Changes in groundwater chemistry before two consecutive earthquakes in Iceland. Nature Geoscience, 7(10), 752.

Skelton, A., Liljedahl-Claesson, L., Wästeby, N., Andrén, M., Stockmann, G., Sturkell, E., ... & Keller, N. (2019). Hydrochemical changes before and after earthquakes based on long term measurements of multiple parameters at 2 sites in northern Iceland–a review. Journal of Geophysical Research: Solid Earth.

Sondergeld, C.H., and Turcotte, D.L. (1978) Flow visualization studies of two-phase thermal convection in a porous layer: Pure and Applied Geophysics , v. 117, p. 321–330, https://doi.org/10.1007/BF00879757.

Steckler, M. S., Nooner, S. L., Akhter, S. H., Chowdhury, S. K., Bettadpur, S., Seeber, L., Kogan, M. G. (2010) Modeling earth deformation from monsoonal flooding in bangladesh using hydrographic, gps, and gravity recovery and climate experiment (grace) data. Journal of Geophysical Research: Solid Earth 115 (B8).

Sterling, A., and Smets, E. (1971). "Study of earth tides, earthquakes and terrestrial spectroscopy by analysis of the level fluctuations in a borehole at Heibaart (Belgium)." Geophysical Journal International, 23, no. 2: 225-242.

Sturtevant, B., Kanamori, H. and Brodsky, E.E. (1996). Seismic triggering by rectified diffusion in geothermal systems. Journal of Geophysical Research, 101, 25269-25282.

Sutherland, R., Toy, V. G., Townend, J., Cox, S. C., Eccles, J. D., Faulkner, D. R., ... & Carpenter, B. M. (2012). Drilling reveals fluid control on architecture and rupture of the Alpine fault, New Zealand. Geology, 40(12), 1143-1146.

Taira, T. A., Brenguier, F., & Kong, Q. (2015). Ambient noise-based monitoring of seismic velocity changes associated with the 2014 Mw 6.0 South Napa earthquake. Geophysical Research Letters, 42(17), 6997-7004.

Tanaka, S., 2012. Tidal triggering of earthquakes prior to the 2011 tohoku-oki earthquake (M 9.1). Geophysical Research Letters 39 (7).

Thomas, A. M., Nadeau, R. M., Bürgmann, R. (2009) Tremor-tide correlations and near-lithostatic pore pressure on the deep san andreas fault. Nature 462 (7276), 1048–1051.

Thomas, M. Y., Avouac, J. P., Champenois, J., Lee, J. C., & Kuo, L. C. (2014). Spatiotemporal evolution of seismic and aseismic slip on the Longitudinal Valley Fault, Taiwan. Journal of Geophysical Research: Solid Earth, 119(6), 5114-5139.

Thomas, M. Y., Avouac, J. P., Gratier, J. P., & Lee, J. C. (2014). Lithological control on the deformation mechanism and the mode of fault slip on the Longitudinal Valley Fault, Taiwan. Tectonophysics, 632, 48-63.

Tiwari, V., Wahr, J., Swenson, S. (2009) Dwindling groundwater resources in northern india, from satellite gravity observations. Geophysical Research Letters 36 (18).

Todd, D. K. (1961) Ground water hydrology. Quarterly Journal of the Royal Meteorological Society 87 (371), 122–122.

Tsai, C. C., Hsu, S. Y., Wang, K. L., Yang, H. C., Chang, W. K., Chen, C. H., & Hwang, Y. W. (2018). Geotechnical Reconnaissance of the 2016 ML6. 6 Meinong Earthquake in Taiwan. Journal of Earthquake Engineering, 22(9), 1710-1736.

Tsai, V. C. (2011) A model for seasonal changes in gps positions and seismic wave speeds due to thermoelastic and hydrologic variations. Journal of Geophysical Re- search: Solid Earth 116 (B4).

Udell, K.S. (1985) Heat transfer in porous media considering phase change and capillarity—The heat pipe effect: International Journal of Heat and Mass Transfer , v. 28, p. 485–495, https://doi.org/10.1016/0017-9310(85)90082-1.

van Dam, T., Wahr, J., Milly, P., Shmakin, A., Blewitt, G., Lavallée, D., Larson, K., 2001. Crustal displacements due to continental water loading. Geophysical Research Letters

28 (4), 651–654.

van Stiphout, T., Zhuang, J., Marsan, D. (2012) Seismicity declustering. Community Online Resource for Statistical Seismicity Analysis 10.

Vandemeulebrouck, J., Stemmelen, D., Hurst, T., and Grangeon, J. (2005) Analogue modeling of instabilities in crater lake hydrothermal systems: Journal of Geophysical Research , v. 110, B02212, https://doi.org/10.1029/2003JB002794.

Velasco, A.A., Hernandez, S., Parsons, T. and Pankow, K. (2008). Global ubiquity of dynamic earthquake triggering. Nature Geoscience, 1, 375-379.

Wallace, P.J., Dufek, J., Anderson, A.T., and Zhang, Y. (2002) Cooling rates of Plinian-fall and pyroclastic-flow deposits in the Bishop Tuff: Inferences from water speciation in quartz-hosted glass inclusions: Bulletin of Volcanology , v. 65, p. 105–123, https://doi.org/10.1007/s00445-002-0247-9.

Wang, C. S. (1976). The Lichi Formation of the Coastal Range and arc-continent collision in eastern Taiwan. Bull. Geol. Surv. Taiwan, 25, 73-86.

Wang, C. Y., & Manga, M. (2010). Hydrologic responses to earthquakes and a general metric. Geofluids, 10(1-2), 206-216.

Wang, C. Y., & Manga, M. (2015). New streams and springs after the 2014 Mw6. 0 South Napa earthquake. Nature communications, 6, 7597.

Wang, C. Y., Cheng, L. H., Chin, C. V., & Yu, S. B. (2001). Coseismic hydrologic response of an alluvial fan to the 1999 Chi-Chi earthquake, Taiwan. Geology, 29(9), 831-834.

Wang, C. Y., Liao, X., Wang, L. P., Wang, C. H., & Manga, M. (2016). Large earthquakes create vertical permeability by breaching aquitards. Water Resources Research, 52(8), 5923-5937.

Wang, C. Y., Manga, M., Wang, C. H., & Chen, C. H. (2012). Transient change in groundwater temperature after earthquakes. Geology, 40(2), 119-122.

Wang, C. Y., Wang, C. H., & Manga, M. (2004). Coseismic release of water from mountains: Evidence from the 1999 (Mw= 7.5) Chi-Chi, Taiwan, earthquake. Geology, 32(9), 769-772.

Wang, C.Y., Chia, Y., Wang, P.L. and Dreger, D. (2009). Role of S waves and Love waves in coseismic permeability enhancement. Geophysical Research Letters, 36(9).

Wang, K., Hu, Y., & He, J. (2012). Deformation cycles of subduction earthquakes in a viscoelastic Earth. Nature, 484(7394), 327.

Weingarten, M. and Ge, S. (2014). Insights into water level response to seismic waves: A 24 year high-fidelity record of global seismicity at Devils Hole. Geophysical Research Letters, 41, 74-80.

Wilcock, W. S. (2001) Tidal triggering of microearthquakes on the juan de fuca ridge. Geophys. Res. Lett 28 (20), 3999–4002.

Woods, A.W. (1999) Liquid and vapor flow in superheated rock: Annual Review of Fluid Mechanics , v. 31, p. 171–199, https://doi.org/10.1146/annurev.fluid.31.1.171.

Xue, L., Li, H. B., Brodsky, E. E., Xu, Z. Q., Kano, Y., Wang, H., ... & Yang, G. (2013). Continuous permeability measurements record healing inside the Wenchuan earthquake fault zone. Science, 340(6140), 1555-1559.

Yang, T. F., Yeh, G. H., Fu, C. C., Wang, C. C., Lan, T. F., Lee, H. F., ... & Sung, Q. C. (2004). Composition and exhalation flux of gases from mud volcanoes in Taiwan. Environmental Geology, 46(8), 1003-1011.

You, C. F., Gieskes, J. M., Lee, T., Yui, T. F., & Chen, H. W. (2004). Geochemistry of mud volcano fluids in the Taiwan accretionary prism. Applied Geochemistry, 19(5), 695-707.

Zhang, Y., Fu, L.Y., Huang, F. and Chen, X. (2015). Coseismic water-level changes in a well induced by teleseismic waves from three large earthquakes. Tectonophysics, 651, 232-241.

Zhuang, J., Harte, D., Werner, M., Hainzl, S., Zhou, S. (2012) Basic models of seismicity: temporal models, community online resource for statistical seismicity analysis.

Zoback, M. D., Townend, J. (2001) Implications of hydrostatic pore pressures and high crustal strength for the deformation of intraplate lithosphere. Tectonophysics 336 (1), 19–30.

Zoback, M. D., Townend, J., Grollimund, B. (2002) Steady-state failure equilibrium and deformation of intraplate lithosphere. International Geology Review 44 (5), 383–401.